Carbon Derived Electrodes and Electrolytes for Electrochemical Energy Systems

A Thesis

Submitted in Partial Fulfilment of the Requirements

for the Degree of

Doctor of Philosophy

by

Mr. Manu Gautam

(ID: 20153407)

Department of Chemistry

Indian Institute of Science Education and Research (IISER)

Pune, India – 411008

Dedicated to

My Beloved

Parents

भारतीय विज्ञान विक्षा एिं अनुसंधान संस्थान, पुणे

INDIAN INSTITUTE OF SCIENCE EDUCATION AND RESEARCH (IISER), PUNE

(An Autonomous Institution, Ministry of Human Resource Development, Govt. of India)

Dr. Homi Bhabha Road, Pune – 411 008

CERTIFICATE

This is to certify that this thesis entitled "Carbon Derived Electrodes and Electrolytes for Electrochemical Energy Systems" towards the partial fulfilment of Ph.D. programme at the Indian Institute of Science Education and Research, Pune represents original research carried out by Mr. Manu Gautam at Indian Institute of Science Education and Research, Pune under the supervision of Prof. Muhammed Musthafa O. T., Associate Professor, Department of Chemistry and Centre for Energy Science, IISER Pune during the academic year 2015 - 2021 and that no part of it has been included in any other thesis submitted previously for the award of any degree.

Signature of the Thesis Supervisor   Date: 10th March, 2021

Dr. Muhammed Musthafa O. T.

Associate Professor,

Department of Chemistry and Centre for Energy Science,

IISER Pune.

DECLARATION

I hereby declare that the work embodied in the thesis entitled "Carbon Derived Electrodes and Electrolytes for Electrochemical Energy Systems" are the results of the investigations carried out by me at the Department of Chemistry and Centre for Energy Science of the Indian Institute of Science Education and Research, under the supervision of Prof. Muhammed Musthafa O. T., Associate Professor, Department of Chemistry and Centre for Energy Science, IISER Pune and that no part of this thesis has been included in any other thesis submitted previously for the award of any degree.

Signature of the student   Date: 10th March, 2021

Mr. Manu Gautam

Reg. No: 20153407

IISER Pune

ACKNOWLEDGEMENT

At the outset, I, would like to express my sincere thanks and regards to everyone who has helped me in one way or the other and thereby contributing to this exciting journey of mine towards the fulfilment of my long-cherished dream.

To start with, I would like to express my deepest gratitude towards my supervisor Dr. Muhammed Musthafa O. T. for providing continuous support and guidance throughout my Ph.D. journey. He has provided me the outstanding facilities in the lab and fruitful working environment. He has given me full freedom to pursue various projects without any objection and has given many insightful discussions into each and every minute topic. I am very much thankful to him for his scientific guidance and suggestions. Throughout my entire Ph.D. programme, his patience, enthusiasm, immense knowledge, constant motivation, and positive feedback has helped me to become an independent thinker. Amongst various other things he has instilled in me the importance of always being technically sound and scientifically ethical. His teachings through regular one to one meetings and various informal chats during the morning and afternoon tea sessions were very valuable for making me an independent researcher as well as a good human being.

Also, I would want to express my sincere gratitude and respect to my RAC members Emeritus Prof. Satishchandra B. Ogale and Dr. Pramod Pillai from IISER Pune for their continuous support and extremely valuable scientific inputs and suggestions during the last 4 years, especially during my RAC meetings. My deepest regards are also due to the former director, Prof. K.N. Ganesh and the present director, Prof. Jayant Udgaonkar for providing such state-of-the art facilities in the institute, high-quality research infrastructure and rich academic ambience. The numerous invited talks by experts, symposia and conferences held at IISER Pune always brought rich insights to all of us. I am extremely thankful to IISER Pune MHRD for providing me with the Ph.D. fellowship for the last five years and for their travel support to attend various international conferences. Also, I am thankful to the faculties of the chemistry

Table of Contents

Table of Contents

Synopsis of the thesis entitle "Carbon Derived Electrodes and Electrolytes for Electrochemical Energy Systems"

Inconsiderate consumption of non-renewable energy resources are primarily responsible for catastrophic climate change and global warming.[1] In this context, harvesting renewable energy from their infinite resources (wind, solar, hydropower, biomass etc.) play significant roles in sustainable energy landscape because of their immense environmental advantages.[2,3] However, the intermittent nature and temporal variations of renewable energy resources cause imbalance between power supply and demand and electrochemical energy devices can serve as efficient tools to bridge this mismatch.[3,4] Carbon based materials are ubiquitous as electrodes and electrolytes in electrochemical energy devices because of their desirable properties like high electrical conductivity, high thermal stability, ability to conduct protons, ability to function as molecular fuel barriers etc.[5-7] However, in the context of aqueous metal ion batteries, utilization of carbon materials as electrodes often lead to spontaneous de-insertion reactions, undesirable proton insertions reactions, parasitic hydrogen evolution reactions, unwanted swelling etc.[8,9] Aqueous redox flow batteries based on outer sphere redox molecules suffer from their inferior volumetric energy density due to the underutilization of dissolved electroactive species and even the employment of high surface area carbon nanotube (CNT) electrodes have not made enough advancement beyond a threshold.[10-13] With regard to energy conversion devices such as water electrolysers and fuel cells, though carbon based materials like oxidized graphene are predicted with the capability to conduct protons and to function as effective molecular fuel barriers;[14,15] they have not been explored in their pristine free standing form to shuttle protons in a unitized regenerative fuel cell architecture.

Therefore, the primary aim of this thesis is to exploit carbon derived materials as electrodes in energy storage systems and as electrolytes (membranes) in energy conversion systems to address some of their state-of-the-art issues and challenges and to investigate their unexplored properties. With this aim, this thesis is divided into two parts: **Part I** explores the utilization of carbon derived materials as electrodes in energy storage devices such as aqueous rechargeable sodium ion battery and aqueous redox flow battery and **Part II** deals with the exploitation of carbon derived materials as electrolytes in proton exchange membrane (PEM) fuel cell, PEM water electrolyzer and unitized regenerative fuel cell (URFC). The thesis is divided into following chapters:

Chapter 1.   Introduction: This chapter explains the importance, advantages, issues and challenges of carbon-based materials as electrodes and electrolytes in electrochemical energy storage and conversion devices. Though, carbon-based materials have interesting properties which make them ubiquitous in electrochemical energy systems, its utilization brings forth own challenges and issues. For example, in aqueous metal-ion batteries the employment of carbon-based materials as anode materials often contribute to a range of issues like electrode corrosion, spontaneous de-insertion reaction, undesirable proton insertion reaction, hydrogen evolution reactions, unwanted swelling etc. Secondly, in redox flow batteries based on outer sphere cathodes, even the utilization of high surface area carbon nanotube electrodes so far could not address their inferior volumetric energy density beyond a threshold. Finally, though graphene oxide (GO) has been predicted with the capability to conduct protons and to function as molecular fuel barriers owing to their hydrophilic functionalities, a free-standing GO membrane in their pristine form have not been employed to shuttle protons back and forth in a URFC. Towards the end of this chapter, the aim and scope of the present thesis is outlined, where the approach with carbon derived materials to develop a rechargeable aqueous sodium ion battery, a redox flow battery with high energy density and a low temperature URFC are outlined.

<div align="center">

Part I

</div>

Chapter 2. Coulombic Force Gated Molecular Transport in Redox Flow Batteries: This chapter explains how the activation of coulombic forces at the carbon nanotube (CNT) electrode/electrolyte interface leads to a gated molecular transport in redox flow batteries. In the state of art flow batteries, fuel cells and electrochemical biosensors, interfacial electrochemistry of reversible redox active molecules plays a vital role in dictating their overall performance. Since, the mass transport and electron transport are consecutive processes at the electrode-electrolyte interface; the reaction velocity of reversible species is predominantly mass-transport controlled due to their fast electron transfer events. The dominant mode of transport near the electrode-electrolyte interface is diffusion even under a convective fluid-flow which in turn poses inimitable challenges to explore the maximum potential of reversible redox species either by the electrode or fluid characteristics. In this chapter, how the activation of coulombic forces at the CNT electrode/electrolyte interface gates the molecular transport by generating a directional electrostatic current contribution over the diffusion is demonstrated (Figure 1). In iron based redox flow battery, this gated

molecular flux almost doubles the volumetric energy density without compromising the power capability by extending the concentration polarization regime, Figure 1.
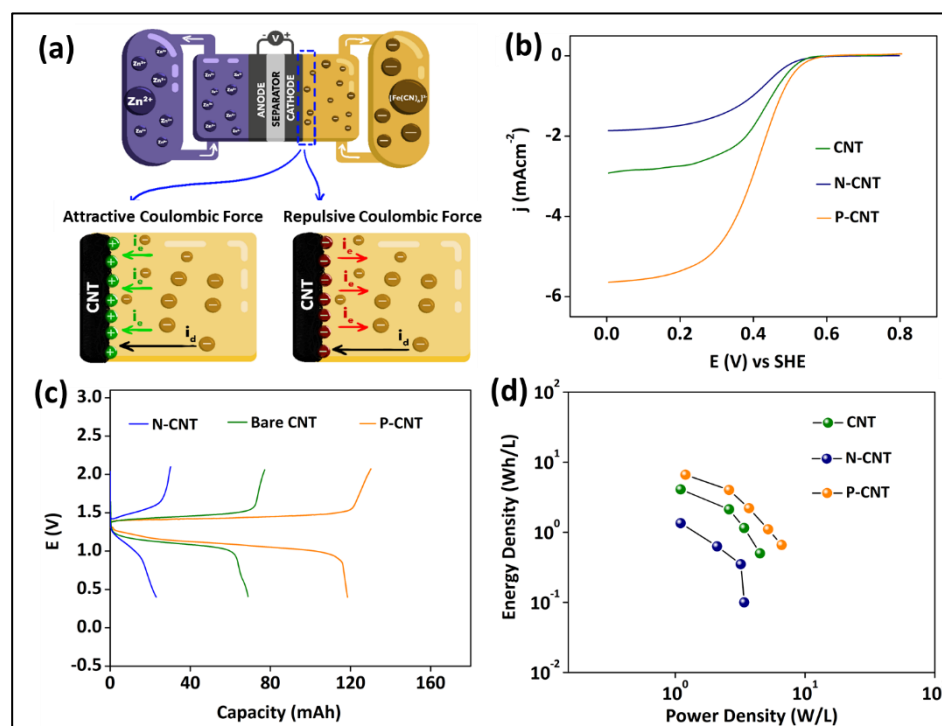
Figure 1: (a) Schematics of Zn-ferricyanide redox flow battery (top). The anodic half-cell is Zn/Zn^{2+} and the cathodic half-cell is ferricyanide/ferrocyanide redox couple separated by Nafion 117 membrane. Bottom scheme shows the representation of coulombic force gated molecular flux at the interface. (b) Rotating disk electrode (RDE) measurements for unmodified CNT, negatively charged CNT (N-CNT) and positively charged CNT (P-CNT) electrodes in 1 M KNO$_3$ containing 10 mM K$_3$[Fe(CN)$_6$] at 1600 rpm and (c) charge-discharge curves of Zn-ferricyanide battery with P-CNT, unmodified CNT and N-CNT electrodes at 20 mA cm^{-2}. (d) Ragone plots for Zn-ferricyanide battery with P-CNT, unmodified CNT, and N-CNT electrodes.

Chapter 3. A Rechargeable Aqueous Sodium Ion Battery with a Capacitive Graphene Anode: This chapter elaborates how the mode of synthesis of graphene anodes influence the performance metrics of an aqueous metal ion battery and explains the factors responsible for it. The state of art anodes in aqueous rechargeable metal ion batteries suffer from various challenges and issues such as unwanted swelling, electrode corrosion, undesirable proton insertion reaction and parasitic hydrogen evolution reaction. This affects the overall reversibility and stability of aqueous rechargeable metal ion batteries. To enhance the reversibility as well as the battery performance in aqueous systems, it is necessary to selectively favor the reversible electrochemical adsorption of active metal ions on the electrode surface by simultaneously preventing the parasitic hydrogen evolution

chemistry. This chapter examines how the mode of synthesis of graphene-based materials improves the quality of reduced graphene oxide material with properties relevant for constructing an aqueous rechargeable sodium ion battery. Various physicochemical analyses shows that the density of hydrophilic functionalities on the graphene electrode affects the reversibility as well as the cyclability of an aqueous sodium ion battery by chemically binding to sodium ions with poor reversibility in its electrochemical adsorption/desorption, Figure 2**.**
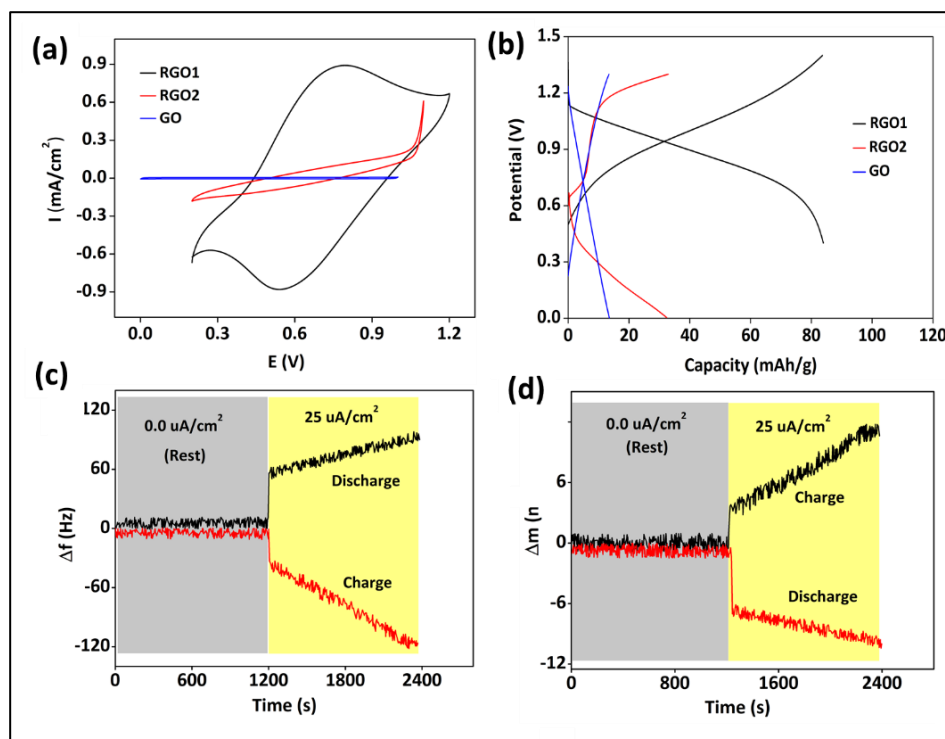
Figure 2: (a) Cyclic voltammetry of sodium ion battery in 3 M NaNO₃ at a scan rate of 5 mV s⁻¹ in two-electrode battery configuration. (b) Charge-discharge curves of Na ion battery in 3 M NaNO₃ solution at a rate of 400 mA g⁻¹. (c) Frequency change vs. time and (d) corresponding mass change vs. time obtained from electrochemical quartz crystal microbalance studies during charge-discharge chemistry of the best performing graphene (RGO1) negative electrode in aqueous sodium ion battery. RGO1 is graphene produced by Fe/HCl method and RGO2 is graphene produced by conventional borohydride method. The battery architecture consists of a graphene negative electrode (RGO1/RGO2) and a hexacyanometallate based positive electrode immersed in 3 M NaNO₃ electrolyte.

Part II

Chapter 4a. An Atmospheric Water Electrolyzer with a Graphene Oxide Proton Exchange Membrane: This chapter elaborates the utilization of freestanding GO membrane in its pristine form as electrolyte to construct a water vapor electrolyzer. GO has been predicted with the capability to conduct protons and to function as molecular fuel

barriers and in this chapter, a freestanding GO membrane is employed as a proton exchange membrane to construct a PEM water vapor electrolyzer. The hydrophilic functionalities of GO like -OH, -COOH, -C-O, -COC etc., are responsible for shuttling the protons from the anodic to the cathodic side during the splitting of water vapor into molecular fuels, Figure 3. The ability of GO based water vapour electrolyzer to split water vapour into H_2 and O_2 at a stoichiometric ratio of 2:1 is demonstrated by in-situ electrochemical mass spectrometry, Figure 3. The hydrophilic functionalities in GO even provided access to the universal feedstock of water in earth's atmosphere, which in turn could be converted into fuel molecules via electrochemical processes coupled to renewable energy, Figure 3.
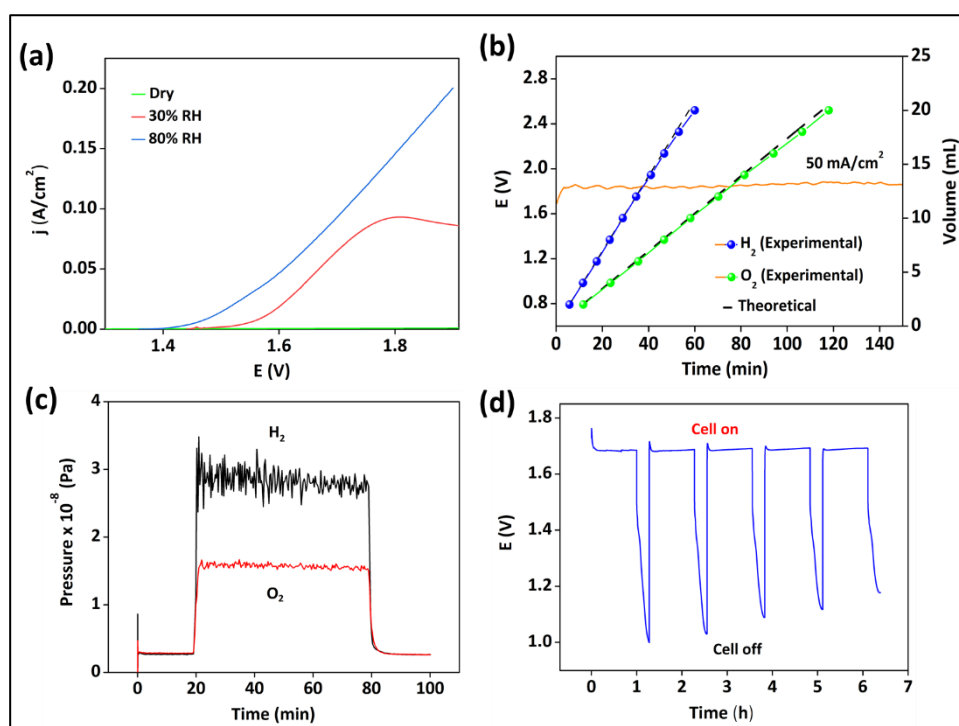
Figure 3: (a) Polarization curve of GO based water vapour electrolyzer at different relative humidity. (b) Galvanostatic polarization of GO based water vapor electrolyzer at 50 mA cm^{-2} density along with H_2 and O_2 quantification, (c) in-situ electrochemical mass spectrometric analysis of evolved H_2 and O_2 and (d) galvanostatic polarization at 50 mA cm^{-2} density when the electrolyzer is in the ON-OFF modes.

Chapter 4b. Proton Conducting Graphene Oxide Membrane for Unitized Regenerative Fuel Cell: This chapter explores the utilization of free-standing GO membrane as electrolyte to construct a low temperature URFC which is known to play vital roles in sustainable energy landscape in producing and utilizing the H_2 fuel with a near zero carbon foot print. The polarization studies in the water electrolyzer mode and H_2-O_2 fuel cell mode attest the capability of free-standing GO membrane to shuttle the protons back and forth in a URFC, Figure 4. The stability of the three-phase boundary constituting the

frees standing GO membrane in the URFC configuration is demonstrated by the long term galvanostatic measurements and post mortem analysis, Figure 4.
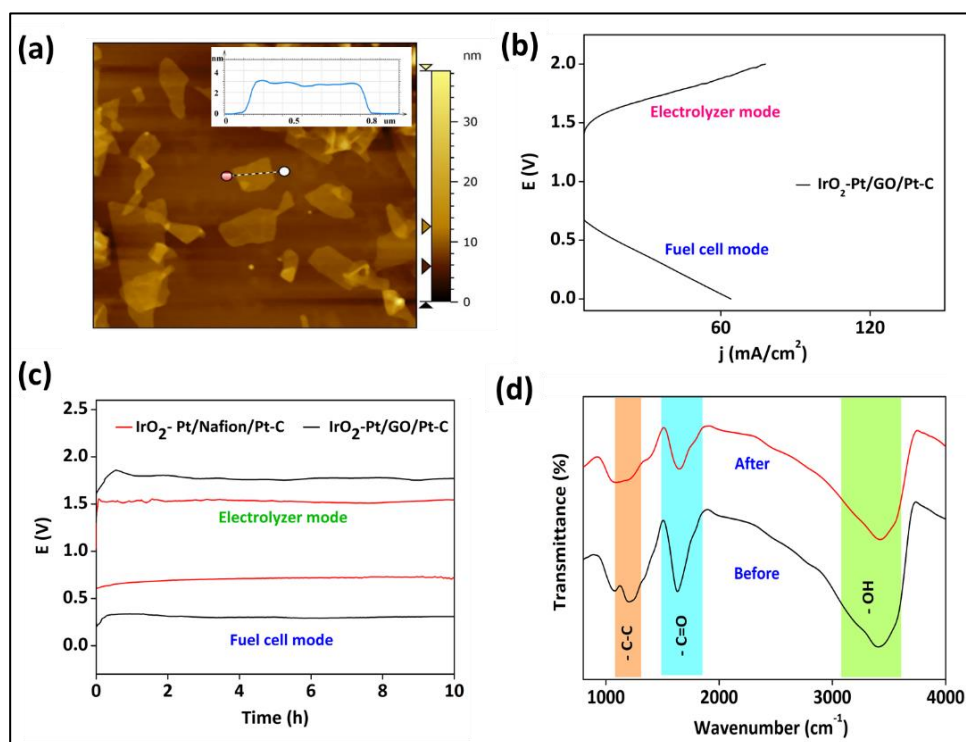
Figure 4: (a) Atomic force microscopy (AFM) image of GO flakes. Inset shows the corresponding height profile. (b) Polarization curves of GO membrane based URFC in the fuel cell and water elecrolyzer modes, (c) chronopotentiometric performance up to 10 hours at 30 mA cm^{-2} current density for GO based (thickness = ~25 μm) and Nafion 211 (thickness = ~25 μm) based URFC and (d) FTIR spectra of GO membrane before and after the long term galvanostatic measurements.

Chapter 5a. Amplification of Proton Conduction in Graphene Oxide Proton Exchange Membrane: This chapter discusses how the proton conduction capability of GO membrane can be improved so as to bridge the performance gap between GO based PEM and Nafion based PEM. The proton conductivity of GO membrane is ~10 times lower than state of the art Nafion membrane.[15,16] Since hydrophilic functionalities like -OH, -COOH, -C-O, -COC etc. are responsible for shuttling the protons in GO, any attempts to improve its hydrophilicity to increase its proton conduction capability on one hand will affect the mechanical stability of membrane in aqueous environment. On the other hand, the introduction of more hydrophobic functionalities so as to prevent the mechanical disintegration of the GO membrane will decrease its proton exchange capacity. This indicates a trade-off between proton conductivity and hydrophobicity/hydrophilicity in GO membrane which is indeed a challenge to amplify its room temperature fuel cell

performance metrics. In this chapter, proton conduction capability of pristine GO membrane is amplified by introducing to its interlayer's proton carrying quinone molecules bearing proton shuttling sulfonic acid groups. The hydrogen carrying capability of quinone functionality and proton conduction capability of sulfonic acid moiety in GO's matrices substantially improved its overall proton conduction (~7 times compared to pristine GO) capability and consequently its overall fuel cell performance metrics, Figure 5.
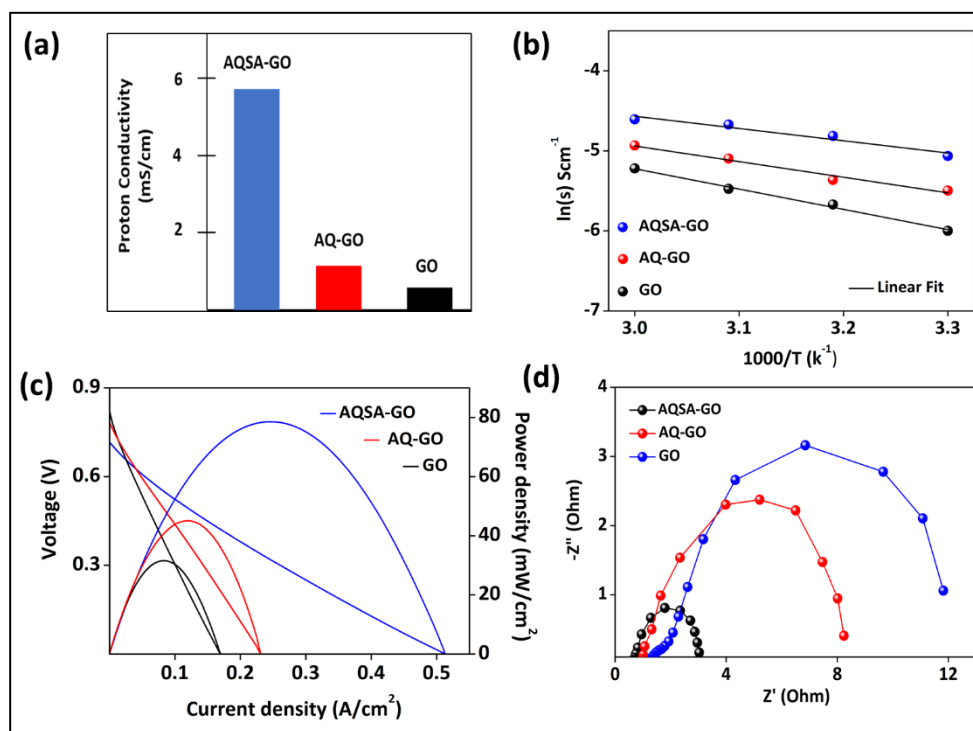
Figure 5: (a) Proton conductivities of GO, AQ-GO (~0.5 mmol g^{-1} anthraquinone composite with GO) and AQSA-GO (~0.5 mmol g^{-1} anthraquinone-2-sulphonic acid composite with GO) membranes extracted from impedance analysis. (b) Arrhenius plots for GO, AQ-GO and AQSA-GO membranes. (c) Fuel cell polarization curves of GO, AQ-GO and AQSA-GO membrane-based fuel cells at 25 $^{\circ}$C (at 30 % RH) with a H$_2$-O$_2$ flow rate of 100 mL min^{-1} and (d) electrochemical impedance plot of GO, AQ-GO and AQSA-GO membrane-based fuel cells in the frequency range of 100 kHz to 10 mHz at 0 V vs. open circuit voltage with a 10 mV excitation signal. Anode and cathode Pt/C loadings were ~0.3 mg cm^{-2}.

Chapter 5b. Implications of Thickness Reduction of Graphene Oxide Membrane in its Fuel Cell Performance: The randomly distributed non-conductive sp^3-C domains with planar acidity make GO a suitable electronic insulator as well as proton conductor. This coupled with its ability to act as a barrier to molecular fuels make it a promising inexpensive proton exchange membrane for room temperature PEM fuel cell. However, the proton conductivity of the GO is almost 10 times lower than the state of art Nafion membrane

and as explained in chapter 5a, this gap can be bridged by introducing suitable molecules into GO interlayers. Another straight forward approach to improve the proton conduction capability of GO membrane is thickness reduction as membrane thickness is directly related to membrane bulk resistance.[17,18] This chapter investigates the implications of reducing the thickness of GO membrane in the performance metrics of a GO based H_2–O_2 fuel cell system. Thin layer GO membrane of ~3 μm thickness demonstrated a larger (~3 times) proton flux compared to GO membrane of higher thickness (~25 μm), Figure 6. This higher proton flux is further responsible for its nearly 5 times higher fuel cell performance metrics in terms of current density and power density, Figure 6. The stability of this thin layer GO based fuel cell system is investigated by galvanostatic analysis at different current densities which signifies the stability of the three-phase boundary formed by the thin film GO membrane, Figure 6. However, thickness reduction accelerates fuel crossover from anodic to cathodic side by nearly ~3 times, Figure 6. Therefore, though proton flux across the membrane increases on thickness reduction, fuel crossover also increases simultaneously, Figure 6, which needs to be adequately addressed by materials engineering strategies like introducing suitable fillers and additives, adding other polymeric materials to make composite GO membranes etc., if this higher fuel cell performance metrics have to exploited for practical applications.
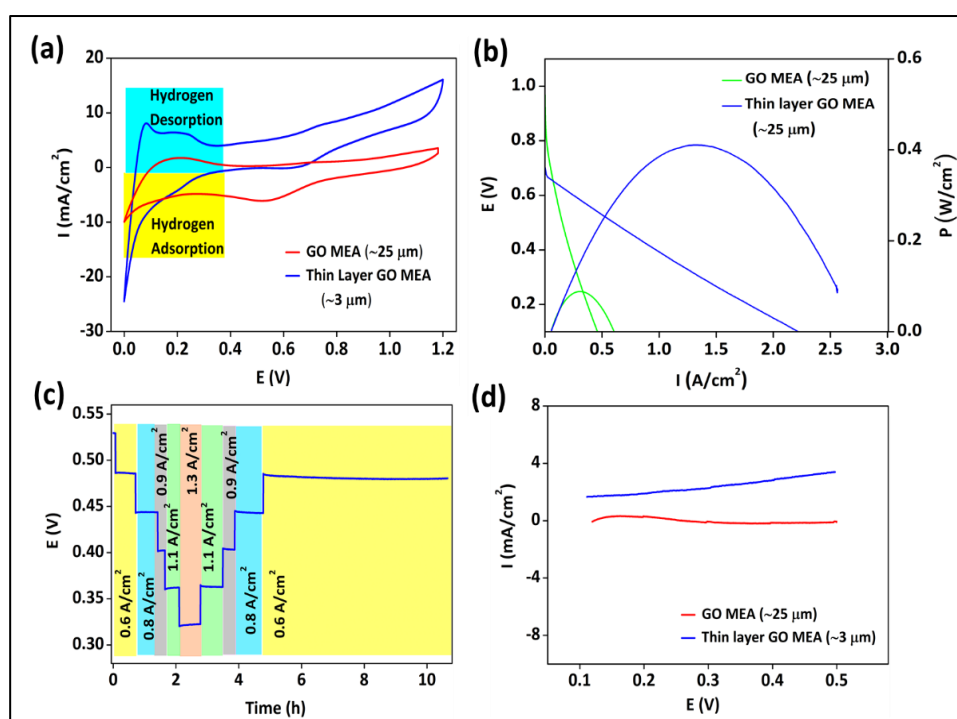
Figure 6: (a) Cyclic voltammograms at 20 mV s^{-1} of GO membrane electrode assembly (MEA) based fuel cell with the cathode (Pt/C under N_2 atmosphere) as the working electrode. The Pt/C anode was kept under H_2 atmosphere. (b) Room temperature (25 $^\circ$C)

fuel cell polarization of GO based fuel cell at 30 % RH with a H_2-O_2 flow rate of 100 mL min^{-1}, (c) rate capability of thin film GO MEA based fuel cell at different current densities and (d) H_2 cross over study in GO based fuel cells obtained by scanning the potential of the cathode positively from the open circuit voltage at 1 mV s^{-1}.

Chapter 6. This chapter provides the concluding remarks and future outlook.

References

1.   Höök, M.; Tang, X., Depletion of fossil fuels and anthropogenic climate change—A review. *Energy Policy* **2013,** *52*, 797-809.

2.   Yang, Z.; Zhang, J.; Kintner-Meyer, M. C. W.; Lu, X.; Choi, D.; Lemmon, J. P.; Liu, J., Electrochemical Energy Storage for Green Grid. *Chem. Rev.* **2011,** *111* (5), 3577-3613.

3.   Badwal, S. P. S.; Giddey, S. S.; Munnings, C.; Bhatt, A. I.; Hollenkamp, A. F., Emerging electrochemical energy conversion and storage technologies. *Front. Chem.* **2014,** *2* (79).

4.   Winter, M.; Brodd, R. J., What Are Batteries, Fuel Cells, and Supercapacitors? (Chem. Rev. 2003, 104, 4245−4269. Published on the Web 09/28/2004.). *Chem. Rev.* **2005,** *105* (3), 1021-1021.

5.   Zhang, P.; Wang, F.; Yu, M.; Zhuang, X.; Feng, X., Two-dimensional materials for miniaturized energy storage devices: from individual devices to smart integrated systems. *Chem. Soc. Rev.* **2018,** *47* (19), 7426-7451.

6.   Yang, Z.; Ren, J.; Zhang, Z.; Chen, X.; Guan, G.; Qiu, L.; Zhang, Y.; Peng, H., Recent Advancement of Nanostructured Carbon for Energy Applications. *Chem. Rev.* **2015,** *115* (11), 5159-5223.

7.   Liu, X.-M.; Huang, Z. d.; Oh, S. w.; Zhang, B.; Ma, P.-C.; Yuen, M. M. F.; Kim, J.-K., Carbon nanotube (CNT)-based composites as electrode material for rechargeable Li-ion batteries: A review. *Compos. Sci. Technol.* **2012,** *72* (2), 121-144.

8. Sun, J.; Iakunkov, A.; Rebrikova, A. T.; Talyzin, A. V., Exactly matched pore size for the intercalation of electrolyte ions determined using the tunable swelling of graphite oxide in supercapacitor electrodes. *Nanoscale* **2018,** *10* (45), 21386-21395.

9. Iakunkov, A.; Skrypnychuk, V.; Nordenström, A.; Shilayeva, E. A.; Korobov, M.; Prodana, M.; Enachescu, M.; Larsson, S. H.; V.Talyzin, A., Activated graphene as a material for supercapacitor electrodes: effects of surface area, pore size distribution and hydrophilicity. *Phys Chem Chem Phys* **2019,** *21* (32), 17901-17912.

10. Luo, J.; Wu, W.; Debruler, C.; Hu, B.; Hu, M.; Liu, T. L., A 1.51 V pH neutral redox flow battery towards scalable energy storage. *J. Mater. Chem. A* **2019,** *7* (15), 9130-9136.

11. Chang, Y.-C.; Shih, Y.-C.; Chen, J.-Y.; Lin, G.-Y.; Hsu, N.-Y.; Chou, Y.-S.; Wang, C.-H., High efficiency of bamboo-like carbon nanotubes on functionalized graphite felt as electrode in vanadium redox flow battery. *RSC Adv.* **2016,** *6* (104), 102068-102075.

12. Park, M.; Jung, Y.-j.; Kim, J.; Lee, H. i.; Cho, J., Synergistic Effect of Carbon Nanofiber/Nanotube Composite Catalyst on Carbon Felt Electrode for High-Performance All-Vanadium Redox Flow Battery. *Nano Lett.* **2013,** *13* (10), 4833-4839.

13. Munaiah, Y.; Suresh, S.; Dheenadayalan, S.; Pillai, V. K.; Ragupathy, P., Comparative Electrocatalytic Performance of Single-Walled and Multiwalled Carbon Nanotubes for Zinc Bromine Redox Flow Batteries. *J. Phys. Chem. C* **2014,** *118* (27), 14795-14804.

14. Dikin, D. A.; Stankovich, S.; Zimney, E. J.; Piner, R. D.; Dommett, G. H. B.; Evmenenko, G.; Nguyen, S. T.; Ruoff, R. S., Preparation and characterization of graphene oxide paper. *Nature* **2007,** *448* (7152), 457-460.

15. Karim, M. R.; Hatakeyama, K.; Matsui, T.; Takehira, H.; Taniguchi, T.; Koinuma, M.; Matsumoto, Y.; Akutagawa, T.; Nakamura, T.; Noro, S.-i.; Yamada, T.; Kitagawa, H.; Hayami, S., Graphene Oxide Nanosheet with High Proton Conductivity. *J. Am. Chem. Soc.* **2013,** *135* (22), 8097-8100.

16.   He, G.; He, X.; Wang, X.; Chang, C.; Zhao, J.; Li, Z.; Wu, H.; Jiang, Z., A highly proton-conducting, methanol-blocking Nafion composite membrane enabled by surface-coating crosslinked sulfonated graphene oxide. *Chem. Commun.* **2016**, *52* (10), 2173-2176.

17.   Shinde, D. B.; Vlassiouk, I. V.; Talipov, M. R.; Smirnov, S. N., Exclusively Proton Conductive Membranes Based on Reduced Graphene Oxide Polymer Composites. *ACS Nano* **2019,** *13* (11), 13136-13143.

18.   Cornet, N.; Diat, O.; Gebel, G.; Jousse, F.; Marsacq, D.; Mercier, R.; Pineri, M., Sulfonated polyimide membranes: A new type of ion-conducting membrane for electrochemical applications. *J. New Mater. Electrochem. Syst.* **2000,** *3*, 33-42.
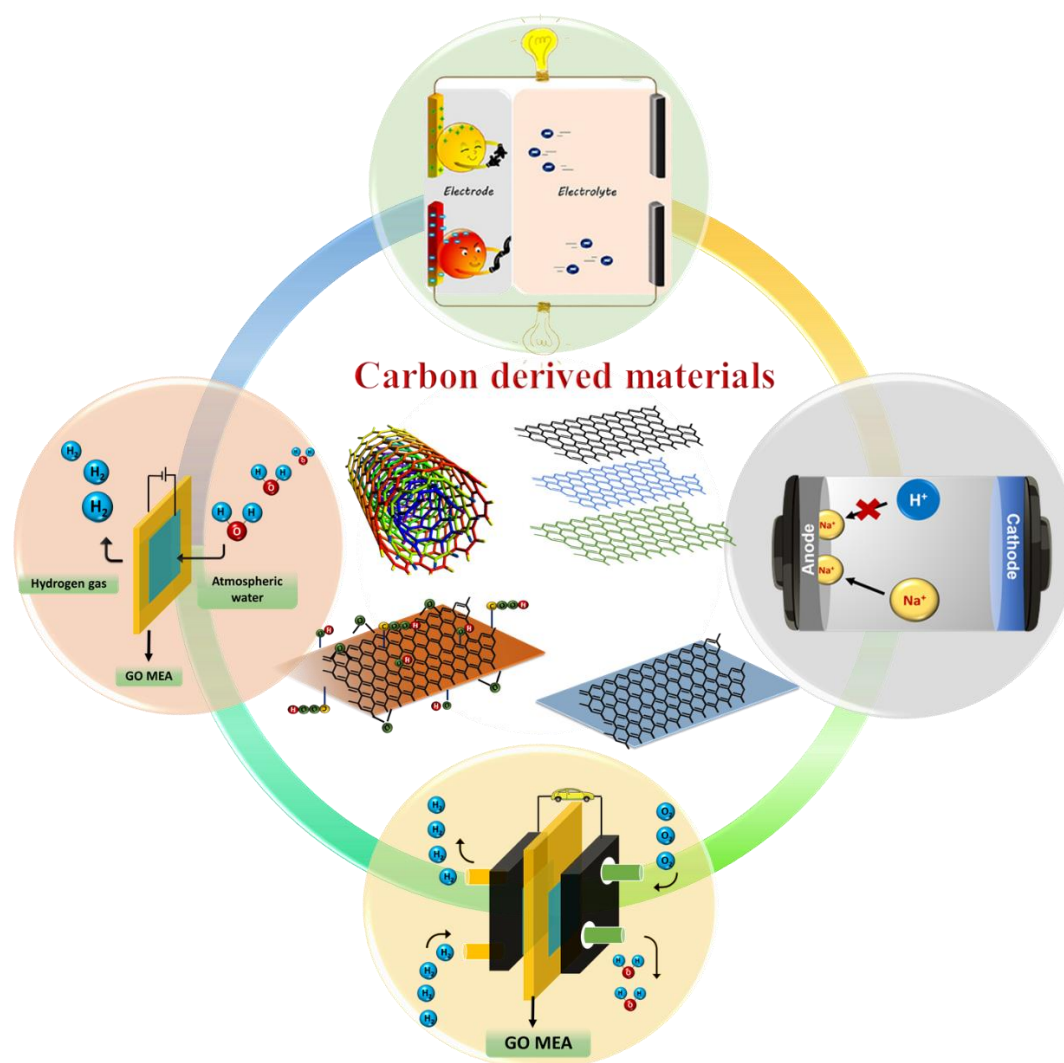
Chapter 1

Introduction

Abstract

The substantial increase in demands of energy for the social order arises the question on exploitation of different energy resources for energy conversion and storage. The shifting of demands of energy from non-renewable sources to renewable sources opens the blockades for the electrochemical energy devices in the energy sectors. In the framework of these electrochemical energy devices, carbon-based materials have gained the higher consideration in scientific community because of their various properties and high abundance. As for any electrochemical energy device, the important components are its electrodes and electrolytes but in the present scenario of these components of electrochemical energy devices, the state-of-the-art carbon-based electrodes and electrolytes face various challenges which are described in this chapter in detail. Therefore, the present dissertation focuses on the engineering of carbon-based materials so as to address the state of the art challenges and issues posed when they are utilized as electrodes and electrolytes in various electrochemical energy devices. The current chapter draws out the consideration towards the important types and properties of carbon-based materials which make them unique over other materials in electrochemical energy applications. This chapter also describes how carbon-based materials can be engineered to make them promising candidates as electrodes and electrolytes in various types of electrochemical energy storage and conversion devices such as low temperature PEM fuel cell, unitized regenerative fuel cell, aqueous rechargeable batteries and redox flow batteries.

1.1   Present global necessity and consumption of energy

Energy, which undeniably is accountable for being the heart of the growth of any society and civilization, needs no other overview for its description. It is the part of the lifecycle which has been utilized in various forms for various purposes and can be interconverted from one form to another form. There are various sources of energy such as oil, hydrogen, biomass, solar, natural gas, coal, etc. which are utilized for industrial, commercial and residential applications. In recent years, energy utilization has been increasing in the world at a faster rate. Figure 1.1 expresses the increasing rates of consumption of energy in various sectors. The main causes of higher energy consumption are increasing populations and growing industrialization.[1] This higher rate of consumption of energy resources further poses questions on the availability of energy resources and their impact on the environment.
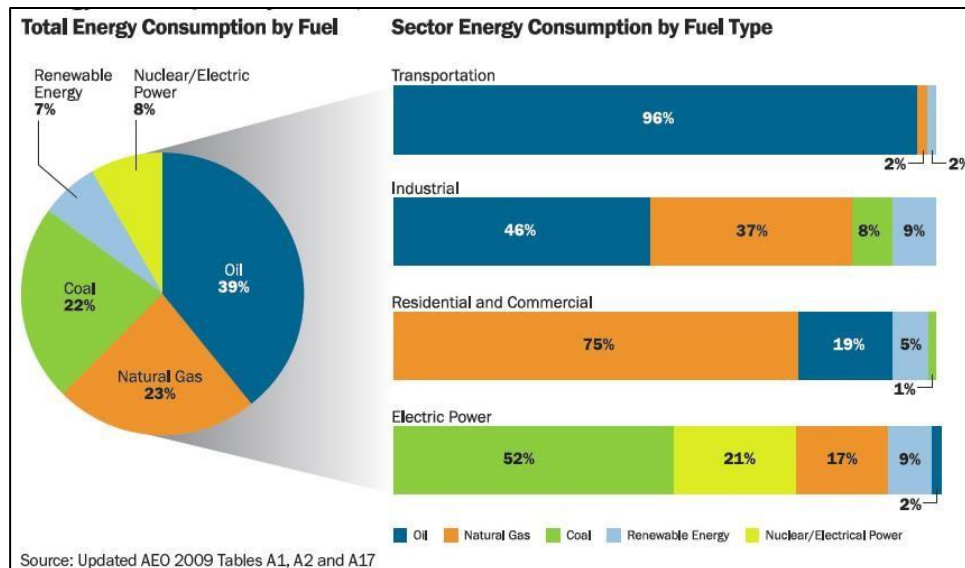
Figure 1.1 Energy consumption percentage in different sectors. (Source: https://www.bitlanders.com/blogs /comparison-of-energy-sources-with-our-daily-uses).

1.2   Types of energy resources

Energy resources can be broadly divided into two categories, Figure 1.2. 1) Non-renewable resources and 2) renewable resources:

1.2.1   Non-renewable resources

These are the limited resources of energy that were formed due to the decomposition of organic matter over millions of years. These are generally present in the

earth's crust.[2] Examples of these non-renewable resources are fossil fuel, natural gas, coal, etc. Due to their limited availability, these non-renewable resources are exhausting day by day with the increasing consumption rate of energy. Apart from their limited availability, these resources create a detrimental effect on the environment due to the emission of greenhouse gases like CO_2, SO_2, etc.[3]
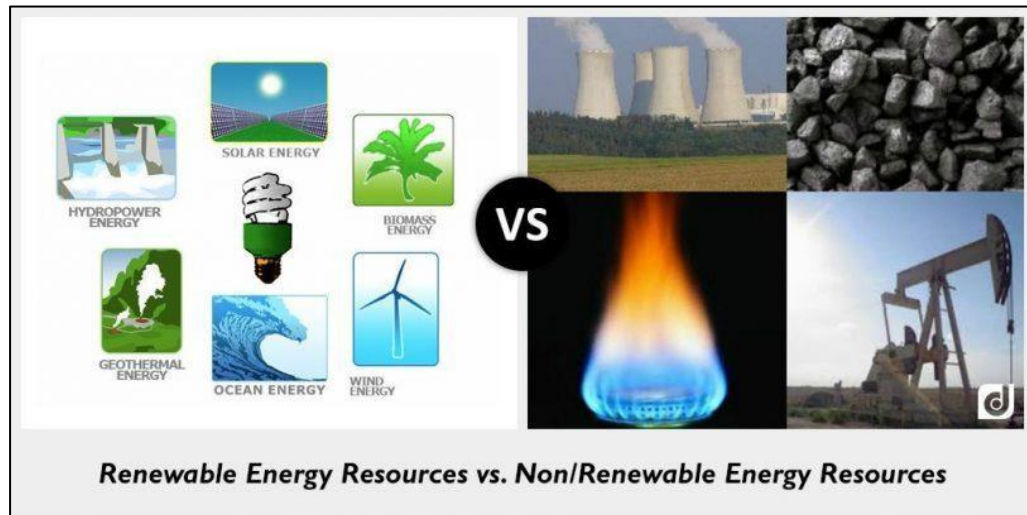
Figure 1.2 Renewable vs non-renewable resources. (Source: https://www.picemaps.com/images-of-non- renewable-resources/).

1.2.2   Renewable resources

Unlike non-renewable resources, these are the naturally occurring sources of energy that are present in abundance and are far away from the peril of complete exploitation.[2] These resources do not generate any harmful byproducts to the environment. Thus, these sources can be used as alternatives for non-renewable resources of energy. Examples of such resources are solar, biomass, ocean, wind, etc.

Due to the inadequate availability of non-renewable resources and their harmful environmental impact, the world is shifting from non-renewable resources to renewable resources of energy. These renewable energy resources are emission-free which would be the ideal solution to energy harvesting without creating harmful impact on the environment. Now, it is more important to understand the vital role that these renewable energy sources would play to fulfill the requirements of future energy sectors. The "sustainable future" state of the International Energy Agency (IEA) illustrates 57% of world's electricity would be supplied by renewable energy sources by 2050.[4] This indicates the importance of renewable energy sources such as wind and solar, etc. in the production of electrical energy which is the ultimate necessity. Regardless of having significant

advantages of these renewable energy sources over non-renewable energy sources, still they are far away for providing sufficient energy to different energy sectors. This is mainly due to their intermittent nature, temporal variations and geographic fluctuations.[5] This creates a mismatch between energy demand and energy supply and electrochemical energy storage and conversion devices can efficiently bridge this gap. This clearly highlights the role of electrochemical energy devices to store and generate electrical energy in sustainable energy landscape.

1.3   Importance of electrochemical energy devices

The electrochemical energy devices play a crucial role in energy sustainability. These devices can serve as tools for addressing the temporal and geographic fluctuations of renewable energy sources. There are various types of electrochemical energy storage and conversion devices with properties relevant to different sectors like pollution control/monitoring, greenhouse gas reduction, etc. Generally, these electrochemical energy devices offer high efficiency with low pollution to the environment and are also flexible with their construction. These properties signify the importance of these electrochemical energy devices to bridge the gap between energy demand and supply in sustainable energy landscape.[6,7] Often, these electrochemical energy devices involve hydrogen (H_2) as a fuel for energy conversion/energy storage. As we know, unlike the other sources, H_2 is the clean energy carrier molecule, because electric power production via H_2 redox reaction will not create harmful impact on the environment.[8,9] Thus, production of H_2 to fulfill the energy requirement is a global necessity. The production of H_2 from the non-renewable sources evolve various types of greenhouse gases which are responsible for climate change. This is why the arena of the electrical energy production from H_2 without the involvement of any harmful gases is always the topic of interest for the research community since decades. In this way, these electrochemical energy devices have come up as promising candidates in energy storage and conversion which can be easily coupled to renewable resources to address the mismatch between energy demand and energy supply.

1.4   Types of electrochemical energy devices

There are various types of electrochemical energy devices, Figure 1.3. Fuel cells and water electrolyzers are considered to be electrochemical energy conversion devices that convert one form of energy to another form of energy whereas batteries and

supercapacitors are energy storage devices that differ in their charge storage mechanisms.[7,8] As discussed, to accomplish the global requirements of clean energy, these energy devices play the vital roles and often a choice is made based on the requirement. The architectural components of these devices i.e., mainly electrodes and electrolytes are integral to energy storage and conversion. Electrodes are primarily responsible for the electron transfer and electrolytes mainly act as a medium and host for redox couples and ion transport.[10, 11] Based on their energy and power capabilities, these devices have been classified as shown in the Ragone plot, Figure. 1.4.
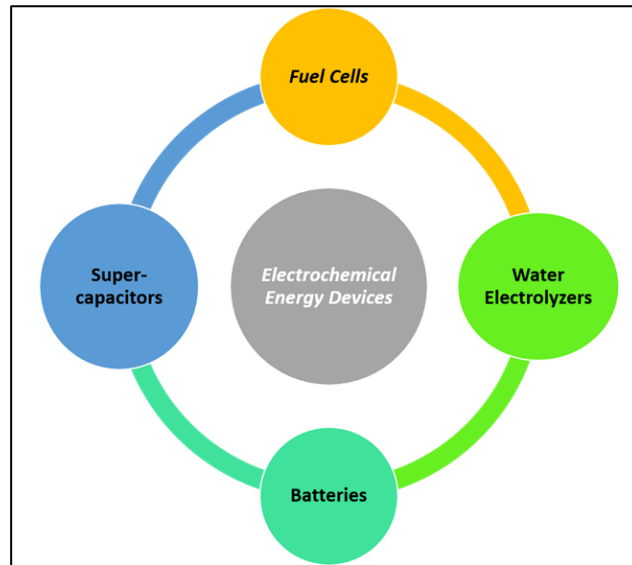
Figure 1.3   Types of electrochemical energy devices.

From the Ragone plot, one can clearly notice that the supercapacitors occupy the higher power density position whereas fuel cells possess higher energy density. The energy and power densities are the important parameters to define the output performance of any electrochemical device.[12,13] Energy density is the measure of how much energy an electrochemical energy device can store whereas power density defines how quickly the device can deliver the stored energy. In the case of energy storage devices like batteries, as these occupy the moderate positions in the Ragone plot, major focus of research has been to increase its energy density without compromising the power capability whereas, in the case of fuel cells which is an energy conversion device and converts chemical energy to electrical energy, the focus has been to increase its power density by inventing various catalysts and combinations.[14, 15]
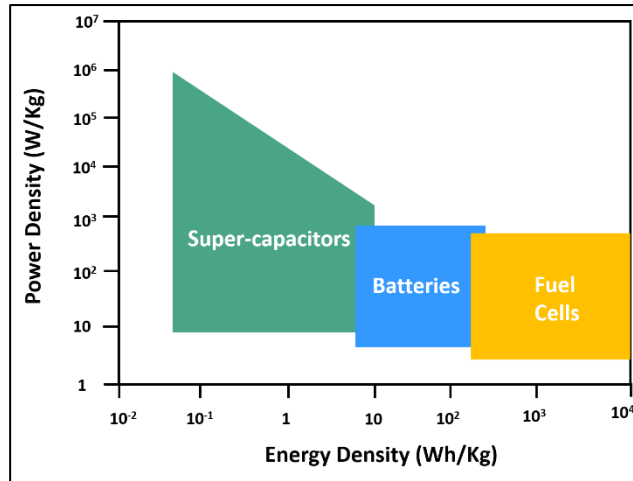
Figure 1.4 Ragone plot representing the energy and power density distribution of electrochemical energy devices.

1.4.1 Fuel Cells

Fuel cells are the electrochemical energy conversion devices that convert chemical energy to electrical energy. Figure 1.5, shows the architectural components of a fuel cell. Fuel cells consist of the electrodes (anode and cathode) which are responsible for charge transfer reactions and electrolyte which act as a medium for the ion transport during the operation of the fuel cell system.[16,17] In the case of the fuel cells, the membrane is considered to be the electrolyte as it acts as the medium for ion transport during the reactions. The fuel cell converts the chemical energy of fuel into electrical energy. At the anode of the fuel cell, the continuously flowing fuel (e.g., H_2) gets oxidized with the simultaneous reduction of O_2 at the cathode leading to the production of electricity in the external load. The basic electrochemical redox reactions of the hydrogen-oxygen fuel cell are:

At anode: $H_2 \rightarrow 2H^+ + 2e^-$ $\qquad$ ($E^0 = 0$ V vs. SHE) $\quad$ (1.1)

At cathode: $\frac{1}{2} O_2 + 2H^+ + 2e^- \rightarrow H_2O$ $\qquad$ ($E^0 = 1.23$ V vs. SHE) (1.2)
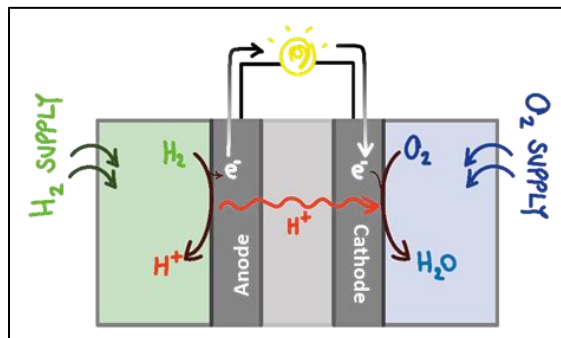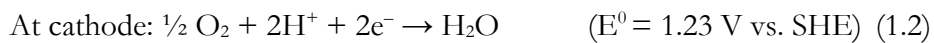
Figure 1.5 Schematic representation of a polymer electrolyte membrane (PEM) fuel cell.

Table 1.1. Different types of fuel cells with different electrolytes and operating temperatures.

Fuel Cell Types	Anode Reaction	Cathode Reaction	Operating Temperature (° C)	Mobile Ion
Proton Exchange Membrane (PEM) Fuel Cell	$H_2 \rightarrow 2H^+ + 2e^-$	$\frac{1}{2} O_2 + 2H^+ + 2e^- \rightarrow H_2O$	< 75	H^+
Direct Methanol Fuel Cell	$CH_3OH + H_2 \rightarrow CO_2 + 6H^+ + 6e^-$	$\frac{1}{2} O_2 + 2H^+ + 2e^- \rightarrow H_2O$	< 75	H^+
Alkaline Fuel Cell	$H_2 + OH^- \rightarrow 2H_2O + 2e^-$	$\frac{1}{2} O_2 + H_2O + 2e^- \rightarrow 2OH^-$	80	OH^-
Phosphoric Acid Fuel Cell	$H_2 \rightarrow 2H^+ + 2e^-$	$\frac{1}{2} O_2 + 2H^+ + 2e^- \rightarrow H_2O$	200	H^+
Molten Carbonate Fuel Cell	$H_2 + CO_3^{-2} \rightarrow H_2O + CO_2 + 2e^-$	$\frac{1}{2} O_2 + CO_2 + 2e^- \rightarrow CO_3^{-2}$	650	CO_3^{-2}
Solid Oxide Fuel Cell	$H_2 + O^{-2} \rightarrow H_2O + 2e^-$	$\frac{1}{2} O_2 + 2e^- \rightarrow O^{-2}$	800-1000	O^{-2}

The first successful fuel cell using hydrogen and oxygen was developed by Francis Bacon in 1932 by using the alkaline electrolyte and nickel electrodes which produced 5 kW of power output.[18] From the above equations, one can clearly perceive that hydrogen plays a crucial role in the generation of electricity as it is a clean energy carrier molecule. There are different types of fuel cells based on their electrolytes and operating temperatures, Table 1.1. Different types of fuel cells work at different operating temperatures to deliver power output catering to needs, for example, solid oxide fuel cell operating at 800-1000° C is suitable for stationary applications whereas polymer electrolyte membrane (PEM) fuel cells working at < 75° C is suited for mobile applications such as electric vehicles. Anodic, as well as cathodic reactions in these fuel cells, are electrocatalyzed reactions and continuous feeding of fuels to the electrodes are required for sustainable operation. Generally, elevated temperature fuel cells such as solid oxide fuel cell and molten carbon fuel cell possess higher performance metrics but due to the drastic operating temperature, these fuel cells usually suffer from the instabilities of the electrodes and electrolyte materials.[19, 20]

1.4.1.1 Importance of PEM fuel cell

PEM fuel cells are currently gaining attention for power generation for automotive and portable applications[21] mainly because of their lower operating temperature and higher efficiency. Some of the advantages of PEM fuel cells over other types of fuel cells are their continuous energy supply with minimum maintenance, easy and safe handling, and their fast start-up time.[22]

1.4.1.2 Architectural components of PEM fuel cell

The most important architectural component of the PEM fuel cell is its membrane electrode assembly (MEA) which consists of the membrane (electrolyte) which is sandwiched between the anodic and cathodic electrocatalysts, Figure 1.6.[23,24] These electrocatalysts are generally coated on the carbon-based gas diffusion electrodes such as carbon cloth and carbon paper.[25, 26]. The gas diffusion electrodes act as the current collector with the simultaneous diffusion of feeding fuels to the electrocatalysts where the corresponding charge transfer reactions will be catalyzed. The MEA is prepared by hot pressing of the membrane with the electrocatalyst coated electrodes.
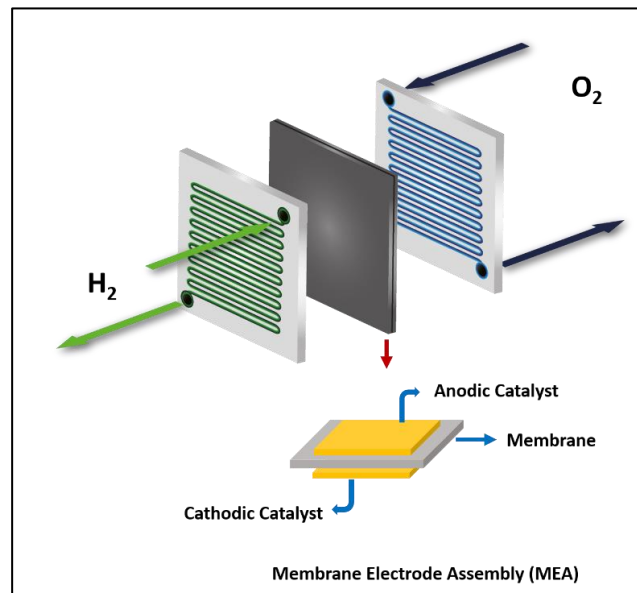
Figure 1.6 Schematic representation of components of a PEM fuel cell.

Platinum-based electrocatalysts are fruitfully utilized for both anodic and cathodic reactions because of their lower overpotential and higher exchange current densities. As can be seen from the volcano plot of catalysts, Figure 1.7, platinum attained the peak position in the plot which signifies the moderate free energy of hydrogen adsorption and

desorption which explains the higher electrocatalytic activity on Pt. The half-cell equations for a PEM fuel cell, (equations 1.1 and 1.2), i.e., hydrogen oxidation reaction (HOR) and oxygen reduction reaction (ORR) are catalyzed by platinum (Pt) which is presently the benchmark electrocatalysts for these reactions.[27] The other important part of MEA is the membrane (electrolyte) which plays a vital role in shuttling the protons across the half cells. At the same time, it acts as a barrier to molecular fuels, i.e., it doesn't allow gases to intermix with each other.
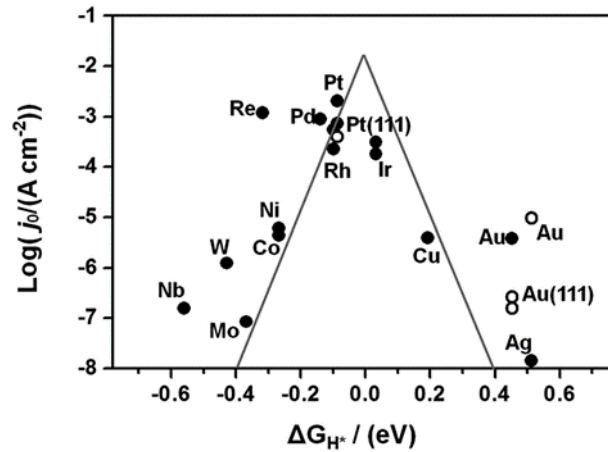
Figure 1.7 Volcano plot representing the electrocatalytic activity of various metals for hydrogen oxidation reaction (HOR).[28]

1.4.1.3   Role and properties of membrane

The membrane usually used for PEM fuel cell is called polymer electrolyte membrane, which is made up of Teflon backbone with ionic sites designed to conduct the ions. An ideal membrane should have low electronic conductivity and high ionic conductivity and the former is extremely important to prevent the short circuiting of the system and the latter crucially decides the efficiency of energy conversion.[29,30] The membrane is typically sandwiched between the electrodes of the PEM fuel cell. An excellent membrane should have a high proton conductivity value in the range of 0.01 to 0.1 $S.cm^{-1}$, a high value of ion exchange capacity (0.9 to 2 meq g^{-1}), and low fuel crossover value. Also, it should possess high mechanical, chemical, and thermal stability.[31] All of these important properties have been demonstrated in state of the art Nafion membrane which was developed by Walther Grot from DuPont in the 1960s.[32] In Nafion, the hydrophilic sulfonate ($-SO_3^-$) functionality is responsible for its higher proton shuttling capability and hydrophobic Teflon backbone ($-CF_2-$) prevents this membrane from disintegration, Figure 1.8. [29, 30]
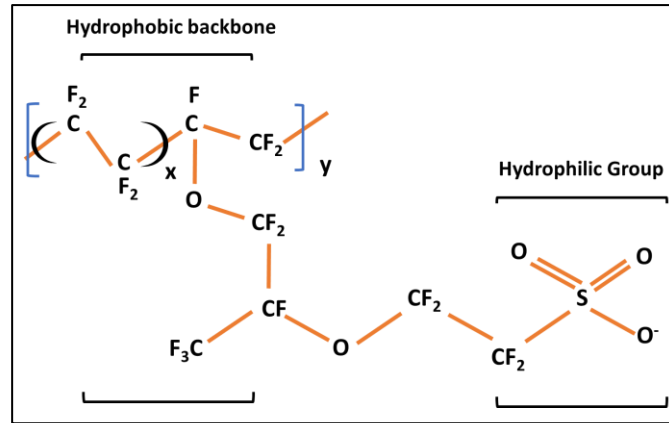
Figure 1.8 Structure of Nafion membrane.

1.4.1.4   Proton conduction mechanisms

There are two types of proton conduction mechanisms in polymer electrolyte membrane, one is the vehicular mechanism in which the proton conduction occurs by diffusion of hydronium ion. Another proton conduction mechanism is the Grotthus mechanism which requires the hydration environment to conduct the protons through the membrane and proton conduction happens by hopping of protons from one site to another site through H-bonded network.[33,34] As shown in Figure 1.9, the protons mobility in the case of Grotthus mechanism depends on the hydrogen-bonded clusters in an aqueous environment such as H_3O^+, $H_5O_2^+$, etc. and the hopping of protons takes place from one water cluster to another whereas in vehicular mechanism proton physically diffuse as hydronium ion across the membrane.[33,34]
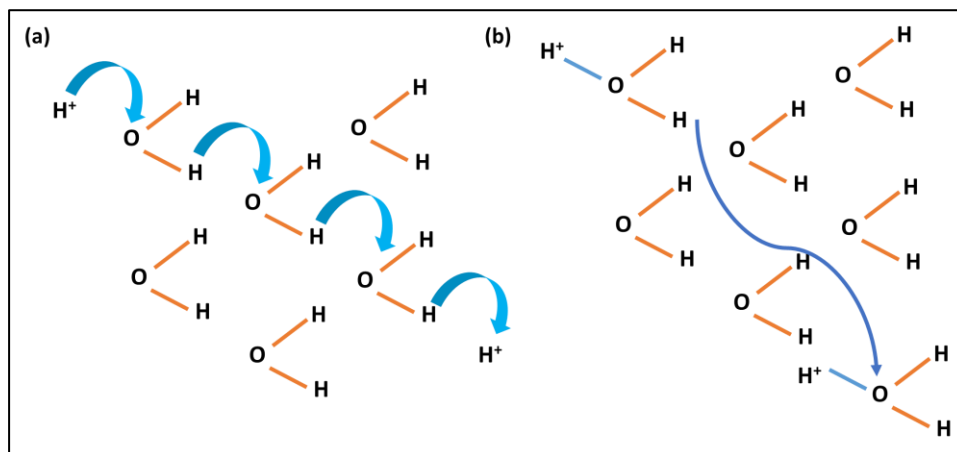
Figure 1.9 Proton conduction mechanisms (a) Grotthus mechanism and (b) vehicular mechanism.[34]

1.4.2 Water electrolyzers

Hydrogen, which is considered being a clean fuel for energy generation poses challenges with respect to its production. Industrial source of hydrogen generation is mainly by steam reforming of natural gases such as methane and propane, or other fossil fuels.[35, 36] However, these processes are highly energy demanding and generate low purity of hydrogen with the simultaneous generation of carbon containing impurities such as carbon monoxide (CO) and CO_2. The generation of this carbonaceous species during this process further shifts the focus to a clean source for the generation of hydrogen and the current focus is water, an abundant resource in our planet. High quality hydrogen is produced during the electrolysis of water without any generation carbonaceous products in water electrolyzers. These are electrolytic devices that converts water to hydrogen and oxygen by consuming electrical energy:

$$H_2O \rightarrow H_2 + \frac{1}{2} O_2 \qquad (1.3)$$
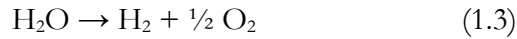
There are three types of water electrolysis: alkaline water electrolysis, solid oxide water electrolysis and PEM water electrolysis, Figure 1.10.
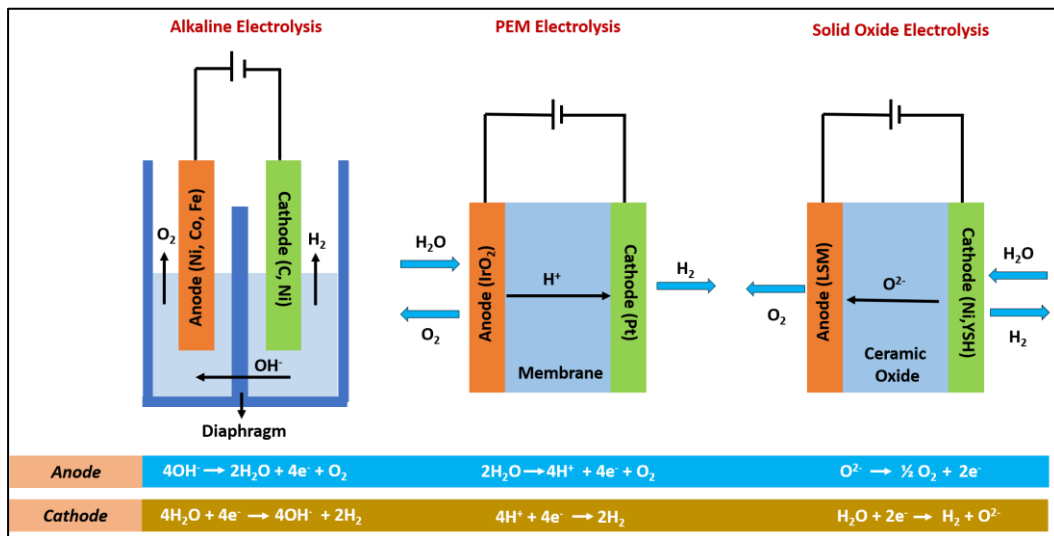
Figure 1.10 Types of water electrolyzer and the corresponding half-cell reactions.

These three types of water electrolyzers are different based on their half-cell reactions and their operating conditions.[37] Alkaline electrolyzer is characterized by possessing two electrodes immersed in a highly alkaline solution separated by a diaphragm, which plays a vital role in separating the two evolved molecular fuels (H_2 and O_2). However, alkaline electrolyzer is struggling for its existence because of its lower energy density and lower partial load. This usually occurs due to the diffusion of the molecular

fuels through the diaphragm which results in lowering of its efficiency. Another challenge with this alkaline electrolysis is the higher ohmic resistance across the liquid electrolyte and the diaphragm which further lowers the current density. Another type of water electrolyzer is solid oxide water electrolyzer which requires relatively higher temperature to operate. Donitz and Erdle first reported results on solid oxide water electrolysis in 1980s by using tubular electrolyte.[38] Afterwards this electrolyzer had got the attention towards converting electrical energy to chemical energy because of its higher efficiency. Subsequently, Westinghouse Electric Corporation Research and Development Centre also contributed to the growth of solid oxide water electrolyzer with prodigious interest.[37] Recently, Fujishiro et al., has developed the nanocomposite electrodes for high current density over $3 \, A \, cm^{-2}$ for solid oxide water electrolysis.[39] They utilized the bimodal-structured nanocomposite oxygen electrodes where nanometer-scale $Sm_{0.5}Sr_{0.5}CoO_{3-\delta}$ and $Ce_{0.8}Sm_{0.2}O_{1.9}$ are well dispersed to form conductive networks with broad pore channels. The solid oxide electrolyzer constructed by this electrode is responsible for providing $3.13 \, A \, cm^{-2}$ at 750 °C and $4.08 \, A \, cm^{-2}$ at 800 °C corresponding to a hydrogen production rate of 1.31 and $1.71 \, L \, h^{-1} \, cm^{-2}$ respectively.[39] However, this mode of electrolysis is also suffering with some challenges such as durability of the ceramic material at a higher temperature and bulk system design which further limits its commercial applications.[37]

Another type of water electrolyzer is the proton exchange membrane (PEM) water electrolyzer which consists of the compact cell assembly of anodic and cathodic electrocatalysts separated by the cation exchange membrane.[40] Typically, Pt based electrodes are used as benchmark electrocatalysts for hydrogen evolution reaction (HER) and IrO_2 based electrodes are used for oxygen evolution reaction (OER).This concept of PEM water electrolyzer was idealized by Grubb,[41] where he utilized the solid sulfonated polystyrene membrane as a polymer electrolyte to exchange the ions from anodic to cathodic side. This membrane acts as an effective barrier to the molecular fuel and is responsible for its higher performance in terms of good partial load range and current density.

1.4.2.1 Importance of PEM water electrolyzer

Clean, sustainable, and highly efficient generation of hydrogen from electrochemical energy conversion devices is gaining the attention in the scientific community to reduce the mismatch between energy demand and supply of renewable energy resources.[42] PEM water electrolysis technology is getting the focus in this direction

as they are well suitable for their utilization in mobile and portable applications. The technology is based on the exchange of ions through the proton exchange membrane which at the same time is responsible for acting as an efficient barrier to molecular fuels. Generally, state of the art Nafion membrane is utilized to act as a proton exchange because of its important properties such as higher proton conductivity, higher mechanical stability and molecular barrier nature, which make this membrane a suitable candidate for PEM water electrolysis.[43] These properties of the proton exchange membrane are responsible for its higher conversion efficiency by minimizing the ohmic loss during the electrolysis period. The lower crossover rate of the membrane further allows the electrolyzer to work under a varied range of power output. All these properties of the proton exchange membrane make this water electrolyzer a highly efficient candidate to generate molecular fuel by splitting of water and because of this reason this technology is attaining the attention of the scientific community.

1.4.3 Batteries

A battery is an electrochemical energy storage device that stores the charge via electrochemical faradaic reactions.[44] These faradaic reactions consist of electrochemical oxidation as well as reduction reaction during the charging and discharging chemistry. Typically, the storage of charge happens in the bulk of the electrode rather than on the surface of electrodes, Figure 1.11. The battery usually consists of an insertion electrode to
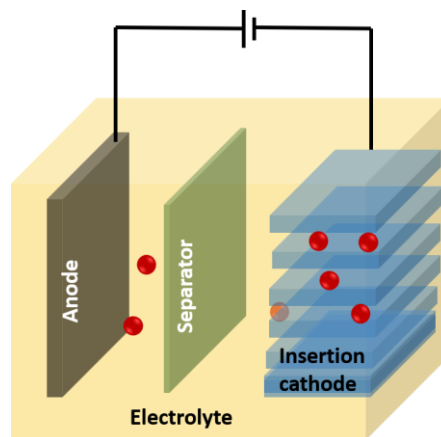
Figure 1.11 Schematic representation of components of a battery.

accommodate the metal ions into its interlayers during the charge/discharge chemistry. Non aqueous batteries generally consist of a wide potential range compared to aqueous batteries. Batteries occupy the higher energy density position in Ragone plot, Figure 1.4,

compared to supercapacitors. The power capability of the battery can be increased by increasing the storage capability of the electrodes.[45]

1.4.3.1 Types of batteries

Based on the reversibility, batteries can be classified into two categories: Primary battery and secondary battery.

1.4.3.1.1 Primary batteries: These are the batteries that can be utilized only once and their cell reactions cannot be reversed after the complete discharge of the battery. So, these are non-rechargeable batteries and for further utilization of the electrical energy, the battery components need to be replaced. Examples include zinc-carbon battery and alkaline battery.

1.4.3.1.2 Secondary batteries: These are the rechargeable batteries. Once the battery is completely discharged, its half-cell reactions can be reversed by supplying an electrical power input. They generally possess a longer lifetime. Examples include, lead-acid battery, lithium-ion battery, etc.

1.4.4 Supercapacitors

Supercapacitors are also electrochemical energy storage devices that differ in their charge storage mechanism compared to batteries.[44] In supercapacitors, charge storage is surface-confined, i.e., charge storage occurs via non-faradaic process in the electrochemical double layer (Figure 1.12) or by surface confined faradaic reactions, supercapacitors store the charge via electrostatic interactions on the electrode surface. They exhibit a higher pow-
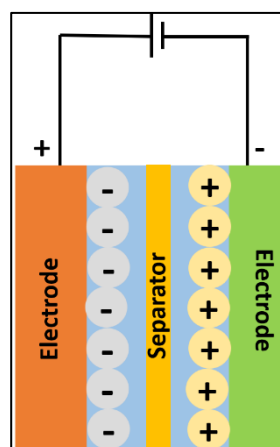
Figure 1.12 Schematic representation of components of a supercapacitor.

-er density compared with other electrochemical energy devices because of their fast rate of storage and release of the ions on the electrode surface and that is why supercapacitors are generally utilized for the high-power output applications.

1.4.4.1 Types of supercapacitors

Based on their charge storage mechanisms, these supercapacitors can be classified in two ways: Electrochemical Double Layer Capacitors and Pseudocapacitors.

1.4.4.1.1 Electrochemical double layer capacitors (EDLCs)

These are energy storage devices which store the charge via non-faradaic process in the electrochemical double layer.[46] These are generally highly stable and robust in nature as there is no any involvement of electrochemical reaction.[47] Charging and discharging of these devices are based on the ion adsorption and desorption on the electrode's surface and typically higher rates and larger numbers of cycles are possible with these devices without encountering phase transition, Figure 1.13.
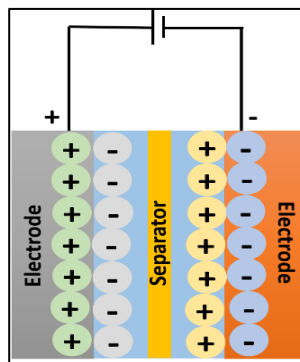
Figure 1.13   Schematic representation of electrochemical double layer capacitor.
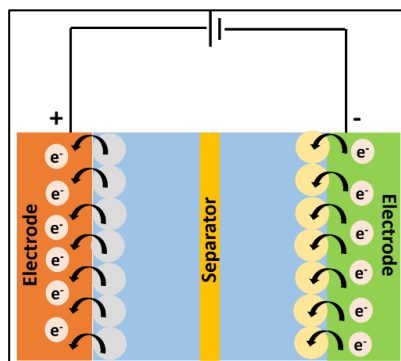
Figure 1.14   Schematic representation of a pseudocapacitor.

1.4.4.1.2 Pseudocapacitors

These are similar to EDLCs however, these devices store the charge via surface confined faradaic reactions along with the electrochemical double layer formation, Figure 1.14. Faradaic behaviour of pseudocapacitors follow the electrochemical redox reaction and intercalation mechanisms based on the nature of the electrode surface.[48]

1.5   Carbon-based materials in electrochemical energy systems

Carbon-based materials are ubiquitous in electrochemical energy storage and conversion application in various forms.[49] Carbon exists in various forms because of its peculiar properties such as catenation and tendency to exist in various hybridizations e.g., sp, sp^2, sp^3. Because of these properties, carbon-based materials have been recognized by the valuable and prestigious scientific honors which include the 1996 noble prize awarded to Robert F. Curl Jr, Sir Harold W. Kroto, and Richard E. Smalley for their primary role in the discovery of Fullerene.[50] Kavli Prize in nanoscience to Dr. Sumio Iijima for his contributions in the field of carbon nanotubes in 2008 [51] and the 2010 Nobel prize in physics for Andre Geim and Konstantin Novoselov for groundbreaking investigations towards the 2D-material graphene are other examples.[52] Carbon based materials are ubiquitous as electrodes and electrolytes in electrochemical energy devices because of their desirable properties like high electrical conductivity, high thermal stability, ability to conduct protons, ability to function as molecular fuel barriers etc.[53-55] Therefore, these carbon-based materials have been widely utilized as electrodes in energy storage devices such as batteries and as electrolytes (membrane) in energy conversion devices such as PEM fuel cells.

1.6   Importance of carbon-based materials as electrodes in energy storage devices

Carbon-based materials in various forms such as graphite, carbon nanotube (CNT), reduced graphene oxide (RGO), Mxenes etc., have been widely explored as electrode materials in energy storage devices such as batteries and supercapacitors because of their various important properties such as their higher electrical conductivity, higher thermal stability, higher surface area etc.[54, 55]

1.6.1   Graphite as electrode material

Graphite is a widely utilized carbon-based material as an electrode in energy storage purposes because of its various promising properties such as higher electrical and thermal conductivity (about $2.26 \times 104\ \Omega^{-1}\ cm^{-1}$ and 140 to 500 W mK^{-1}), inexpensive nature and suitable interlayer distance to accommodate the metal ions.[56,57] Graphite consists of multilayer structure of sp^2 hybridized carbon atoms with Π-Π interactions between basal planes and edge planes, Figure 1.15. This interlayer structure of graphite makes it a suitable candidate for the intercalation of metal ions in batteries. Because of all these important properties, graphite has been widely explored as electrodes in various investigations. Graphite has been already commercialized as an anode material in lithium-ion batteries. Developments and growths have been made by various researchers to maximize the utilization of lithium-ion insertion into the graphite interlayers for improving the energy storage applications of the battery.[56]
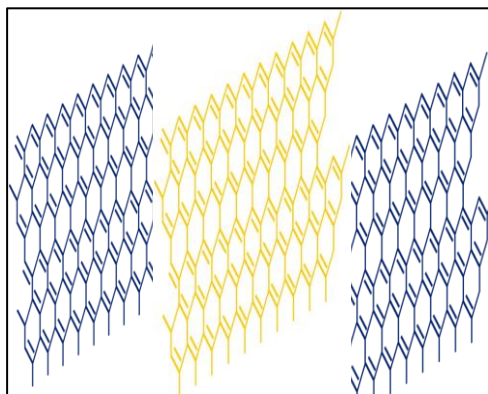
Figure 1.15 Schematic representation of layer structure of graphite.

Initially, efforts have been carried out in the 1970s to electrochemically reverse the intercalation of lithium ions into the interlayers of graphite, however, they had faced the challenge of continuous co-intercalation and decomposition of the generally used liquid organic electrolytes (e.g., propylene carbonate) which gave the ultimate result of exfoliation of graphite layers.[58,59] The first fruitful effort came into the light in 1983 by Yazami and Touzain with the utilization of a solid polymer electrolyte.[56,60] The first lithium-ion battery was commercialized by Sony in 1991 with the employment of propylene carbonate as electrolyte.[61] Since then, investigations have been going on to increase the coulombic efficiency of the lithium-ion battery, as shown in Figure 1.16. This graphite material is not only limited to lithium-ion batteries but also explored in other batteries like sodium-ion batteries (NIB), lithium-sulfur batteries, aluminium chloride batteries, etc.[62,57]
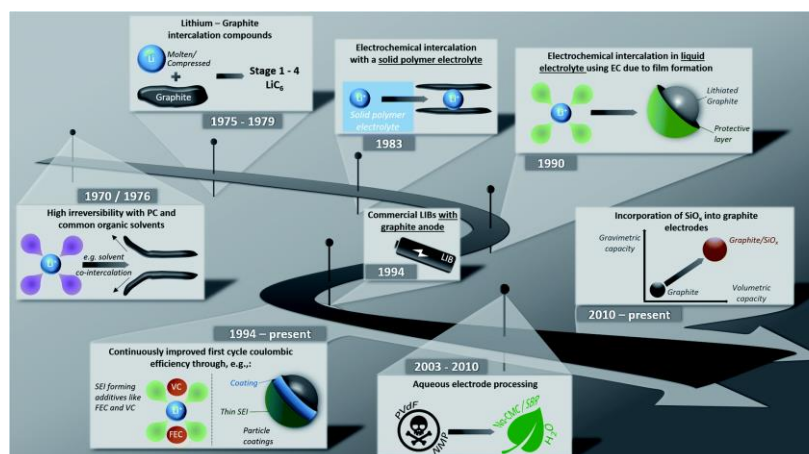
Figure 1.16 Demonstrative summary of major marks on the expansion of graphite as negative electrodes for lithium-ion batteries.[56]

Yang et al.,[63] reported the study of expanded graphite with a long-range-ordered layered structure as sodium-ion battery (NIB) anodes. Unlike other carbonaceous NIB anodes, expanded graphite stores Na^+ mostly by interlayer intercalation, which has been confirmed by cyclic voltammetry and in situ TEM observations through reversible interlayer expansion/shrinkage of the graphite material during the sodiation and desodiation.[63] Wang et al.,[64] reported the construction of aluminum ion battery (AIB) using graphite flake film as the cathode combined with an aluminium anode in an ionic liquid electrolyte. The specific capacity of the Al/graphite flake film battery was significantly greater than that of a similar cell made with pyrolytic graphite (an increase to $\sim$110 mAh g^{-1} from $\sim$66 mAh g^{-1}).[64] Fan et al.,[65] reported the exploitation of graphite anode for a potassium-ion battery (KIB) with higher performance. They developed the cell by using a concentrated electrolyte and demonstrated the formation of a robust inorganic-rich passivation layer on the graphite anode that could resolve the problems of the short life cycle of K^+ ion batteries. Consequently, the KIBs with graphite anode could operate for over 2000 cycles with negligible capacity decay, and had a high areal capacity over 7.36 mAh cm^{-2} with a high mass loading of 28.56 mg cm^{-2}.[65]

1.6.2 Carbon nanotubes (CNTs) as electrode material

Carbon nanotubes (CNTs) are the class of carbon-based materials that are atomically well defined and hollow tubular-shaped with sp^2 hybridized carbon atoms. They consist of 1D form of carbon aligned with van der Waal interactions with diameters in the range of 4 nm to 30 nm and length from nanometer to microns.[66] The study of CNTs was first reported in 1959 by Roger Bacon who formed the images of nanotubes.[67] The excited

properties of nanotubes made them the one of the promising materials for energy storage applications. Based on their number of layers, CNTs can be classified into two types; single-walled carbon nanotubes (SWCNTs) and multi-walled carbon nanotubes (MWCNTs), Figure 1.17.
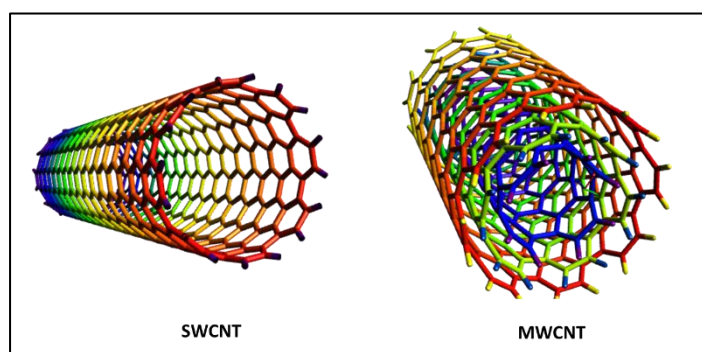
Figure 1.17 Schematic representation of SWCNT and MWCNT.

CNTs have various promising properties which make them unique over graphite such as its extraordinary flexibility under large strains. People have observed reversible, periodic buckling of nanotubes consistent with calculations extrapolated from continuum mechanics. Local strains as large as 16 % can be sustained without separating a nanotube.[68] This further indicates the higher mechanical strength of CNTs. CNTs possess the higher electrical conductivity ($\sim10^4$-10^5 Ω^{-1} cm^{-1}) as well as the higher surface area which further results in specific energy as high as $\sim$300 Wh/kg when employed in batteries.[69] Because of all these important properties, CNTs play a vital role as the electrodes in energy storage devices such as batteries and supercapacitors. For e.g., Yan et al., reported the investigation of 3D conductive networks of CNTs in sodium trimesic to improve the sodium ion storage inside the anodic electrode which resulted in the higher performance of sodium ion battery with capacity of 214.6 mA h g^{-1} at 0.1 A g^{-1}. The device exhibited excellent rate performance with the specific capacities of 149 and 87.5 mA h g^{-1} at 1 and 10 A g^{-1}, respectively.[70] James et al.,[71] reported the study of polyimide/MWCNTs nanocomposite and gel polymer electrolytes for high-performance sodium-ion battery which showed a high discharge capacity close to 100 % of the theoretical value at 0.1 C-rate and an ultralong life span of 3000 cycles at 5 C-rate.[71]

Apart from these, CNTs have been widely utilized as electrodes in redox flow batteries. For e.g., Luo et al.,[72] reported the study of MWCNT-loaded graphite felt (MWCNT@GF) as electrodes for the Br^{3-}/Br$^-$ redox couple.[72] They have reported 78 % energy efficiency and 227 mW cm^{-2} power density at 100 % state of charge.[72] Munaiah et

al.,[73] investigated applications of CNTs as electrode materials in rechargeable zinc-bromine redox flow batteries.[73] Park et al., investigated the synergistic effect of the carbon nanofiber (CNF)/carbon nanotube (CNT) composite electrocatalysts in vanadium redox flow battery.[74] CNF/CNT electrodes showed better capacity retention, very good rate capability up to 100 mA·cm^{-2} and lower polarization with significantly improved electron transfer.[74] These studies highlight the importance of CNTs as electrodes in energy storage applications.

1.6.3 Graphene and graphene composites as electrode materials

Graphene is considered to be the first 2D carbon material. Prof. Geim and Novoselov (University of Manchester, UK) have got the Nobel prize in 2010 for their breakthrough origination to mechanically exfoliate the sheets of graphene from graphite by Scotch tape method in 2004 and measured the electrical properties of graphene layers.[75] Graphene is a single layer of sp^2 carbon atoms aligned in hexagonal pattern and has come up as promising material in energy storage applications because of its higher intrinsic carrier mobility (350000 cm^2 V^{-1}s^{-1}), its higher theoretical specific surface area (2630 m^2 g^1), higher thermal conductivity (3000 Wm^{-1} K^{-1}) and mechanical strength, Figure 1.18.
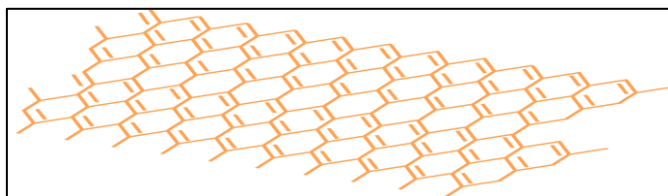
Figure 1.18 Schematic representation of a single layer of graphene.

These properties make graphene-based materials as a promising candidate to be utilized as electrodes in energy storage devices. The noticeably higher Li-ion diffusivity on a graphene plane has also motivated the applications of graphene as electrodes with higher ionic conductivity.[75] In recent years, graphene and graphene-based materials such as few-layer graphene (FLG), reduced graphene oxide (RGO), and graphene 3D structures have attracted extensive research interests due to decent electrical, thermal, mechanical, and chemical properties.[49,76] It is well reported that expandable graphite after being treated thermally, can be exploited to form RGO which has come up as a widely utilized anode material for batteries where the most commonly used synthesis procedure to form RGO is direct exfoliation of graphene oxide (GO) followed by its reduction.[77] Studies have been reported on RGO as electrodes in energy storage devices because of its higher surface area

($\sim$800 m^2/g), higher electrical conductivity ($\sim$10^3-10^4 S/m) and decent thermal stability.[78,79] Song et al., reported the NaTi$_2$(PO$_4$)$_3$/reduced graphene oxide (NTP/RGO) composite electrode synthesized by polyol-assisted pyro synthesis for Na-ion battery with high rate capacities (95 mA h g^{-1} at 9.2C and 78 mA h g^{-1} at 36.8C). [80] Plawan et al., reported the study of RGO formed by FeCl$_3$/HCl method for capacitive applications ($\sim$282 F/g at 1.8 A/g current density).[81]

1.7 Importance of carbon-based materials as electrolytes (membranes) in energy conversion devices

Carbon-based materials have also been widely explored as fillers in polymer electrolytes or to form composite membranes for improving the overall performance metrics of energy conversion devices. The importance of these carbon-based materials as electrolytes (membrane) in energy conversion devices such as fuel cells and water electrolyzers is mainly because of their ability to act as an effective barrier to molecular fuels, high proton conductivity and their ability to improve the mechanical properties. Towards this direction, CNTs and their composites have been widely utilized as the fillers in state-of-the-art Nafion membrane to improve the proton conduction capability, mechanical properties, and thermal stability of the membrane in PEM fuel cell configuration.[82-84] Apart from CNTs, graphene/GO and its composites also have been exploited as membranes in the state-of-the-art PEM fuel cell systems.[85, 86]

1.7.1 CNTs as filler in electrolytes (membranes)

Carbon nanotubes (CNTs) are the widely exploited class of carbon-based materials that have been utilized for the functionalization of polymer electrolyte membrane to improve its vital properties towards developing high performance fuel cell. This is because of their high aspect ratios (100$\sim$1000), high specific surface areas, higher mechanical and thermal stability and its ability to act as an effective barrier to molecular fuels.[82, 83] Introduction of CNTs into the matrix of state-of-the-art polymer electrolyte leads to substantial enhancement in mechanical properties and proton conduction capabilities of the composite membranes.[87] The most typical challenge with CNTs to be utilized as the fillers is the risk of the short-circuiting because of the higher electrical conductivity of the CNTs. Liu et al, in 2006 have come up with an investigation in which they have reported the optimum utilization of CNT contents below the percolation threshold.[88] They have optimized the weight % of CNT to introduce as the filler in state-of-the-art Nafion

membrane without short-circuiting. To further improve the proton conduction capabilities of CNTs composite with state-of-the-art Nafion® membranes efforts have been carried out in various directions. Thomassin et al. in 2010 have tried to improve the proton conduction capability as well as mechanical properties of the state-of-the-art Nafion membrane by introducing carboxylic acid-functionalized MWCNTs into the Nafion membrane by maintaining the weight % of MWCNTs. They have reported the increment in Young's modulus by 160 % in the composite membrane.[89] Also, SWCNTs have also been exploited to improve the proton conduction capability and mechanical properties of composite membranes in fuel cell applications. Kannan et al.[90] in 2008, reported the sulfonated functionalized SWCNTs to enhance the proton conduction capability of state-of-the-art Nafion membrane from 0.09 to 0.56 S cm^{-1} in fuel cell configuration. They proposed the generation of channel-like networks in the sulfonated SWCNT-modified Nafion membrane which was attributed to its higher fuel cell performance.[90]

1.7.2 Graphene based fillers as electrolytes (membranes)

Graphene is a 2D material that has been widely utilized in various forms to form composite membrane to improve the properties of the state of the art Nafion membrane in fuel cell configuration.[84] Due to their 2D layer structure, these forms of carbonaceous materials have reported excellent physical properties such as high surface area (2630 m^2 g^{-1}), high thermal conductivity (4.9*10^3 Wm^{2}k^{-1}), decent proton conductivity (0.1 mS/cm), and high carrier mobility.[84,91] For the preparation of graphene materials, two well-known strategies are reported: a bottom-up approach (chemical vapor deposition) and a top-down approach (Hummer's method).[92, 93] Yan et al., reported the study of a monolayer graphene sandwiched between two thin Nafion membranes to take advantage of monolayer graphene's selective permeability to only protons in methanol fuel cell system.[92]

From the past decade, functionalized graphene materials have got higher attention in the scientific community in terms of energy conversion applications. It can be easily functionalized with the single atoms like N, P, S and also with organic functionalities such as -NH$_2$, -SO$_3$H, -OH etc. to improve the properties of the polymer electrolyte membrane.[94,95] Functionalized graphene oxide (GO) with state of the art Nafion membrane has been widely explored as a highly promising proton-conducting membrane in H$_2$ and O$_2$ fuel cell configuration because of its ability to conduct the protons, its ability to act as an effective barrier to molecular fuel and because of its decent mechanical properties. Zarrin et al., reported a composite membrane based on functionalized graphene oxide and

Nafion (F-GO/Nafion) for high-temperature PEM fuel cell applications.[96] Mohanraj et al., reported a composite membrane of iron oxide (Fe_3O_4) nanoparticles anchored over sulfonated graphene oxide (SGO) with state-of-the-art Nafion membrane for high performance fuel cell applications.[97] They reported a peak power density of 258.82 mW cm^{-2} at a load current density of 640.73 mA cm^{-2}. These studies indicate that graphene based composite membranes can act as an efficient proton exchange membrane in energy conversion devices. It is to be noted that, no such studies have been reported with pristine GO as electrolytes in energy conversion devices such as unitized regenerative fuel cells and water electrolyzers.

1.8   Important properties of graphene oxide (GO) membrane

Dikin et al.[98] and karim et al.[99] first predicted that GO can be utilized as proton conducting membrane in energy conversion devices such as fuel cells and water electrolyzers owing to its ability to conduct the protons because of its hydrophilic functio-
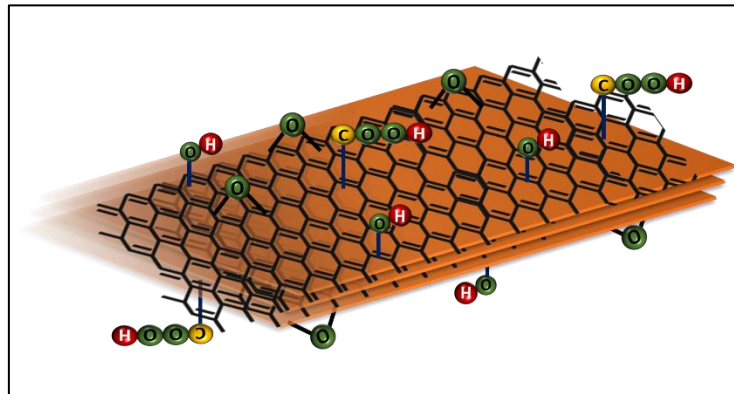
Figure 1.19 Schematic representation of graphene oxide (GO) with oxygen containing functionalities.

-nalities ($-O-$, C=O, $-OH$, $-COOH$ etc.,), Figure 1.19. It is reported that they can act as effective barrier to molecular fuels such as H_2 and O_2. This makes GO a potential candidate to be utilized as proton exchange membrane and it also shows decent mechanical stability due to its 2D carbon network which makes it more compact and flexible.[99] For a proton exchange membrane, the first priority is that the membrane must be an electronic insulator to prevent any kind of short-circuiting. The electrical conductivity of GO is very low which is of the order of 10^{-8}-10^{-9} S/cm compared with pristine graphite ($\sim 10^3$).[100,101] This is because of high density of the hydrophilic functionalities in GO membrane ($-O-$, $-OH$, C=O, and $-COOH$) which makes GO a suitable candidate to be utilized as proton exchange membrane in energy conversion devices, Figure 1.19.[102]   The chemically

exfoliated nanosheets of GO usually are discrete due to the oxygen-rich functionalities and this creates a hydrogen-bonding network of adsorbed water molecules connecting the hydrophilic sites of GO which is reported to result in faster ionic movement.[98]

Dikin et al.,[98] also reported that the proton conduction capability of GO increased with the amount of area occupied by multilayers compared with the single-layer nanosheets and this further evidenced that increment in proton conductivity can be obtained by fabricating multilayers of GO. Matsui et al.,[103] also reported alike trend in a uniform multilayer of poly(N-dodecylacrylamide-co-2-acrylamido-2-methylpropanesulfonic acid) (p(DDA/AMPS)) polymer nanosheet. The proton conductivity of the multilayer film was of the order of 1×10^{-5} S/cm at 100% RH with 20 °C and increased to 1×10^{-2} S/cm at 70 °C.[103]

The synthesis of GO is classified into two categories. In the bottom-up approach, graphene nanosheets are typically formed by chemical vapor deposition. The top-down approach usually includes the exfoliation of sheets of graphene. In terms of scalability and time consumption, the top-down approach is a widely exploited approach to synthesize the GO.[104-106] In 1859, Brodie[107] initially synthesized graphite oxide by the utilization of po-
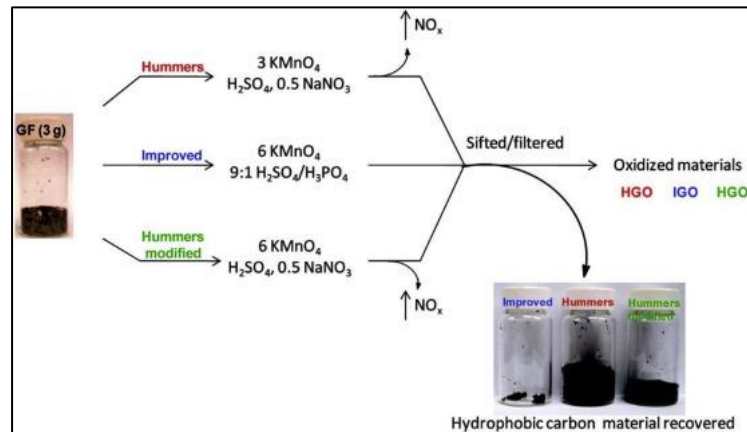
Figure 1.20 Schematics of the most common GO synthesis methods. (Adapted from ref. 103 from the American chemical society with permission).

-tassium chlorate with the help of fuming nitric acid. After that Staudenmaier improvised this approach by substituting fuming HNO_3 with concentrated H_2SO_4.[108] Hummers and Offeman[109] introduced another oxidation approach in 1958, called the Hummer's method, in which they have used $NaNO_3$ and $KMnO_4$ with H_2SO_4 to exfoliate the sheets of graphite into graphite oxide. Marcano et al.,[106] reported an improved Hummer's method with the utilization of H_2SO_4 and H_3PO_4 with $KMnO_4$ which produced a higher yield of graphene oxide, Figure 1.20. Recently, Huitao et al.,[105] have further improvised the approach with

$NaNO_3$-free Hummers methods by partly replacing $KMnO_4$ with K_2FeO_4 which in turn also suppressed the consumption of concentrated H_2SO_4, Figure 1.20.

Dikin et al.,[98] also reported decent tensile strength for graphene oxide paper with Young's modulus ∼35 GPa (∼5.2 um thick graphene oxide paper) which indicates its stiffness and makes it a suitable candidate as a proton exchange membrane in PEM fuel cell and water electrolyzer. Also, Ravikumar et al,.[110] first reported the application of sulfonated GO freestanding paper fabricated by vacuum filtration of a colloidal solution of sulfonated graphite oxide for polymer electrolyte fuel cell applications. All above-mentioned studies highlight the important properties of GO membrane to be utilized as proton exchange membrane in energy conversion systems such as PEM fuel cells and PEM water electrolyzers. However, no such studies have been reported on pristine graphene oxide as electrolytes (membranes) in energy conversion devices such as unitized regenerative fuel cells and water electrolyzers.

1.9   Challenges and issues with carbon-based materials

Aforementioned discussion highlights that carbon based materials are ubiquitous as electrodes and electrolytes in electrochemical energy devices because of their desirable properties like high electrical conductivity, high thermal stability, ability to conduct protons, ability to function as molecular fuel barriers etc.[53,54] However, in the context of aqueous metal ion batteries, utilization of carbon materials as electrodes often lead to spontaneous de-insertion reactions, undesirable proton insertion reactions, parasitic hydrogen evolution reactions, unwanted swelling etc.[111-114] Carbon based materials when employed in energy devices are prone to corrosion in aqueous electrolytes which further contributes to instability of the electrode materials.[115,116] It has been reported in the literature that there is exfoliation of graphene layers because of the generation of radical species (e.g., hydroxyl radicals) at larger applied potentials which is known to degrade the carbon lattice thereby suppressing the performance matrics of the energy device.[117,18] When it comes to the applications of these carbon-based materials in aqueous metal-ion batteries, they often facilitate parasitic hydrogen evolution reaction which in turn seriously affect the round trip efficiency.[113, 114, 119, 120] Aqueous redox flow batteries based on outer sphere redox molecules suffer from their inferior volumetric energy density due to the underutilization of dissolved electroactive species and even the employment of high surface area carbon nanotube (CNT) electrodes have not made enough advancement beyond a threshold.[72, 74, 121] With regard to energy conversion devices such

as water electrolysers and unitized regenerative fuel cell, though carbon based materials like oxidized graphene are predicted with the capability to conduct protons and to function as effective molecular fuel barriers;[98,99] they have not been explored in their pristine free standing form to shuttle protons.

1.10   Aim and scope of the thesis

The primary aim of this thesis is to exploit carbon derived materials as electrodes in energy storage systems and as electrolytes (membranes) in energy conversion systems to address some of their state-of-the-art issues and challenges and to investigate their unexplored properties. With this aim, this thesis is divided into two parts: **Part I** explores the utilization of carbon derived materials as electrodes in energy storage devices such as aqueous rechargeable sodium ion battery and aqueous redox flow battery and **Part II** deals with the exploitation of carbon derived materials as electrolytes in proton exchange membrane (PEM) fuel cell, PEM water electrolyzer and unitized regenerative fuel cell (URFC). The thesis is divided into following chapters:

Chapter 1 explains the importance, advantages, issues, and challenges of carbon-based materials as electrodes and electrolytes in electrochemical energy storage and conversion devices. This chapter describes the importance of carbon-based materials and their classification as well as their challenges and prospects in energy storage and conversion devices. This chapter highlights the utilization of carbon-derived materials as electrodes for electrochemical energy storage devices such as aqueous rechargeable sodium-ion battery and redox flow battery and as electrolytes in electrochemical energy conversion devices such as PEM fuel cell, water electrolyzer, and unitized regenerative fuel cell (URFC).

Part I

Chapter 2 describes the investigation on how activation of coulombic forces can gate the molecular transport in redox flow battery and how this gated molecular transport can be utilized to enhance the energy density of redox flow battery without compromising its power capability. In this chapter, how the activation of coulombic forces at the CNT electrode/electrolyte interface gates the molecular transport by generating a directional electrostatic current contribution over the diffusion is demonstrated. In iron based redox flow battery, this gated molecular flux almost doubles the volumetric energy density

without compromising the power capability by extending the concentration polarization regime.

Chapter 3 shows how the mode of synthesis of graphene-based materials improves the quality of reduced graphene oxide material with properties relevant for constructing an aqueous rechargeable sodium ion battery by suppressing the parasitic hydrogen evolution reaction chemistry during the charge chemistry. Various physicochemical analyses shows that the density of hydrophilic functionalities on the graphene electrode affects the reversibility as well as the cyclability of an aqueous sodium ion battery by chemically binding to sodium ions with poor reversibility in its electrochemical adsorption/desorption.

Part II

Chapter 4a describes the utilization of freestanding GO membrane in its pristine form as electrolyte to construct a water vapor electrolyzer. GO has been predicted with the capability to conduct protons and to function as molecular fuel barriers and in this chapter, a freestanding GO membrane is employed as a proton exchange membrane to construct a PEM water vapor electrolyzer. The hydrophilic functionalities of GO like -OH, -COOH, -C=O, -COC etc., are responsible for shuttling the protons from the anodic to the cathodic side during the splitting of water vapor into molecular fuels. The ability of GO based water vapour electrolyzer to split water vapour into H_2 and O_2 at a stoichiometric ratio of 2:1 is demonstrated by in-situ electrochemical mass spectrometry. The hydrophilic functionalities in GO even provided access to the universal feedstock of water in earth's atmosphere, which in turn could be converted into fuel molecules via electrochemical processes coupled to renewable energy.

Chapter 4b explores the utilization of free-standing GO membrane as electrolyte to construct a low temperature URFC which is known to play vital roles in sustainable energy landscape in producing and utilizing the H_2 fuel with a near zero carbon foot print. The polarization studies in the water electrolyzer mode and H_2-O_2 fuel cell mode attest the capability of free-standing GO membrane to shuttle the protons back and forth in a URFC. The stability of the three-phase boundary constituting the free-standing GO membrane in the URFC configuration is demonstrated by the long term galvanostatic measurements and post mortem analysis.

Chapter 5a discusses how the proton conduction capability of GO membrane can be improved so as to bridge the performance gap between GO based PEM and Nafion based PEM. The proton conductivity of GO membrane is ~10 times lower than state of the art Nafion membrane. Since hydrophilic functionalities like -OH, -COOH, -C=O, -COC etc., are responsible for shuttling the protons in GO, any attempts to improve its hydrophilicity to increase its proton conduction capability on one hand will affect the mechanical stability of membrane in aqueous environment. On the other hand, the introduction of more hydrophobic functionalities so as to prevent the mechanical disintegration of the GO membrane will decrease its proton exchange capacity. This indicates a trade-off between proton conductivity and hydrophobicity/hydrophilicity in GO membrane which is indeed a challenge to amplify its room temperature fuel cell performance metrics. In this chapter, proton conduction capability of pristine GO membrane is amplified by introducing to its interlayer's proton carrying quinone molecules bearing proton shuttling sulfonic acid groups. The hydrogen carrying capability of quinone functionality and proton conduction capability of sulfonic acid moiety in GO's matrices substantially improved its overall proton conduction (~7 times compared to pristine GO) capability and consequently its overall fuel cell performance metrics.

Chapter 5b investigates the implications of reducing the thickness of GO membrane in the performance metrics of a GO based H_2–O_2 fuel cell system. Thin layer GO membrane of ~3 μm thickness demonstrated a larger (~3 times) proton flux compared to GO membrane of higher thickness (~25 μm). This higher proton flux is further responsible for its nearly 5 times higher fuel cell performance metrics in terms of current density and power density. The stability of this thin layer GO based fuel cell system is investigated by galvanostatic analysis at different current densities which signifies the stability of the three-phase boundary formed by the thin film GO membrane. However, thickness reduction accelerates fuel crossover from anodic to cathodic side by nearly ~3 times. Therefore, though proton flux across the membrane increases on thickness reduction, fuel crossover also increases simultaneously, which needs to be adequately addressed by materials engineering strategies like introducing suitable fillers and additives, adding other polymeric materials to make composite GO membranes etc., if this higher fuel cell performance metrics have to exploited for practical applications.

Chapter 6. This chapter provides the concluding remarks and future outlook.

1.11   References

1.   Kim, H.; Kim, H.; Ding, Z.; Lee, M. H.; Lim, K.; Yoon, G.; Kang, K., Recent Progress in Electrode Materials for Sodium-Ion Batteries. *Adv. Energy Mater.* **2016,** *6* (19), 1600943.

2.   Gevorkyan, A., Renewable versus nonrenewable resources: an analysis of volatility in futures prices. *Aust. J. Agric. Resour. Econ.* **2017,** *61* (1), 19-35.

3.   Höök, M.; Tang, X., Depletion of fossil fuels and anthropogenic climate change—A review. *Energy Policy* **2013,** *52*, 797-809.

4.   Islam, M. A.; Hasanuzzaman, M.; Rahim, N. A.; Nahar, A.; Hosenuzzaman, M., Global Renewable Energy-Based Electricity Generation and Smart Grid System for Energy Security. *Sci. World J.* **2014,** *2014*, 197136.

5.   Baños, R.; Manzano-Agugliaro, F.; Montoya, F. G.; Gil, C.; Alcayde, A.; Gómez, J., Optimization methods applied to renewable and sustainable energy: A review. *Renew. Sustain. Energy Rev.* **2011,** *15* (4), 1753-1766.

6.   Badwal, S. P. S.; Giddey, S. S.; Munnings, C.; Bhatt, A. I.; Hollenkamp, A. F., Emerging electrochemical energy conversion and storage technologies. *Front Chem.* **2014,** *2*, 79-79.

7.   Winter, M.; Brodd, R. J., What Are Batteries, Fuel Cells, and Supercapacitors? *Chem. Rev.* **2004,** *104* (10), 4245-4270.

8.   Eftekhari, A.; Fang, B., Electrochemical hydrogen storage: Opportunities for fuel storage, batteries, fuel cells, and supercapacitors. *Int. J. Hydrogen Energy* **2017,** *42* (40), 25143-25165.

9.   Schlapbach, L.; Züttel, A., Hydrogen-storage materials for mobile applications. *Nature* **2001,** *414* (6861), 353-358.

10.   Liu, Z.; Yu, Q.; Zhao, Y.; He, R.; Xu, M.; Feng, S.; Li, S.; Zhou, L.; Mai, L., Silicon oxides: a promising family of anode materials for lithium-ion batteries. *Chem. Soc. Rev.* **2019,** *48* (1), 285-309.

11.   Wang, Y.-J.; Wilkinson, D. P.; Zhang, J., Noncarbon Support Materials for Polymer Electrolyte Membrane Fuel Cell Electrocatalysts. *Chem. Rev.* **2011,** *111* (12), 7625-7651.

12.   Vladimir S. Bagotsky, A. M. Yurij M. Volfkovich, *Electrochemical Power Sources: Batteries, Fuel Cells, and Supercapacitors.* Wiley: 2015.

13.   Marichi, R. B.; Sahu, V.; Sharma, R. K.; Singh, G., Efficient, Sustainable, and Clean Energy Storage in Supercapacitors Using Biomass-Derived Carbon Materials. In *Handbook of Ecomaterials*, Martínez, L. M. T.; Kharissova, O. V.; Kharisov, B. I., Eds. Springer International Publishing: Cham, 2017; pp 1-26.

14.   Manthiram, A., A reflection on lithium-ion battery cathode chemistry. *Nat. Commun* **2020,** *11* (1), 1550.

15.   Kongkanand, A.; Subramanian, N. P.; Yu, Y.; Liu, Z.; Igarashi, H.; Muller, D. A., Achieving High-Power PEM Fuel Cell Performance with an Ultralow-Pt-Content Core–Shell Catalyst. *ACS Catal.* **2016,** *6* (3), 1578-1583.

16.   Kraytsberg, A.; Ein-Eli, Y., Review of Advanced Materials for Proton Exchange Membrane Fuel Cells. *Energy & Fuels* **2014,** *28* (12), 7303-7330.

17.   Wang, C.-Y., Fundamental Models for Fuel Cell Engineering. *Chem. Rev.* **2004,** *104* (10), 4727-4766.

18.   Bacon, F. T. a. T. M. F., Series A, Mathematical and Physical Sciences. *Proc. R. Soc. London, Ser. A 334*, 1599.

19.   Chroneos, A.; Yildiz, B.; Tarancón, A.; Parfitt, D.; Kilner, J. A., Oxygen diffusion in solid oxide fuel cell cathode and electrolyte materials: mechanistic insights from atomistic simulations. *Energy Environ. Sci.* **2011,** *4* (8), 2774-2789.

20.   Ormerod, R. M., Solid oxide fuel cells. *Chem. Soc. Rev.* **2003,** *32* (1), 17-28.

21.   Taner, T., Energy and exergy analyze of PEM fuel cell: A case study of modeling and simulations. *Energy* **2018,** *143*, 284-294.

22. Wang, Y.; Ruiz Diaz, D. F.; Chen, K. S.; Wang, Z.; Adroher, X. C., Materials, technological status, and fundamentals of PEM fuel cells – A review. *Mater. Today* **2020,** *32*, 178-203.

23. Wang, L.; Advani, S. G.; Prasad, A. K., Membrane Electrode Assembly with Enhanced Membrane/Electrode Interface for Proton Exchange Membrane Fuel Cells. *J. Phys. Chem. C* **2013,** *117* (2), 945-948.

24. Yang, C.; Han, N.; Wang, Y.; Yuan, X.-Z.; Xu, J.; Huang, H.; Fan, J.; Li, H.; Wang, H., A Novel Approach to Fabricate Membrane Electrode Assembly by Directly Coating the Nafion Ionomer on Catalyst Layers for Proton-Exchange Membrane Fuel Cells. *ACS Sustain. Chem. Eng.* **2020,** *8* (26), 9803-9812.

25. Park, S.; Popov, B. N., Effect of a GDL based on carbon paper or carbon cloth on PEM fuel cell performance. *Fuel* **2011,** *90* (1), 436-440.

26. Benziger, J.; Nehlsen, J.; Blackwell, D.; Brennan, T.; Itescu, J., Water flow in the gas diffusion layer of PEM fuel cells. *J. Membr. Sci.* **2005,** *261* (1), 98-106.

27. Borup, R. L.; Davey, J. R.; Garzon, F. H.; Wood, D. L.; Inbody, M. A., PEM fuel cell electrocatalyst durability measurements. *J. Power Sources* **2006,** *163* (1), 76-81.

28. Nørskov, J. K.; Bligaard, T.; Logadottir, A.; Kitchin, J. R.; Chen, J. G.; Pandelov, S.; Stimming, U., Trends in the Exchange Current for Hydrogen Evolution. *J. Electrochem. Soc.* **2005,** *152* (3), J23.

29. Banerjee, S.; Curtin, D. E., Nafion® perfluorinated membranes in fuel cells. *J. Fluorine Chem.* **2004,** *125* (8), 1211-1216.

30. Liu, F.; Yi, B.; Xing, D.; Yu, J.; Zhang, H., Nafion/PTFE composite membranes for fuel cell applications. *J. Membr. Sci.* **2003,** *212* (1), 213-223.

31. Kumar, R.; Xu, C.; Scott, K., Graphite oxide/Nafion composite membranes for polymer electrolyte fuel cells. *RSC Adv.* **2012,** *2* (23), 8777-8782.

32. Knights, S. D.; Colbow, K. M.; St-Pierre, J.; Wilkinson, D. P., Aging mechanisms and lifetime of PEFC and DMFC. *J. Power Sources* **2004,** *127* (1), 127-134.

33. Agmon, N., The Grotthuss mechanism. *Chem. Phys. Lett.* **1995,** *244* (5), 456-462.

34. Junoh, H.; Jaafar, J.; Nordin, N. A. H. M.; Ismail, A. F.; Othman, M.; Rahman, M. A.; Aziz, F.; Yusof, N.; Salleh, W. N. W. J. J. o. M. S.; Research, Porous Proton Exchange Membrane Based Zeolitic Imidazolate Framework-8 (ZIF-8), *Journal of Membrane Science and Research* **2019,** *5*, 65-75.

35. Ni, M.; Leung, D. Y. C.; Leung, M. K. H., A review on reforming bio-ethanol for hydrogen production. *Int. J. Hydrogen Energy* **2007,** *32* (15 SPEC. ISS.), 3238-3247.

36. Carmo, M.; Fritz, D. L.; Mergel, J.; Stolten, D., A comprehensive review on PEM water electrolysis. *Int. J. Hydrogen Energy* **2013,** *38* (12), 4901-4934.

37. Sapountzi, F. M.; Gracia, J. M.; Weststrate, C. J.; Fredriksson, H. O. A.; Niemantsverdriet, J. W., Electrocatalysts for the generation of hydrogen, oxygen and synthesis gas. *Prog. Energy Combust. Sci.* **2017,** *58*, 1-35.

38. Laguna-Bercero, M. A., Recent advances in high temperature electrolysis using solid oxide fuel cells: A review. *J. Power Sources* **2012,** *203*, 4-16.

39. Shimada, H.; Yamaguchi, T.; Kishimoto, H.; Sumi, H.; Yamaguchi, Y.; Nomura, K.; Fujishiro, Y., Nanocomposite electrodes for high current density over 3 A cm−2 in solid oxide electrolysis cells. *Nat. Commun.* **2019,** *10* (1), 5432.

40. da Silva, G. C.; Fernandes, M. R.; Ticianelli, E. A., Activity and Stability of Pt/IrO2 Bifunctional Materials as Catalysts for the Oxygen Evolution/Reduction Reactions. *ACS Catal.* **2018,** *8* (3), 2081-2092.

41. Grubb, W. T., Ionic Migration in Ion-exchange Membranes. *J. Phys. Chem.* **1959,** *63* (1), 55-58.

42. Giovanni, C. D.; Reyes-Carmona, Á.; Coursier, A.; Nowak, S.; Grenèche, J. M.; Lecoq, H.; Mouton, L.; Rozière, J.; Jones, D.; Peron, J.; Giraud, M.; Tard, C., Low-Cost Nanostructured Iron Sulfide Electrocatalysts for PEM Water Electrolysis. *ACS Catal.* **2016,** *6* (4), 2626-2631.

43. Ito, H.; Maeda, T.; Nakano, A.; Takenaka, H., Properties of Nafion membranes under PEM water electrolysis conditions. *Int. J. Hydrogen Energy* **2011,** *36* (17), 10527-10540.

44. Dubal, D. P.; Ayyad, O.; Ruiz, V.; Gómez-Romero, P., Hybrid energy storage: the merging of battery and supercapacitor chemistries. *Chem. Soc. Rev.* **2015,** *44* (7), 1777-1790.

45. Nayak, P. K.; Yang, L.; Brehm, W.; Adelhelm, P., From Lithium-Ion to Sodium-Ion Batteries: Advantages, Challenges, and Surprises. *Angew. Chem. Int. Ed.* **2018,** *57* (1), 102-120.

46. Frackowiak, E.; Fic, K.; Meller, M.; Lota, G., Electrochemistry Serving People and Nature: High-Energy Ecocapacitors based on Redox-Active Electrolytes. *ChemSusChem* **2012,** *5* (7), 1181-1185.

47. Akinwolemiwa, B.; Peng, C.; Chen, G. Z., Redox Electrolytes in Supercapacitors. *J. Electrochem. Soc.* **2015,** *162* (5), A5054-A5059.

48. Yu, X.; Yun, S.; Yeon, J. S.; Bhattacharya, P.; Wang, L.; Lee, S. W.; Hu, X.; Park, H. S., Emergent Pseudocapacitance of 2D Nanomaterials. *Adv. Energy Mater.* **2018,** *8* (13), 1702930.

49. Hou, J.; Shao, Y.; Ellis, M. W.; Moore, R. B.; Yi, B., Graphene-based electrochemical energy conversion and storage: fuel cells, supercapacitors and lithium ion batteries. *Phys. Chem. Chem. Phys.* **2011,** *13* (34), 15384-15402.

50. Prato, M., Fullerene chemistry for materials science applications. *J. Mater. Chem.* **1997,** *7* (7), 1097-1109.

51. Javey, A., The 2008 Kavli Prize in Nanoscience: carbon nanotubes. *ACS Nano* **2008,** *2* (7), 1329-1335.

52. Gerstner, E., Nobel Prize 2010: Andre Geim & Konstantin Novoselov. *Nat. Phys.* **2010,** *6* (11), 836-836.

53. Zhang, P.; Wang, F.; Yu, M.; Zhuang, X.; Feng, X., Two-dimensional materials for miniaturized energy storage devices: from individual devices to smart integrated systems. *Chem. Soc. Rev.* **2018,** *47* (19), 7426-7451.

54. Yang, Z.; Ren, J.; Zhang, Z.; Chen, X.; Guan, G.; Qiu, L.; Zhang, Y.; Peng, H., Recent Advancement of Nanostructured Carbon for Energy Applications. *Chem. Rev.* **2015,** *115* (11), 5159-5223.

55. Liu, X.-M.; Huang, Z. d.; Oh, S. w.; Zhang, B.; Ma, P.-C.; Yuen, M. M. F.; Kim, J.-K., Carbon nanotube (CNT)-based composites as electrode material for rechargeable Li-ion batteries: A review. *Compos. Sci. Technol.* **2012,** *72* (2), 121-144.

56. Asenbauer, J.; Eisenmann, T.; Kuenzel, M.; Kazzazi, A.; Chen, Z.; Bresser, D., The success story of graphite as a lithium-ion anode material – fundamentals, remaining challenges, and recent developments including silicon (oxide) composites. *Sustain. Energy Fuels* **2020**.

57. Goktas, M.; Bolli, C.; Berg, E. J.; Novák, P.; Pollok, K.; Langenhorst, F.; Roeder, M. v.; Lenchuk, O.; Mollenhauer, D.; Adelhelm, P., Graphite as Cointercalation Electrode for Sodium-Ion Batteries: Electrode Dynamics and the Missing Solid Electrolyte Interphase (SEI). *Adv. Energy Mater.* **2018,** *8* (16), 1702724.

58. Besenhard, J. O., The electrochemical preparation and properties of ionic alkali metal-and NR4-graphite intercalation compounds in organic electrolytes. *Carbon* **1976,** *14* (2), 111-115.

59. Dey, A. N.; Sullivan, B. P., The Electrochemical Decomposition of Propylene Carbonate on Graphite. *J. Electrochem. Soc.* **1970,** *117* (2), 222.

60. Yazami, R.; Touzain, P., A reversible graphite-lithium negative electrode for electrochemical generators. *Journal of Power Sources* **1983,** *9* (3), 365-371.

61. Nishi, Y., Lithium ion secondary batteries; past 10 years and the future. *J. Power Sources* **2001,** *100* (1), 101-106.

62. Kravchyk, K. V.; Wang, S.; Piveteau, L.; Kovalenko, M. V., Efficient Aluminum Chloride–Natural Graphite Battery. *Chem. Mater.* **2017,** *29* (10), 4484-4492.

63. Wen, Y.; He, K.; Zhu, Y.; Han, F.; Xu, Y.; Matsuda, I.; Ishii, Y.; Cumings, J.; Wang, C., Expanded graphite as superior anode for sodium-ion batteries. *Nat. Commun.* **2014,** *5* (1), 4033.

64.   Wang, D.-Y.; Wei, C.-Y.; Lin, M.-C.; Pan, C.-J.; Chou, H.-L.; Chen, H.-A.; Gong, M.; Wu, Y.; Yuan, C.; Angell, M.; Hsieh, Y.-J.; Chen, Y.-H.; Wen, C.-Y.; Chen, C.-W.; Hwang, B.-J.; Chen, C.-C.; Dai, H., Advanced rechargeable aluminium ion battery with a high-quality natural graphite cathode. *Nat. Commun* **2017,** *8* (1), 14283.

65.   Fan, L.; Ma, R.; Zhang, Q.; Jia, X.; Lu, B., Graphite Anode for a Potassium-Ion Battery with Unprecedented Performance. *Angew. Chem. Int. Ed.* **2019,** *58* (31), 10500-10505.

66.   Muratore, C.; Reed, A. N.; Bultman, J. E.; Ganguli, S.; Cola, B. A.; Voevodin, A. A., Nanoparticle decoration of carbon nanotubes by sputtering. *Carbon* **2013,** *57*, 274-281.

67.   American Chemical Society National Historic Chemical Landmarks. High Performance Carbon fibre, **2003**.

68.   Falvo, M. R.; Clary, G. J.; Taylor, R. M.; Chi, V.; Brooks, F. P.; Washburn, S.; Superfine, R., Bending and buckling of carbon nanotubes under large strain. *Nature* **1997,** *389* (6651), 582-584.

69.   Lee, J. H.; Yoon, C. S.; Hwang, J.-Y.; Kim, S.-J.; Maglia, F.; Lamp, P.; Myung, S.-T.; Sun, Y.-K., High-energy-density lithium-ion battery using a carbon-nanotube–Si composite anode and a compositionally graded $Li[Ni_{0.85}Co_{0.05}Mn_{0.10}]O_2$ cathode. *Energy Environ. Sci.* **2016,** *9* (6), 2152-2158.

70.   Yan, X.; Ye, H.; Wu, X.-L.; Zheng, Y.-P.; Wan, F.; Liu, M.; Zhang, X.-H.; Zhang, J.-P.; Guo, Y.-G., Three-dimensional carbon nanotube networks enhanced sodium trimesic: a new anode material for sodium ion batteries and Na-storage mechanism revealed by ex situ studies. *J. Mater. Chem. A* **2017,** *5* (32), 16622-16629.

71.   Manuel, J.; Zhao, X.; Cho, K.-K.; Kim, J.-K.; Ahn, J.-H., Ultralong Life Organic Sodium Ion Batteries Using a Polyimide/Multiwalled Carbon Nanotubes Nanocomposite and Gel Polymer Electrolyte. *ACS Sustain. Chem. Eng.* **2018,** *6* (7), 8159-8166.

72.   Luo, J.; Wu, W.; Debruler, C.; Hu, B.; Hu, M.; Liu, T. L., A 1.51 V pH neutral redox flow battery towards scalable energy storage. *J. Mater. Chem. A* **2019,** *7* (15), 9130-9136.

73.   Munaiah, Y.; Suresh, S.; Dheenadayalan, S.; Pillai, V. K.; Ragupathy, P., Comparative Electrocatalytic Performance of Single-Walled and Multiwalled Carbon Nanotubes for Zinc Bromine Redox Flow Batteries. *J. Phys. Chem. C* **2014,** *118* (27), 14795-14804.

74.   Park, M.; Jung, Y.-j.; Kim, J.; Lee, H. i.; Cho, J., Synergistic Effect of Carbon Nanofiber/Nanotube Composite Catalyst on Carbon Felt Electrode for High-Performance All-Vanadium Redox Flow Battery. *Nano Lett.* **2013,** *13* (10), 4833-4839.

75.   Van Noorden, R., Production: Beyond sticky tape. *Nature* **2012,** *483* (7389), S32-S33.

76.   Cai, X.; Lai, L.; Shen, Z.; Lin, J., Graphene and graphene-based composites as Li-ion battery electrode materials and their application in full cells. *J. Mater. Chem. A* **2017,** *5* (30), 15423-15446.

77.   Raccichini, R.; Varzi, A.; Wei, D.; Passerini, S., Critical Insight into the Relentless Progression Toward Graphene and Graphene-Containing Materials for Lithium-Ion Battery Anodes. *Adv. Mater.* **2017,** *29* (11), 1603421.

78.   Viet Hung, P.; Pham, D.; Dang, T.; Hur, S.; Kim, E.; Kong, B.-S.; Kim, S.; Chung, J. S., Chemical reduction of an aqueous suspension of graphene oxide by nascent hydrogen. *J. Mater. Chem.* **2012,** *22.*

79.   Garcia, H.; Montes-Navajas, P.; Asenjo, N.; Santamaría, R.; Menendez, R.; Corma, A., Surface Area Measurement of Graphene Oxide in Aqueous Solutions. *Langmuir : the ACS journal of surfaces and colloids* **2013,** *29.*

80.   Song, J.; Park, S.; Gim, J.; Mathew, V.; Kim, S.; Jo, J.; Kim, S.; Kim, J., High rate performance of a $NaTi_2(PO_4)_3$/rGO composite electrode via pyro synthesis for sodium ion batteries. *J. Mater. Chem. A* **2016,** *4* (20), 7815-7822.

81. Jha, P. K.; Singh, S. K.; Kumar, V.; Rana, S.; Kurungot, S.; Ballav, N., High-Level Supercapacitive Performance of Chemically Reduced Graphene Oxide. *Chem* **2017,** *3* (5), 846-860.

82. Yin, C.; Li, J.; Zhou, Y.; Zhang, H.; Fang, P.; He, C., Enhancement in Proton Conductivity and Thermal Stability in Nafion Membranes Induced by Incorporation of Sulfonated Carbon Nanotubes. *ACS Appl. Mater. Interfaces* **2018,** *10* (16), 14026-14035.

83. Liu, Y.-L.; Su, Y.-H.; Chang, C.-M.; Suryani; Wang, D.-M.; Lai, J.-Y., Preparation and applications of Nafion-functionalized multiwalled carbon nanotubes for proton exchange membrane fuel cells. *J. Mater. Chem.* **2010,** *20* (21), 4409-4416.

84. Shaari, N.; Kamarudin, S. K., Recent advances in additive-enhanced polymer electrolyte membrane properties in fuel cell applications: An overview. *Int. J. Energy Res.* **2019,** *43* (7), 2756-2794.

85. Fang, M.; Wang, K.; Lu, H.; Yang, Y.; Nutt, S., Covalent polymer functionalization of graphene nanosheets and mechanical properties of composites. *J. Mater. Chem.* **2009,** *19* (38), 7098-7105.

86. Ramanathan, T.; Abdala, A. A.; Stankovich, S.; Dikin, D. A.; Herrera-Alonso, M.; Piner, R. D.; Adamson, D. H.; Schniepp, H. C.; Chen, X.; Ruoff, R. S.; Nguyen, S. T.; Aksay, I. A.; Prud'Homme, R. K.; Brinson, L. C., Functionalized graphene sheets for polymer nanocomposites. *Nat. Nanotechnol.* **2008,** *3* (6), 327-331.

87. Coleman, J. N.; Khan, U.; Blau, W. J.; Gun'ko, Y. K., Small but strong: A review of the mechanical properties of carbon nanotube–polymer composites. *Carbon* **2006,** *44* (9), 1624-1652.

88. IEA (2012), World Energy Outlook 2012, IEA, Paris https://www.iea.org/reports/world-energy-outlook-2012. 2012.

89. Thomassin, J.-M.; Kollar, J.; Caldarella, G.; Germain, A.; Jérôme, R.; Detrembleur, C., Beneficial effect of carbon nanotubes on the performances of Nafion membranes in fuel cell applications. *J. Membr. Sci.* **2007,** *303* (1), 252-257.

90.   Kannan, R.; Kakade, B. A.; Pillai, V. K., Polymer Electrolyte Fuel Cells Using Nafion-Based Composite Membranes with Functionalized Carbon Nanotubes. *Angew. Chem. Int. Ed.* **2008,** *47* (14), 2653-2656.

91.   Lee, C.; Wei, X.; Kysar, J. W.; Hone, J., Measurement of the Elastic Properties and Intrinsic Strength of Monolayer Graphene. *Science* **2008,** *321* (5887), 385.

92.   Yan, X. H.; Wu, R.; Xu, J. B.; Luo, Z.; Zhao, T. S., A monolayer graphene – Nafion sandwich membrane for direct methanol fuel cells. *J. Power Sources* **2016,** *311*, 188-194.

93.   Ismach, A.; Druzgalski, C.; Penwell, S.; Schwartzberg, A.; Zheng, M.; Javey, A.; Bokor, J.; Zhang, Y., Direct Chemical Vapor Deposition of Graphene on Dielectric Surfaces. *Nano Lett.* **2010,** *10* (5), 1542-1548.

94.   Enotiadis, A.; Angjeli, K.; Baldino, N.; Nicotera, I.; Gournis, D., Graphene-Based Nafion Nanocomposite Membranes: Enhanced Proton Transport and Water Retention by Novel Organo-functionalized Graphene Oxide Nanosheets. *Small* **2012,** *8* (21), 3338-3349.

95.   Kim, K.; Bae, J.; Lim, M.-Y.; Heo, P.; Choi, S.-W.; Kwon, H.-H.; Lee, J.-C., Enhanced physical stability and chemical durability of sulfonated poly(arylene ether sulfone) composite membranes having antioxidant grafted graphene oxide for polymer electrolyte membrane fuel cell applications. *J. Membr. Sci.* **2017,** *525*, 125-134.

96.   Zarrin, H.; Higgins, D.; Jun, Y.; Chen, Z.; Fowler, M., Functionalized Graphene Oxide Nanocomposite Membrane for Low Humidity and High Temperature Proton Exchange Membrane Fuel Cells.   *J. Phys. Chem. C* **2011,** *115* (42), 20774-20781.

97.   Vinothkannan, M.; Kim, A. R.; Gnana kumar, G.; Yoo, D. J., Sulfonated graphene oxide/Nafion composite membranes for high temperature and low humidity proton exchange membrane fuel cells. *RSC Adv.* **2018,** *8* (14), 7494-7508.

98.   Dikin, D. A.; Stankovich, S.; Zimney, E. J.; Piner, R. D.; Dommett, G. H. B.; Evmenenko, G.; Nguyen, S. T.; Ruoff, R. S., Preparation and characterization of graphene oxide paper. *Nature* **2007,** *448* (7152), 457-460.

99. Karim, M. R.; Hatakeyama, K.; Matsui, T.; Takehira, H.; Taniguchi, T.; Koinuma, M.; Matsumoto, Y.; Akutagawa, T.; Nakamura, T.; Noro, S.-i.; Yamada, T.; Kitagawa, H.; Hayami, S., Graphene Oxide Nanosheet with High Proton Conductivity. *J. Am. Chem. Soc.* **2013,** *135* (22), 8097-8100.

100. Marinho, B.; Ghislandi, M.; Tkalya, E.; Koning, C. E.; de With, G., Electrical conductivity of compacts of graphene, multi-wall carbon nanotubes, carbon black, and graphite powder. *Powder Technol.* **2012,** *221*, 351-358.

101. Matsumoto, N.; Oshima, A.; Yumura, M.; Hata, K.; Futaba, D. N., Crystalline and Electrical Property Improvement of Filtrated, Exfoliated Graphite Sheets by an In-Plane Current and Heating Treatment. *Nanoscale Res. Lett.* **2020,** *15* (1), 195.

102. Shi, B.; Wu, H.; Shen, J.; Cao, L.; He, X.; Ma, Y.; Li, Y.; Li, J.; Xu, M.; Mao, X.; Qiu, M.; Geng, H.; Yang, P.; Jiang, Z., Control of Edge/in-Plane Interactions toward Robust, Highly Proton Conductive Graphene Oxide Membranes. *ACS Nano* **2019,** *13* (9), 10366-10375.

103. Matsui, J.; Miyata, H.; Hanaoka, Y.; Miyashita, T., Layered Ultrathin Proton Conductive Film Based on Polymer Nanosheet Assembly. *ACS Appl. Mater. Interfaces* **2011,** *3* (5), 1394-1397.

104. Smith, A. T.; LaChance, A. M.; Zeng, S.; Liu, B.; Sun, L., Synthesis, properties, and applications of graphene oxide/reduced graphene oxide and their nanocomposites. *Nano Materials Science* **2019,** *1* (1), 31-47.

105. Yu, H.; Zhang, B.; Bulin, C.; Li, R.; Xing, R., High-efficient Synthesis of Graphene Oxide Based on Improved Hummers Method. *Sci. Rep.* **2016,** *6* (1), 36143.

106. Marcano, D. C.; Kosynkin, D. V.; Berlin, J. M.; Sinitskii, A.; Sun, Z.; Slesarev, A.; Alemany, L. B.; Lu, W.; Tour, J. M., Improved Synthesis of Graphene Oxide. *ACS Nano* **2010,** *4* (8), 4806-4814.

107. Brodie, B. C., XIII. On the atomic weight of graphite. *Philosophical Transactions of the Royal Society of London* **1859,** *149*, 249-259.

108. Staudenmaier, L., Verfahren zur Darstellung der Graphitsäure. *Ber. Dtsch. Chem. Ges.* **1898,** *31* (2), 1481-1487.

109. Hummers Jr, W. S.; Offeman, R. E. J. Preparation of graphitic oxide, *J. Am. Chem. Soc.* **1958**, *80*, 6, 1339.

110. Ravikumar; Scott, K., Freestanding sulfonated graphene oxide paper: a new polymer electrolyte for polymer electrolyte fuel cells. *Chem. Commun.* **2012,** *48* (45), 5584-5586.

111. Sun, J.; Iakunkov, A.; Rebrikova, A. T.; Talyzin, A. V., Exactly matched pore size for the intercalation of electrolyte ions determined using the tunable swelling of graphite oxide in supercapacitor electrodes. *Nanoscale* **2018,** *10* (45), 21386-21395.

112. Iakunkov, A.; Skrypnychuk, V.; Nordenström, A.; Shilayeva, E. A.; Korobov, M.; Prodana, M.; Enachescu, M.; Larsson, S. H.; V.Talyzin, A., Activated graphene as a material for supercapacitor electrodes: effects of surface area, pore size distribution and hydrophilicity. *Phys. Chem. Chem. Phys.* **2019,** *21* (32), 17901-17912.

113. Bin, D.; Wang, F.; Tamirat, A. G.; Suo, L.; Wang, Y.; Wang, C.; Xia, Y., Progress in Aqueous Rechargeable Sodium-Ion Batteries. *Adv. Energy Mater.* **2018,** *8* (17), 1703008.

114. Qiu, Y.; Yu, Y.; Xu, J.; Liu, Y.; Ou, M.; Sun, S.; Wei, P.; Deng, Z.; Xu, Y.; Fang, C.; Li, Q.; Han, J.; Huang, Y., Redox potential regulation toward suppressing hydrogen evolution in aqueous sodium-ion batteries: $Na_{1.5}Ti_{1.5}Fe0_{.5}(PO_4)_3$. *J. Mater. Chem.* **2019,** *7* (43), 24953-24963.

115. Yi, Y.; Weinberg, G.; Prenzel, M.; Greiner, M.; Heumann, S.; Becker, S.; Schlögl, R., Electrochemical corrosion of a glassy carbon electrode. *Catal. Today* **2017,** *295*, 32-40.

116. Kinoshita, K.; Bett, J., Electrochemical oxidation of carbon black in concentrated phosphoric acid at 135°C. *Carbon* **1973,** *11* (3), 237-247.

117. Munuera, J. M.; Paredes, J. I.; Enterría, M.; Pagán, A.; Villar-Rodil, S.; Pereira, M. F. R.; Martins, J. I.; Figueiredo, J. L.; Cenis, J. L.; Martínez-Alonso, A.; Tascón,

J. M. D., Electrochemical Exfoliation of Graphite in Aqueous Sodium Halide Electrolytes toward Low Oxygen Content Graphene for Energy and Environmental Applications. *ACS Appl. Mater. Interfaces* **2017,** *9* (28), 24085-24099.

118.   Abdelkader, A. M.; Cooper, A. J.; Dryfe, R. A. W.; Kinloch, I. A., How to get between the sheets: a review of recent works on the electrochemical exfoliation of graphene materials from bulk graphite. *Nanoscale* **2015,** *7* (16), 6944-6956.

119.   Wang, F.; Lin, C.-F.; Ji, X.; Rubloff, G. W.; Wang, C., Suppression of hydrogen evolution at catalytic surfaces in aqueous lithium ion batteries. *J. Mater. Chem.* **2020,** *8* (30), 14921-14926.

120.   Schweiss, R.; Pritzl, A.; Meiser, C., Parasitic Hydrogen Evolution at Different Carbon Fiber Electrodes in Vanadium Redox Flow Batteries. *J. Electrochem. Soc.* **2016,** *163* (9), A2089-A2094.

121.   Chang, Y.-C.; Shih, Y.-C.; Chen, J.-Y.; Lin, G.-Y.; Hsu, N.-Y.; Chou, Y.-S.; Wang, C.-H., High efficiency of bamboo-like carbon nanotubes on functionalized graphite felt as electrode in vanadium redox flow battery. *RSC Adv.* **2016,** *6* (104), 102068-102075.

Chapter 2

Coulombic Force Gated Molecular Transport in Redox Flow Batteries

Abstract

Interfacial electrochemistry of reversible redox molecules is central to state-of-the-art flow batteries, fuel cells and electrochemical biosensors. At electrochemical interfaces since the physical processes of mass transport occurs independently and in series to electron transport; the reaction rate in reversible species is predominantly mass-transport controlled due to their adiabatic electron transfer events. Spatial structuring of solution near the electrode surface force diffusion to dominate the transport phenomena even under convective fluid-flow which in-turn pose unique challenges to utilize the maximum potential of reversible species either by electrode or fluid characteristics. In this chapter, we discuss coulombic force gated molecular flux at the interface to target the transport velocity of reversible species; that in turn triggers a directional electrostatic current over the diffusion current within the reaction zone. In iron based redox flow battery, this gated molecular flux almost doubles the volumetric energy density without compromising the power capability.
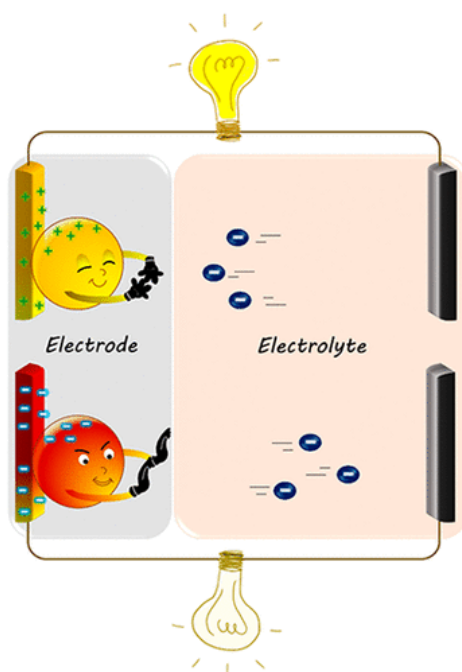
Declaration: The work has been published in the following journal:

J. Phys. Chem. Lett. 2021, 12, 5, 1374–1383. Copyright. American Chemical Society.

2.1. Introduction

The electrochemistry of outer-sphere redox molecules often plays pivotal roles in the chemistry of state-of-the-art energy storage and conversion devices and electrochemical biosensors.[1-11] In this direction, negatively charged co-ordination complexes such as ferricyanide has been widely employed as positive electrodes in all alkaline quinone flow batteries, iron flow batteries, direct alcohol fuel cells etc.[12-22] Since, ferricyanide is an outer-sphere redox molecule, its interfacial behavior is predominantly diffusion controlled which in turn pose unique challenges to target its overall reaction rate by electrocatalysis.[23-26] It is worthy to note that even under convective fluid flow, the major mode of transport within the reaction zone is by simple diffusion because of larger thickness of hydrodynamic boundary layer compared to the diffusion layer.[27,28] In electrochemical energy devices, this diffusion limited reaction velocity prevents the utilization of the maximum potential of reversible species either by electrode or fluid characteristics which in turn is primarily responsible for their extremely low volumetric energy density (∼20% of its theoretical value).[13,20] Although efforts are dedicated to overcome these hurdles primarily by increasing the solubility of the redox species[18,29] and recently by chemical regeneration of the active species in external tanks[30] the root of the problem being their transport controlled reaction rate is often overlooked. In this chapter, we show that by activating coulombic forces at the interface, gated molecular flux with a precise control over its direction can be achieved to target the overall reaction velocity of reversible species within the reaction zone. We demonstrate that this coulombic force gated molecular flux can trigger an electrostatic current contribution parallel to the diffusion current within the reaction zone. By incorporating coulombic forces in an iron based redox flow battery, we show that gated reaction velocity almost doubles their volumetric energy density irrespective of the molecule's solubility limits by extending the concentration polarization regime beyond conventionally accessible limits. We note that there exists a few reports on surface functionalization of electrodes for improving the flow battery performance especially in vanadium based flow batteries, however; it should be noted that these attempts were mainly dedicated at electrocatalytic reactions of vanadium redox species involving significant bond rearrangements.[31-35] Our approach is fundamentally different as it is concerned with outer-sphere redox couples where the

reaction kinetics is limited by a physical process rather than a chemical process making it independent of the presence of catalytic domains on the electrode surface. In the present work, precise directionality is exerted on this physical process by the nature of the interfacial Coulomb's force which in turn offers a remarkable control over its overall transport velocity within the reaction zone.

2.2. Experimental

2.2.1. Materials and reagents

H_2SO_4 (99.99 %), HNO_3 (99.99 %), HCl (99.99 %), Polydiallyldimethylammonium chloride (20 wt% in H_2O) and multi-walled carbon nanotube ($\geq$ 98%) were obtained from Sigma Aldrich, India. Zinc Foil (99.98%, 0.25 mm thick) was purchased from Alfa Aesar, India. KNO_3, $K_3[Fe(CN)_6]$, $ZnSO_4.7H_2O$ and $(NH_4)_2SO_4$ were purchased from S.D Fine Chemicals, India. Toray carbon gas diffusion paper was obtained from fuel cell store, USA.

2.2.2. Modification of carbon nanotubes (CNTs)

The negatively charged carbon nanotube (N-CNT) was prepared by the chemical oxidation of raw carbon nanotube (CNT), Scheme 2.1.[36-38] The raw CNT (100mg) was first purified by the continuous stirring in 200 mL of conc. HCl for 2 hrs in a conical flask. Treatment in conc. HCl is well known method for removing the impurities present in raw CNT. After that it was filtered and precipitate was washed with deionized water. This purified CNT was labelled as unmodified CNT. This unmodified CNT was further oxidized by treating with conc. HNO_3. 100 mg of this unmodified CNT was refluxed in 200 mL of HNO_3 at 120°C. The resulting oxidized compound was filtered and washed with deionized water. The sample was dried in vacuum oven at 60°C. This oxidized CNT was labelled as negatively charged CNT (N-CNT), Scheme 2.1.

For making the positively charged CNT (P-CNT), polyelectrolyte functionalization method was used.[39-42] 100 mg of unmodified CNT was first dispersed in 200 mL of deionized water followed by the addition of PDDA polymer in different weight percentages. Then, the reaction mixture was ultrasonicated for 2 h. The composite was filtered followed by washing with deionized water and then kept for drying. This dried composite was labelled as positive CNT (P-CNT), Scheme 2.1.

2.2.3. Physicochemical characterizations

ATIR-FTIR (Bruker Alpha) was performed on the electrodes before and after the battery performance to investigate the stability of the electrodes. Raman spectra were recorded by using a Raman microscope (LabRAM HR, Horbia Jobin Yvon). The Zeta potential of charged and uncharged CNTs were measured in Nano ZS90 (Malvern) Zetasizer. Biologic VMP 300 potentiostat/galvanostat was used for electrochemical studies such as cyclic voltammetry, chronomaperometry and electrochemical impedance spectroscopy. Rotating disk electrode (RDE) measurements were carried out by PARSTAT MC, AMETEK. X-ray photoelectron spectroscopy (XPS) analysis were performed by Thermo Scientific K-Alpha with Al-Kα as an excitation source. Hydrophilicity/hydrophobicity of the unmodified and modified CNTs were carried out using Holmarc's Contact Angle Meter. The specific surface area (m^2/g) for the unmodified and modified (positive and negative) CNTs were calculated by BET method from the nitrogen adsorption/desorption isotherm at 77 K using Micromeritics 3-FLEX pore and surface area analyzer.
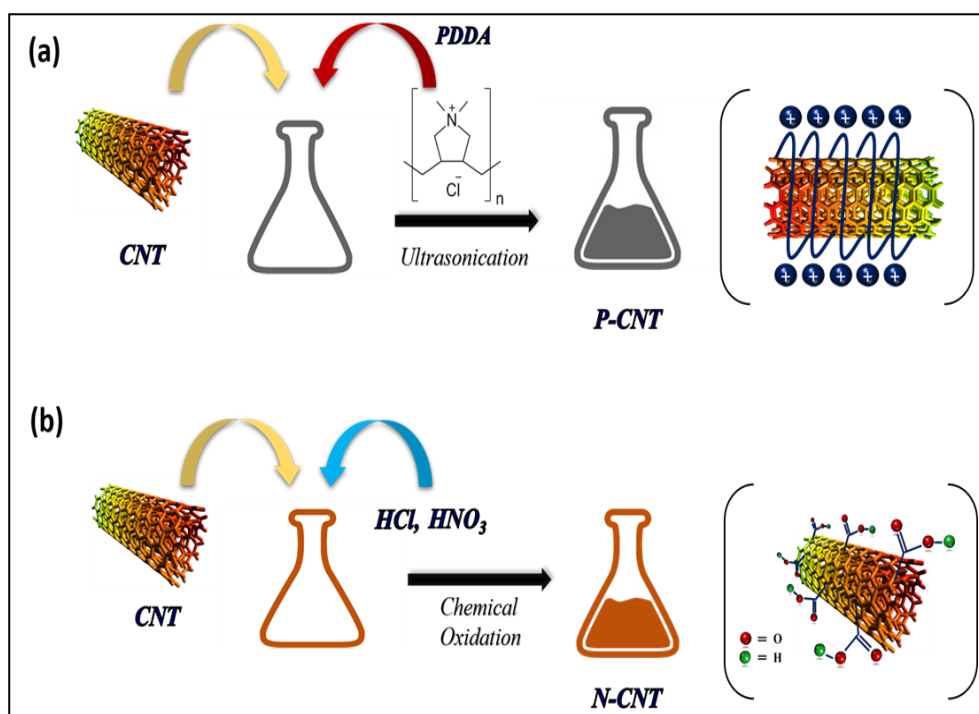
Scheme 2.1: Scheme showing the steps involved in the preparation of (a) P-CNT and (b) N-CNT.

2.2.4. Electrochemical characterizations

Rotating disk electrode (RDE) studies of $K_3[Fe(CN)_6]$ were carried out in nitrogen purged 1 M KNO_3 solution at a scan rate of 5 mV s^{-1} in a three electrode system with a glassy carbon (GC) disc as the working electrode, Ag/AgCl (3 M KCl) as the

reference electrode and platinum foil as the counter electrode at different RPM values (100, 400, 900, 1600, 3600). Analysis of the RDE data were carried out by Koutecky-Levich equation (equation 2.1) to find the number of electrons and kinetic parameters.

$$1/j = 1/j_k + 1/j_l \qquad (2.1)$$

where, j is the total current density, j_k is kinetic current density and j_l is the limiting current density which is defined by equation 2.2.

$$j_l = 0.62 n F D^{2/3} v^{-1/6} C \, \omega^{1/2} \qquad (2.2)$$

where, n - number of electrons, F - faraday constant (96485 C mol^{-1}), D - diffusion coefficient (cm^2 s^{-1}), v - kinematic viscosity (cm^2 s^{-1}), C - concentration (mol cm^{-3}) and ω - rotation rate (rad s^{-1}).

Electrochemical impedance spectroscopy (EIS) measurements were carried out using three electrode assembly in equimolar (10 mM) mixture of $K_3[Fe(CN)_6]$/ $K_2[Fe(CN)_6]$ in 1 M KNO$_3$ solution in the frequency range of 100 kHz to 5 mHz at 0 V vs. open circuit voltage with a 10 mV (peak to peak) AC excitation signal. The Warburg coefficients (σ) of the electrodes were determined from the slope of the plot of real part of the impedance in the low frequency region vs. $1/\sqrt{\omega}$, where $\omega = 2\pi f$.[43,44] Cyclic voltammograms of $K_3[Fe(CN)_6]$ in 1 M KNO$_3$ were recorded at 20 mV s^{-1} scan rate. Cyclic voltammetry and chronoamperometric investigations were carried out for P-CNT, N-CNT and unmodified CNT working electrodes on a glassy carbon electrode (3 mm diameter) in three electrode assembly with Ag/AgCl (3 M KCl) as the reference electrode and Pt foil as the counter electrode in 10 mM $K_3[Fe(CN)_6]$ dissolved in 1 M KNO$_3$ solution. CNT ink was prepared by dispersing the definite amount of CNTs (~3 mg) in the isopropyl alcohol (~0.5 mL) with 5 wt% PTFE as the binder. A definite amount of the ink was drop casted on a GC electrode for electrochemical experiments. The areal loadings of CNT samples in all the three cases (P-CNT, N-CNT and unmodified CNT) were nearly 0.1 mg cm^{-2}. Before performing the experiment, the solutions were purged with the N$_2$ gas for about 20 minutes. Each time the GC electrode was first manually cleaned by polishing with 0.05 micron alumina powder and then by electrochemical cycling in the 0.5 M H$_2$SO$_4$. All the potentials are converted to standard hydrogen scale (SHE) unless and otherwise specified. Faradaic charges were calculated from chronoamperometric traces. Chronocoulometry invetsigation has been performed in order to contruct the Anson plot.[45, 46] The mass transfer coefficients (k_m) reflecting the characteritisc rate of a diffusion process for unmodified CNT, N-CNT and P-CNT electrodes were investigated from RDE

measurements in 1 M KNO_3 containing 10 mM $K_3[Fe(CN)_6]$ at 1600 rpm. Equation 2.3 was used to calculate the k_m values from limiting currents (I_l).[47,48]

$$k_m = I_l/(nFAC) \qquad\qquad (2.3)$$

where, I_l is the limiting current, n is the number of electrons, A is the area of the electrode and C is the bulk concentration of the electrolyte.

2.2.5. Fabrication of battery

Battery was fabricated in a two-compartment flood cell configuration with inlets and outlets for liquid flow. The half-cells were separated by a Nafion 117 polymer electrolyte membrane for ion communication. Anodic half-cell is fabricated by immersing a zinc foil in an electrolyte mixture containing 0.1 M $ZnSO_4$ and 1 M $(NH_4)_2SO_4$ whereas cathodic half-cell contains 1 M ferricyanide dissolved in 1 M KNO_3. The geometric area of the reactor was approximately 3 cm². A Toray carbon paper coated with positively charged carbon nanotube (P-CNT), or negatively charged CNT (N-CNT) or unmodified CNT was used as the driving electrode for ferricyanide half-cell. The CNT ink was prepared by mixing its required amounts with 5 % PTFE solution in 2-propanol followed by ultrasonication for 1 hour. The ink was then brush coated over the Toray carbon paper at a loading of 3 mg cm^{-2}. Anolyte and catholyte were pumped into the cell at 2 mL min^{-1} flow-rate. Prior to the charge/discharge experiments the electrolytes were flown through the electrode assembly till a stable open-circuit voltage (OCV) was obtained. The galvanostatic charge/discharge experiments were carried out at different current rates (20, 50, 70, 90, 110 mA cm^{-2}). The cycling stability test was carried out at 100 mA cm^{-2} current density.

2.3. Results and discussion

2.3.1. Coulombic force gated molecular flux

Interfacial chemistry of ferricyanide is ubiquitous in flow batteries and fuel cells because of its ability to undergo facile electron transfer even on carbon-based electrodes at relatively positive reduction potentials.[17-20] For aforementioned reasons, ferricyanide redox chemistry is employed as the electron-accepting half-cell chemistry in classical Zn-ferricyanide flow batteries.[13,21,22,30] Even though the interfacial electron transfer rate is very fast for a ferricyanide half-cell because of its outer-sphere electron transfer with minimal bond rearrangements, intriguingly the same half-cell often limits overall performance

metrics in flow batteries. [18,30] In order to verify this, a Zn-ferricyanide flow battery was fabricated which consists of a Zn strip immersed in a mixture of $ZnSO_4$ (0.1 M) and $(NH_4)_2SO_4$ (1 M) solution (details are provided in the experimental section) as the anodic half-cell, Nafion[®] 117 membrane as the separator and $[Fe(CN)_6]^{3-}$ (1 M) dissolved in KNO_3 (1 M) as the cathodic half-cell (Scheme 2.2).
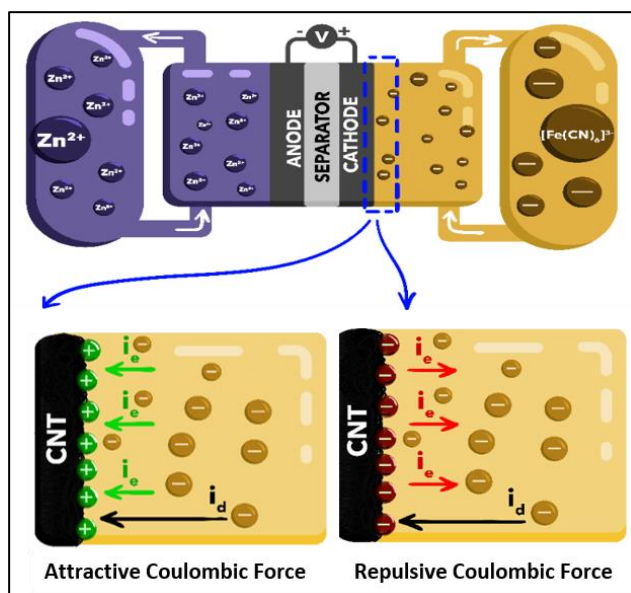
Scheme 2.2: Schematics of Zn-ferricyanide redox flow battery (top). The anodic half-cell is Zn/Zn^{2+} and cathodic half-cell is ferricyanide/ferrocyanide separated by Nafion 117 membrane. Bottom shows the schematic representation of coulombic force gated molecular flux at electrochemical interfaces. The interfacial chemistry of driving carbon nanotube (CNT) electrode is tuned to positive and negative (please refer experimental section for details) respectively to achieve coulombic attraction and repulsion towards negatively charged ferricyanide. I_d is the diffusion current contribution and I_e is the electrostatic current contribution.
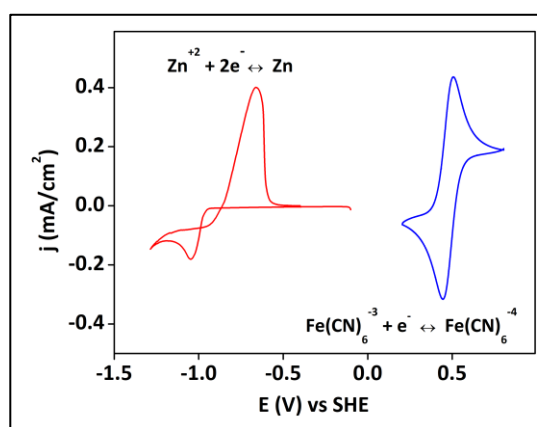
Figure 2.1: Cyclic voltammograms showing the potential difference between Zn/Zn^{2+} couple in 0.1 M $ZnSO_4$ + 1 M $(NH_4)_2SO_4$ electrolyte and $Fe(CN)_6^{3-}/Fe(CN)_6^{4-}$ redox couple in 1 M KNO_3.

A carbon nanotube coated (CNT) Toray carbon paper electrode was employed to drive the ferricyanide redox reaction. A Zn-ferricyanide battery configuration is feasible because of the positive electromotive force between ferrocyanide/ferricyanide redox reaction and Zn/Zn^{2+} redox reaction in chosen electrolytes, Figure 2.1, and the battery half-cell and full cell chemistries are in accordance with equations 2.4-2.6.[6,49,50]

Anodic Reaction:

$[ZnSO_4(H2O)_5] + 2e- \rightleftarrows Zn + SO_4^{-2} + 5H_2O$, E^0 = -1.16 vs SHE   (2.4)

Cathodic Reaction:

$2[Fe(CN)_6^{3-}] + 2e^- \rightleftarrows 2[Fe(CN)_6^{4-}]$, E^0 = 0.35 vs SHE   (2.5)

Total Cell Reaction:

$Zn + SO_4^{-2} + 5H_2O + 2[Fe(CN)_6^{3-}] \rightleftarrows [ZnSO_4(H_2O)_5] + 2[Fe(CN)_6^{4-}]$, E^0 = 1.51 V vs SHE (2.6)
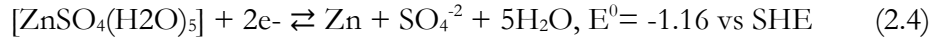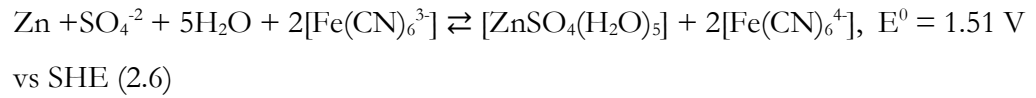
With an unmodified carbon nanotube (CNT) electrode as the driving electrode for ferricyanide, the half-cell electrode polarization with respect to a common reference electrode suggest that ferricyanide half-cell limits the overall device performance, Figure 2.2a. This is further clear from galvanostatic charge-discharge curves which suggest that the discharge capacity is scaling up with the concentration of ferricyanide, Figure 2.2b. Furthermore, the gravimetric discharge capacity (theoretical) of ferricyanide is ~10 times lower than that of Zn.[13,51,52] Taken together, in a classical Zn-ferricyanide battery, cathodic half-cell limits the overall performance metrics and any strategy to improve the performance metrics should be targeted towards the interfacial chemistry of the ferricyanide half-cell.
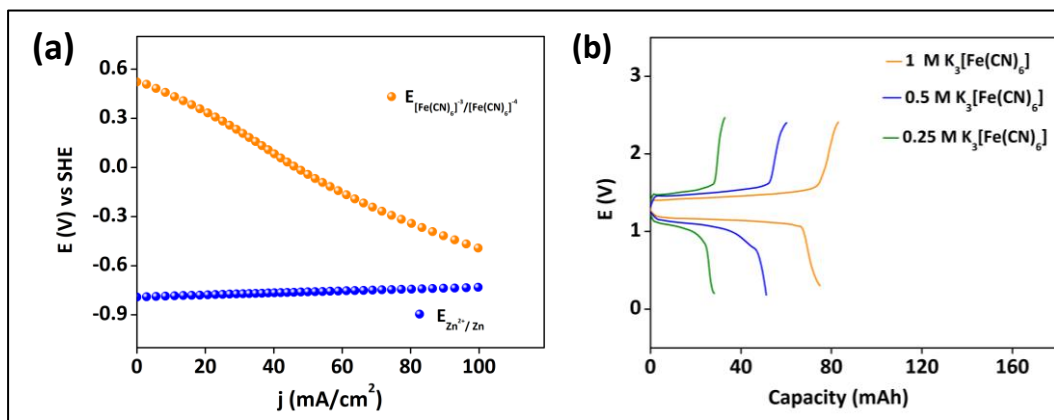
Figure 2.2: (a) Half-cell electrode polarizations for Zn-ferricyanide battery with an unmodified carbon nanotube (CNT) as the driving electrode for the ferricyanide half-cell. (b) Charge discharge curves of Zn-ferricyanide battery at 20 mA cm^{-2} current density with

an unmodified CNT as the driving electrode for the cathodic species with different concentrations of $[Fe(CN)_6]^{3-}$ in 1 M KNO$_3$.

Since, ferricyanide is a reversible redox species, their reaction rate is dominantly mass-transport controlled making it independent of inherent electrode characteristics, area normalized cyclic voltammograms on Au, Pt and glassy carbon (GC) electrodes, Figure 2.3a. Near the electrode surface, spatial structuring of solution force simple diffusion to dominate the transport phenomena even under convective fluid flow that in turn pose unique challenges to utilize the maximum potential of the molecule either by electrode (electrocatalysis) or fluid characteristics (fluid flow).[53,54] It is to be noted that the negative charge on the ferricyanide complex provides an extra handle to amplify its interfacial electr-
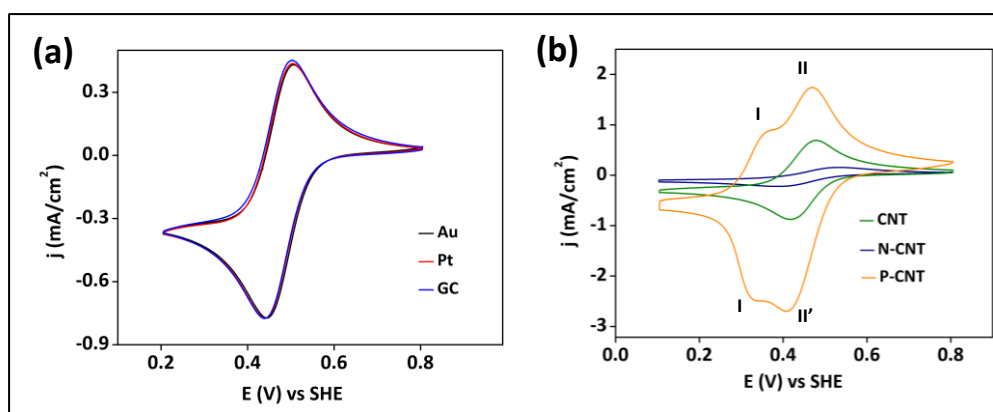
Figure 2.3: (a) Cyclic voltammograms of Au, glassy carbon (GC) and Pt electrodes. (b) Cyclic voltammograms of unmodified CNT, negatively charged CNT (N-CNT) and positively charged CNT (P-CNT) with 10 mM $[Fe(CN)_6]^{3-}$ in 1 M KNO$_3$ at 20 mV s^{-1} scan rate.

-ochemistry because it offers the possibility of attracting/repelling the molecule electrostatically at the interface. To make this possible, coulombic forces were activated at the driving carbon nanotube (CNT) electrode/electrolyte interface by tuning the surface charge of CNT electrode from positive to negative (as discussed in the experimental section) to respectively exert electrostatic attraction and repulsion towards negatively charged ferricyanide complex (Scheme 2.2). Positively and negatively charged CNT electrodes are respectively prepared by covering CNT electrode with a positively charged charged polymeric species such as polydiallyldimethylammonium chloride (PDDA) and by oxidizing the CNT in HNO$_3$ medium.[36-42] The former strategy is expected to make the CNT surface positively charged which in turn should electrostatically pull the negatively charged ferricyanide species towards the electrode surface. In line with this anticipation, with a positively charged carbon nanotube (P-CNT) electrode, the redox currents are

significantly amplified (cyclic voltammogram, orange trace, Figure 2.3b with a decrease in peak potential separation (ΔEp) for the peak pair II, II' compared to unmodified CNT green trace, Figure 2.3b and Table 2.1. The redox activity decreased and ΔEp increased noticeably (blue trace, Figure 2.3b and Table 2.1) with a negatively charged CNT (N-CNT), pointing the origin of this to coulombic forces.

Table 2.1: Electrochemical parameters extracted from Figure 2.3b.

Material	ΔEp (mV)
CNT	~70
P- CNT	~63
N- CNT	~135

In line with these, the chronoamperometric traces in the diffusion limited region (at a potential of ~405 mV vs. SHE) demonstrated noticeably higher steady state currents on P-CNT compared to unmodified and N-CNT electrodes, Figure 2.4a, reflecting substantially higher mass transport of ferricyanide towards the former electrode. The Anson plot[45,46] with ferricyanide clearly indicates that the overall charge transferred is higher on P-CNT electrode, Figure 2.4b. Therefore, the positive surface charge on the driving electrode pre-concentrates the negatively charged ferricyanide species at its interface and significantly improve the overall transport velocity of the reversible species within the diffusion layer.
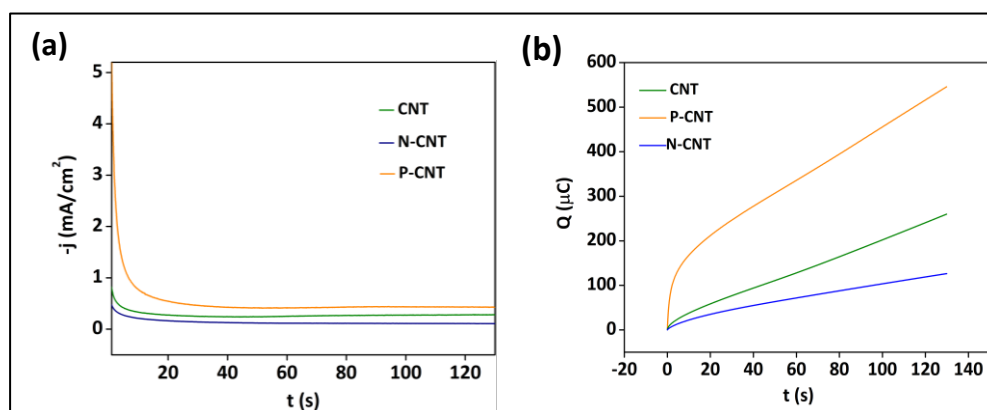
Figure 2.4: (a) Chronoamperometry studies on P-CNT, unmodified CNT and N-CNT electrodes at 405 mV vs. SHE in 1 M KNO_3 containing 10 mM $[Fe(CN)_6]^{3-}$ and (b) Anson plot of charge vs. time extracted from Figure 2.4a.

Electrochemical impedance spectroscopy (EIS) was employed to investigate the interfacial effects of activating coulombic forces, Figure 2.5a. EIS data was fitted with an equivalent circuit (inset of Figure 2.5a) to model the interface. The high frequency resistance R_1 represents the solution resistance which is nearly the same in all the three electrodes, Table 2.2. High frequency RC circuit represents the GC/CNT interface with CPE1 and R_2 as interface capacitance and contact resistance respectively. CPE2 represents the double layer capacitance and R_3 stands for the charge transfer resistance (R_{ct}). W is the Warburg impedance which models the diffusion process. It is clear that the charge transfer resistance (R_{ct}) is relatively decreased in case of P-CNT electrode and increased in case of N-CNT electrode as compared to unmodified CNT electrode, Figure 2.5a and Table 2.2. The plausible explanation can be the favourable electron transfer in P-CNT due to the attractive force exerted by the electrode (decrease in the energy barrier). In similar lines, the negative charge on N-CNT may hinder the electron transfer due to the repulsive interactions exerted by the electrode (increase in the energy barrier). This can be explained by Marcus theory where the heterogenous electron transfer rate constant (k_{ET}) is related to equilibrium constant (K_P) for the activated complex, reorganization energy (λ) and electron tunneling probability (κ_{el}) in the transition state as follows,[55]

$$k_{ET} = \kappa_{el} \cdot K_P \cdot \nu_n \cdot e^{\frac{(\lambda + \Delta G^0)^2}{4 \cdot \lambda \cdot R \cdot T}} \qquad 2.7$$

where ν_n is the frequency of crossing the free energy barrier.

According to Marcus theory, a weak electronic interaction between the electrode and the reacting molecule is sufficient for the occurrence of electron transfer. If electron transfer occurs by tunneling the κ_{el} is given by the following equation,[56,57]

$$\kappa_{el} = \kappa_{el}^0 \cdot e^{-\beta \cdot d} \qquad 2.8$$

Where d is the distance between the electrode and the molecule at the electrode-electrolyte interface. This says that when d increases, κ_{el} will decrease and consequently k_{ET} will also decrease and vice versa. For a positively charged electrode d can be much smaller compared to a negatively charged electrode. This should lead to an increase in electron tunneling probability in the positively charged electrode and a decrease in negatively charged electrode as compared to uncharged electrode. In order to investigate the effects of coulombic forces on the electrode towards the transport velocity of redox species, real part of the impedance (Z') was plotted against the inverse of square root of

frequency in the lower frequency region, Figure 2.5b, and it shows that slope of P-CNT electrode is the lowest and N-CNT is the highest. The slope of this plot is known as the Warburg coefficient (σ) which is inversely related to the transport velocity of the redox species towards the electrode.[43,44] The lower slope with P-CNT shows that the positive charge on the electrode significantly enhances the transport velocity of ferricyanide. On the other hand, the transport velocity of ferricyanide with N-CNT decreases even below that of unmodified CNT due to the negative charge on the former electrode. Taken together, comparatively lower Warburg coefficient with a P-CNT electrode compared to an N-CNT electrode reflect the fact that coulombic forces can be exploited to gate the molecular transport of ionic redox species with in the reaction zone. When the electrode charge is positive, it exerts an attractive force on negatively charged ferricyanide leading to an amplification in its redox behaviour and vice versa. Therefore, it can be concluded that the current amplification observed in Figure 2.3b with P-CNT electrode is primarily due to an electrostatic current contribution parallel to diffusion current (Scheme 2.2). On the other hand, with N-CNT electrode the decrease in redox current is mainly due to an opposing electrostatic current with respect to diffusion current, Figure 2.3b and Scheme 2.2.
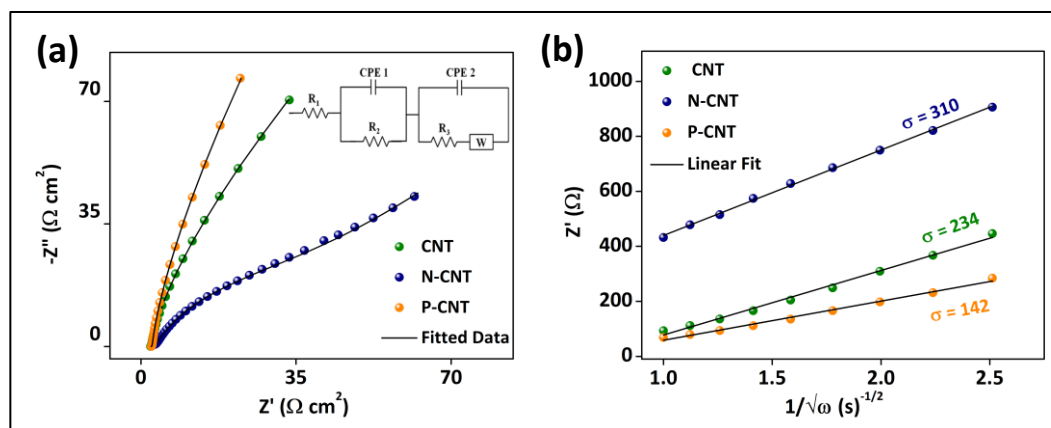
Figure 2.5: (a) Nyquist plots of unmodified CNT, N-CNT and P-CNT with 10 mM $[Fe(CN)_6]^{3-}/[Fe(CN)_6]^{4-}$ in 1 M KNO_3 in the frequency range of 100 kHz to 5 mHz at 0 V vs. open circuit voltage with a 10 mV (peak to peak) AC excitation signal. Inset shows the equivalent circuit. (b) The plot of real part of impedance (Z') vs. inverse square root of angular frequency in the low frequency Warburg region (extracted from Figure 2.5a).

Table 2.2: Electrochemical parameters extracted from Figure 2.5.

Material	R_1 (Ω)	R_2 (Ω)	R_3 or R_{ct} (Ω)	Warburg Coefficient (Ω sec$^{-1/2}$)

CNT	31.46	5.103	236.8	234
N-CNT	34.95	12.39	606.8	310
P-CNT	33.49	3.418	64.97	142

It should be noted that the voltammograms on P-CNT demonstrate multiple peaks (Figure 2.3b) and the first peak pair at more negative potentials (peak pair I, I') is attributed to adsorbed ferricyanide on P-CNT or ferricyanide trapped in the polymer matrix of P-CNT. Concentration and scan rate dependent cyclic voltammograms, Figure 2.6a and 2.6b, indicate both the redox currents of both the peak pairs increase with respect to the scan rate and concentration of ferricyanide. However, the plot of peak current (Ip) vs. square root of scan rate (ν) for the peak pair I, I' was non-linear, Figure 2.6c. The corresponding plot of log (Ip) vs. log (ν) yielded a slope of ~1 suggesting the situation res-
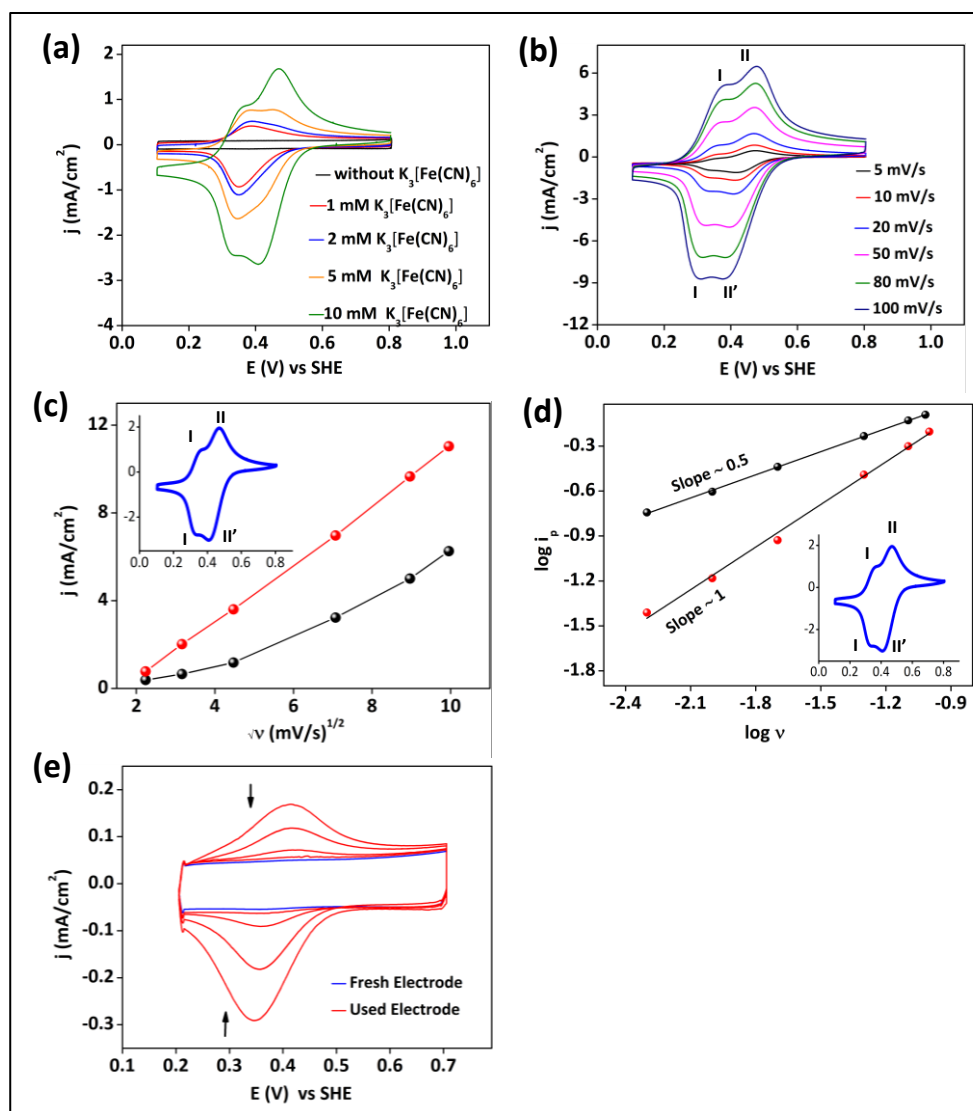
Figure 2.6: (a) Cyclic voltammograms of P-CNT electrode (a) at different concentrations of $K_3[Fe(CN)_6]$ in 1 M KNO_3 at 20 mV s^{-1} scan rate and (b) at different scan rates with 10 mM $K_3[Fe(CN)_6]$ in 1 M KNO_3, (c) Plot of peak currents (i_p) vs. square root of scan rate (v) for peak pair (I, I') and (II, II'), (d) corresponding logarithmic plots and (e) cyclic voltammograms of P-CNT electrode in 1 M KNO_3 before (fresh electrode) and after cycling (used electrode) in 1 M KNO_3 containing 10 mM $K_3[Fe(CN)_6]$. Used P-CNT electrode was thoroughly washed with deionized water before cycling in 1 M KNO_3 solution.

-embling a thin layer diffusion, Figure 2.6d. The P-CNT electrode after incubating in ferricyanide solution for an hour, when tested in ferricyanide free solution (after thorough washing) demonstrated a redox pair in the potential region where thin layer behavior was observed (I, I' in Figure 2.3b) whose intensity gradually decreased as a function of cycling, Figure 2.6e. This indicates that I, I' peak pair in P-CNT arise mainly from surface confined ferricyanide. The peak pairs I, I' and II, II' evidenced peak potential separations of ~20 mV and ~62 mV respectively, further suggesting that the former arise primarily from surface confined ferricyanide. The second peak pair (II, II') close to the formal potential 435 mV with respect to SHE on P-CNT electrode correspond to freely diffusing ferricyanide redox species as similar features existed on unmodified CNT, Figure 2.3b. The concentration and scan rate dependence of the peak pair II, II' on P-CNT electrode demonstrates a diffusion-controlled behavior with a log (I_p) vs. log (v) slope of ~0.5, Figure 2.6a-Figure 2.6d. Ideally, the peak separation of thin layer diffusion should not increase with respect to the scan rate. However, it is observed that there is increase in peak separation in first peak pair (Figure 2.6c) with respect to scan rate from ~20 mV at 5mVs^{-1} scan rate to ~65 mV at 100 mVs^{-1} scan rate. This behavior may be due to the coexistence of both the peak pairs because of diffusion controlled and thin layer-controlled processes.

The rotating disk electrode (RDE) measurements and the corresponding Koutecky-Levich (K-L) plots suggest that the number of electrons transferred on P-CNT, N-CNT and unmodified CNT are close to 1, Figure 2.7a and Figure 2.7b. The noticeably higher currents on P-CNT compared to N-CNT and unmodified CNT even under forced convection reflect that the flux towards P-CNT is inherently higher due to coulombic attraction, Figure 2.7a. Typically for aqueous media under forced convection, the thickness of the Prandtl layer or hydrodynamic boundary layer is ~10 fold larger than the diffusion layer.[27,28] This indicates the contribution of convection near the electrode surface is negligible and the major mode of transport is by simple diffusion. Therefore, the increase

in the limiting current in P-CNT electrode compared to other electrodes even under convective fluid flow is due to overall increase in interfacial transport velocity of molecules due to electrostatic attraction exerted by positively charged electrode on negatively char ferricyanide species. This is substantiated by extracting mass transfer coefficient (k_m) from limiting currents (please refer experimental section for more details) in Figure 2.7c, which demonstrate ~2 times higher value with P-CNT electrode compared to unmodified electr-
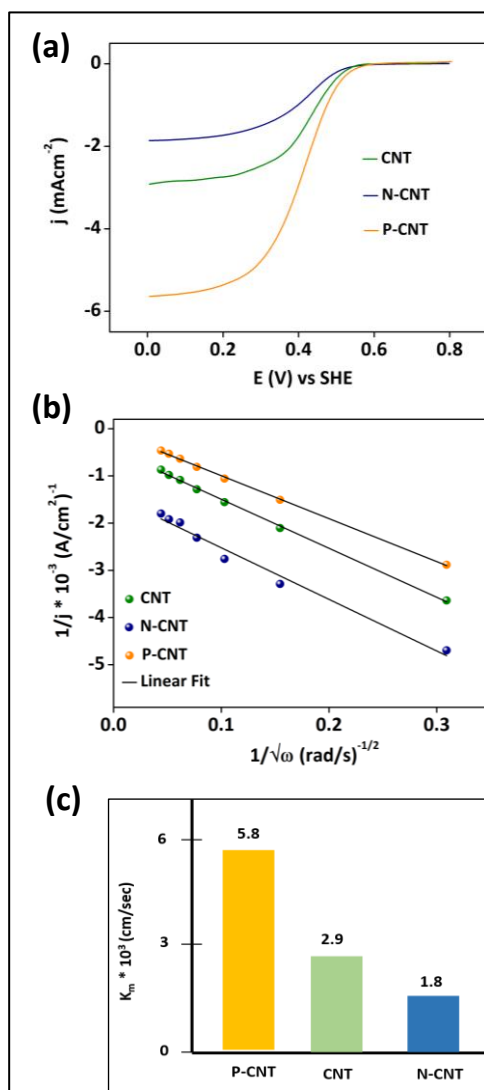
Figure 2.7: (a) Rotating disk electrode (RDE) measurements for unmodified CNT, N-CNT and P-CNT electrodes in 1 M KNO_3 containing 10 mM $K_3[Fe(CN)_6]$ at 1600 rpm, (b) corresponding Koutecky−Levich (K-L) plots at 465 mV vs. SHE and (c) mass transfer coefficients extracted from the limiting currents in Figure 2.7a.

-ode. Furthermore, the k_m value for N-CNT electrode is even smaller than that of unmodified CNT, Figure 2.7c. It may be noted that the unit of k_m is cm s^{-1} and hence it reflects the rate constant for a purely transport controlled reaction.[58] Therefore, Figures

2.7a-2.7c clearly reveal that the nature of the interfacial Coulomb's force exerts a directivity on the physical process of interfacial molecular transport. However, it may be argued that the changes in redox currents (Figure 2.3b and Figure 2.7a) are due to surface area difference/changes in wettability of modified electrodes compared to unmodified electrodes. In order to investigate this, we have carried out the surface area measurement using Brunauer–Emmett–Teller (BET) analysis which shows that surface area follows the trend; N-CNT > P-CNT > CNT, Figure 2.8a and 2.8b, which is also in line with the literature.[36,59]

To further strengthen our claim, we have also carried out the contact angle measurements to assess the wettability of the electrode surfaces. These measurements (Figure 2.8c) demonstrate that the contact angle of P-CNT (~142°) is only slightly lower than the unmodified electrode (~147°). On the other hand, the contact angle of N-CNT electrode (~85°) is substantially lower than P-CNT electrode which are more or less in accordance with the literature.[38,41] These suggest that N-CNT electrode is hydrophilic whereas P-CNT and unmodified CNT electrodes are hydrophobic in nature. Therefore, the incorporation of PDDA on CNT does not change noticeably the wettability of electrodes, however, the presence of oxygen rich functionalities in N-CNT does change the wettability substantially. Based upon the BET and contact angle measurements one would expect N-CNT to show higher performance because of higher surface area and better wettability, however the experimental results are opposite with P-CNT showing the superior performance. Therefore, the surface area/wettability are not primary factors contributing to the alterations in redox currents of negatively charged ferricyanide but the coulombic force gated molecular transport within the reaction zone. It is to be noted that with CNT as the reference point, the increase in current density in P-CNT is higher than the decrease current density in N-CNT, Figures 2.7a. This shows that even though the directional electrostatic current is a consequence of the surface charge of the electrode, the density of charged functional groups affects its quantitative value. In the present work, our primary objective is to demonstrate directional molecular transport of reversible redox molecules within the reaction zone and as such the density of charged functionalities on the electrode surface were not controlled. It is to be noted that controlling the density of surface charge centers demands separate investigation which is beyond the scope of the present chapter. In essence, electrochemical and hydrodynamic investigation demonstrate that activation of coulombic forces at the interface can amplify the interfacial electrochemistry of ionic redox species with fast electron transfer events which will be

beneficial to boost the performance metrics of flow batteries employing reversible redox molecules as demonstrated below.
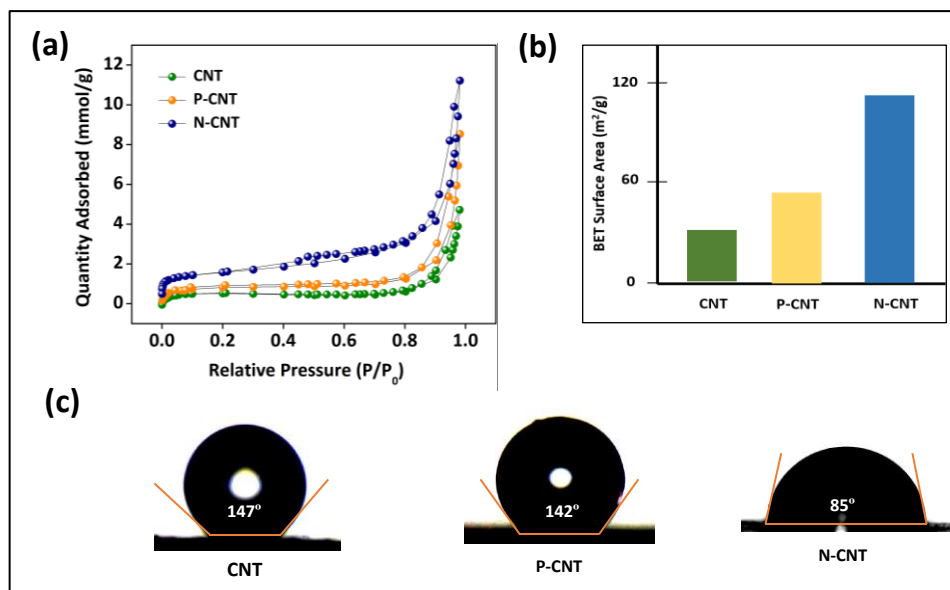
Figure 2.8: (a) and (b) BET surface area of P-CNT, unmodified CNT and N-CNT electrodes and (c) contact angle images of unmodified CNT, P-CNT and N-CNT electrodes.

2.3.2. Characterization of modified and unmodified CNT electrodes

Positively and negatively charged carbon nanotubes (CNTs) were prepared by making a composite of CNT with polydiallyldimethylammonium chloride (PDDA) and by oxidizing the CNT in HNO₃ medium respectively (please refer experimental section for more details). Their surface charges are confirmed to be positive and negative respectively by zeta potential measurements, Figure 2.9a. FTIR spectra shows the presence of PDDA and CNT features in positive CNT (P-CNT) and carboxylic acid and -OH functionalities in negative CNT, Figure 2.9b and Figure 2.9c. Raman spectra demonstrate the presence of D and G bands in all the compounds and the I_D/I_G ratios (intensity of defect band/intensity of graphitic band) indicates the effectiveness of the functionalization, Figure 2.9d and Table 2.3. D band reflects the defect density whereas G band defines the sp^2 carbon moieties present in the CNT.[60,61] The change in the ratio of I_D and I_G defines the functionalization of the MWCNT. The lower and higher I_D/I_G ratios respectively (Figure 2.9d and Table 2.3) in P-CNT and N-CNT are attributed to covering of CNT surface by PDDA polymer in the former and higher amounts of oxidized carbon in the latter.[62,63] C 1s XPS spectra of P-CNT electrode show the presence of C-C binding energies at ~284.5

eV, C-H binding energies at ~285.0 eV and C-N binding energies at ~285.7 eV in indicating the incorporation of PDDA on CNT surface (Figures 2.10a and 2.10b) which is in line with the literature.[64,65] On the other hand, N-CNT electrode shows binding energies corresponding to oxidized carbons, Figure 2.10a. N 1S XPS spectra show its dominant presence in P-CNT compared to unmodified CNT and N-CNT due to the presence quaternary ammonium groups in the former, Figure 2.10b. The microscopic images of CNT coated electrodes, Figure 2.11(a-c), are collected by SEM and it shows a fairly uniform coating of CNTs on all the three electrodes.
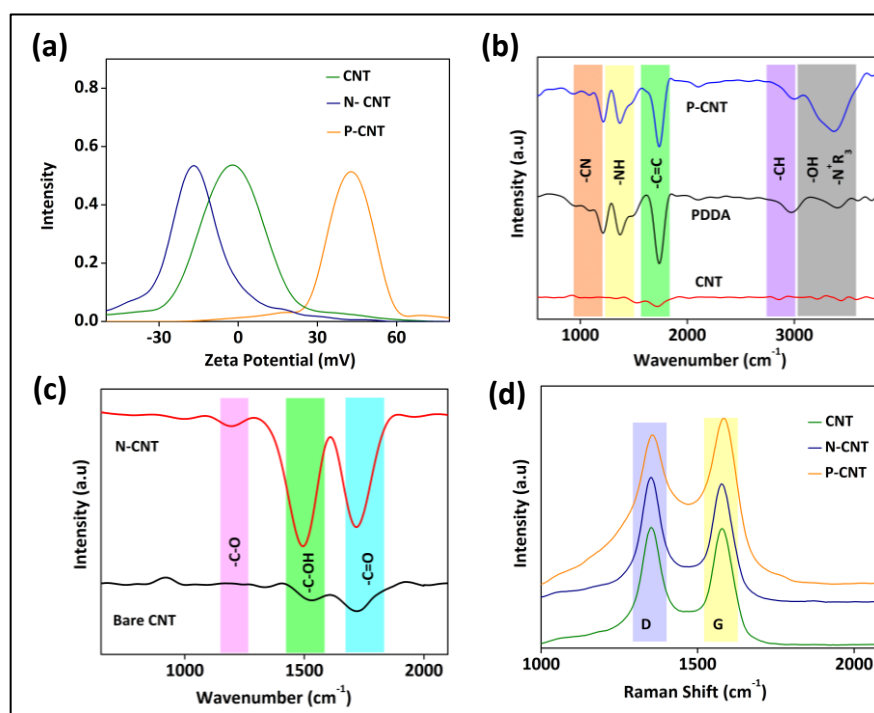
Figure 2.9: (a) Zeta potential measurements of P-CNT, unmodified CNT and N-CNT and (b), (c) FTIR spectra of P-CNT, N-CNT and individual components and (d) Raman spectra of P-CNT, N-CNT and unmodified CNT.

Table 2.3: I_D/I_G ratio extracted from Figure 2.9d.

Material	I_D / I_G
N- CNT	1.10
CNT	1.01
P- CNT	0.88
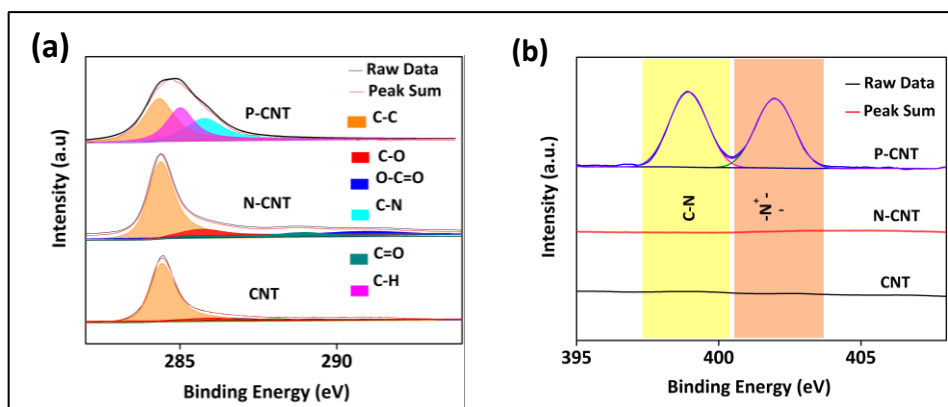
Figure 2.10: (a) C1s XPS spectra and (b) N1s XPS spectra of P-CNT, N-CNT and unmodified CNT.
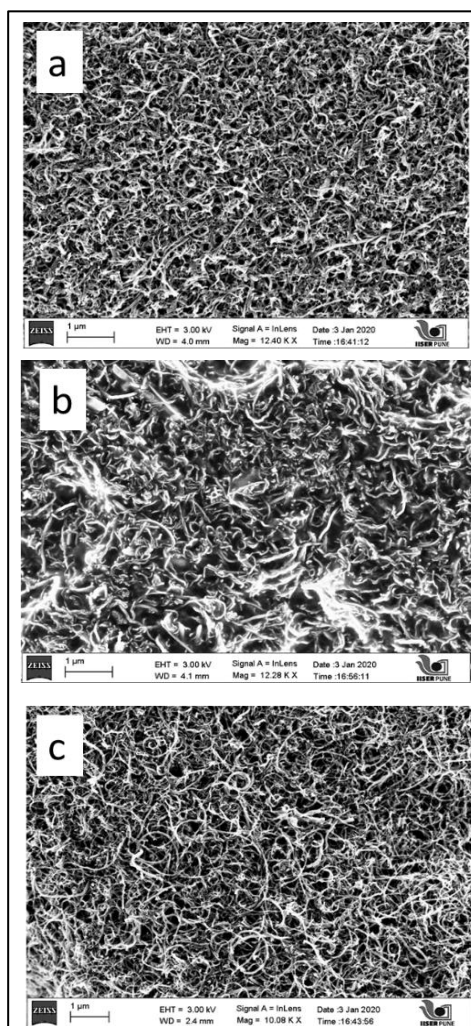
Figure 2.11: SEM images of (a) unmodified CNT, (b) P-CNT and (c) N-CNT coated on Toray carbon paper.

2.3.3. Gated molecular flux in iron redox flow battery

The discharge curves of the flow battery employing a ferricyanide cathode with P-CNT, N-CNT and unmodified CNT are shown in Figure 2.12a. The discharge capacities are noticeably increased with P-CNT compared to unmodified CNT however, with N-CNT electrode it was very inferior validating the fact that the battery performance with negatively charged ferricyanide species can be targeted by activating coulombic forces. The higher battery performance with P-CNT compared to N-CNT is mainly due to gated mol-
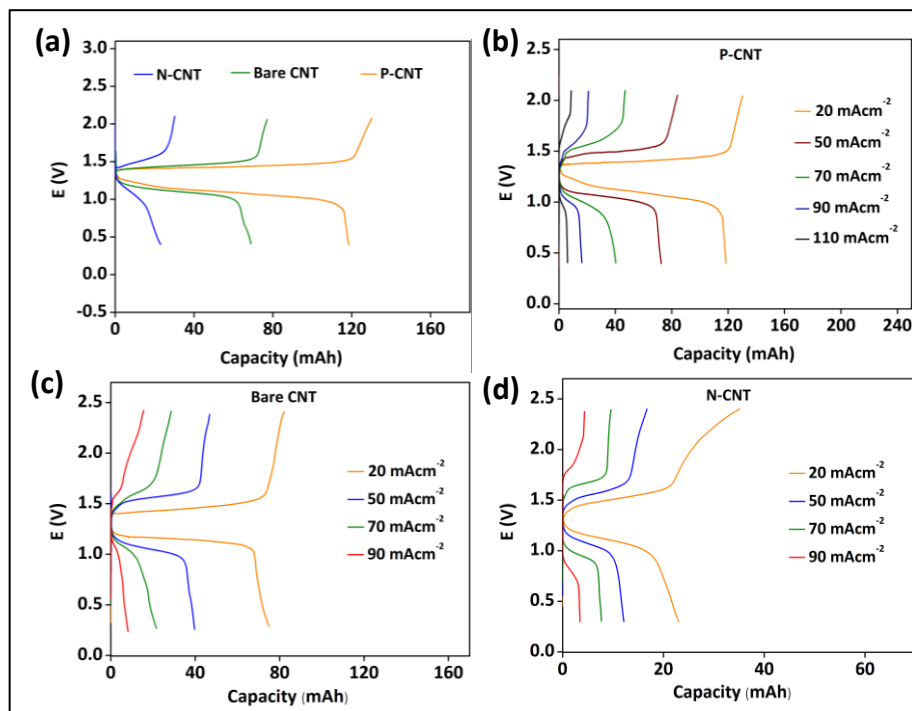
Figure 2.12: (a) Charge-discharge curves for Zn-ferricyanide battery with P-CNT, unmodified CNT and N-CNT electrodes at 20 mA cm^{-2}. Rate capability plot with (b) P-CNT electrode, (c) bare CNT electrode and (d) N-CNT electrode.

-ecular flux at the interface resulting in an electrostatic current contribution parallel to diffusion current which in turn can extend the concentration polarization region, Figure 2.12 (a-d). It is to be noted that the voltage efficiency of our Zn-ferricyanide battery is in par with the values reported in the literature (Table 2.4). The cycle stability, Figure 2.13(a), suggest that P-CNT electrode could be cycled for almost 100 cycles with decent capacity retention. The analysis of P-CNT electrode during extended cycling suggests an intact PDDA layer over 100 cycles remarking its stability at the interface, FTIR spectra, Figure 2.13b. Features of ferricyanide are seen in the cycled P-CNT electrode which is due to the adsorption of ferricyanide on the electrode surface as discussed earlier. Since the time of discharge at a particular current density is extended noticeably with P-CNT electrode due to electrostatic current contribution parallel to diffusion current contribution, the volumetric energy density is almost doubled without compromising the power capability,

Figure 2.13c. Taken together, the higher performance of Zn-ferricyanide battery with P-CNT electrode is primarily due to coulombic force gated molecular flux within the reaction zone that triggers an electrostatic current contribution parallel to diffusion current.
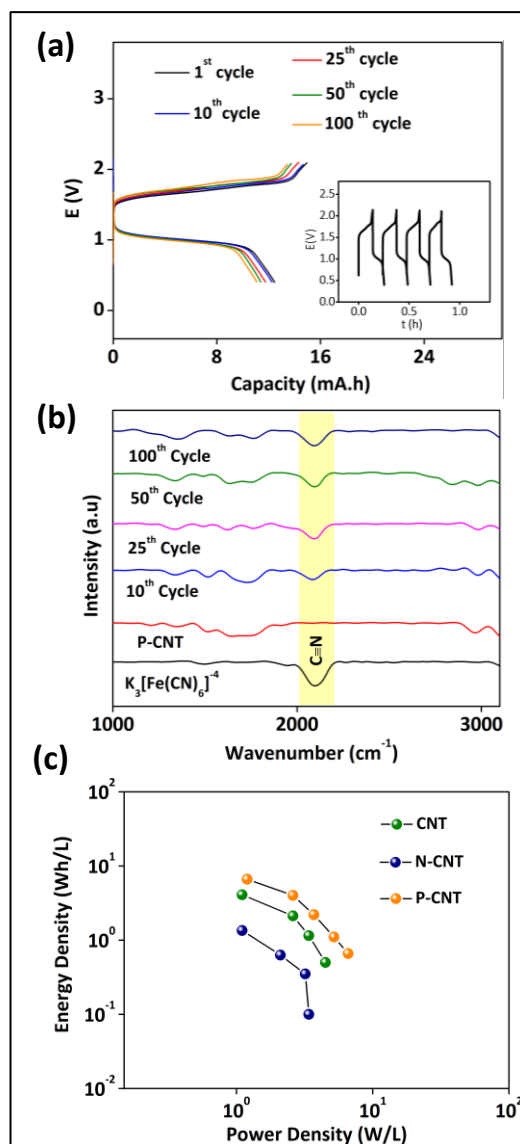
Figure 2.13: (a) Extended cyclability of the battery at 100 mA cm^{-2} current density with P-CNT electrode, (b) FTIR spectra of P-CNT electrode during 100 cycles and (c) Ragone plots for Zn-ferricyanide battery with P-CNT, unmodified CNT and N-CNT electrodes. Inset of Figure 2.13a shows the continuous charge-discharge cycles.

Table 2.4: Voltage efficiency comparison for iron based redox flow batteries.

S. No.	Catholyte	Charge/discharge current density	Voltage efficiency	Reference

1	1.5 M (NH4)$_3$[Fe(CN)$_6$] in 1.0 M NH$_4$Cl	40 mA cm^{-2}	~75%	Joule (2019) 3, 149–163.
2	0.2 M Na$_3$[Fe(CN)]$_6$ in 0.5 M NaOH	40 mA cm^{-2}	~78%	ACS Energy Lett. 2016, 1, 89−93.
3	1 M K$_3$[Fe(CN)]$_6$ in 3 M KOH	80 mA cm^{-2}	~79%	iScience (2018) 3, 40–49.
4	1 M FeCl$_3$ in 1.5 M H$_2$SO$_4$	30 mA cm^{-2}	~72%	Journal of Energy Chemistry, (2016), 25(3), 495–499.
5	1 M K$_3$[Fe(CN)]$_6$ in 1 M KNO$_3$	50 mA cm^{-2}	~71%	Present work
6	1 M K$_3$[Fe(CN)]$_6$ in 1 M KNO$_3$	20 mA cm^{-2}	~80%	Present work

2.4.   Conclusions

The physical processes of molecular transport play central role in the electrochemical behavior of reversible redox species as their extremely faster electron transfer event demands the reacting species to reach the interface by diffusion. Even under convective fluid flow as the thickness of hydrodynamic boundary layer or Prandtl layer is ~10 times larger than the diffusion layer, simple diffusion predominates the transport phenomena within the reaction zone. Therefore, these ubiquitous physical phenomena pose unique challenges to utilize the maximum potential of reversible redox molecules either by electrode or fluid characteristics. This study shows that by activating coulombic forces at electrochemical interface, molecular transport can be directed towards the electrode with an electrostatic current contribution parallel to the diffusion current. We show that coulombic force gated molecular transport can almost double the volumetric energy density of iron flow batteries by extending the battery performance well beyond the conventional concentration polarization regime.

2.5.   References

1.   Mourad, E.; Coustan, L.; Lannelongue, P.; Zigah, D.; Mehdi, A.; Vioux, A.; Freunberger, Stefan A.; Favier, F.; Fontaine, O., Biredox ionic liquids with solid-like redox density in the liquid state for high-energy supercapacitors. *Nat. Mater.* **2017,** *16* (4), 446-453.

2. Kwak, W.-J.; Kim, H.; Petit, Y. K.; Leypold, C.; Nguyen, T. T.; Mahne, N.; Redfern, P.; Curtiss, L. A.; Jung, H.-G.; Borisov, S. M.; Freunberger, S. A.; Sun, Y.-K., Deactivation of redox mediators in lithium-oxygen batteries by singlet oxygen. *Nat. Commun.* **2019,** *10* (1), 1380.

3. Park, M.; Ryu, J.; Wang, W.; Cho, J., Material design and engineering of next-generation flow-battery technologies. *Nat. Rev. Mater.* **2016,** *2* (1), 16080.

4. Kwabi, D. G.; Ji, Y.; Aziz, M. J., Electrolyte Lifetime in Aqueous Organic Redox Flow Batteries: A Critical Review. *Chem. Rev.* **2020,** *120* (14), 6467-6489.

5. Miroshnikov, M.; Divya, K. P.; Babu, G.; Meiyazhagan, A.; Reddy Arava, L. M.; Ajayan, P. M.; John, G., Power from nature: designing green battery materials from electroactive quinone derivatives and organic polymers. *J. Mater. Chem. A* **2016,** *4* (32), 12370-12386.

6. Gong, K.; Xu, F.; Grunewald, J. B.; Ma, X.; Zhao, Y.; Gu, S.; Yan, Y., All-Soluble All-Iron Aqueous Redox-Flow Battery. *ACS Energy Lett.* **2016,** *1* (1), 89-93.

7. Zhou, Y.; Cong, G.; Chen, H.; Lai, N.-C.; Lu, Y.-C., A Self-Mediating Redox Flow Battery: High-Capacity Polychalcogenide-Based Redox Flow Battery Mediated by Inherently Present Redox Shuttles. *ACS Energy Lett.* **2020,** *5* (6), 1732-1740.

8. Li, B.; Nie, Z.; Vijayakumar, M.; Li, G.; Liu, J.; Sprenkle, V.; Wang, W., Ambipolar zinc-polyiodide electrolyte for a high-energy density aqueous redox flow battery. *Nat. Commun* **2015,** *6* (1), 6303.

9. Drummond, T. G.; Hill, M. G.; Barton, J. K., Electrochemical DNA sensors. *Nat. Biotechnol.* **2003,** *21* (10), 1192-1199.

10. Liu, T.; Wei, X.; Nie, Z.; Sprenkle, V.; Wang, W., A Total Organic Aqueous Redox Flow Battery Employing a Low Cost and Sustainable Methyl Viologen Anolyte and 4-HO-TEMPO Catholyte. *Adv. Energy Mater.* **2016,** *6* (3), 1501449.

11. Ding, Y.; Yu, G., A Bio-Inspired, Heavy-Metal-Free, Dual-Electrolyte Liquid Battery towards Sustainable Energy Storage. *Angew. Chem. Int. Ed.* **2016,** *55* (15), 4772-4776.

12. Lin, K.; Gómez-Bombarelli, R.; Beh, E. S.; Tong, L.; Chen, Q.; Valle, A.; Aspuru-Guzik, A.; Aziz, M. J.; Gordon, R. G., A redox-flow battery with an alloxazine-based organic electrolyte. *Nat. Energy* **2016,** *1* (9), 16102.

13. Yuan, Z.; Duan, Y.; Liu, T.; Zhang, H.; Li, X., Toward a Low-Cost Alkaline Zinc-Iron Flow Battery with a Polybenzimidazole Custom Membrane for Stationary Energy Storage. *iScience* **2018,** *3*, 40-49.

14. Selverston, S.; Savinell, R. F.; Wainright, J. S., Zinc-Iron Flow Batteries with Common Electrolyte. *J. Electrochem. Soc.* **2017,** *164* (6), A1069-A1075.

15. Arthur J. Esswein, J. G., Desiree Amadeo, High solubility iron hexacyanides. *U. S. Patent App. US20140051003 A1* **2014,** *1*.

16. Gong, K.; Ma, X.; Conforti, K. M.; Kuttler, K. J.; Grunewald, J. B.; Yeager, K. L.; Bazant, M. Z.; Gu, S.; Yan, Y., A zinc–iron redox-flow battery under $100 per kW h of system capital cost. *Energy Environ. Sci.* **2015,** *8* (10), 2941-2945.

17. Bhat, Z. M.; Thimmappa, R.; Devendrachari, M. C.; Shafi, S. P.; Aralekallu, S.; Kottaichamy, A. R.; Gautam, M.; Thotiyl, M. O., A Direct Alcohol Fuel Cell Driven by an Outer Sphere Positive Electrode. *J. Phys. Chem. Lett.* **2017,** *8* (15), 3523-3529.

18. Luo, J.; Hu, B.; Debruler, C.; Bi, Y.; Zhao, Y.; Yuan, B.; Hu, M.; Wu, W.; Liu, T. L., Unprecedented Capacity and Stability of Ammonium Ferrocyanide Catholyte in pH Neutral Aqueous Redox Flow Batteries. *Joule* **2019,** *3* (1), 149-163.

19. Orita, A.; Verde, M. G.; Sakai, M.; Meng, Y. S., A biomimetic redox flow battery based on flavin mononucleotide. *Nat. Commun.* **2016,** *7* (1), 13230.

20.   Luo, J.; Sam, A.; Hu, B.; DeBruler, C.; Wei, X.; Wang, W.; Liu, T. L., Unraveling pH dependent cycling stability of ferricyanide/ferrocyanide in redox flow batteries. *Nano Energy* **2017,** *42*, 215-221.

21.   Winsberg, J.; Hagemann, T.; Janoschka, T.; Hager, M. D.; Schubert, U. S., Redox-Flow Batteries: From Metals to Organic Redox-Active Materials. *Angew. Chem. Int. Ed.* **2017,** *56* (3), 686-711.

22.   Ventosa, E.; Amedu, O.; Schuhmann, W., Aqueous Mixed-Cation Semi-solid Hybrid-Flow Batteries. *ACS Appl. Energy Mater.* **2018,** *1* (10), 5158-5162.

23.   Ji, X.; Banks, C. E.; Crossley, A.; Compton, R. G., Oxygenated Edge Plane Sites Slow the Electron Transfer of the Ferro-/Ferricyanide Redox Couple at Graphite Electrodes. *ChemPhysChem* **2006,** *7* (6), 1337-1344.

24.   Nugent, J. M.; Santhanam, K. S. V.; Rubio, A.; Ajayan, P. M., Fast Electron Transfer Kinetics on Multiwalled Carbon Nanotube Microbundle Electrodes. *Nan-*

-o Lett. **2001,** *1* (2), 87-91.

25.   Curtis, J. C.; Meyer, T. J., Outer-sphere charge transfer in mixed-metal ion pairs. *Inorg. Chem.* **1982,** *21* (4), 1562-1571.

26.   Velický, M.; Bradley, D. F.; Cooper, A. J.; Hill, E. W.; Kinloch, I. A.; Mishchenko, A.; Novoselov, K. S.; Patten, H. V.; Toth, P. S.; Valota, A. T.; Worrall, S. D.; Dryfe, R. A. W., Electron Transfer Kinetics on Mono- and Multilayer Graphene. *ACS Nano* **2014,** *8* (10), 10089-10100.

27.   Shevchuk, I., Heat and Mass Transfer of a Free Rotating Disk for the Prandtl and Schmidt Numbers Larger than Unity. *Lecture Notes in Applied and Computational Mechanics* **2009,** *45*.

28.   Wang, J., Analytical Electrochemistry, Third Edition **2006**.

29.   Kim, S.; Vijayakumar, M.; Wang, W.; Zhang, J.; Chen, B.; Nie, Z.; Chen, F.; Hu, J.; Li, L.; Yang, Z., Chloride supporting electrolytes for all-vanadium redox flow batteries. *Phys. Chem. Chem. Phys.*   **2011,** *13* (40), 18186-18193.

30.   Chen, Y.; Zhou, M.; Xia, Y.; Wang, X.; Liu, Y.; Yao, Y.; Zhang, H.; Li, Y.; Lu, S.; Qin, W.; Wu, X.; Wang, Q., A Stable and High-Capacity Redox Targeting-Based Electrolyte for Aqueous Flow Batteries. *Joule* **2019,** *3* (9), 2255-2267.

31.   Noh, C.; Lee, C. S.; Chi, W. S.; Chung, Y.; Kim, J. H.; Kwon, Y., Vanadium Redox Flow Battery Using Electrocatalyst Decorated with Nitrogen-Doped Carbon Nanotubes Derived from Metal-Organic Frameworks. *J. Electrochem. Soc.* **2018,** *165* (7), A1388-A1399.

32.   González, Z.; Álvarez, P.; Blanco, C.; Vega-Díaz, S.; Tristán-López, F.; Rajukumar, L. P.; Cruz-Silva, R.; Elías, A. L.; Terrones, M.; Menéndez, R., The influence of carbon nanotubes characteristics in their performance as positive electrodes in vanadium redox flow batteries. *Sustain. Energy Techn.* **2015,** *9*, 105-110.

33.   Sun, B.; Skyllas-Kazacos, M., Chemical modification of graphite electrode materials for vanadium redox flow battery application—part II. Acid treatments. *Electrochim. Acta* **1992,** *37* (13), 2459-2465.

34.   Greco, K. V.; Forner-Cuenca, A.; Mularczyk, A.; Eller, J.; Brushett, F. R., Elucidating the Nuanced Effects of Thermal Pretreatment on Carbon Paper Electrodes for Vanadium Redox Flow Batteries. *ACS Appl. Mater.* **2018,** *10* (51), 44430-44442.

35.   Park, M.; Jung, Y.-j.; Kim, J.; Lee, H. i.; Cho, J., Synergistic Effect of Carbon Nanofiber/Nanotube Composite Catalyst on Carbon Felt Electrode for High-Performance All-Vanadium Redox Flow Battery. *Nano Lett.* **2013,** *13* (10), 4833-4839.

36.   Li, Y.-H.; Wang, S.; Luan, Z.; Ding, J.; Xu, C.; Wu, D., Adsorption of cadmium(II) from aqueous solution by surface oxidized carbon nanotubes. *Carbon* **2003,** *41* (5), 1057-1062.

37.   Datsyuk, V.; Kalyva, M.; Papagelis, K.; Parthenios, J.; Tasis, D.; Siokou, A.; Kallitsis, I.; Galiotis, C., Chemical oxidation of multiwalled carbon nanotubes. *Carbon* **2008,** *46* (6), 833-840.

38.   Pavese, M.; Musso, S.; Bianco, S.; Giorcelli, M.; Pugno, N., An analysis of carbon nanotube structure wettability before and after oxidation treatment. *J. Phys.: Condens. Matter* **2008,** *20* (47), 474206.

39.   Zhang, X.; Chen, M.; Yu, Y.; Yang, T.; Wang, J., Polyelectrolyte-modified multi-walled carbon nanotubes for the adsorption of chromium(vi). *Anal. Methods* **2011,** *3* (2), 457-462.

40.   Kaur, P.; Shin, M.-S.; Joshi, A.; Kaur, N.; Sharma, N.; Park, J.-S.; Sekhon, S. S., Interactions between Multiwall Carbon Nanotubes and Poly(diallyl dimethylammonium) Chloride: Effect of the Presence of a Surfactant. *J. Phys. Chem. B* **2013,** *117* (11), 3161-3166.

41.   Mo, C.; Jian, J.; Li, J.; Fang, Z.; Zhao, Z.; Yuan, Z.; Yang, M.; Zhang, Y.; Dai, L.; Yu, D., Boosting water oxidation on metal-free carbon nanotubes via directional interfacial charge-transfer induced by an adsorbed polyelectrolyte. *Energy Environ. Sci.* **2018,** *11* (12), 3334-3341.

42.   Wang, S.; Yu, D.; Dai, L., Polyelectrolyte Functionalized Carbon Nanotubes as Efficient Metal-free Electrocatalysts for Oxygen Reduction. *J. Am. Chem. Soc.* **2011,** *133* (14), 5182-5185.

43.   Xiao, P.; Cai, Y.; Chen, X.; Sheng, Z.; Chang, C., Improved electrochemical performance of $LiFe_{0.4}Mn_{0.6}PO_4/C$ with Cr^{3+} doping. *RSC Adv.* **2017,** *7* (50), 31558-31566.

44.   Guo, H.; Zhang, X.; He, W.; Yang, X.; Liu, Q.; Li, M.; Wang, J., Fabricating three-dimensional mesoporous carbon network-coated $LiFePO_4/Fe$ nanospheres using thermal conversion of alginate-biomass. *RSC Adv.* **2016,** *6* (21), 16933-16940.

45. Li, J.; Feng, H.; Jiang, J.; Feng, Y.; Xu, Z.; Qian, D., One-pot in situ synthesis of a $CoFe_2O_4$ nanoparticle-reduced graphene oxide nanocomposite with high performance for levodopa sensing. *RSC Adv.* **2015,** *5* (121), 99669-99677.

46. Mohammadi, N.; Adeh, N. B.; Najafi, M., A highly defective mesoporous carbon – ionic liquid paste electrode toward the sensitive electrochemical determination of rutin. *Anal. Methods* **2017,** *9* (1), 84-93.

47. Fadel, M.; Daurelle, J.-V.; Fourmond, V.; Vicente, J., A new electrochemical cell with a uniformly accessible electrode to study fast catalytic reactions. *Phys. Chem. Chem. Phys.* **2019,** *21* (23), 12360-12371.

48. Kear, G.; Barker, B. D.; Stokes, K.; Walsh, F. C., Flow influenced electrochemical corrosion of nickel aluminium bronze – Part I. Cathodic polarisation. *J. Appl. Electrochem.* **2004,** *34* (12), 1235-1240.

49. Yang, Z.; Tong, L.; Tabor, D. P.; Beh, E. S.; Goulet, M.-A.; De Porcellinis, D.; Aspuru-Guzik, A.; Gordon, R. G.; Aziz, M. J., Alkaline Benzoquinone Aqueous Flow Battery for Large-Scale Storage of Electrical Energy. *Adv. Energy Mater.* **2018,** *8* (8), 1702056.

50. Granados-Ner, M.; Huizar, L. H. M.; Rios-Reyes, C. H., Electrochemical study about zinc electrodeposition onto GCE and HOPG substrates Quím. Nova **2011,** *34*, 439-443.

51. Hosseini, S.; Lao-atiman, W.; Han, S. J.; Arpornwichanop, A.; Yonezawa, T.; Kheawhom, S., Discharge Performance of Zinc-Air Flow Batteries Under the Effects of Sodium Dodecyl Sulfate and Pluronic F-127. *Sci. Rep.* **2018,** *8* (1), 14909.

52. Wan, F.; Zhang, L.; Dai, X.; Wang, X.; Niu, Z.; Chen, J., Aqueous rechargeable zinc/sodium vanadate batteries with enhanced performance from simultaneous insertion of dual carriers. *Nat. Commun.* **2018,** *9* (1), 1656.

53. Mooste, M.; Kibena-Põldsepp, E.; Marandi, M.; Matisen, L.; Sammelselg, V.; Tammeveski, K., Electrochemical properties of gold and glassy carbon electrodes

electrografted with an anthraquinone diazonium compound using the rotating disc electrode method. *RSC Adv.* **2016,** *6* (47), 40982-40990.

54.   Tucceri, R., The charge transport process at gold electrodes modified by thick nickel hydroxide films. A study employing rotating disc electrode voltammetry in the presence of the $Fe(CN)_6^{3-/4-}$ redox couple. *J. Electroanal. Chem.* **2016,** *782*, 125-132.

55.   Clegg, A. D.; Rees, N. V.; Klymenko, O. V.; Coles, B. A.; Compton, R. G. Marcus Theory of Outer-Sphere Heterogeneous Electron Transfer Reactions: Dependence of the Standard Electrochemical Rate Constant on the Hydrodynamic Radius from High Precision Measurements of the Oxidation of Anthracene and Its Derivatives in Nonaqueous Solvents Using the High-Speed Channel Electrode. *J. Am. Chem. Soc.* **2004,** *126* (19), 6185–6192.

56.   Fawcett, W. R.; Opallo, M. On the Differences in the Magnitude of the Observed Solvent Effect in the Kinetics of Simple Heterogeneous Electron Transfer Reactions. *J. Electroanal. Chem.* **1993,** *349* (1–2), 273–284.

57.   Savéant, J. M. Effect of the Electrode Continuum of States in Adiabatic and Nonadiabatic Outer-Sphere and Dissociative Electron Transfers. Use of Cyclic Voltammetry for Investigating Nonlinear Activation-Driving Force Laws. *J. Phys. Chem. B* **2002,** *106* (36), 9387–9395.

58.   Bard, A. J. a. F., L. , Electrochemical Methods and Applications, 2nd Edition. *Wiley* **2000**.

59.   Yang, G.-h.; Bao, D.-d.; Zhang, D.-q.; Wang, C.; Qu, L.-l.; Li, H.-t., Removal of Antibiotics From Water with an All-Carbon 3D Nanofiltration Membrane. Nanoscale Research Letters **2018**, 13 (1), 146.

60.   Wang, S.; Zhao, X.; Cochell, T.; Manthiram, A., Nitrogen-Doped Carbon Nanotube/Graphite Felts as Advanced Electrode Materials for Vanadium Redox Flow Batteries. *J. Phys. Chem. Lett.* **2012,** *3* (16), 2164-2167.

61.   Ek-Weis, J.; Costa, S.; Frank, O.; Kalbac, M., Heating Isotopically Labeled Bernal Stacked Graphene: A Raman Spectroscopy Study. *J. Phys. Chem. Lett.* **2014,** *5* (3), 549-554.

62.   Wang, D.; Lu, S.; Kulesza, P. J.; Li, C. M.; De Marco, R.; Jiang, S. P., Enhanced oxygen reduction at Pd catalytic nanoparticles dispersed onto heteropolytungstate-assembled poly(diallyldimethylammonium)-functionalized carbonnanotubes. *Phys. Chem. Chem. Phys.* **2011,** *13* (10), 4400-4410.

63.   Wang, S.; Jiang, S. P.; Wang, X., Polyelectrolyte functionalized carbon nanotubes as a support for noble metal electrocatalysts and their activity for methanol oxidation. *Nanotechnology* **2008,** *19* (26), 265601.

64.   Yang, D.-Q.; Rochette, J.-F.; Sacher, E., Spectroscopic Evidence for $\pi-\pi$ Interaction between Poly(diallyl dimethylammonium) Chloride and Multiwalled Carbon Nanotubes. *J. Phys. Chem. B* **2005,** *109* (10), 4481-4484.

65.   Gao, L.; Zhang, Q.; Zhu, M.; Zhang, X.; Sui, G.; Yang, X., Polyhedral oligomeric silsesquioxane modified carbon nanotube hybrid material with a bump structure via polydopamine transition layer. *Mater. Lett.* **2016,** *183*, 207-210.

Chapter 3

A Rechargeable Aqueous Sodium Ion Battery with a Capacitive Graphene Anode

Abstract

In this chapter, the construction of a rechargeable sodium ion battery in aqueous environment with reduced graphene oxide (RGO) as the capacitive anode and hexacyanometallate as the insertion cathode is discussed. Specifically, how mode of synthesis of graphene materials improves the qualities of reduced graphene oxide (RGO) material with properties relevant to construct an aqueous rechargeable sodium ion battery is discussed. Reduction of graphene oxide (GO) by Fe/HCl method suppress the O/C ratio (relatively higher hydrophobic surface) and enhances the electronic transport in the resulting reduced graphene oxide (RGO) that in turn favor the reversible adsorption of sodium ions electrochemically. The presence of hydrophilic functionalities in the RGO produced by conventional sodium borohydride method, mainly resulted in binding to Na^+ ions chemically than electrochemically leading to poor electrochemical reversibility. The hydrophobicity of RGO material produced by Fe/HCl also suppresses the interactions with H^+ ions thereby largely preventing the widely encountered parasitic chemistry of hydrogen ion insertion/H_2 evolution. A rechargeable battery with the relatively hydrophobic graphene anode and hexacyanometallate insertion cathode in aqueous environment significantly improved the reversibility and extended cyclability of the sodium ion battery during charge discharge chemistry.
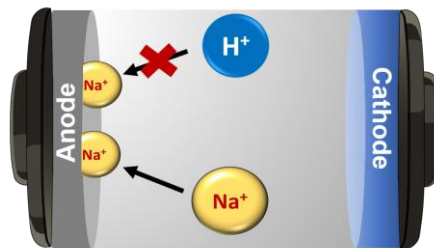
3.1. Introduction

In the context of the geographic and temporal variations of renewable energy resources, metal ion batteries and new generation supercapacitors assume larger space as efficient energy storage modules. [1-16] So far non-aqueous metal ion batteries have dominated the consumer electronics, transport technologies and electrical grid as the prime storage technology. [17-19] Recently, aqueous metal ion batteries have come up as promising candidate in terms of energy storage applications because of, environmental advantages, low manufacturing cost, fast ionic movement, low flammability etc. [20-22] Carbon based materials have shown their various advantages in aqueous metal ion batteries because of their higher surface area, higher thermal stability, higher electrical conductivity etc. [23-26] Although, these carbon based materials have shown their tremendous applications in energy storage devices, in the context of aqueous batteries of these carbon based materials pose their own challenges and issues. [27,28] They suffer from unwanted swelling, undesirable proton insertion and parasitic H_2 evolution reactions, consequently degrading the anode entity during the long run. [29-34] It has been also reported in the literature that there is exfoliation of layers of graphene-based materials because of the generation radical species (e.g., hydroxyl radicals) from aqueous electrolyte especially at larger positive potentials which further results in the degradation of carbon lattice and its cyclability. [35, 36] The seminal works of Goodenough et. al., Wainwright et al, Yi Cui et. al, and Kang Kisuk et al., to improve the performance metrics of aqueous metal ion batteries are noteworthy in this direction. [37-40]

In this chapter, carbon derived materials are explored as electrodes in aqueous sodium ion battery to address some of the above-mentioned challenges and issues. This chapter discusses how the mode of synthesis of carbon materials can improve the qualities of reduced graphene oxide (RGO) material for constructing an aqueous rechargeable sodium ion battery with extended cyclability and reversibility. For the construction of aqueous rechargeable sodium ion battery, RGO materials were synthesized with two different approaches i.e., Fe powder/HCl method (Fe/HCl) and conventional $NaBH_4$ method. [41-44] The resulting RGOs were exploited as capacitive anodes in the construction of aqueous rechargeable sodium ion battery with widely utilized metal hexacyanoferrate (MHF) as the insertion cathode. [45-48] With regard to the construction of an aqueous rechargeable battery,

the quality of RGO material produced by the Fe/HCl method was superior to the conventional sodium borohydride method as the latter predominantly yielded incompletely reduced GO thereby affecting its O/C ratio and consequently its electrochemical properties.[41,42] The reduction in O/C ratio in the RGO electrode produced by Fe/HCl method favoured the reversible interaction with sodium ions electrochemically and suppressed the parasitic hydrogen ion insertion/hydrogen evolution leading to an aqueous rechargeable sodium ion battery with extended cyclability. On the other hand, the hydrophilic surface of RGO electrode produced by conventional sodium borohydride method largely favoured the interaction with sodium ions chemically which in turn lead to poor electrochemical reversibility.

3.2. Experimental

3.2.1. Materials and reagents

H_2SO_4 (99.99 %), H_3PO_4 (99.99 %), HCl (99.99 %), $KMnO_4$ (98.0 %), H_2O_2 (30 wt%), Nafion® (5.0 wt% solution in isopropyl alcohol) was obtained from Sigma Aldrich, KCl, $K_3[Fe(CN)_6]$ (99.0 %) were purchased from Rankem, India. Fe powder (+100 mesh) and $NaBH_4$ (98.0 %) were purchased from S.D Fine chemical limited, India. $FeCl_3$ was purchased from Rankem, India. Toray carbon diffusion paper was obtained from fuel cell store, USA. Graphite flakes (10 microns, 99.0 %) were obtained from Alfa Aesar.

3.2.2. Synthesis of graphene oxide

Graphene oxide (GO) was synthesized by improved Hummer's method. [49,50] 3.0 g of graphite flakes were taken in a round bottomed flask containing acid mixture of 320 mL of H_2SO_4 and 80 mL of H_3PO_4 (4:1). This was stirred well to obtain homogenous reaction mixture. To this mixture 18.0 g of potassium permanganate was added slowly with constant stirring. The stirring was continued for 3 days for the completion of the reaction. 15 mL of H_2O_2 was added drop wise to this mixture until the colour changed from pink to golden yellow colour and the reaction mixture was stirred for another 1 h. Finally, the product was collected by centrifugation and washed with 1 M HCl solution to remove the inorganic impurities which was followed by water wash. The dispersed graphene oxide in water was drop casted and dried on glass slides to obtain thin films of GO.

3.2.3. Preparation of reduced graphene oxides (RGOs)

About 1.0 g of Fe powder with 20 mL HCl (35 wt %) were directly added to the 100 mL GO suspension. The mixture was kept to stirring for 30 min. After the completion of reaction, the black coloured product was collected by filtration and washed with 15-20 mL HCl (35 wt %) to remove the unreacted Fe powder which was followed by washing with plenty of distilled water and ethanol. The final product was dried in a vacuum oven for about 24 hrs. The produced RGO by this method is labelled as RGO1. We have also synthesised RGO by $NaBH_4$ method.[42,51] About 0.8 g of $NaBH_4$ was introduced to the 100 mL GO suspension. The mixture was kept to stirring for 30 min. After this the reduced graphene oxide was collected by filtration and washed thoroughly with water and ethanol, dried well in a vacuum oven for about 24 hrs. The RGO produced by this method is labelled as RGO2.

3.2.4. Physicochemical characterizations

ATIR-FTIR (Bruker Alpha) was performed on the electrodes before and after the battery performance to investigate the stability of the electrodes. UV-Vis spectroscopy (Perkin Elmer Lambda 950) was carried out in the range of 200-800 nm. Raman spectra were recorded by using a Raman microscope (LabRAM HR, Horbia Jobin Yvon). AFM images were recorded for GO and RGO using Agilent instruments. Mica sheets were used for drop casting diluted samples. I–V characteristics were investigated by four probe conductivity measurements using a Keithley 2400. EDS spectra of RGOs were obtained by using Zeiss Ultraplus - 4095. Contact angle measurements were carried out using Holmarc's Contact Angle Meter. In-situ spectro-electrochemistry data was collected for sodiated Prussian blue analogue coated on indium tin oxide (ITO) working electrode, using Ag/AgCl (3 M KCl) as reference electrode and platinum wire as counter electrode. Biologic VMP 300 potentiostat/galvanostat was used for electrochemical studies. XPS analysis were performed by Thermo Scientific K-Alpha with Al-Kα as excitation source. Quartz Crystal Microbalance (QCM) measurements were carried out in three-electrode assembly using Au coated quartz resonator (8.95 MHz) as the working electrode, Ag/AgCl (3 M KCl) as reference electrode and platinum wire as counter electrode. RGOs were drop casted on the resonator and the shift in frequency was correlated with the mass change with the help of Sauerbrey equation, (equation 3.1),[52,53]

$$\Delta m = (-c)\frac{\Delta f}{n} \tag{3.1}$$

where, c is the sensitivity sensitivity of the QCM crystal which is 5.608 ng cm^{-2} Hz^{-1}, Δf is

the resonance frequency shift during adsorption and desorption, n is the odd overtone number.[54,55]

3.2.5. Preparation of electrode materials

Cathode material was prepared by electrodeposition of Prussian blue $NaFe[Fe(CN)_6]$ (Fe^{3+}/Fe^{2+}) on indium tin oxide coated (ITO) glass.[49,50] Prussian blue was prepared by mixing a solution of 20 mM $Na_4[Fe(CN)]_6$ and 20 mM $FeCl_3$ in in 100 mM NaCl solution. It was then electrodeposited on ITO glass slide (8-12 Ohm cm^2). Electrodeposition was carried out in three electrode assembly with ITO glass as the working electrode, platinum wire as the counter electrode and Ag/AgCl (3 M KCl) as the reference electrode, by applying a constant current density of 100 μA cm^{-2}. Deposition was continued till the required loading was achieved. Anode material (RGOs) was prepared by dispersing known amount of RGO material in isopropyl alcohol with 5 wt% Nafion binder and by sonicating the slurry for almost 2 h. After that, the slurry was coated on a Toray carbon paper electrode.

3.2.6. Fabrication of rechargeable aqueous sodium ion battery

The battery consisted of a RGO anode at a loading of 3 mg cm^{-2} and a sodiated Prussian blue analogue cathode material at a loading of 1 mg cm^{-2}. These electrodes were placed in a single compartment flooded cell having 3 M $NaNO_3$ as the electrolyte. The distance between the electrodes were ~0.5 cm. A Biologic VMP 300 electrochemical instrument was used to evaluate the battery performance.

3.3. Results and discussion

3.3.1. Physiochemical characterization of RGOs

RGOs formed by two types of reduction processes are compared here, one by the Fe/HCl reduction method and the other by sodium borohydride reduction method (see experimental section for more details). Few layers structure of graphene formed by the two reduction methods are evident in their atomic force microscopy (AFM) images and the corresponding line profiles, Figures 3.1a and 3.1b, indicate that each flake approximately contains 3-4 graphene layers of thickness 2-4 nm. RGOs produced by Fe/HCl method and $NaBH_4$ method are labelled as RGO1 and RGO2, respectively.
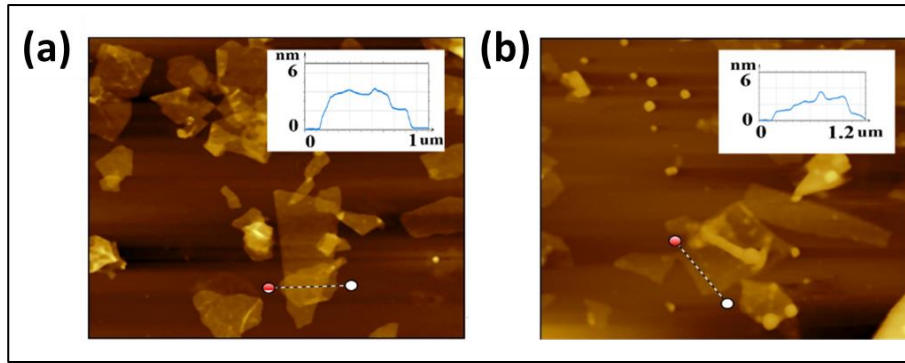
Figure 3.1: AFM images of RGOs obtained by (a) Fe powder reduction method (RGO1) and (b) NaBH₄ meyhod (RGO2).

The Raman spectra demonstrates a higher I_D/I_G ratio (intensity of defect band/intensity of graphitic band) for the RGO2 formed by borohydride reduction method compared to the corresponding RGO1 obtained by Fe/HCl reduction method, Figure 3.2a, suggesting the presence of more hydrophilic functionalities in the former.[41,56] This further indicates the quality of RGO1 in terms of their O/C ratio should be much better than RGO2.[42,57] This indicates the Fe powder reduction is much more extensive for the reduction of GO to RGO than NaBH₄ reduction.[41, 56] This is further supported by their corresponding FTIR spectra, Figure 3.2b. FTIR spectra suggest the density of hydrophilic functionalities in RGO2 are higher than RGO1 material. These characterizations clearly suggest that the Fe/HCl reduction method results in extensive reduction of GO which in turn suppress the O/C ratio in the produced RGO1.
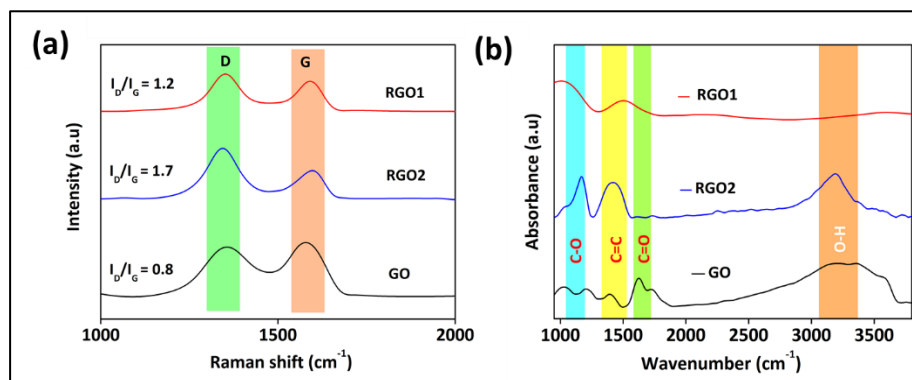
Figure 3.2: (a) Raman spectra and (b) FTIR spectra of GO and RGOs obtained by Fe powder reduction method (RGO1) and NaBH₄ method (RGO2).

The qualities of RGOs produced are further confirmed by their I-V measurements, Figure 3.3a. RGO1 demonstrates a higher slope in I-V characteristics than RGO2 indicating the more electrical conductivity of the former compared to the latter, Figure 3.3a. This may be due to the high density of the hydrophilic functionalities in RGO2 compared with RGO1 which is further supported by their contact angle images, Figure

3.3b. As shown RGO1 surface is more hydrophobic (~117°) than RGO2 (~81°), Figure 3.3b, which can be attributed to the reduction of O/C ratio in the former compared to the latter. This O/C ratio is probed by EDS analysis which confirm that RGO1 has lower density of hydrophilic functionalities than RGO2, Figure 3.3 (c and d) and Table 3.1. Taken together, all these studies indicate that RGO1 has a relatively more hydrophobic surface than RGO2.
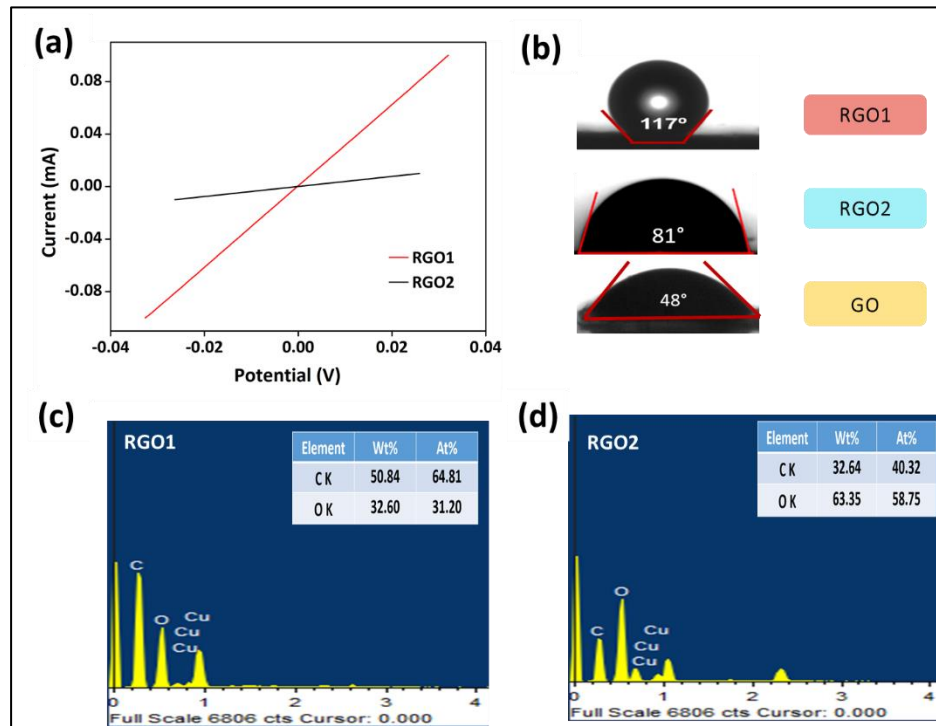
Figure 3.3: (a) Four probe I-V measurements for RGO1 and RGO2 and (b) contact angle images of RGO1, RGO2 and GO. (c) and (d) EDS analysis of (c) RGO1 and (d) RGO2.

Table 3.1: O/C ratio of the synthesised RGOs estimated from Figure 3.3c and 3.3d.

Material	O/C ratio
RGO1	~0.6
RGO2	~1.9

3.3.2. Electrochemical characterization of metal hexacyanoferrate (MHF)

To investigate the effect of qualities of these RGOs on the performance of aqueous rechargeable sodium ion battery, they were utilized as capacitive graphene anodes in aqueous rechargeable sodium ion battery with widely explored metal hexacyanoferrate (MHF) based insertion cathode,[45, 58-60] Figure 3.4a. The cyclic voltammogram (CV) of

insertion MHF cathode shows two pairs of redox peaks corresponding to successive redox transitions of transition metal ions with concomitant insertion/deinsertion of sodium ions as shown in equations 3.2 and 3.3:

$$Na_2Fe[Fe(CN_6)](Fe^{+2}/Fe^{+2}) \rightleftarrows NaFe[Fe(CN)_6](Fe^{+3}/Fe^{+2}) + Na^+ + e^- \qquad (3.2)$$

$$NaFe[Fe(CN_6)](Fe^{+3}/Fe^{+2}) \rightleftarrows Fe[Fe(CN)_6](Fe^{+3}/Fe^{+3}) + Na^+ + e^- \qquad (3.3)$$
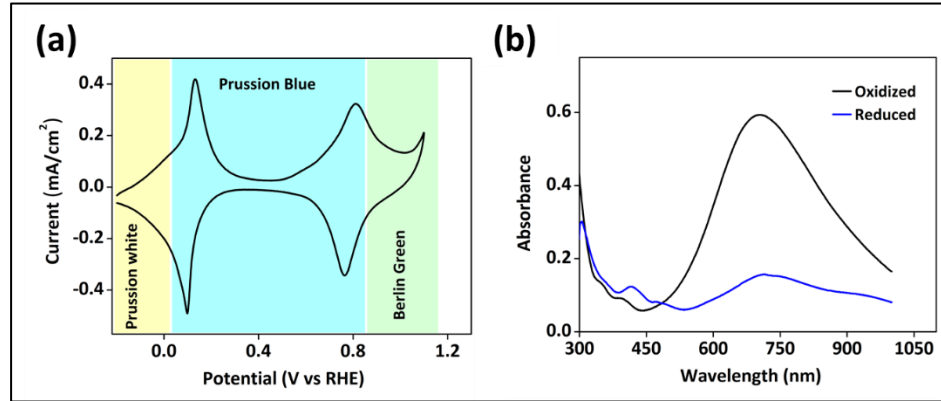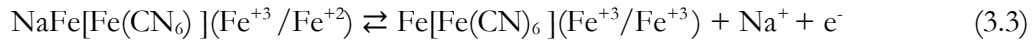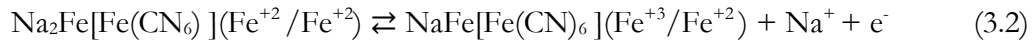
Figure 3.4. (a) Cyclic voltammogram (CV) of insertion MHF cathode and (b) in-situ UV-Vis spectroelectrochemical mesurements of MHF cathode material.

The UV-Vis spectroelectrochemistry data (Figure 3.4b) of the insertion cathode during CV measurements between 0 V and 0.6 V vs. RHE shows its transition between colourless (Fe^{2+}/Fe^{2+}) and blue (Fe^{3+}/Fe^{2+}) states due to intervalence charge transfer, indicating the electrochemistry of transition metal ions as responsible factors for the redox transitions.[61-64] These studies highlight the importance of MHF for sodium ion insertion/deinsertion which suggests that it can be utilized as positive electrode in aqueous rechargeable sodium ion battery for sodium ion insertion/deinsertion during discharging and charging chemistry. The effect of the quality of the produced RGOs in their sodium ion battery performance were then investigated by coupling it with MHF cathode as shown in Figure 3.5a.

3.3.3. Battery characteristics of RGOs based aqueous rechargeable sodium ion battery

When RGO1 and MHF are coupled together, the resulting electrochemical device delivered an open circuit voltage (OCV) of ~1.3 V, Figure 3.5a. The reversible charge-discharge curves with RGO1, Figure 3.5a, at a rate of 400 mA g^{-1} yielded a discharge capacity of ~83 mAh g^{-1} which is ~80% of the theoretical capacity of MHF and the decrease in experimental discharge capacity is attributed to lower electronic and ionic conductivity

of insertion cathodes.[65-68] The decrease in discharge capacity with respect to theoretical value can also be due to the capacitive nature of the graphene anode which may limit the quantity of sodium ions available to the MHF cathode during the discharge chemistry. Charge-discharge profiles with the corresponding RGO2 anode (produced by borohydride method) was more capacitive than faradaic without a proper discharge plateau, Figure 3.5a (red line) indicating the advantages of RGO1 anode as a metal ion adsorption anode. Further, the GO as the positive electrode demonstrated almost a resistive behavior. This reversible behavior with RGO1 negative electrode is further confirmed by cyclic voltammetry in two electrode configurations, Figure 3.5b. RGO1 demonstrates more reversible faradaic features during oxidative and reductive scans compared with the RGO2 which showed more capacitive behavior. The performance is more resistive with GO (Figure 3.5b, blue trace) in line with their charge-discharge behavior, Figure 3.5a. The higher performance of RGO1 compared with RGO2 may be due the relatively lower density of hydrophilic functionalities in the former. Hydrophilic functionalities can result in ionic bond formation with the Na$^+$ ions which may affect their capability for electrochemical adsorption/desorption of sodium ions. Therefore, the mode of synthesis of these RGO materials can significantly affect their electrochemical performance in aqueous sodium ion battery architecture.
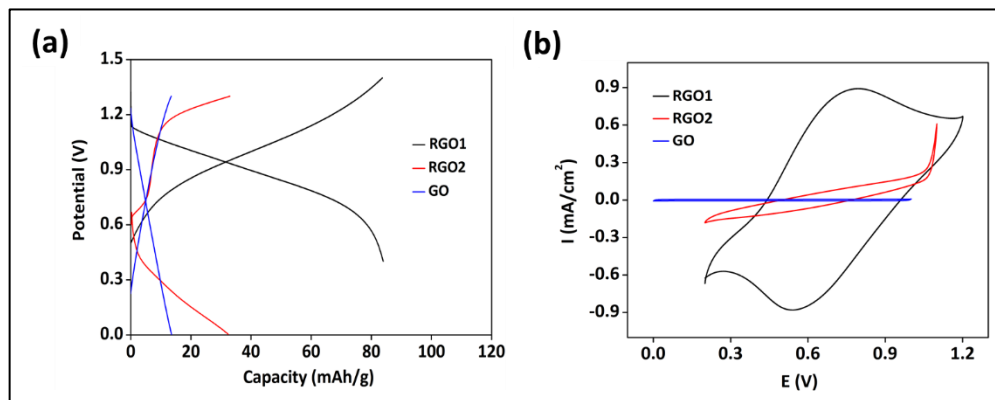
Figure 3.5: (a) Charge-discharge curves of Na ion battery in 3 M NaNO$_3$ solution at 400 mA g^{-1} and (b) cyclic voltammetry collected in the two electrode battery configuration.

To further investigate this highly reversible behaviour of RGO1 material we have carried out the energy dispersive X-ray mapping during charging and discharging chemistries, Figure 3.6. The appearance of strong sodium signal in the energy dispersive X-ray spectral (EDS) pattern during charge chemistry and its diminishing during discharge chemistry (Figure 3.6a and Figure 3.6b) demonstrate the adsorption and desorption of sodium ions at the RGO1 electrode. While in case of RGO2, sodium ion signals did not

diminish in intensity during discharge chemistry, suggesting poor reversibility at its interface, Figure 3.6c, Figure 3.6d. As mentioned earlier this could be due to higher density of hydrophilic functionalities in RGO2 which can participate in ionic bond formation with sodium ions, affecting their charge discharge chemistry. The lower density of hydrophilic functionality may preclude chemical interactions with sodium ions resulting in superior electrochemical reversibility in RGO1 material. Hydrophilicity should enhance the interactions of the electrode surface with water molecules which in turn can increase the rate of parasitic hydrogen evolution reaction; a challenge faced by aqueous batteries during the charge chemistry.[22, 31, 69-71] The rate of hydrogen evolution reaction (HER) on both the RGOs were investigated by linear sweep voltammetry, Figure 3.7. Rate of HER at a given applied potential on RGO1 electrode is decreased markedly when compared to the RGO2
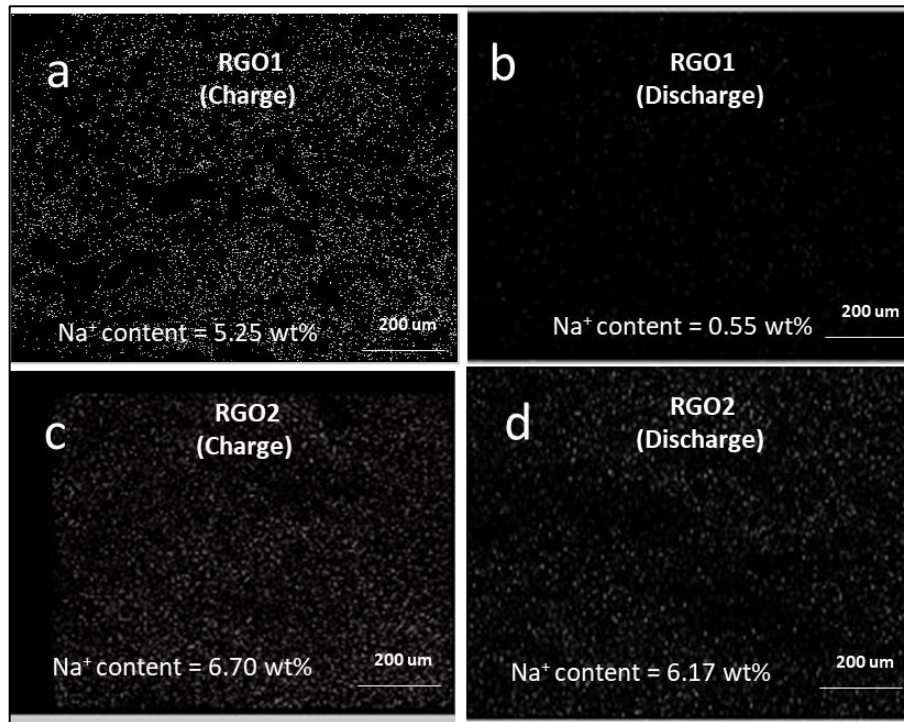
Figure 3.6: (a) Sodium ion mapping by Energy dispersive X-ray spectra (EDS) in RGO1 (a and b) and RGO2 (c and d) electrode during charge chemistry (a and c) and discharge chemistry (b and d).

counterpart, Figure 3.7. As discussed earlier RGO2 electrode has more density of hydrophilic functionalities than RGO1. Owing to the large difference between the ionic radii of Na^+ and H^+ (102 pm vs. 37 pm)[72, 73], H^+ ion can be heavily hydrated compared to Na^+ ion. Adsorption into a more hydrophobic environment as in RGO1 requires shedding of the hydration layer which will be energetically unfavorable for H^+ ion, resulting in better selectivity for Na^+ adsorption and lower rate for parasitic HER. On the other hand, H^+ ion adosrption can be relatively easier in the case of RGO2 electrode leading to higher rate for

parasitic HER. The single electrode potentials of RGO1 anode and metal hexacyanoferrate (MHF) cathode were -0.10 V and 1.2 V vs. SHE, respectively. The pH of the electrolyte used in the present investigation was 6.5. The H_2 evolution potential at this pH is calculated to be -0.38 V vs. SHE which is more negative than the single electrode potential of RGO1 anode making it a suitable candidate for metal ion adsorption without the complexity of H_2 evolution. This indicates the mode of synthesis of these materials can suppress the parasitic hydrogen evolution reaction which in turn can improve the charge-discharge performance of aqueous rechgeable sodium ion battery.
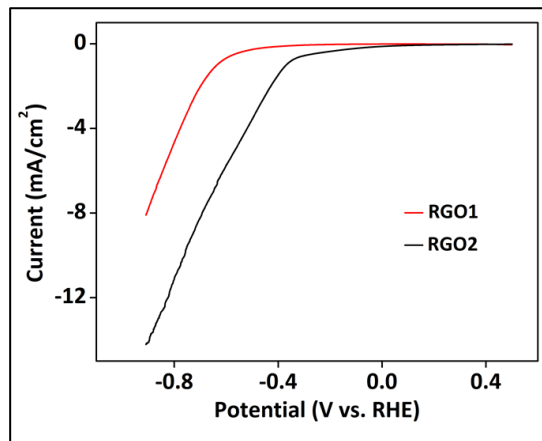
Figure 3.7: Linear sweep voltammetric curves for hydrogen evolution reaction on RGO1 and RGO2 at 5 mV s^{-1} in N_2 saturated 0.5 M H_2SO_4 electrolyte.
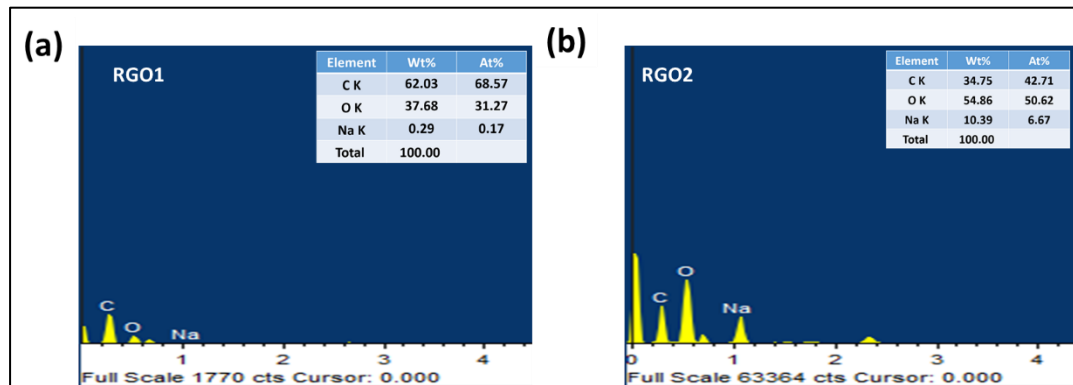
Figure 3.8: EDS analysis of (a) RGO1 and (b) RGO2 after keeping the samples in 1 M NaNO$_3$ for an hour. The samples were washed with distilled water before EDS analysis.

It is well reported in the literature that these RGO and GO materials can be utilized to adsorb the metal ions from aqueous solutions.[74,75] It is known that hydrophilic functionalities drive this chemical interaction of metal ions with the graphene materials.[74-77] Higher the density of the hydrophilic functionalities higher would be the chemical interactions and vice versa. Since, RGO2 has higher density of hydrophilic functionalities

(Figures 3.2 and 3.3), the interactions between the Na^+ with the electrode surface will be more chemical leading to poor reversibility with respect to their electrochemical sodium ion adsorption/desorption, Figure 3.8. On the other hand, in RGO1, since the O/C ratio and consequently the density of hydrophilic functionalities are relatively much lower, chemical interactions between the Na^+ with the electrode surface will not be dominant leading to better reversibility with respect to their electrochemical sodium ion adsorption/desorption, Figure 3.8.

The higher reversibility of RGO1 material is due to lower O/C ratio, higher electronic conductivity and lower density of hydrophilic functionalities. The data outlined in this chapter show that the mode of synthesis affects the quality of RGO material with regard to their electrochemical behavior in batteries. As explained in the experimental sect-
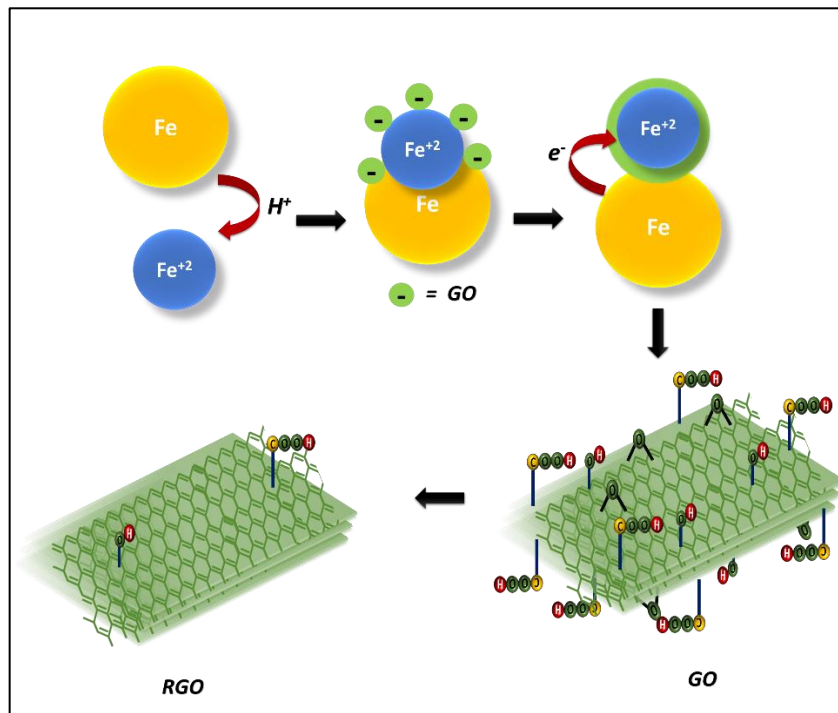
Scheme 3.1: Schematic representation of the mechanism of reduction of graphene oxide (GO) to reduced graphene oxide (RGO1) by Fe powder/HCl reduction method.

-ion RGO1 is formed by Fe/HCl reduction method and RGO2 is formed by sodium borohydride reduction method. Fan et al.[41] recently have exploited Fe powder/HCl method to reduce the graphene oxide to reduced graphene oxide and the production of higher quality of RGO material is explained as follows. Initially, the Fe particles present in the GO's dispersive solution will react with the H^+ to form Fe^{+2} species which will be adsorbed on the surface of Fe particles. The surface charge on the GO is negative due to higher density of hydrophilic functionalities. The negatively charged GO will cover the

positively charged Fe particles which will further facilitate the transfer of electron from Fe/Fe^{+2} to the functionalities of GO to produce reduced graphene oxide, Scheme 3.1 and equation 3.4. It has been also mentioned by Fan et al.,[41] that the introduction of HCl not only increase the rate of dissolution of GO but also enhances the reduction potential of the Fe/Fe^{+2}. We also believe that, the above-mentioned mechanism is responsible for the superior quality RGO produced by the Fe/HCl method compared to borohydride reduction method which in tune improves the reversibility and cyclability of RGO1 in their sodium ion battery architecture.

$$GO + Fe + aH^+ + be^- \rightarrow Fe^{+2} + RGO + cH_2O \qquad (3.4)$$
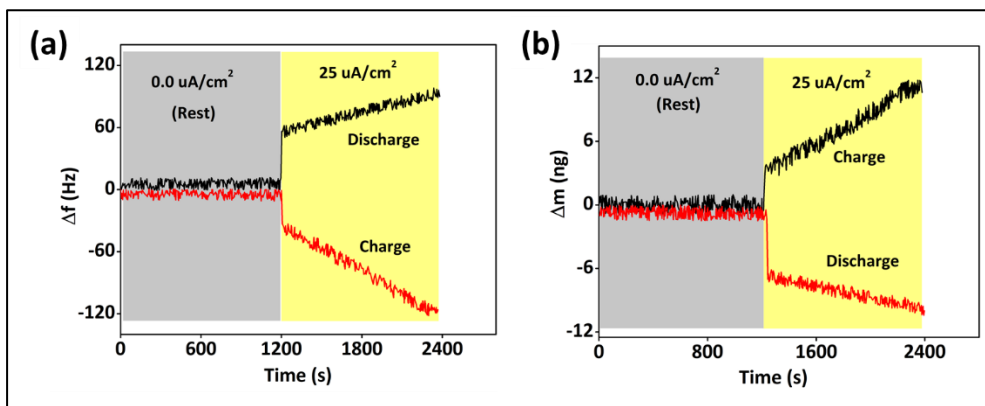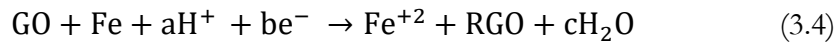
Figure 3.9: (a) Frequency change vs. time and (b) corresponding mass change vs. time obtained from electrochemical quartz crystal microbalance studies during charge-discharge chemistry at the RGO1 anode in RGO1-MHF battery configuration.

Since RGO1 is better than RGO2 as a capacitive anode to construct the aqueous rechargeable batteries, its charge discharge characteristics are further investigated by electrochemical quartz crystal microbalance and electrochemical impedance spectroscopy, Figure 3.9 and Figure 3.10. The relative frequency and mass shift during discharge chemistry is reversed compared to that of charge chemistry in RGO1 anode demonstrating higher reversibility in ion adsorption/desorption at its interface, Figure 3.9a and 3.9b. Electrochemical reversibility in aqueous battery with RGO1 electrode is further investigated by extracting the charge transfer resistance from the electrochemical impedance spectra of MHF cathode, Figure 3.10. EIS data demonstrate an increase and a decrease in semicircle diameter. This is because of the insertion/deinsertion of sodium ion on the cathode material during charging and discharging. During charging, sodium ion will move towards the RGO electrode which will further increase the charge transfer resistance of cathode (sodiated Prussian blue) which further decreases during charging chemistry as

amount of sodium ion will increase on the cathode during charging. This reflects reversibility at respective interfaces during charge and discharge chemistry, Figure 3.10a and Figure 3.10b.
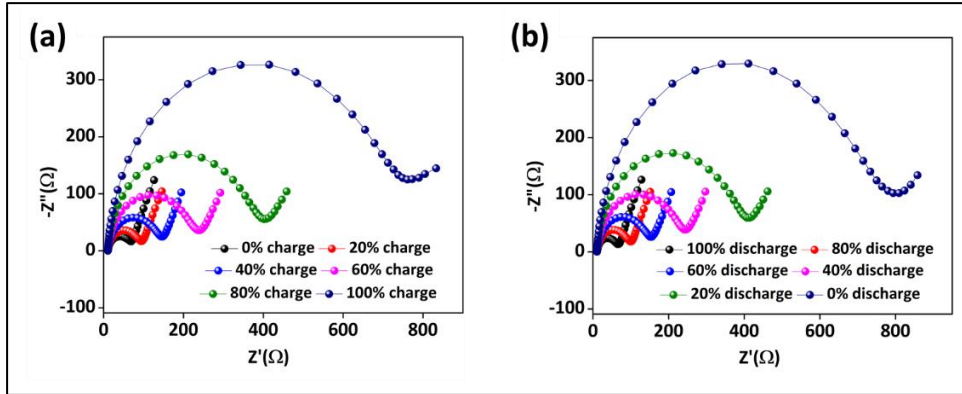
Figure 3.10: Nyquist impedance plots of the MHF cathode in RGO1-MHF battery during (a) charging and (b) discharging chemistries.
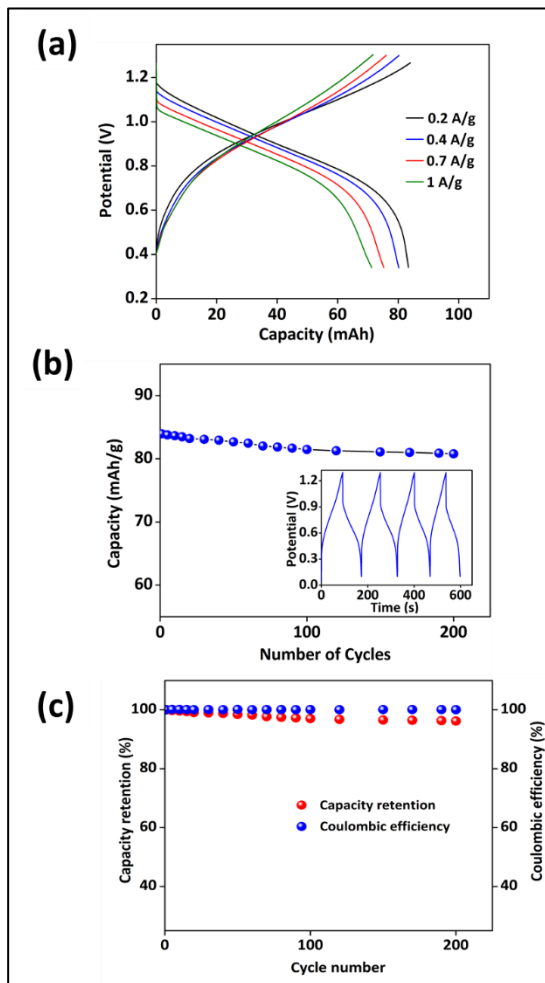
Figure 3.11: (a) Charge and discharge curves of RGO1-MHF battery in 3 M NaNO₃ solution at different current rates, (b) capacity with respect to cycle number and (c) capacity

retention and coulombic efficiency with respect to the number of cycles. Inset in Figure b is the continuous charge discharge cycles.

The extended cyclability of RGO1-MHF battery is investigated by galvanostatic charge discharge measurements, Figure 3.11. The cell delivered decent rate capability, cyclic stability, capacity retention and columbic efficiency, Figure 3.11. The discharge capacity demonstrated a decrease with the discharge rate possibly due to the electron and ion transport limitations at higher rates, Figure 3.11a. Nevertheless, ~90% of its capacity (at 0.2 A g^{-1}) is maintained at higher rates (1 A g^{-1}), Figure 3.11b, suggesting the architecture possess decent rate capability. Coulombic efficiencies are maintained at a value >98% at all assessed rates, indicating good reversibility at respective interfaces, Figure 3.11c. The cyclic stability of the battery at a discharge rate of 400 mA g^{-1} demonstrate a decent response without noticeable voltage hysteresis during extended cycling, Figure 3.11b and Figure 3.11c. Taken together, these indicate higher reversibility of sodium ion adsorption/desorption during charge discharge chemistry in RGO1-MHF battery.

3.4. Conclusions

A rechargeable aqueous sodium ion battery is demonstrated in this chapter by utilizing reduced graphene oxide (RGO) as capacitive anode and Fe (II) hexacyanoferrate (III) as the cathode material. The results demonstrate that the mode of synthesis of graphene materials can significantly influence the qualities and properties of RGO anode to construct a rechargeable sodium ion battery in aqueous environment. RGO1 produced by Fe/HCl possessed lower O/C ratio, higher electronic conductivity and lower density of hydrophilic functionalities. On the other hand, O/C ratio and the density of hydrophilic functionalities were substantially higher in the case of RGO2 produced by conventional sodium borohydride method. The higher density of hydrophilic functionalities in RGO2 favored chemical adsorption of sodium ions leading to poor electrochemical reversibility in its sodium ion adsorption/desorption. The lower density of hydrophilic functionalities in RGO1, decreased the extent of chemical interactions with cations leading better electrochemical reversibility in its sodium ion adsorption/desorption. Lower density of hydrophilic functionalities in RGO1 also suppressed the parasitic hydrogen evolution reaction; which is a challenge encountered more often in aqueous batteries. Therefore, the mode of synthesis and hence the quality of carbon materials produced can significantly affect their electrochemical behavior in electrochemical energy storage devices.

3.5. References

1.   Mourad, E.; Coustan, L.; Lannelongue, P.; Zigah, D.; Mehdi, A.; Vioux, A.; Freunberger, Stefan A.; Favier, F.; Fontaine, O., Biredox ionic liquids with solid-like redox density in the liquid state for high-energy supercapacitors. *Nat. Mater.* **2017,** *16* (4), 446-453.

2.   Peng, Z.; Freunberger, S. A.; Chen, Y.; Bruce, P. G., A reversible and higher-rate Li-O$_2$ battery. *Science* **2012,** *337* (6094), 563.

3.   Bella, F.; Griffini, G.; Correa-Baena, J.-P.; Saracco, G.; Grätzel, M.; Hagfeldt, A.; Turri, S.; Gerbaldi, C., Improving efficiency and stability of perovskite solar cells with photocurable fluoropolymers. *Science* **2016,** *354* (6309), 203.

4.   Maiyalagan, T.; Alaje, T. O.; Scott, K., Highly Stable Pt–Ru Nanoparticles Supported on Three-Dimensional Cubic Ordered Mesoporous Carbon (Pt–Ru/CMK-8) as Promising Electrocatalysts for Methanol Oxidation. *J. Phys. Chem. C* **2012,** *116* (3), 2630-2638.

5.   Miroshnikov, M.; Divya, K. P.; Babu, G.; Meiyazhagan, A.; Reddy Arava, L. M.; Ajayan, P. M.; John, G., Power from nature: designing green battery materials from electroactive quinone derivatives and organic polymers. *J. Mater. Chem. A* **2016,** *4* (32), 12370-12386.

6.   del Cueto, M.; Ocón, P.; Poyato, J. M. L., Comparative Study of Oxygen Reduction Reaction Mechanism on Nitrogen-, Phosphorus-, and Boron-Doped Graphene Surfaces for Fuel Cell Applications. *J. Phys. Chem.* **2015,** *119* (4), 2004-2009.

7.   Liu, Y.; Liu, X.; Wang, T.; Fan, L.-Z.; Jiao, L., Research and application progress on key materials for sodium-ion batteries. *Sustain. Energy Fuels* **2017,** *1* (5), 986-1006.

8.   Kundu, S.; Nagaiah, T. C.; Xia, W.; Wang, Y.; Dommele, S. V.; Bitter, J. H.; Santa, M.; Grundmeier, G.; Bron, M.; Schuhmann, W.; Muhler, M.,

Electrocatalytic Activity and Stability of Nitrogen-Containing Carbon Nanotubes in the Oxygen Reduction Reaction. *J. Phys. Chem. C* **2009,** *113* (32), 14302-14310.

9. Lin, M.-C.; Gong, M.; Lu, B.; Wu, Y.; Wang, D.-Y.; Guan, M.; Angell, M.; Chen, C.; Yang, J.; Hwang, B.-J.; Dai, H., An ultrafast rechargeable aluminium-ion battery. *Nature* **2015,** *520* (7547), 324-328.

10. Li, Y.; Hu, Y.-S.; Titirici, M.-M.; Chen, L.; Huang, X., Hard Carbon Microtubes Made from Renewable Cotton as High-Performance Anode Material for Sodium-Ion Batteries. *Adv. Energy Mater.* **2016,** *6* (18), 1600659.

11. Fabian, D. M.; Hu, S.; Singh, N.; Houle, F. A.; Hisatomi, T.; Domen, K.; Osterloh, F. E.; Ardo, S., Particle suspension reactors and materials for solar-driven water splitting. *Energy Environ. Sci.* **2015,** *8* (10), 2825-2850.

12. Wu, S.; Xu, R.; Lu, M.; Ge, R.; Iocozzia, J.; Han, C.; Jiang, B.; Lin, Z., Lithium-Ion Batteries: Graphene-Containing Nanomaterials for Lithium-Ion Batteries (Adv. Energy Mater. 21/2015). *Adv. Energy Mater.* **2015,** *5* (21).

13. Schafzahl, L.; Mahne, N.; Schafzahl, B.; Wilkening, M.; Slugovc, C.; Borisov, S. M.; Freunberger, S. A., Singlet Oxygen during Cycling of the Aprotic Sodium–O_2 Battery. *Angew. Chem. Int. Ed.* **2017,** *56* (49), 15728-15732.

14. Pramudita, J. C.; Pontiroli, D.; Magnani, G.; Gaboardi, M.; Riccò, M.; Milanese, C.; Brand, H. E. A.; Sharma, N., Graphene and Selected Derivatives as Negative Electrodes in Sodium- and Lithium-Ion Batteries. Negative Electrodes in Sodium-and Lithium-Ion Batteries. *ChemElectroChem* **2015,** *2* (4), 600-610.

15. Farbod, B.; Cui, K.; Kalisvaart, W. P.; Kupsta, M.; Zahiri, B.; Kohandehghan, A.; Lotfabad, E. M.; Li, Z.; Luber, E. J.; Mitlin, D., Anodes for Sodium Ion Batteries Based on Tin–Germanium–Antimony Alloys. *ACS Nano* **2014,** *8* (5), 4415-4429.

16. Li, H.; Wang, X.; Zhao, Z.; Tian, Z.; Zhang, D.; Wu, Y., Ni_2P Nanoflake Array/Three Dimensional Graphene Architecture as Integrated Free-Standing

Anode for Boosting the Sodiation Capability and Stability. *ChemElectroChem* **2019,** *6* (2), 404-412.

17.   Coromina, H. M.; Adeniran, B.; Mokaya, R.; Walsh, D. A., Bridging the performance gap between electric double-layer capacitors and batteries with high-energy/high-power carbon nanotube-based electrodes. *J. Mater. Chem. A* **2016,** *4* (38), 14586-14594.

18.   Soloveichik, G. L., Battery Technologies for Large-Scale Stationary Energy Storage. *Annu. Rev. Chem. Biomol. Eng.* **2011,** *2* (1), 503-527.

19.   Cavaliere, S.; Subianto, S.; Savych, I.; Jones, D. J.; Rozière, J., Electrospinning: designed architectures for energy conversion and storage devices. *Energy Environ. Sci.* **2011,** *4* (12), 4761-4785.

20.   Zhang, H.; Qin, B.; Han, J.; Passerini, S., Aqueous/Nonaqueous Hybrid Electrolyte for Sodium-Ion Batteries. *ACS Energy Lett.* **2018,** *3* (7), 1769-1770.

21.   Chen, L.; Cao, L.; Ji, X.; Hou, S.; Li, Q.; Chen, J.; Yang, C.; Eidson, N.; Wang, C., Enabling safe aqueous lithium ion open batteries by suppressing oxygen reduction reaction. *Nat. Commun.* **2020,** *11* (1), 2638.

22.   Shen, Y.; Han, X.; Cai, T.; Hu, H.; Li, Y.; Zhao, L.; Hu, H.; Xue, Q.; Zhao, Y.; Zhou, J.; Gao, X.; Xing, W.; Wang, X., High-performance aqueous sodium-ion battery using a hybrid electrolyte with a wide electrochemical stability window. *RSC Adv.* **2020,** *10* (43), 25496-25499.

23.   Yang, C.; Chen, J.; Ji, X.; Pollard, T. P.; Lü, X.; Sun, C.-J.; Hou, S.; Liu, Q.; Liu, C.; Qing, T.; Wang, Y.; Borodin, O.; Ren, Y.; Xu, K.; Wang, C., Aqueous Li-ion battery enabled by halogen conversion–intercalation chemistry in graphite. *Nature* **2019,** *569* (7755), 245-250.

24.   Yang, C.; Chen, J.; Qing, T.; Fan, X.; Sun, W.; von Cresce, A.; Ding, M. S.; Borodin, O.; Vatamanu, J.; Schroeder, M. A.; Eidson, N.; Wang, C.; Xu, K., 4.0 V Aqueous Li-Ion Batteries. *Joule* **2017,** *1* (1), 122-132.

25. Liu, G.; Chi, Q.; Zhang, Y.; Chen, Q.; Zhang, C.; Zhu, K.; Cao, D., Superior high rate capability of MgMn$_2$O$_4$/rGO nanocomposites as cathode materials for aqueous rechargeable magnesium ion batteries. *Chem. Commun.* **2018,** *54* (68), 9474-9477.

26. Yin, F.; Liu, Z.; Zhao, Y.; Feng, Y.; Zhang, Y., Electrochemical Properties of an Na4Mn9O18-Reduced Graphene Oxide Composite Synthesized via Spray Drying for an Aqueous Sodium-Ion Battery. *Nanomaterials* **2017,** *7* (9).

27. Yi, Y.; Weinberg, G.; Prenzel, M.; Greiner, M.; Heumann, S.; Becker, S.; Schlögl, R., Electrochemical corrosion of a glassy carbon electrode. *Catal. Today* **2017,** *295*, 32-40.

28. Kinoshita, K.; Bett, J., Electrochemical oxidation of carbon black in concentrated phosphoric acid at 135°C. *Carbon* **1973,** *11* (3), 237-247.

29. Sun, J.; Iakunkov, A.; Rebrikova, A. T.; Talyzin, A. V., Exactly matched pore size for the intercalation of electrolyte ions determined using the tunable swelling of graphite oxide in supercapacitor electrodes. *Nanoscale* **2018,** *10* (45), 21386-21395.

30. Iakunkov, A.; Skrypnychuk, V.; Nordenström, A.; Shilayeva, E. A.; Korobov, M.; Prodana, M.; Enachescu, M.; Larsson, S. H.; V.Talyzin, A., Activated graphene as a material for supercapacitor electrodes: effects of surface area, pore size distribution and hydrophilicity. *Phys. Chem. Chem. Phys.* **2019,** *21* (32), 17901-17912.

31. Wang, F.; Lin, C.-F.; Ji, X.; Rubloff, G. W.; Wang, C., Suppression of hydrogen evolution at catalytic surfaces in aqueous lithium ion batteries. *J. Mater. Chem. A* **2020,** *8* (30), 14921-14926.

32. Schweiss, R.; Pritzl, A.; Meiser, C., Parasitic Hydrogen Evolution at Different Carbon Fiber Electrodes in Vanadium Redox Flow Batteries. *J. Electrochem. Soc.* **2016,** *163* (9), A2089-A2094.

33. Qiu, Y.; Yu, Y.; Xu, J.; Liu, Y.; Ou, M.; Sun, S.; Wei, P.; Deng, Z.; Xu, Y.; Fang, C.; Li, Q.; Han, J.; Huang, Y., Redox potential regulation toward suppressing hydrogen evolution in aqueous sodium-ion batteries: $Na_{1.5}Ti_{1.5}Fe_{0.5}(PO_4)_3$. *J. Mater. Chem. A* **2019,** *7* (43), 24953-24963.

34. Bin, D.; Wang, F.; Tamirat, A. G.; Suo, L.; Wang, Y.; Wang, C.; Xia, Y., Progress in Aqueous Rechargeable Sodium-Ion Batteries. *Adv. Energy Mater.* **2018,** *8* (17), 1703008.

35. Munuera, J. M.; Paredes, J. I.; Enterría, M.; Pagán, A.; Villar-Rodil, S.; Pereira, M. F. R.; Martins, J. I.; Figueiredo, J. L.; Cenis, J. L.; Martínez-Alonso, A.; Tascón, J. M. D., Electrochemical Exfoliation of Graphite in Aqueous Sodium Halide Electrolytes toward Low Oxygen Content Graphene for Energy and Environmental Applications. *ACS Appl. Mater. Interfaces* **2017,** *9* (28), 24085-24099.

36. Abdelkader, A. M.; Cooper, A. J.; Dryfe, R. A. W.; Kinloch, I. A., How to get between the sheets: a review of recent works on the electrochemical exfoliation of graphene materials from bulk graphite. *Nanoscale* **2015,** *7* (16), 6944-6956.

37. Zhao, Y.; Ding, Y.; Song, J.; Peng, L.; Goodenough, J. B.; Yu, G., A reversible Br_2/Br^- redox couple in the aqueous phase as a high-performance catholyte for alkali-ion batteries. *Energy Environ. Sci.* **2014,** *7* (6), 1990-1995.

38. Wessells, C.; La Mantia, F.; Deshazer, H.; Huggins, R. A.; Cui, Y., Synthesis and Electrochemical Performance of a Lithium Titanium Phosphate Anode for Aqueous Lithium-Ion Batteries. *J. Electrochem. Soc.* **2011,** *158* (3), A352.

39. Pasta, M.; Wessells, C. D.; Huggins, R. A.; Cui, Y., A high-rate and long cycle life aqueous electrolyte battery for grid-scale energy storage. *Nat. Commun.* **2012,** *3* (1), 1149.

40. Lee, M. H.; Kim, S. J.; Chang, D.; Kim, J.; Moon, S.; Oh, K.; Park, K.-Y.; Seong, W. M.; Park, H.; Kwon, G.; Lee, B.; Kang, K., Toward a low-cost high-voltage sodium aqueous rechargeable battery. *Mater. Today* **2019,** *29*, 26-36.

41.   Fan, Z.-J.; Kai, W.; Yan, J.; Wei, T.; Zhi, L.-J.; Feng, J.; Ren, Y.-m.; Song, L.-P.; Wei, F., Facile Synthesis of Graphene Nanosheets via Fe Reduction of Exfoliated Graphite Oxide. *ACS Nano* **2011,** *5* (1), 191-198.

42.   Guex, L. G.; Sacchi, B.; Peuvot, K. F.; Andersson, R. L.; Pourrahimi, A. M.; Ström, V.; Farris, S.; Olsson, R. T., Experimental review: chemical reduction of graphene oxide (GO) to reduced graphene oxide (rGO) by aqueous chemistry. *Nanoscale* **2017,** *9* (27), 9562-9571.

43.   Fernández-Merino, M. J.; Guardia, L.; Paredes, J. I.; Villar-Rodil, S.; Solís-Fernández, P.; Martínez-Alonso, A.; Tascón, J. M. D., Vitamin C Is an Ideal Substitute for Hydrazine in the Reduction of Graphene Oxide Suspensions. *J. Phys. Chem. C* **2010,** *114* (14), 6426-6432.

44.   Chua, C. K.; Pumera, M., Chemical reduction of graphene oxide: a synthetic chemistry viewpoint. *Chem. Soc. Rev.* **2014,** *43* (1), 291-312.

45.   Wang, B.; Han, Y.; Wang, X.; Bahlawane, N.; Pan, H.; Yan, M.; Jiang, Y., Prussian Blue Analogs for Rechargeable Batteries. *iScience* **2018,** *3*, 110-133.

46.   Targholi, E.; Mousavi-Khoshdel, S. M.; Rahmanifara, M.; Yahya, M. Z. A., Cu-and Fe-hexacyanoferrate as cathode materials for Potassium ion battery: A First-principles study. *Chem. Phys. Lett.* **2017,** *687*, 244-249.

47.   Omarova, M.; Koishybay, A.; Yesibolati, N.; Mentbayeva, A.; Umirov, N.; Ismailov, K.; Adair, D.; Babaa, M.-R.; Kurmanbayeva, I.; Bakenov, Z., Nickel Hexacyanoferrate Nanoparticles as a Low Cost Cathode Material for Lithium-Ion Batteries. *Electrochim. Acta* **2015,** *184*, 58-63.

48.   Huggins, R. A., Review—A New Class of High Rate, Long Cycle Life, Aqueous Electrolyte Battery Electrodes. *J. Electrochem. Soc.* **2017,** *164* (1), A5031-A5036.

49.   Xavier, P.; Sharma, K.; Elayaraja, K.; Vasu, K. S.; Sood, A. K.; Bose, S., Reduced graphene oxide induced phase miscibility in polystyrene–poly(vinylmethyl ether) blends. *RSC Adv.* **2014,** *4* (24), 12376-12387.

50. Marcano, D. C.; Kosynkin, D. V.; Berlin, J. M.; Sinitskii, A.; Sun, Z.; Slesarev, A.; Alemany, L. B.; Lu, W.; Tour, J. M., Improved Synthesis of Graphene Oxide. *ACS Nano* **2010,** *4* (8), 4806-4814.

51. Shin, H.-J.; Kim, K. K.; Benayad, A.; Yoon, S.-M.; Park, H. K.; Jung, I.-S.; Jin, M. H.; Jeong, H.-K.; Kim, J. M.; Choi, J.-Y.; Lee, Y. H., Efficient Reduction of Graphite Oxide by Sodium Borohydride and Its Effect on Electrical Conductance. *Adv. Funct. Mater.* **2009,** *19* (12), 1987-1992.

52. Mokrani, C.; Fatisson, J.; Guérente, L.; Labbé, P., Structural Characterization of (3-Mercaptopropyl)sulfonate Monolayer on Gold Surfaces. *Langmuir* **2005,** *21* (10), 4400-4409.

53. Vogt, B. D.; Lin, E. K.; Wu, W.-l.; White, C. C., Effect of Film Thickness on the Validity of the Sauerbrey Equation for Hydrated Polyelectrolyte Films. *J. Phys. Chem. B.* **2004,** *108* (34), 12685-12690.

54. Kottaichamy, A. R.; Begum, S.; Devendrachari, M. C.; Bhat, Z. M.; Thimmappa, R.; Nimbegondi Kotresh, H. M.; Vinod, C. P.; Thotiyl, M. O., Geometrical Isomerism Directed Electrochemical Sensing. *Anal. Chem.* **2020,** *92* (6), 4541-4547.

55. Kottaichamy, A. R.; Begum, S.; Nazrulla, M. A.; Dargily, N. C.; Devendrachari, M. C.; Manzoor Bhat, Z.; Thimmappa, R.; Makri Nimbegondi Kotresh, H.; Vinod, C. P.; Thotiyl, M. O., Unprecedented Isomerism–Activity Relation in Molecular Electrocatalysis. *J. Phys. Chem. Lett.* **2020,** *11* (1), 263-271.

56. Jha, P. K.; Singh, S. K.; Kumar, V.; Rana, S.; Kurungot, S.; Ballav, N., High-Level Supercapacitive Performance of Chemically Reduced Graphene Oxide. *Chem* **2017,** *3* (5), 846-860.

57. Fathy, M.; Gomaa, A.; Taher, F. A.; El-Fass, M. M.; Kashyout, A. E.-H. B., Optimizing the preparation parameters of GO and rGO for large-scale production. *J. Mater. Sci.* **2016,** *51* (12), 5664-5675.

58.   Nakamoto, K.; Sakamoto, R.; Sawada, Y.; Ito, M.; Okada, S., Over 2 V Aqueous Sodium-Ion Battery with Prussian Blue-Type Electrodes. *Small Methods* **2019,** *3* (4), 1800220.

59.   Wang, B.; Wang, X.; Liang, C.; Yan, M.; Jiang, Y., An All-Prussian-Blue-Based Aqueous Sodium-Ion Battery. *ChemElectroChem* **2019,** *6* (18), 4848-4853.

60.   Qian, J.; Wu, C.; Cao, Y.; Ma, Z.; Huang, Y.; Ai, X.; Yang, H., Prussian Blue Cathode Materials for Sodium-Ion Batteries and Other Ion Batteries. *Adv. Energy Mater.* **2018,** *8*, 1702619.

61.   Lu, H.-C.; Kao, S.-Y.; Chang, T.-H.; Kung, C.-W.; Ho, K.-C., An electrochromic device based on Prussian blue, self-immobilized vinyl benzyl viologen, and ferrocene. *Sol. Energy Mater. Sol. Cells* **2016,** *147*, 75-84.

62.   Liao, T.-C.; Chen, W.-H.; Liao, H.-Y.; Chen, L.-C., Multicolor electrochromic thin films and devices based on the Prussian blue family nanoparticles. *Sol. Energy Mater. Sol. Cells* **2016,** *145*, 26-34.

63.   Itaya, K.; Uchida, I., Nature of intervalence charge-transfer bands in Prussian blues. *Inorg. Chem.* **1986,** *25* (3), 389-392.

64.   Rogers, D.; Johansson, O., Metal-to-metal charge-transfer transitions in Prussian blue hexacyanochromate analogues. *Mater. Sci. Eng. B* **2017,** *227*, 28.

65.   Nie, P.; Yuan, J.; Wang, J.; Le, Z.; Xu, G.; Hao, L.; Pang, G.; Wu, Y.; Dou, H.; Yan, X.; Zhang, X., Prussian Blue Analogue with Fast Kinetics Through Electronic Coupling for Sodium Ion Batteries. *ACS Appl. Mater. Interfaces* **2017,** *9* (24), 20306-20312.

66.   Chen, M.; Zhang, Z.; Liu, X.; Li, Y.; Wang, Y.; Fan, H.; Liang, X.; Chen,Q., Prussian blue coated with reduced graphene oxide as high-performance cathode for lithium–Sulfur batteries. *RSC Adv.* **2020,** *10* (53), 31773-31779.

67.   Jiang, Y.; Yu, S.; Wang, B.; Li, Y.; Sun, W.; Lu, Y.; Yan, M.; Song, B.; Dou, S., Prussian Blue@C Composite as an Ultrahigh-Rate and Long-Life Sodium-Ion Battery Cathode. *Adv. Funct. Mater.* **2016,** *26* (29), 5315-5321.

68.   Fu, H.; Xia, M.; Qi, R.; Liang, X.; Zhao, M.; Zhang, Z.; Lu, X.; Cao, G., Improved rate performance of Prussian blue cathode materials for sodium ion batteries induced by ion-conductive solid-electrolyte interphase layer. *J. Power Sources* **2018,** *399*, 42-48.

69.   Mathew, V.; Sambandam, B.; Kim, S.; Kim, S.; Park, S.; Lee, S.; Alfaruqi, M. H.; Soundharrajan, V.; Islam, S.; Putro, D. Y.; Hwang, J.-Y.; Sun, Y.-K.; Kim, J., Manganese and Vanadium Oxide Cathodes for Aqueous Rechargeable Zinc-Ion Batteries: A Focused View on Performance, Mechanism, and Developments. *ACS Energy Lett.* **2020,** *5* (7), 2376-2400.

70.   Sun, C.-N.; Delnick, F. M.; Baggetto, L.; Veith, G. M.; Zawodzinski, T. A., Hydrogen evolution at the negative electrode of the all-vanadium redox flow batteries. *J. Power Sources* **2014,** *248*, 560-564.

71.   Malkhandi, S.; Yang, B.; Manohar, A. K.; Prakash, G. K. S.; Narayanan, S. R., Self-Assembled Monolayers of n-Alkanethiols Suppress Hydrogen Evolution and Increase the Efficiency of Rechargeable Iron Battery Electrodes. *J. Am. Chem. Soc.* **2013,** *135* (1), 347-353.

72.   Ong, S. P.; Chevrier, V. L.; Hautier, G.; Jain, A.; Moore, C.; Kim, S.; Ma, X.; Ceder, G., Voltage, stability and diffusion barrier differences between sodium-ion and lithium-ion intercalation materials. *Energy Environ. Sci.* **2011,** *4* (9), 3680-3688.

73.   Reddy, J. M. B. a. K. A., Modern Electrochemistry, 2nd ed., Plenum Press: New York **1970,** *729*.

74.   Ramesha, G. K.; Vijaya Kumara, A.; Muralidhara, H. B.; Sampath, S., Graphene and graphene oxide as effective adsorbents toward anionic and cationic dyes. *J. Colloid Interface Sci.* **2011,** *361* (1), 270-277.

75. Liu, Z.; Rios-Carvajal, T.; P. Andersson, M.; Ceccato, M.; Stipp, S. L. S.; Hassenkam, T., Ion effects on molecular interaction between graphene oxide and organic molecules. *Environ. Sci. Nano* **2019,** *6* (7), 2281-2291.

76. Wei, M.-p.; Chai, H.; Cao, Y.-l.; Jia, D.-z., Sulfonated graphene oxide as an adsorbent for removal of Pb^{2+} and methylene blue. *J. Colloid Interface Sci.* **2018,** *524*, 297-305.

77. Sitko, R.; Musielak, M.; Zawisza, B.; Talik, E.; Gagor, A., Graphene oxide/cellulose membranes in adsorption of divalent metal ions. *RSC Adv.* **2016,** *6* (99), 96595-96605.

Chapter 4a

An Atmospheric Water Vapor Electrolyzer with Graphene Oxide Proton Exchange Membrane

Abstract

This chapter reports the generation of pure molecular hydrogen by the electrolysis of humid air. Compared to the global mean temperatures in mid-19th century, the planet earth is ~1.2 °C hotter nowadays. Evidences suggest that inconsiderate human activities may provide enough momentum to cross the ultimate threshold in climate change triggering a self-perpetuating global warming event. The Arctic sea ice melting into open ocean is one of the natural drivers of global warming because the former can reflect Sun's radiative force and the latter instead absorbs it. This, on one hand will increase the amounts of atmospheric water, which indeed will have warming effect on the planet. On the other hand, if new chemistries can be developed, earth's atmosphere will provide a universal feedstock of water, which can potentially be converted into fuel molecules via electrochemical processes coupled to renewable energy. Here we show that the abundance of hydrophilic functionalities in graphene oxide (GO) provide access to atmospheric water; which coupled with its molecular fuel barrier nature and proton conduction capability allow electrolysis of atmospheric water to molecular fuels. GO based water vapour electrolyzer provides ~200 mA cm^{-2} of current density (at 2 V) at 80 % relative humidity with a H_2:O_2 stoichiometric ratio of nearly 2:1.
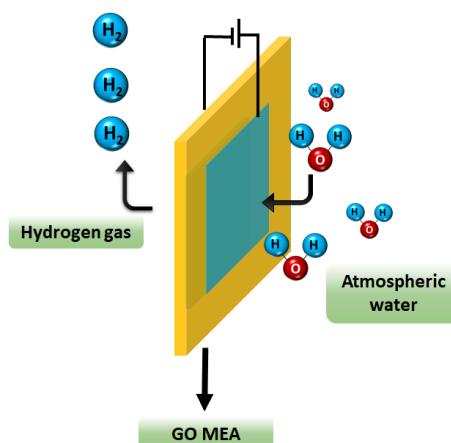
Declaration: The work in this chapter is original and has not yet been published anywhere. (Manuscript under preparation)

4a.1 Introduction

Recent interests in harvesting renewable energy due to the serious environmental impacts of fossil fuel consumption have projected hydrogen economy as a viable alternative.[1-4] "Hydrogen economy" is a carbon neutral energy pathway for stabilizing global mean temperatures and generation of molecular hydrogen is an integral part of this chain.[5-7] Since molecular hydrogen is an energy carrier molecule with significantly higher energy density (140 MJ kg^{-1}) than typical solid fuels (50 MJ kg^{-1}), there exists enormous interests in storing the renewable energy in the chemical bonds of hydrogen fuel which in turn offers a feasible solution to address the geographic and temporal variations of renewable energy resources.[8-10] Currently, the global H_2 generation is around 500 billion cubic meter per year.[1,11,12] Nevertheless, industrial sources of molecular hydrogen are steam reformation of the natural gases, but this pathway involves significant green-house gas emissions.[13-18] Further, state of the art steam reforming of hydrogen storage molecules is prohibitively expensive as it requires high temperatures > 200°C and high pressures > 25 bar.[19-21] Further, it is well known that even under these extreme conditions the generated hydrogen fuel stream is contaminated with carbon containing impurities, and consequently; it cannot be directly utilized in a fuel cell for energy conversion.[22-24] These are responsible for the tremendous interest in electrochemical water electrolysis as a pathway to generate hydrogen as it is able to generate hydrogen fuel in high purity with a near zero carbon footprint.[25-28] To date various catalysts and combinations have been designed for water electrolysis, however a practical water electrolyzer require deionized water for its operation because of the interference and parasitic chemistry arising out of dissolved salts.[29-32] The latter aspect limit commercial prospect of water electrolyzers especially for electric vehicles as there exists multiple engineering and technological challenges in terms of continuous deionized water supply.[33-37]

It should be borne in mind that the thermodynamic potential of water electrolysis is 1.23 V and proton exchange membrane (PEM) based water electrolyzer is one of the matured strategy for the generation of molecular fuel with O_2 as the byproduct.[38-43] In PEM water electrolyzer, Nafion membrane (tetrafluoroethylene-perfluoro-3,6-dioxa-4-methyl-7-octenesulfonic acid copolymer) is used because of its higher proton conduction capability (~0.1 S cm^{-1}), higher value of ion exchange capacity (0.9 to 2 meq g^{-1}), lower rate

of fuel crossover and high chemical and mechanical stabilities.[44-49] However, this membrane is known to undergo chemical degradation by peroxide intermediates which can attack the hydrophilic functionalities (for example, SO_3^-) of Nafion membrane.[50-57] Secondly, its higher cost also makes the fuel production expensive by PEM water electrolysis.[58-61] These challenges prompted the exploration of different types of proton exchange membranes in PEM water electrolysis. Membranes like polyfluorosulfonic acid (PFSA), polystyrene sulfonic acid (PSSA), sulfonated poly(ether ether ketone) (SPEEK), sulfonated polyethersulfone (SPES) etc., have come into the light as proton exchange membrane because of their ability to conduct protons and to function as molecular fuel barriers.[44, 62-66] In the attempts to improve the performance of Nafion based membranes for water electrolysis, its composites with inorganic metal oxides have also been utilized.[67-70] For example, Baglio et al. reported a composite of Nafion-TiO_2 membrane as a high performance solid polymer electrolyte (SPE) in water electrolyzer.[71] The increase in performance of water electrolyzer is mainly attributed to the water retention properties of the inorganic fillers and an increment in electrical efficiency was recorded at low current densities for the composite membrane-based SPE electrolyzer at high temperature compared to conventional membrane-based devices.[71] Siracusano et al. studied the sulfated titania as additive in Nafion membranes for water electrolysis applications and reported higher electrolysis performances at 100 °C as compared to undoped Nafion.[72] Higher current densities of 4 A cm^{-2} and 3 A cm^{-2} were found at a terminal voltage of 2 V for the composite and plain membrane, respectively.[72]

In this context, graphene oxide (GO) is an attractive material to be exploited in PEM water electrolyzers because Dikin et al. [73] & karim et al. [57] predicted the ability of GO to conduct protons due to the presence of hydrophilic functionalities (C−O−C, -C-O −OH, −COOH etc.) and to function as a barrier to molecular fuels. Secondly, the abundance of hydrophilic functionality should also allow GO to retain water molecules in its interlayers.[74,75] Liu et al., examined the moisture absorption of graphene oxide papers with different amounts of oxygen-containing functional groups and attributed the higher water absorption capacity of graphene oxide paper to its hydrophilic functionalities.[76] This makes GO membrane as a potential candidate to be utilized as proton exchange membrane to construct an atmospheric water electrolyzer. This assumes significance because earth's atmosphere provides a universal feedstock of water, carbon dioxide, and nitrogen, and the ability of GO to hold water molecules allow its conversion into fuel molecules via electrochemical processes coupled to renewable energy. Since, we know that 2% of the

atmospheric composition is water vapour which is also responsible for the warming effect. Although the earth's surface is covered 70% by water bodies but most of it is in saline form whereas the atmospheric water is accessible in pure form without any salts in it which makes it an interesting stock for the electrolyzers.

This chapter deals with the construction of a graphene oxide paper-based water vapor electrolyzer with performance metrics ∼200 mA cm^{-2} at a terminal voltage of 2 V at 80 % relative humidity. This water vapor electrolyzer splits the water molecules present in the carrier gas and the ability of hydrophilic functionalities in GO to pre-concentrate water molecules make it feasible for the device to electrolyze the atmospheric water even in open air to generate pure hydrogen fuel. The architectural configuration of the electrolyzer encompass an air tight cathodic half-cell with a Pt/C as cathode electrocatalyst and an air breathing anodic half-cell with IrO_2 as anode electrocatalyst (Scheme 4a.1). The anode and cathodes were separated by GO paper membrane (thickness ∼50 μm) for proton shuttling. The entire assembly is kept in humid open air to harvest renewable energy as hydrogen fuel. It should be noted that no additional water is supplied for electrolysis and the hydrogen fuel is generated by electrolyzing the humidity present in the air. The ease of production GO membranes coupled with the water pre-concentration capability of GO allow direct access to the universal feedstock of water in earth's atmosphere for the interconversion of renewable energy.

4a.2   Experimental

4a.2.1   Materials

H_2SO_4 (99.99 %), H_3PO_4 (99.99 %), HCl (99.99 %), $KMnO_4$ (98.0 %), H_2O_2 (30 wt%), Nafion (5.0 wt% solution in isopropyl alcohol), Graphite flakes, IrO_2 were obtained from Sigma Aldrich. Pt supported on carbon (20 wt % of Pt/C) catalyst was procured from Jhonson-Mathey, India. Nafion® 212 membrane was obtained from Fuel Cell Store (USA).

4a.2.2   Preparation of graphene oxide (GO) paper

Graphene oxide (GO) was synthesized by improved Hummers method as per the literature.[77, 78] 4:1 ratio of acidic mixture of H_2SO_4:H_3PO_4 was added to 3.0 g of graphite flakes followed by the addition of 18 g of $KMnO_4$ and the mixture was continuously stirred for 3 days. Then, 15 mL of 36% H_2O_2, was added to the mixture and stirred for another 3

h. Graphene oxide was collected by centrifugation and then washed with HCl and de-ionized water several times. After washing GO with water, it is spread over the petry dish and kept it for air drying. The thickness of GO paper is maintained by controlling the weight % of the GO in the dispersion used for drop casting. After drying, the GO paper was peeled off from the petri dish.

4a.2.3 Physicochemical characterizations

X-ray diffraction (XRD) was collected using a Bruker D8 Advance X-ray diffraction machine and Fourier transform infrared spectroscopy (FTIR) was collected using Bruker Alpha FTIR spectrometer system in the mid IR region. Raman spectrum were recorded using Raman microscope (LabRAM HR, Horbia). The thermal stability of the membrane was analyzed by thermo-gravimetric analysis using a STA6000 machine over the temperature range of $25 - 600°$ C with a scan rate of 5 °C min^{-1} under nitrogen flow (30 mL min^{-1}). The cross-sectional morphology of the membrane electrode assembly (MEAs) was investigated by a JSM-5300LV (Japan) scanning electron microscope (SEM). AFM images were recorded for GO by using Agilent instruments. Cleaned mica sheets were used for drop casting diluted samples of GO. For water electrolyzer's performance evaluation, photovoltaic/fuel cell techniques which are available under the 'Electrochemical Applications' in Biologic VMP 300 equipment were utilized. Galvanostatic measurements in single step current mode were investigated by using chronopotentiometric techniques available in Biologic VMP 300. Galvanostatic techniques were performed to quantify the gases evolved from the electrolyzer. In situ electrochemical mass spectrometry was carried out with an HPR-20 R&D (Hiden analytical) Quadruple mass analyzer. Electrochemical impedance measurements (available in Biologic VMP 300) were used to carry out the proton conductivity of the membranes. The frequency range was 100 kHz to 10 mHz and the amplitude of AC was 10 mV. The GO membrane was sandwiched between two Pt disc electrodes. By using the equation 4a.1, the proton conductivity of the membrane was calculated.

$$\sigma = T/(R*A) \hspace{3cm} (4a. 1)$$

where, R is the bulk resistance recorded from electrochemical impedance analysis from the real axis intercept at higher frequency, T is the thickness of the membrane and A is the area of the membrane in cm^2. Ion exchange capacity (IEC) of the membrane was measured by using the classical acid base titration techniques. Membrane was soaked in 0.1 M HCl solution for 24 h followed by washing with distilled water to remove excess HCl. After

that samples were placed in NaCl aqueous solution for 24 h to release the protons from membrane. Back titration was carried out with standardized 0.1 M NaOH aqueous solution with phenolphthalein indicator to measure the H^+ ions concentration in the solution. By using the following equation, the IEC values in meq g^{-1} were calculated.[79, 80]

$$IEC = (V_{NaOH} * C_{NaOH})/W_{dry} \qquad (4a.\ 2)$$

where, V_{NaOH} is the consumed volume of NaOH, C_{NaOH} is the concentration of the NaOH and W_{dry} is the weight of the completely dry membranes (g). The activation energy of GO membrane is estimated from Arrhenius plot by estimating the proton conductivities at different temperatures. The activation energy is calculated by the following equation:[81, 82]

$$\ln \sigma = \ln \sigma_0 - E_a/RT \qquad (4a.\ 3)$$

where, where σ is the proton conductivity (mS cm^{-1}), σ_0 is the pre-exponential factor (mS cm^{-1}), E_a is the activation energy required for proton transport (kJ mol^{-1}), R is the gas constant (J K^{-1} mol^{-1}) and T is the temperature (Kelvin). Water uptake of the GO membrane is estimated my keeping the GO membrane in humidified chamber for an hour where humidified N_2 gas is continuously purged. The water uptake value is calculated by the following equation:

$$\text{Water uptake} = (W_{wet} - W_{dry}/\ W_{dry})*100 \qquad (4a.\ 4)$$

where, W_{wet} is the weight of the wet membrane before keeping the membrane in the humidified chamber for an hour and W_{dry} is the weight of the dry membrane.

4a.2.4 MEA preparation and PEM water electrolyzer assembly

The catalyst inks for cathode Pt/C (3 mg cm^{-2}) and anode IrO$_2$ (3 mg cm^{-2}) were prepared by ultrasonicating with isopropanol with 5 wt% Nafion solution. The inks were sprayed on either side of the graphene oxide paper. Toray carbon gas diffusion electrode was used on Pt/C side and titanium mesh was used on the IrO$_2$ side. Membrane electrode assembly (MEA) was constructed by sandwiching the GO membrane between the anodic and cathodic electrocatalysts. The assembly was subsequently hot-pressed at a pressure of 10 MPa at 50 °C for 5 min. MEA was placed between two graphite blocks with an active electrode area of 1 cm^2 formed by the serpentine gas flow channels. N_2 gas at a flow rate of 0.1 dm^3 min^{-1} was used as the carrier gas to carry water vapor to the anode at different relative humidity values. Water vapor was supplied to the PEM water electrolyzer by purging the N_2 gas (0.1 dm^3 min^{-1}) through a water bubbler maintained at different temperatures. The temperature of the bubbler was varied to maintain the required relative

humidity of N_2 carrier gas. Produced H_2 and O_2 were quantified using water displacement method.

4a.3   Results and discussion

### 4a.3.1   Physiochemical characterizations of GO

GO was prepared by improved Hummer's method (see the experimental section).[77,78] The synthesized GO membrane was then characterized by different physicochemical techniques. Atomic force microscopy (AFM) suggests GO flakes of ~3-4 nm thickness (Figure 4a.1a) and Raman analysis shows the presence of defect and graphitic bands respectively at ~1350 cm^{-1} and ~1590 cm^{-1} with an I_D/I_G ratio (intensity of defect band/intensity of graphitic band) of ~0.9 signaling the formation of GO,[83, 84] Figure 4a.1b. The FTIR spectra of GO shows rich presence of hydrophilic functionalities like -OH, -C-O, C-O-C, -COOH, -C=O etc., suggesting the oxidation of the starting material graphite, Figure 4a.1c. These peaks in FTIR spectra of GO typically appear due to the chemical exfoliation and oxidation of graphitic layers. The broad peak around ~3000 cm^{-1} in GO corresponds to -OH stretching vibration. The peak at ~1730 cm^{-1} is attributed to -C=O stretching vibration from the carboxyl group. Peaks at ~1200 cm^{-1} and ~1000 cm^{-1} are generally because of stretching vibrations of -C-OH and -C-O respectively.[85-87] X-ray diffraction patterns demonstrate the disappearance of intense diffraction pattern of graphite at 2θ value of ~26° (002 plane) and the appearance of a downshifted diffraction pattern at 2θ value close to ~10° (001 plane) after the exfoliation process which signals the formation of GO (Figure 4a.1d). All these suggest the exfoliation of graphite planes on oxidation and the formation of GO.[88,89] Thermogravimetric analysis (TGA) of GO suggests the weight loss till 200°C due to the loss of bound and free water molecules and weight loss after ~200°C is due to the pyrolysis of oxygen rich functionalities (Figure 4a.1e) which are in line with the literature.[90, 91] Contact angle images of starting material graphite while evidencing a relatively hydrophobic surface (contact angle ~116°), the final GO product revealed a relatively hydrophilic surface (contact angle ~46°), pointing to the dense presence of hydrophilic functionalities in GO (Figure 4a.1f). All these further supports the successful formation of graphene oxide from graphite.
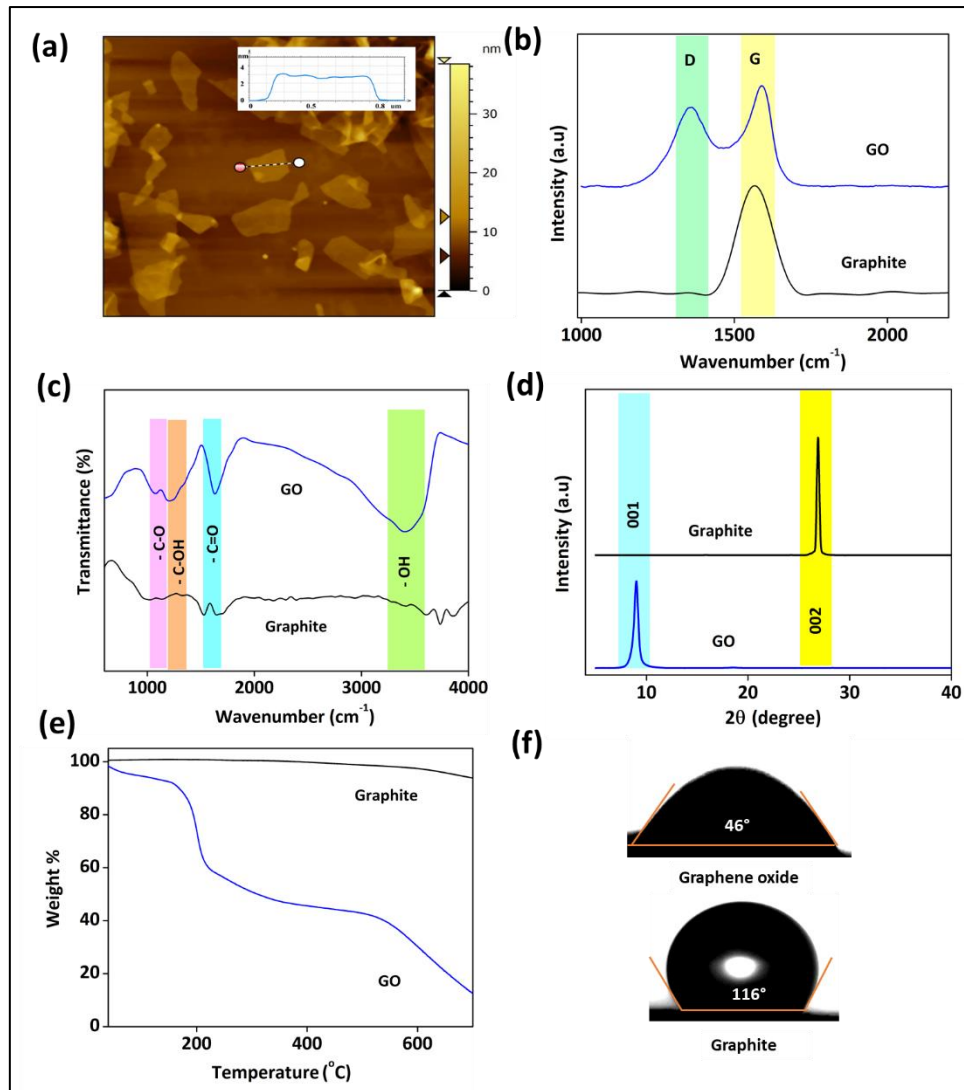
Figure 4a.1 (a) AFM image, (b) Raman spectra, (c) FTIR spectra, (d) XRD (e) thermogravimetric analysis (TGA) and (f) contact angle images of GO and starting material graphite.

As prepared GO flakes were dispersed in water by sonicating it for several minutes and then cast as membrane on smooth petri dish by allowing the solvent to evaporate under ambient conditions. After that membrane was peeled off from the petri dish and used for thickness and conductivity measurements. The membrane thickness was optimized by controlling the volume and weight percent of GO in the dispersion used for coating. For all the experiments a GO membrane of ~50 μm was used, Figure 4a.2a. The room temperature proton conductivity of this membrane determined from electrochemical impedance spectroscopy is ~0.01 mS cm^{-1}, Figure 4a.2b. Though the proton conductivity is lower for GO compared to Nafion 212 of approximately similar thickness, Figure 4a.2c, the ease of production GO coupled with the ease of fabrication of the GO membrane make it a competing candidate for energy conversion devices. Further, the activation

energy of GO membrane which indicates the ability of GO membrane to shuttle the protons through its hydrophilic functionalities, was estimated from Arrhenius plot (Figure 4a.2d), which is found to be ~30 kJ mol^{-1} in line with the literature.[81,82] Ion exchange capacity (IEC) value of GO membrane was evaluated using acid-base titration to understand how much protons the hydrophilic functionalities of GO can hold per gram of the material which in turn reflects the number of ion exchange moieties present in the membrane.[79,80] The IEC value GO is ~3 meq g^{-1} which is ~33 % of what is reported for Nafion 212, Figure 4a.2e. All these indicate the ability of GO membrane to function as a proton exchange membrane in electrolyzers and fuel cells.[92-95]
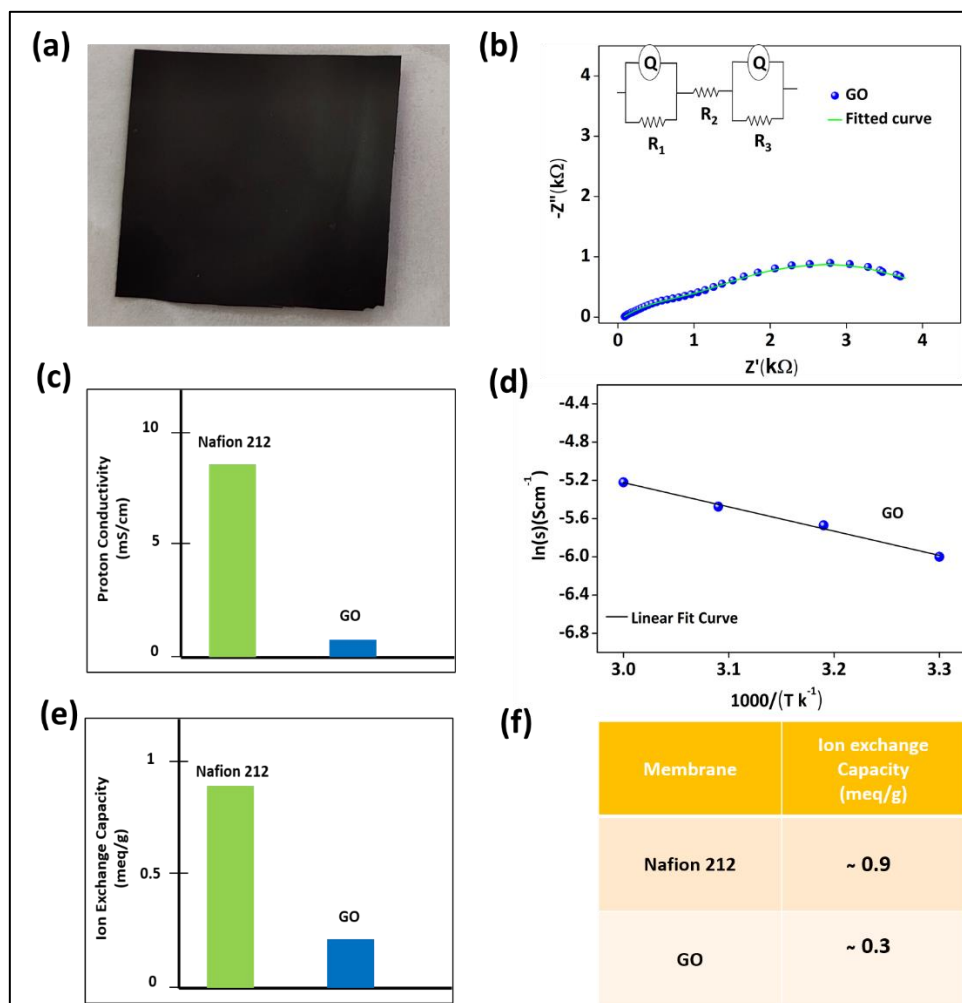
Figure 4a.2 (a) Photograph of free-standing GO membrane of thickness ~50 μm, (b) electrochemical impedance analysis of GO membrane in the frequency range of 100 kHz to 10 mHz with a 10 mV AC excitation signal (inset shows the corresponding fitting circuit), (c) proton conductivities of Nafion 212 and GO membrane, (d) Arrhenius plot for the GO membrane in the temperature range of 30 °C to 60 °C (e) and (f) ion exchange capacity of the Nafion 212 and GO membranes.

After confirming the reasonable proton conductivity of GO membrane, a membrane electrode assembly (MEA) was fabricated with GO membrane as follows. Pt/C catalyst at a loading of 3 mg cm^{-2} was coated on one side of the membrane as hydrogen evolution reaction (HER) catalyst. The opposite side of GO membrane was coated with IrO$_2$ as oxygen evolution reaction (OER) catalyst at a loading of 3 mg cm^{-2}. A Toray carbon gas diffusion layer was employed on HER side and a Titanium (Ti) mesh was employed on the OER side and the whole assembly was hot pressed at a pressure of 10 MPa at a temperature of 50 °C for 5 minutes to form the MEA. The hydrogen half-cell was completely air tight to prevent access of air and the oxygen half-cell was connected to humidified N$_2$ chamber, Scheme 4a.1a. N$_2$ gas at a flow rate of 0.1 dm^3 min^{-1} was used as the carrier gas to carry water vapor from the water bubbler to the anode at different relative humidity. The temperature of bubbler was varied to maintain the different relative humidity of N$_2$ gas. For the constructing an atmospheric water electrolyzer, the device anode was open to the ambient air, Scheme 4a.1b. The photographs of GO MEA is shown in Figure 4a.3a. The SEM cross sectional images show a well contacted GO interface with the catalyst layers, Figure 4a.3b and Figure 4a.3c.
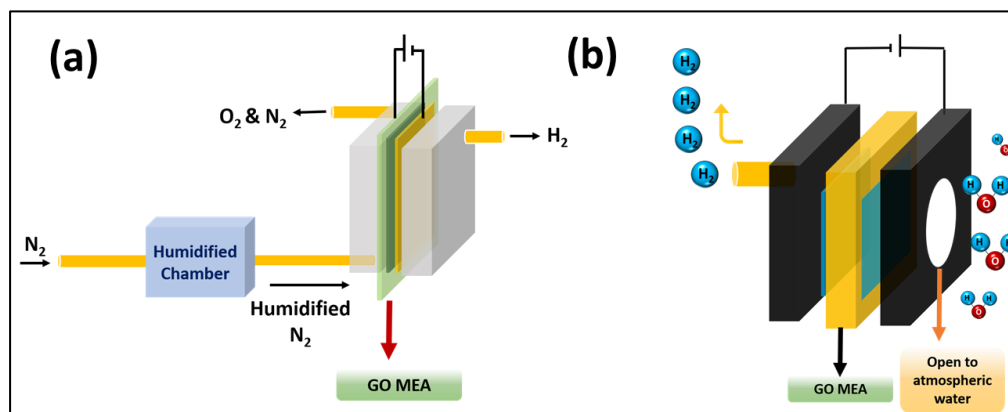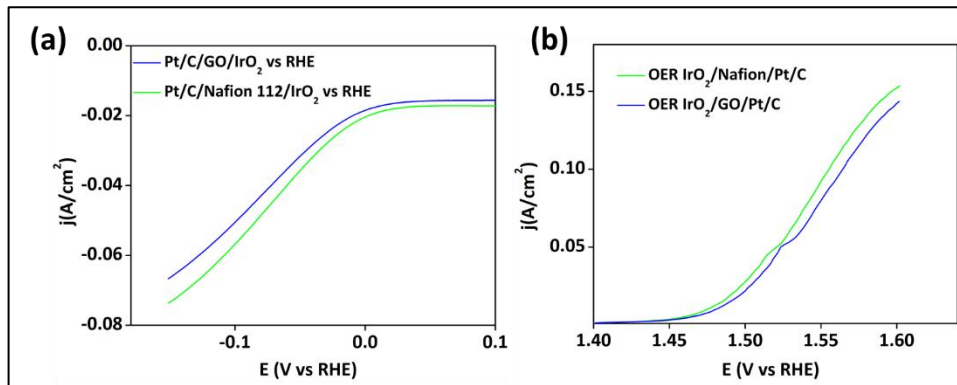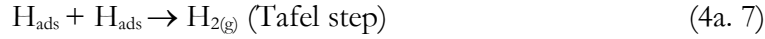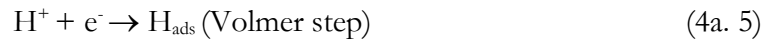

Scheme 4a. 1. (a) Schematic representation of the GO based water vapor electrolyzer where the anodic half-cell is connected to humidified N$_2$ gas at a flow rate of 0.1 dm^3 min^{-1}. (b) For the atmospheric water electrolyzer the anodic half-cell was open to air.
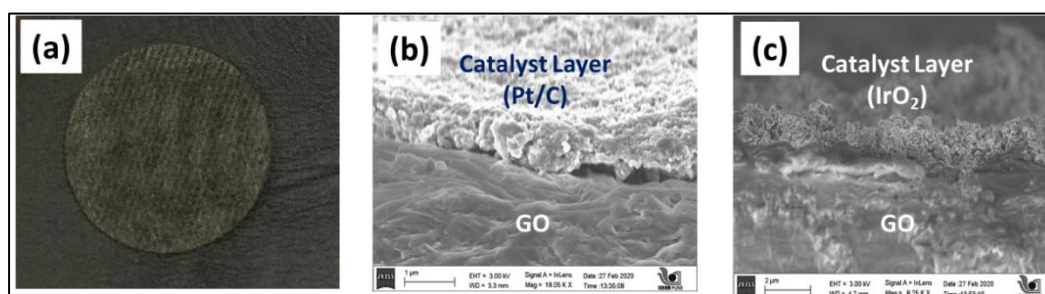
Pt/C and IrO_2 were chosen as electrocatalysts to the water vapor electrolyzer as they are well known HER and OER catalysts respectively.[96-98] Linear sweep voltammograms for HER on Pt/C and OER on IrO_2 (Figure 4a.4a & b) were carried out in the same water vapor electrolyzer set up shown in Scheme 4a. 1 to investigate their catalytic capabilities which in turn suggest the ability of former to catalyze HER and latter to catalyze OER. HER is known to occur in multiple steps as shown in equations 4a.5 to 4a.7. The first charge transfer step (Volmer step) is generally fast, and the second charge transfer step (Heyrovsky step) or atom recombination step (Tafel step) is considered to be rate determining step.[99,100] If the Tafel slope in the Tafel plot for HER comes under the range of 30-39 mV/dec, it is assumed to follow the Tafel step as the rate limiting step. If the Tafel slope comes 40 mV/dec onwards, it is assumed to follow the Heyrovsky step as the rate limiting step.[101-103]

$$H^+ + e^- \rightarrow H_{ads} \text{ (Volmer step)} \tag{4a. 5}$$

$$H_{ads} + H^+_{aq} + e^- \rightarrow H_{2(g)} \text{ (Heyrovsky step)} \tag{4a. 6}$$

$$H_{ads} + H_{ads} \rightarrow H_{2(g)} \text{ (Tafel step)} \tag{4a. 7}$$

Figure 4a.4 (a) HER on Pt/C and (b) OER on IrO_2 collected in the electrolysis set up shown in Scheme 4a.1a.

To construct an efficient practical water vapor electrolyzer, the most critical prerequisite of the membrane is its ability to pre-concentrate water near the electrocatalysts in humid atmosphere. Only when the membrane is able to do so, the electrocatalysts will be able to access the water molecules to perform the desired electrochemical reactions such as OER and HER efficiently. GO membrane has abundance of oxygen rich hydrophilic functionalities like -OH, -C-O, C-O-C, -COOH, -C=O etc., as shown in

Figure 4a.1c. which further contributes to its proton conduction capability.[76] Oxygen rich functionalities in the GO structure widen the interlayer distance between the stacked graphene layers (Figure 4a.1d) which can facilitate the incorporation of water molecules at the interlayers through hydrogen bonding interactions.[104,105] This trapped water molecules are physically adsorbed without forming any chemical bond which further removes the possibility of change in GO's physical properties. This adsorption of water molecules in GO suggest that the adsorbed water molecules are in equilibrium with the surrounding water molecules.[76] Thus, water adsorption capacity or water uptake is an important membrane parameter to define it utility to construct an efficient water vapor electrolyzer. We have estimated the water uptake of GO membrane at different relative humidity (see the experimental section). Water uptake values of GO membrane at 50 % relative humidity is ∼12 % and at 80% relative humidity is ∼57 %. These values are much higher than Nafion 212 membrane which shows the water uptake values at 50 % relative humidity of ∼6 % and at ∼80 % relative humidity of ∼11 %, Figure 4a.5a. This indicates the water holding capacities of the GO membrane is much superior than Nafion 212 membrane due to the higher density of the oxygen rich functionalities. The water holding capacity of the GO membrane is further demonstrated by the down shifting of 2θ value corresponding to the 001 plane of GO when it was incubated in humid atmosphere, XRD pattern, Figure 4a.5b.
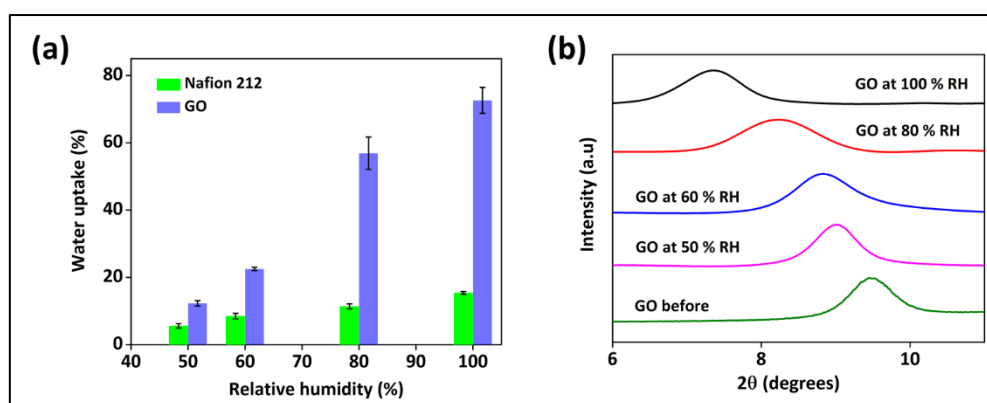
Figure 4a.5 (a) Water uptake of Nafion 212 and GO membrane and (b) XRD of GO demonstrating the downshifting of 001 plane when relative humidity is increased.

4a.3.2 Electrochemical performance of GO membrane-based water vapor electrolyzer

Since GO shows promising characteristics to construct a water vapor electrolyzer because of its water holding capacity and reasonably good proton conduction capability, a GO based MEA was constructed as explained earlier by spray coating Pt/C catalyst

dispersion on one side of the GO membrane and IrO_2 catalyst dispersion on the opposite face. To investigate the electrochemical performance of GO membrane-based water vapor electrolyzer, humidified N_2 was supplied to the anodic side as shown in Scheme 4a.1. On the application of an external potential, the water vapors present in humidified N_2 should be oxidized into O_2 on IrO_2 catalyst liberating protons which will migrate through the GO membrane to the Pt/C cathode catalyst layer where it should be reduced to H_2 as shown in equations 4a.8 and 4a.9. Current-voltage characteristics of water electrolyzer was investigated at different relative humidity to investigate the performance of GO based wat-
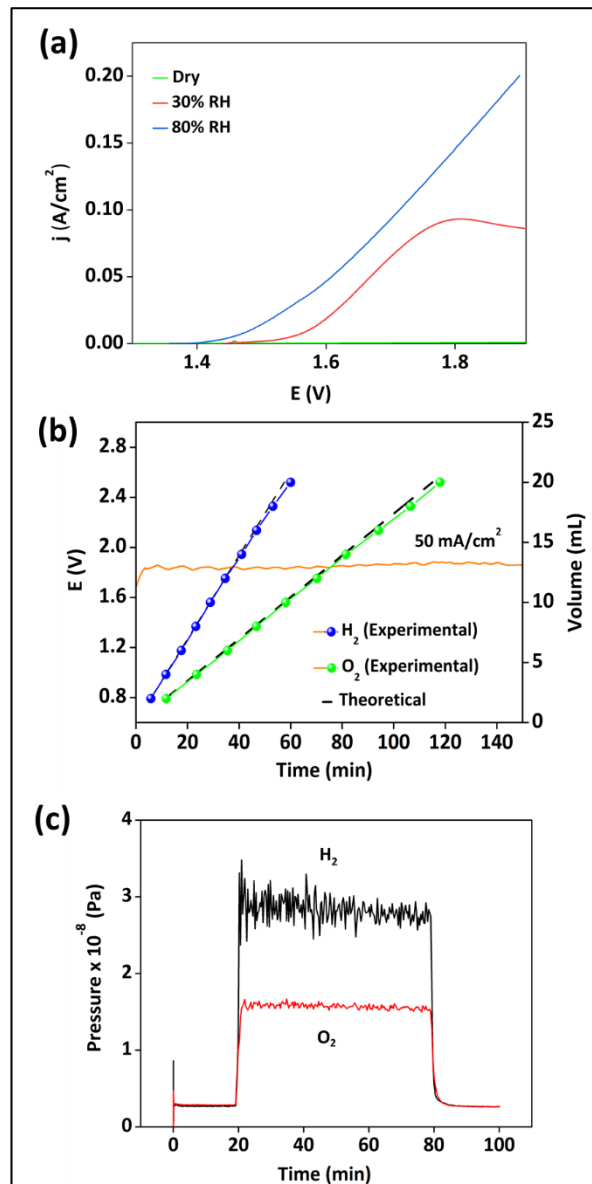
Figure 4a.6. (a) Polarization curves at different relative humidity for the GO based water vapor electrolyzer. (b) Galvanostatic polarization at 50 mA cm^{-2} current density with H_2 and O_2 quantification and (c) in-situ electrochemical mass spectrometric analysis of evolved H_2 and O_2.

-er vapor electrolyzer, Figure 4a.6a. Clearly, on increasing the relative humidity, the electrochemical performance of the device is enhanced, Figure 4a.6a, suggesting that water molecules are the species involved in the electrochemical reactions.

Anodic reaction: $2H_2O \rightarrow 4H^+ + O_2 + 4\,e^-$ (4a.8)

Cathodic reaction: $4H^+ + 4\,e^- \rightarrow 2H_2$ (4a.9)
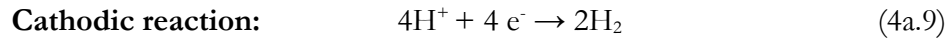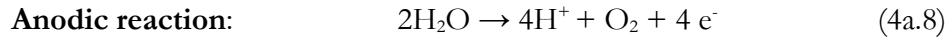
To quantify the evolved gases, galvanostatic polarization techniques were employed and the evolved gaseous species were collected by water displacement technique, Figure 4a.6b and Figure 4a.6c. The stoichiometry of the evolved gases during the electrolysis period was 2:1 and to further characterize these evolved gases, in-situ electrochemical mass spectrometric analysis was employed, which indeed demonstrates that evolved gases are H_2 and O_2 with a stoichiometry of 2:1 between H_2 and O_2, Figure 4a.6c.
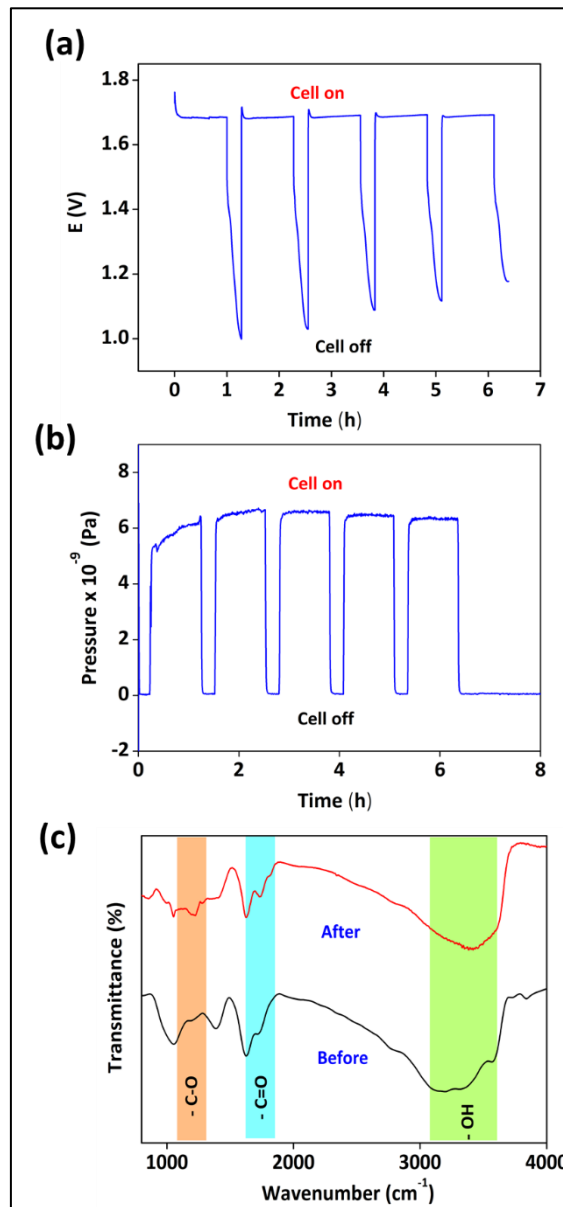
Figure 4a.7: (a) The voltage-time characteristics when the electrolyzer is ON (at 50 mA cm^{-2} current density) and OFF alternatively and (b) in-situ electrochemical mass spectrometric analysis of evolved H$_2$ from the cathode when the electrolyzer is in the ON-OFF modes. (c) FTIR analysis of GO before and after the long-term galvanostatic tests.

To investigate the long-term stability of the GO based water vapor electrolyzer, galvanostatic polarization analysis was carried out by keeping the electrolyzer alternatively in the ON mode and OFF mode, Figure 4a.7a. The cell was kept ON for an hour during the electrolysis and then it was kept off for almost 6 h and this process was repeated for multiple cycles. Clearly, the voltage required during the electrolysis when the cell was ON is almost constant during cycling which highlights the stability of the GO membrane-based water vapor electrolyzer, Figure 4a.7a. This is supported by the in-situ electrochemical mass spectrometry when the device is in the ON-OFF modes, which evidence an approximately constant partial pressure of hydrogen when the cell is ON during continuous cycling of the electrolyzer, Figure 4a.7b. Post characterization study indicates the oxygen rich functi-
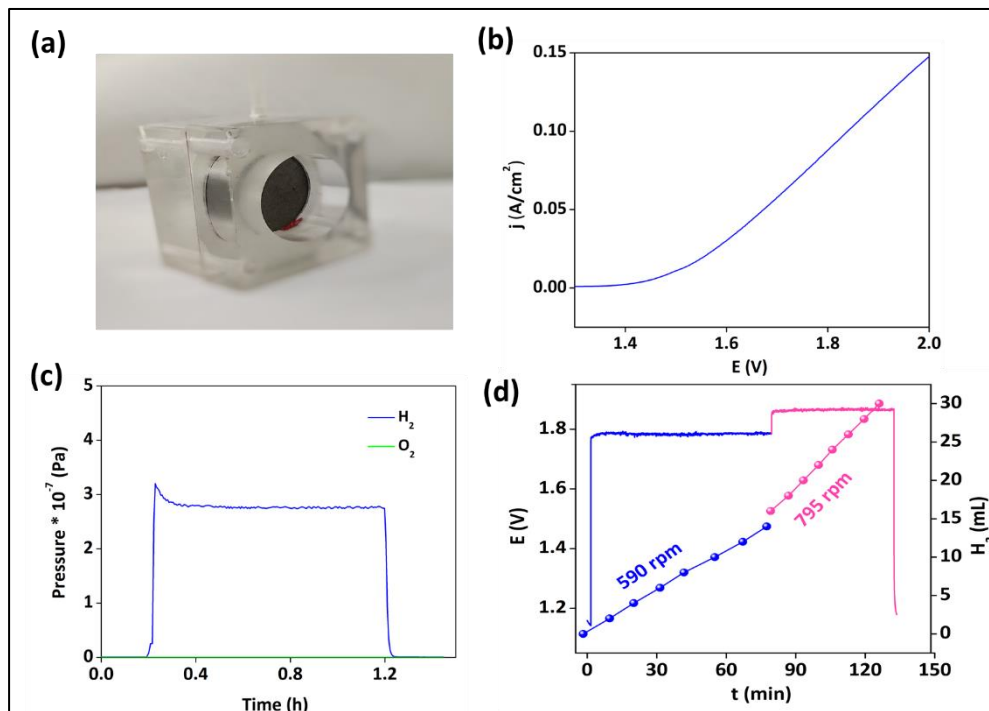
Figure 4a.8: (a) Photograph of the set-up of GO based atmospheric water electrolyzer, (b) polarization curve for the GO based atmospheric water electrolyzer, (c) in-situ electrochemical mass spectrometric analysis of evolved H$_2$ from the cathode and (d) voltage-time characteristics with H$_2$ quantifications when electrolyzer is driven by a windmill at different RPM.

-onalities of GO membrane were intact during this long-term cycling, Figure 4a.7d. All of these studies highlight that GO can be utilized as proton exchange membrane in water

vapor electrolyzers and therefore efforts were dedicated at constructing an atmospheric water electrolyzer. For this, the anode was kept open to the air as shown in Scheme 4a.1b and Figure 4a.8a. The polarization curve of the electrolyzer shows a current density of 150 mA cm^{-2} at a terminal voltage of ~2 V, Figure 4a.8b. The evolved gas was proven to be H$_2$ from the cathodic side, in-situ electrochemical mass spectrometry, Figure 4a.8c. Finally, an atmospheric water electrolyzer device was constructed to harvest the renewable energy, Figure 4a.8d, wherein earth's atmosphere provides a universal feedstock of water which can potentially be converted into molecular fuel via electrochemical processes coupled to renewable energy. Constant current test shows a stable performance, and the quantification suggest H$_2$ is evolved with nearly 100% faradaic efficiency, Figure 4a.8d.

4a.4   Conclusions

In this Chapter, we have shown a GO based atmospheric water vapor electrolyzer. The polarization performance of GO shows a current density of ~80 mA cm^{-2} at 80 % relative humidity and at a terminal potential of ~2 V. The stoichiometry of evolved H$_2$ and O$_2$ gases were 2:1 indicating the near absence of parasitic chemistry, certifying the GO is an effective barrier for molecular fuels and it can conduct protons. The long term galvanostatic polarization indicates that the electrolyzer can be cycled multiple times which indicates the stability of GO membrane in the long run. Post electrochemical characterization study highlights the hydrophilic functionalities of GO membrane which are responsible for proton conduction are intact even after the long-term galvanostatic analysis. All these studies make GO a useful candidate for constructing an atmospheric water electrolyzer wherein earth's atmosphere provides a universal feedstock of water which can potentially be converted into molecular fuel via electrochemical processes coupled to renewable energy.

4a.5   References

1.   Parkinson, B., Advantages of Solar Hydrogen Compared to Direct Carbon Dioxide Reduction for Solar Fuel Production. *ACS Energy Lett.* **2016,** *1* (5), 1057-1059.

2.   Rosen, M. A.; Koohi-Fayegh, S., The prospects for hydrogen as an energy carrier: an overview of hydrogen energy and hydrogen energy systems. *Energ. Ecol. Environ.* **2016,** *1* (1), 10-29.

3. Pareek, A.; Dom, R.; Gupta, J.; Chandran, J.; Adepu, V.; Borse, P. H., Insights into renewable hydrogen energy: Recent advances and prospects. *Mater. Sci. Technol.* **2020,** *3*, 319-327.

4. Martin-Martinez, F. J.; Jin, K.; López Barreiro, D.; Buehler, M. J., The Rise of Hierarchical Nanostructured Materials from Renewable Sources: Learning from Nature. *ACS Nano* **2018,** *12* (8), 7425-7433.

5. Mitrova, T.; Melnikov, Y.; Chugunov, D., *The Hydrogen Economy- a path towards low carbon development.* **2019**.

6. van Bavel, S.; Verma, S.; Negro, E.; Bracht, M., Integrating CO2 Electrolysis into the Gas-to-Liquids–Power-to-Liquids Process. *ACS Energy Lett.* **2020,** *5* (8), 2597-2601.

7. Liguori, S.; Kian, K.; Buggy, N.; Anzelmo, B. H.; Wilcox, J., Opportunities and challenges of low-carbon hydrogen via metallic membranes. *Prog. Energy Combust. Sci.* **2020,** *80*, 100851.

8. Lubitz, W.; Tumas, W., Hydrogen: An Overview. *Chem. Rev.* **2007,** *107* (10), 3900-3903.

9. Hibino, T.; Kobayashi, K.; Ito, M.; Ma, Q.; Nagao, M.; Fukui, M.; Teranishi, S., Efficient Hydrogen Production by Direct Electrolysis of Waste Biomass at Intermediate Temperatures. *ACS Sustain. Chem. Eng.* **2018,** *6* (7), 9360-9368.

10. Staffell, I.; Scamman, D.; Velazquez Abad, A.; Balcombe, P.; Dodds, P. E.; Ekins, P.; Shah, N.; Ward, K. R., The role of hydrogen and fuel cells in the global energy system. *Energy Environ. Sci.* **2019,** *12* (2), 463-491.

11. Rand, D. A. J., A journey on the electrochemical road to sustainability. *J. Solid State Electrochem.* **2011,** *15* (7), 1579-1622.

12. Acar, C.; Dincer, I., Comparative assessment of hydrogen production methods from renewable and non-renewable sources. *Int. J. Hydrogen Energy* **2014,** *39* (1), 1--12.

13. Züttel, A., Hydrogen storage methods. *Naturwissenschaften* **2004,** *91* (4), 157-172.

14. Trane, R.; Dahl, S.; Skjøth-Rasmussen, M. S.; Jensen, A. D., Catalytic steam reforming of bio-oil. *Int. J. Hydrogen Energy* **2012,** *37* (8), 6447-6472.

15. Rahimpour, M. R.; Jafari, M.; Iranshahi, D., Progress in catalytic naphtha reforming process: A review. *Appl. Energy* **2013,** *109*, 79-93.

16. Abdul Mujeebu, M., Hydrogen and syngas production by superadiabatic combustion – A review. *Appl. Energy* **2016,** *173*, 210-224.

17. Wang, D.; Czernik, S.; Chornet, E., Production of Hydrogen from Biomass by Catalytic Steam Reforming of Fast Pyrolysis Oils. *Energy & Fuels* **1998,** *12* (1), 19-24.

18. Marquevich, M.; Czernik, S.; Chornet, E.; Montané, D., Hydrogen from Biomass: Steam Reforming of Model Compounds of Fast-Pyrolysis Oil. *Energy & Fuels* **1999,** *13* (6), 1160-1166.

19. Shagdar, E.; Lougou, B. G.; Shuai, Y.; Ganbold, E.; Chinonso, O. P.; Tan, H., Process analysis of solar steam reforming of methane for producing low-carbon hydrogen. *RSC Adv.* **2020,** *10* (21), 12582-12597.

20. Navarro, R. M.; Sánchez-Sánchez, M. C.; Alvarez-Galvan, M. C.; Valle, F. d.; Fierro, J. L. G., Hydrogen production from renewable sources: biomass and photocatalytic opportunities. *Energy Environ. Sci.* **2009,** *2* (1), 35-54.

21. Hosseini, S. E.; Abdul Wahid, M.; Jamil, M. M.; Azli, A. A. M.; Misbah, M. F., A review on biomass-based hydrogen production for renewable energy supply. *Int. J. Energy Res.* **2015,** *39* (12), 1597-1615.

22.   Ren, S.; Lei, H.; Wang, L.; Bu, Q.; Chen, S.; Wu, J., Hydrocarbon and hydrogen-rich syngas production by biomass catalytic pyrolysis and bio-oil upgrading over biochar catalysts. *RSC Adv.* **2014,** *4* (21), 10731-10737.

23.   Nizamuddin, S.; Baloch, H. A.; Griffin, G. J.; Mubarak, N. M.; Bhutto, A. W.; Abro, R.; Mazari, S. A.; Ali, B. S., An overview of effect of process parameters on hydrothermal carbonization of biomass. *Renew. Sustain. Energy Rev* **2017,** *73*, 1289-1299.

24.   Chiesa, P.; Consonni, S.; Kreutz, T.; Robert, W., Co-production of hydrogen, electricity and CO_2 from coal with commercially ready technology. Part A: Performance and emissions. *Int. J. Hydrogen Energy* **2005,** *30* (7), 747-767.

25.   Cesar, I.; Kay, A.; Gonzalez Martinez, J. A.; Grätzel, M., Translucent Thin Film Fe_2O_3 Photoanodes for Efficient Water Splitting by Sunlight: Nanostructure-Directing Effect of Si-Doping. *J. Am. Chem. Soc.* **2006,** *128* (14), 4582-4583.

26.   Wang, J.; Cui, W.; Liu, Q.; Xing, Z.; Asiri, A. M.; Sun, X., Recent Progress in Cobalt-Based Heterogeneous Catalysts for Electrochemical Water Splitting. *Adv. Mater.* **2016,** *28* (2), 215-230.

27.   Yan, Y.; Xia, B. Y.; Zhao, B.; Wang, X., A review on noble-metal-free bifunctional heterogeneous catalysts for overall electrochemical water splitting. *J. Mater. Chem. A* **2016,** *4* (45), 17587-17603.

28.   Li, X.; Hao, X.; Abudula, A.; Guan, G., Nanostructured catalysts for electrochemical water splitting: current state and prospects. *J. Mater. Chem. A* **2016,** *4* (31), 11973-12000.

29.   Tan, Y.; Wang, H.; Liu, P.; Shen, Y.; Cheng, C.; Hirata, A.; Fujita, T.; Tang, Z.; Chen, M., Versatile nanoporous bimetallic phosphides towards electrochemical water splitting. *Energy Environ. Sci.* **2016,** *9* (7), 2257-2261.

30.   Anantharaj, S.; Ede, S. R.; Sakthikumar, K.; Karthick, K.; Mishra, S.; Kundu, S., Recent Trends and Perspectives in Electrochemical Water Splitting with an

Emphasis on Sulfide, Selenide, and Phosphide Catalysts of Fe, Co, and Ni: A Review. *ACS Catal.* **2016,** *6* (12), 8069-8097.

31. Zhang, J.; Dai, L., Nitrogen, Phosphorus, and Fluorine Tri-doped Graphene as a Multifunctional Catalyst for Self-Powered Electrochemical Water Splitting. *Angew. Chem. Int. Ed.* **2016,** *55* (42), 13296-13300.

32. Fominykh, K.; Feckl, J. M.; Sicklinger, J.; Döblinger, M.; Böcklein, S.; Ziegler, J.; Peter, L.; Rathousky, J.; Scheidt, E.-W.; Bein, T.; Fattakhova-Rohlfing, D., Ultrasmall Dispersible Crystalline Nickel Oxide Nanoparticles as High-Performance Catalysts for Electrochemical Water Splitting. *Adv. Funct. Mater.* **2014,** *24* (21), 3123-3129.

33. Shiva Kumar, S.; Himabindu, V., Hydrogen production by PEM water electrolysis – A review. *Mater. Sci. Technol.* **2019,** *2* (3), 442-454.

34. Aricò, A. S.; Siracusano, S.; Briguglio, N.; Baglio, V.; Di Blasi, A.; Antonucci, V., Polymer electrolyte membrane water electrolysis: status of technologies and potential applications in combination with renewable power sources. *J. Appl. Electrochem.* **2013,** *43* (2), 107-118.

35. Rozain, C.; Mayousse, E.; Guillet, N.; Millet, P., Influence of iridium oxide loadings on the performance of PEM water electrolysis cells: Part I–Pure IrO$_2$-based anodes. *Appl. Catal. B: Environ.* **2016,** *182*, 153-160.

36. Wei, G.; Xu, L.; Huang, C.; Wang, Y., SPE water electrolysis with SPEEK/PES blend membrane. *Int. J. Hydrogen Energy* **2010,** *35* (15), 7778-7783.

37. Zhang, G.; Feng, Y.-S.; Lu, W.-T.; He, D.; Wang, C.-Y.; Li, Y.-K.; Wang, X.-Y.; Cao, F.-F., Enhanced Catalysis of Electrochemical Overall Water Splitting in Alkaline Media by Fe Doping in Ni$_3$S$_2$ Nanosheet Arrays. *ACS Catal.* **2018,** *8* (6), 5431-5441.

38. Li, X.; Zhao, L.; Yu, J.; Liu, X.; Zhang, X.; Liu, H.; Zhou, W., Water Splitting: From Electrode to Green Energy System. *Nanomicro Lett.* **2020,** *12* (1), 131.

39.   Peng, Y.; Jiang, K.; Hill, W.; Lu, Z.; Yao, H.; Wang, H., Large-Scale, Low-Cost, and High-Efficiency Water-Splitting System for Clean H₂ Generation. *ACS Appl. Mater. Interfaces* **2019,** *11* (4), 3971-3977.

40.   Oener, S. Z.; Ardo, S.; Boettcher, S. W., Ionic Processes in Water Electrolysis: The Role of Ion-Selective Membranes. *ACS Energy Lett.* **2017,** *2* (11), 2625-2634.

41.   Huang, J.; Wang, Y., Efficient Renewable-to-Hydrogen Conversion via Decoupled Electrochemical Water Splitting. *Cell Reports Physical Science* **2020,** *1* (8), 100138.

42.   Scott, K., Chapter 1 Introduction to Electrolysis, Electrolysers and Hydrogen Production. In *Electrochemical Methods for Hydrogen Production*, The Royal Society of Chemistry: **2020**, 1-27.

43.   Sun, X.; Ding, R., Recent progress with electrocatalysts for urea electrolysis in alkaline media for energy-saving hydrogen production. *Catal. Sci. Technol.* **2020,** *10* (6), 1567-1581.

44.   Albert, A.; Barnett, A. O.; Thomassen, M. S.; Schmidt, T. J.; Gubler, L., Radiation-Grafted Polymer Electrolyte Membranes for Water Electrolysis Cells: Evaluation of Key Membrane Properties. *ACS Appl. Mater. Interfaces* **2015,** *7* (40), 22203-22212.

45.   Giovanni, C. D.; Reyes-Carmona, Á.; Coursier, A.; Nowak, S.; Grenèche, J. M.; Lecoq, H.; Mouton, L.; Rozière, J.; Jones, D.; Peron, J.; Giraud, M.; Tard, C., Low-Cost Nanostructured Iron Sulfide Electrocatalysts for PEM Water Electrolysis. *ACS Catal.* **2016,** *6* (4), 2626-2631.

46.   Shi, Y.; Lu, Z.; Guo, L.; Yan, C., Fabrication of membrane electrode assemblies by direct spray catalyst on water swollen Nafion membrane for PEM water electrolysis. *Int. J. Hydrogen Energy* **2017,** *42* (42), 26183-26191.

47.   Klose, C.; Trinke, P.; Böhm, T.; Bensmann, B.; Vierrath, S.; Hanke-Rauschenbach, R.; Thiele, S., Membrane Interlayer with Pt Recombination

Particles for Reduction of the Anodic Hydrogen Content in PEM Water Electrolysis. *J. Electrochem. Soc.* **2018,** *165* (16), F1271-F1277.

48.   Xu, T., Ion exchange membranes: State of their development and perspective. *J. Membr. Sci.* **2005,** *263* (1), 1-29.

49.   Spurgeon, J. M.; Lewis, N. S., Proton exchange membrane electrolysis sustained by water vapor. *Energy Environ. Sci.* **2011,** *4* (8), 2993-2998.

50.   Hernández-Flores, G.; Poggi-Varaldo, H. M.; Solorza-Feria, O., Comparison of alternative membranes to replace high cost Nafion ones in microbial fuel cells. *Int. J. Hydrogen Energy* **2016,** *41* (48), 23354-23362.

51.   Patel, H. A.; Mansor, N.; Gadipelli, S.; Brett, D. J. L.; Guo, Z., Superacidity in Nafion/MOF Hybrid Membranes Retains Water at Low Humidity to Enhance Proton Conduction for Fuel Cells. *ACS Appl. Mater. Interfaces* **2016,** *8* (45), 30687-30691.

52.   Simari, C.; Lufrano, E.; Brunetti, A.; Barbieri, G.; Nicotera, I., Highly-performing and low-cost nanostructured membranes based on Polysulfone and layered doubled hydroxide for high-temperature proton exchange membrane fuel cells. *J. Power Sources* **2020,** *471*, 228440.

53.   Tsuneda, T.; Singh, R. K.; Iiyama, A.; Miyatake, K., Theoretical Investigation of the H_2O_2-Induced Degradation Mechanism of Hydrated Nafion Membrane via Ether-Linkage Dissociation. *ACS Omega* **2017,** *2* (7), 4053-4064.

54.   Frühwirt, P.; Kregar, A.; Törring, J. T.; Katrašnik, T.; Gescheidt, G., Holistic approach to chemical degradation of Nafion membranes in fuel cells: modelling and predictions. *Phys Chem Chem Phys* **2020,** *22* (10), 5647-5666.

55.   Kinumoto, T.; Inaba, M.; Nakayama, Y.; Ogata, K.; Umebayashi, R.; Tasaka, A.; Iriyama, Y.; Abe, T.; Ogumi, Z., Durability of perfluorinated ionomer membrane against hydrogen peroxide. *Journal of Power Sources* **2006,** *158* (2), 1222-1228.

56. Chen, C.; Levitin, G.; Hess, D. W.; Fuller, T. F., XPS investigation of Nafion® membrane degradation. *J. Power Sources* **2007,** *169* (2), 288-295.

57. Yu, T. H.; Sha, Y.; Liu, W.-G.; Merinov, B. V.; Shirvanian, P.; Goddard, W. A., Mechanism for Degradation of Nafion in PEM Fuel Cells from Quantum Mechanics Calculations. *J. Am. Chem. Soc.* **2011,** *133* (49), 19857-19863.

58. Murthy, A. P.; Theerthagiri, J.; Madhavan, J., Highly Water Dispersible Polymer Acid-Doped Polyanilines as Low-Cost, Nafion-Free Ionomers for Hydrogen Evolution Reaction. *ACS Appl. Energy Mater.* **2018,** *1* (4), 1512-1521.

59. Reurink, D. M.; te Brinke, E.; Achterhuis, I.; Roesink, H. D. W.; de Vos, W. M., Nafion-Based Low-Hydration Polyelectrolyte Multilayer Membranes for Enhanced Water Purification. *ACS Appl. Polym. Mater.* **2019,** *1* (9), 2543-2551.

60. Vinothkannan, M.; Ramakrishnan, S.; Kim, A. R.; Lee, H.-K.; Yoo, D. J., Ceria Stabilized by Titanium Carbide as a Sustainable Filler in the Nafion Matrix Improves the Mechanical Integrity, Electrochemical Durability, and Hydrogen Impermeability of Proton-Exchange Membrane Fuel Cells: Effects of the Filler Content. *ACS Appl. Mater. Interfaces* **2020,** *12* (5), 5704-5716.

61. Feng, K.; Tang, B.; Wu, P., Ammonia-assisted dehydrofluorination between PVDF and Nafion for highly selective and low-cost proton exchange membranes: a possible way to further strengthen the commercialization of Nafion. *J. Mater. Chem.* **2015,** *3* (24), 12609-12615.

62. Giancola, S.; Zatoń, M.; Reyes-Carmona, Á.; Dupont, M.; Donnadio, A.; Cavaliere, S.; Rozière, J.; Jones, D. J., Composite short side chain PFSA membranes for PEM water electrolysis. *J. Membr. Sci.* **2019,** *570-571*, 69-76.

63. Siracusano, S.; Baglio, V.; Lufrano, F.; Staiti, P.; Aricò, A. S., Electrochemical characterization of a PEM water electrolyzer based on a sulfonated polysulfone membrane. *J. Membr. Sci.* **2013,** *448*, 209-214.

64. Linkous, C. A.; Anderson, H. R.; Kopitzke, R. W.; Nelson, G. L., Development of new proton exchange membrane electrolytes for water electrolysis at higher temperatures. *Int. J. Hydrogen Energy* **1998,** *23* (7), 525-529.

65. Frensch, S. H.; Serre, G.; Fouda-Onana, F.; Jensen, H. C.; Christensen, M. L.; Araya, S. S.; Kær, S. K., Impact of iron and hydrogen peroxide on membrane degradation for polymer electrolyte membrane water electrolysis: Computational and experimental investigation on fluoride emission. *J. Power Sources* **2019,** *420*, 54-62.

66. Sood, R.; Cavaliere, S.; Jones, D. J.; Rozière, J., Electrospun nanofibre composite polymer electrolyte fuel cell and electrolysis membranes. *Nano Energy* **2016,** *26*, 729-745.

67. Aili, D.; Hansen, M. K.; Pan, C.; Li, Q.; Christensen, E.; Jensen, J. O.; Bjerrum, N. J., Phosphoric acid doped membranes based on Nafion®, PBI and their blends – Membrane preparation, characterization and steam electrolysis testing. *Int. J. Hydrogen Energy* **2011,** *36* (12), 6985-6993.

68. Mališ, J.; Mazúr, P.; Paidar, M.; Bystron, T.; Bouzek, K., Nafion 117 stability under conditions of PEM water electrolysis at elevated temperature and pressure. *Int. J. Hydrogen Energy* **2016,** *41* (4), 2177-2188.

69. Ito, H.; Maeda, T.; Nakano, A.; Takenaka, H., Properties of Nafion membranes under PEM water electrolysis conditions. *Int. J. Hydrogen Energy* **2011,** *36* (17), 10527-10540.

70. Liu, G.; Xu, J.; Wang, Y.; Wang, X., An oxygen evolution catalyst on an antimony doped tin oxide nanowire structured support for proton exchange membrane liquid water electrolysis. *J. Mater. Chem* **2015,** *3* (41), 20791-20800.

71. Baglio, V.; Ornelas, R.; Matteucci, F.; Martina, F.; Ciccarella, G.; Zama, I.; Arriaga, L. G.; Antonucci, V.; Aricò, A. S., Solid Polymer Electrolyte Water Electrolyser Based on Nafion-TiO2 Composite Membrane for High Temperature Operation. *Fuel Cells* **2009,** *9* (3), 247-252.

72.	Siracusano, S.; Baglio, V.; Nicotera, I.; Mazzapioda, L.; Aricò, A. S.; Panero, S.; Navarra, M. A., Sulfated titania as additive in Nafion membranes for water electrolysis applications. *Int. J. Hydrogen Energy* **2017,** *42* (46), 27851-27858.

73.	Dikin, D. A.; Stankovich, S.; Zimney, E. J.; Piner, R. D.; Dommett, G. H. B.; Evmenenko, G.; Nguyen, S. T.; Ruoff, R. S., Preparation and characterization of graphene oxide paper. *Nature* **2007,** *448* (7152), 457-460.

74.	Zheng, S.; Tu, Q.; Urban, J. J.; Li, S.; Mi, B., Swelling of Graphene Oxide Membranes in Aqueous Solution: Characterization of Interlayer Spacing and Insight into Water Transport Mechanisms. *ACS Nano* **2017,** *11* (6), 6440-6450.

75.	Iakunkov, A.; Talyzin, A. V., Swelling properties of graphite oxides and graphene oxide multilayered materials. *Nanoscale* **2020,** *12* (41), 21060-21093.

76.	Liu, R.; Gong, T.; Zhang, K.; Lee, C., Graphene oxide papers with high water adsorption capacity for air dehumidification. *Sci. Rep.* **2017,** *7* (1), 9761.

77.	Marcano, D. C.; Kosynkin, D. V.; Berlin, J. M.; Sinitskii, A.; Sun, Z.; Slesarev, A.; Alemany, L. B.; Lu, W.; Tour, J. M., Improved Synthesis of Graphene Oxide. *ACS Nano* **2010,** *4* (8), 4806-4814.

78.	Sohail, M.; Saleem, M.; Ullah, S.; Saeed, N.; Afridi, A.; Khan, M.; Arif, M., Modified and improved Hummer's synthesis of graphene oxide for capacitors applications. *Mod. Electron. Mater.* **2017,** *3* (3), 110-116.

79.	Basso Peressut, A.; Latorrata, S.; Gallo Stampino, P.; Dotelli, G., Development of self-assembling sulfonated graphene oxide membranes as a potential proton conductor. *Mater. Chem. Phys.* **2021,** *257*, 123768.

80.	Kumar, R.; Mamlouk, M.; Scott, K., Sulfonated polyether ether ketone – sulfonated graphene oxide composite membranes for polymer electrolyte fuel cells. *RSC Adv.* **2014,** *4* (2), 617-623.

81.   Joseph, J.; Tseng, C.-Y.; Hwang, B.-J., Phosphonic acid-grafted mesostructured silica/Nafion hybrid membranes for fuel cell applications. *J. Power Sources* **2011,** *196* (18), 7363-7371.

82.   Vinothkannan, M.; Kim, A. R.; Gnana kumar, G.; Yoon, J.-M.; Yoo, D. J., Toward improved mechanical strength, oxidative stability and proton conductivity of an aligned quadratic hybrid (SPEEK/FPAPB/Fe$_3$O$_4$-FGO) membrane for application in high temperature and low humidity fuel cells. *RSC Adv.* **2017,** *7* (62), 39034-39048.

83.   Jhajharia, S. K.; Selvaraj, K., Non-templated ambient nanoperforation of graphene: a novel scalable process and its exploitation for energy and environmental applications. *Nanoscale* **2015,** *7* (46), 19705-19713.

84.   Balaji, S.; Balasubramanian, R.; Rigana M, F.; Sarojadevi, M., Influence of graphene oxide on thermal, electrical, and morphological properties of new achiral polyimide. *Polym. Eng. Sci.* **2018,** *58* (5), 691-700.

85.   Emiru, T. F.; Ayele, D. W., Controlled synthesis, characterization and reduction of graphene oxide: A convenient method for large scale production. *Egypt. J. Basic Appl. Sci.* **2017,** *4* (1), 74-79.

86.   Sharma, N.; Sharma, V.; Jain, Y.; Kumari, M.; Gupta, R.; Sharma, S. K.; Sachdev, K., Synthesis and Characterization of Graphene Oxide (GO) and Reduced Graphene Oxide (rGO) for Gas Sensing Application. *Macromol. Symp.* **2017,** *376* (1), 1700006.

87.   Ossonon, B. D.; Bélanger, D., Synthesis and characterization of sulfophenyl-functionalized reduced graphene oxide sheets. *RSC Adv.* **2017,** *7* (44), 27224-27234.

88.   Wojtoniszak, M.; Mijowska, E., Controlled oxidation of graphite to graphene oxide with novel oxidants in a bulk scale. *J. Nanopart. Res.* **2012,** *14* (11), 1248.

89. Shen, J.; Hu, Y.; Shi, M.; Lu, X.; Qin, C.; Li, C.; Ye, M., Fast and Facile Preparation of Graphene Oxide and Reduced Graphene Oxide Nanoplatelets. *Chem. Mater.* **2009,** *21* (15), 3514-3520.

90. Kuila, T.; Mishra, A. K.; Khanra, P.; Kim, N. H.; Lee, J. H., Recent advances in the efficient reduction of graphene oxide and its application as energy storage electrode materials. *Nanoscale* **2013,** *5* (1), 52-71.

91. Gurzęda, B.; Buchwald, T.; Nocuń, M.; Bąkowicz, A.; Krawczyk, P., Graphene material preparation through thermal treatment of graphite oxide electrochemically synthesized in aqueous sulfuric acid. *RSC Adv.* **2017,** *7* (32), 19904-19911.

92. Farooqui, U. R.; Ahmad, A. L.; Hamid, N. A., Graphene oxide: A promising membrane material for fuel cells. *Renew. Sustain. Energy Rev.* **2018,** *82*, 714-733.

93. Nicotera, I.; Simari, C.; Coppola, L.; Zygouri, P.; Gournis, D.; Brutti, S.; Minuto, F. D.; Aricò, A. S.; Sebastian, D.; Baglio, V., Sulfonated Graphene Oxide Platelets in Nafion Nanocomposite Membrane: Advantages for Application in Direct Methanol Fuel Cells. *J. Phys. Chem. C* **2014,** *118* (42), 24357-24368.

94. Jiang, Z.-J.; Jiang, Z.; Tian, X.; Luo, L.; Liu, M., Sulfonated Holey Graphene Oxide (SHGO) Filled Sulfonated Poly(ether ether ketone) Membrane: The Role of Holes in the SHGO in Improving Its Performance as Proton Exchange Membrane for Direct Methanol Fuel Cells. *ACS Appl. Mater. Interfaces* **2017,** *9* (23), 20046-20056.

95. Kim, Y.; Ketpang, K.; Jaritphun, S.; Park, J. S.; Shanmugam, S., A polyoxometalate coupled graphene oxide–Nafion composite membrane for fuel cells operating at low relative humidity. *J. Mater. Chem.* **2015,** *3* (15), 8148-8155.

96. Song, F.; Bai, L.; Moysiadou, A.; Lee, S.; Hu, C.; Liardet, L.; Hu, X., Transition Metal Oxides as Electrocatalysts for the Oxygen Evolution Reaction in Alkaline Solutions: An Application-Inspired Renaissance. *J. Am. Chem. Soc.* **2018,** *140* (25), 7748-7759.

97.   Jana, R.; Chowdhury, C.; Malik, S.; Datta, A., Pt/Co3O4 Surpasses Benchmark Pt/C: An Approach Toward Next Generation Hydrogen Evolution Electrocatalyst. *ACS Appl. Energy Mater.* **2019,** *2* (8), 5613-5621.

98.   Shinde, D. V.; Kokumai, T. M.; Buha, J.; Prato, M.; De Trizio, L.; Manna, L., A robust and highly active hydrogen evolution catalyst based on Ru nanocrystals supported on vertically oriented Cu nanoplates. *J. Mater. Chem.* **2020,** *8* (21), 10787-10795.

99.   Shinagawa, T.; Garcia-Esparza, A. T.; Takanabe, K., Insight on Tafel slopes from a microkinetic analysis of aqueous electrocatalysis for energy conversion. *Sci. Rep.* **2015,** *5* (1), 13801.

100.   Liu, Y.; Mustain, W. E., Evaluation of tungsten carbide as the electrocatalyst support for platinum hydrogen evolution/oxidation catalysts. *Int. J. Hydrogen Energy* **2012,** *37* (11), 8929-8938.

101.   Li, C.; Gao, H.; Wan, W.; Mueller, T., Mechanisms for hydrogen evolution on transition metal phosphide catalysts and a comparison to Pt(111). *Phys. Chem. Chem. Phys* **2019,** *21* (44), 24489-24498.

102.   Schuler, T.; Kimura, T.; Schmidt, T. J.; Büchi, F. N., Towards a generic understanding of oxygen evolution reaction kinetics in polymer electrolyte water electrolysis. *Energy Environ. Sci.* **2020,** *13* (7), 2153-2166.

103.   Guo, Q.; Mao, J.; Huang, J.; Wang, Z.; Zhang, Y.; Hu, J.; Dong, J.; Sathasivam, S.; Zhao, Y.; Xing, G.; Pan, H.; Lai, Y.; Tang, Y., Reducing Oxygen Evolution Reaction Overpotential in Cobalt-Based Electrocatalysts via Optimizing the "Microparticles-in-Spider Web" Electrode Configurations. *Small* **2020,** *16* (8), 1907029.

104.   Robinson, J. T.; Zalalutdinov, M.; Baldwin, J. W.; Snow, E. S.; Wei, Z.; Sheehan, P.; Houston, B. H., Wafer-scale Reduced Graphene Oxide Films for Nanomechanical Devices. *Nano Lett.* **2008,** *8* (10), 3441-3445.

105. Liu, R.; Arabale, G.; Kim, J.; Sun, K.; Lee, Y.; Ryu, C.; Lee, C., Graphene oxide membrane for liquid phase organic molecular separation. *Carbon* **2014,** *77*, 933-938.

Chapter 4b

Proton Conducting Graphene Oxide Membrane for Unitized Regenerative Fuel Cell

Abstract

Reversible fuel cell (RFC) combines the features of water electrolyzer and fuel cell in the same device and polymer electrolyte membrane plays vital role in proton conduction back and forth during a RFC's operation. The state-of-the-art RFC configuration exploits expensive Nafion membrane as the proton exchange membrane. Though, graphene oxide (GO) is predicted with the capability to conduct protons and to effectively function as fuel barriers, free standing GO membrane has not been exploited for unitized regenerative fuel cell (URFC) architecture. Here we show the successful construction of URFC with a GO based free standing membrane. The barrier nature of GO towards molecular fuels coupled with its ability to conduct proton owing to its hydrophilic functionalities make the membrane a suitable candidate to be utilized in URFCs. The GO based URFC demonstrated ~80 mA cm^{-2} of current density at a terminal voltage of ~2 V (RH = 80%) in the electrolyzer mode and ~60 mA cm^{-2} of peak current density at a peak power density of ~12 mW cm^{-2} (RH = 80%) in fuel cell mode. Long term galvanostatic analysis signifies the stability of GO based MEAs suggesting its feasibility in URFC architecture.
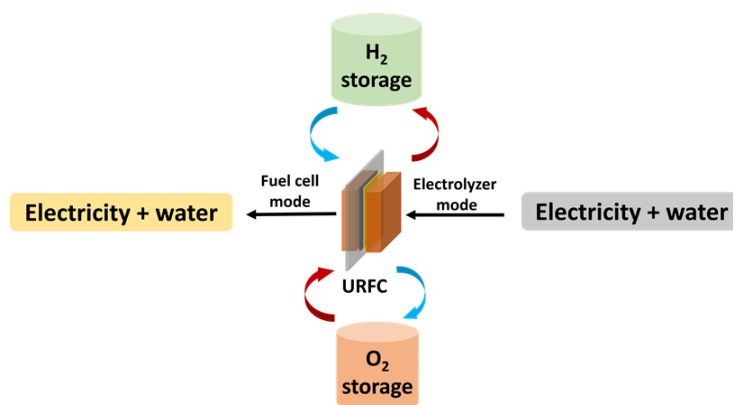
Declaration: The work in this chapter is original and has not yet been published anywhere.

4b.1 Introduction

The inconsiderate consumption of fossil fuels and associated impacts such as climate change and global warming have generated lot interests in harvesting renewable energy resources as clean energy carrier molecule like hydrogen.[1-7] Reversible fuel cells (RFCs) are integral part of renewable energy landscape because of their ability to produce and utilize molecular hydrogen with a near zero carbon foot print.[8-11] RFCs combine the features of a water electrolyzer and a fuel cell in the same device.[12-15] In the water electrolyzer mode renewable energy will be harvested as molecular hydrogen and in the fuel cell mode it will be utilized for the generation of electricity and in this aspect, RFC is a viable platform to bridge the visible mismatch of renewable energy resources in terms of their availability and demand.[16, 17] In a water electrolyzer, water molecules will be split as oxygen at the IrO_2 anode generating protons and electrons and the former will move through the proton exchange membrane (PEM) to the Pt cathode wherein H_2 will be liberated.[18, 19] In a fuel cell, H_2 undergoes oxidation at the Pt anode releasing protons and electrons and the former will move through the PEM to the Pt cathode wherein water will be produced.[20, 21] Therefore, the PEM plays a vital role in RFCs in shuttling protons back and forth.[22, 23] Most of the previous studies in RFCs are carried out with expensive Nafion membrane which adds up to the cost of electrolysis and electricity generation.[24-27] Though, GO is an inexpensive membrane predicted with the capability to conduct protons and to effectively function as molecular fuel barriers, free standing GO PEM have not explored in RFC architecture. Most of the previous studies on RFC are focused on the movements of the water molecules through gas diffusion layer (GDL) and increase in active site of the electrocatalysts.[28-30] Ioroi et al.[28] has reported the IrO_2/Pt electrocatalyst for unitized regenerative fuel cell (URFC) applications. They have utilized a highly active URFC electrode for oxygen evolution and reduction by utilizing a combination of platinum black and high-surface area IrO_2.[28] Moriau et al.[29] reported the synthesis and advanced electrochemical characterization of multifunctional nanocomposite materials for half-cell reactions of URFC. They synthesized highly active multifunctional electrocatalyst of PtCu, Ru, and Ir on graphene-based TiONx to investigate the electrochemical reactions of URFC.[29] Kim et al.[30] investigated the higher electroactivity and stability of nanoporous Pt/Ir based electrocatalyst in URFC. They have explained that np-PtIr showed an

enhanced URFC performance, and approximately about 21 % and 485 % higher round-trip efficiency than that of sole Pt and Ir, respectively.[30] Therefore, most of the studies in RFC are carried out with expensive membranes and electrocatalysts.[24-27, 30]

Here, we demonstrate a graphene oxide (GO) based URFC with performance metrics of ~80 mA cm^{-2} current density at a terminal voltage of 2 V (at RH of 80 %) in the water electrolyzer mode and of ~60 mA cm^{-2} current density at a peak power density of ~12 mW cm^{-2} (at RH = 80 %) in the fuel cell mode. The hydrophilic functionalities in GO membrane are responsible for proton conduction through the channels formed by adsorbed water molecules.[31, 32] Under humidified environment, water molecules generally form the nano-capillaries between GO platelets that act as conduction lane to the protons and the surface defects (holes) within those platelets.[32] This ability of GO for proton conduction coupled by their ease of production and fabrication eventually lead to a potential membrane for URFC architecture.

4b.2   Experimental

The preparation and characterization of graphene oxide (GO) were already discussed in chapter 4a. The catalyst ink for hydrogen evolution reaction (in water electrolysis mode) and hydrogen oxidation reaction (in fuel cell mode) was prepared by ultrasonicating 3 mg cm^{-2} Pt/C, Johnson Mathey with isopropanol and 5 wt% Nafion ionomers in isopropyl alcohol. The catalyst ink for oxygen evolution reaction (in water electrolysis mode) and oxygen reduction reaction (in fuel cell mode) was made by mixing of IrO$_2$ powder and commercially available Pt nanoparticles in definite ratio of 7:3 with 5 wt% of Nafion ionomer in isopropyl alcohol. The catalyst ink for cathode Pt/C (3 mg cm^{-2}) and anode IrO$_2$-Pt (3 mg cm^{-2}) were sprayed on the either side of the graphene oxide paper. Toray carbon gas diffusion electrode was used on Pt/C side and titanium mesh was used on the IrO$_2$-Pt side. Membrane electrode assembly (MEA) was constructed by sandwiching the GO membrane in between the anodic and cathodic electrodes and subsequently hot-pressed with the pressure of 10 MPa at 50 °C for 5 min as explained in chapter 4a. MEA was placed between two graphite blocks with an active electrode area of 1 cm^2 formed by the serpentine gas flow channels. N$_2$ gas at a flow rate of 0.1 dm^3 min^{-1} was used as the carrier gas to carry water vapor to the anode at different relative humidity. All the electrochemical investigations were performed at 80 % relative humidity (RH). RH

was maintained by maintaining the temperature of the water bubbler through which N₂ was purged.

4b.3   Results and discussion

4b.3.1   Physiochemical characterization of bifunctional electrocatalyst and GO based MEA

GO was prepared by improved Hummer's method and it was characterized by various techniques such as AFM, XRD, FTIR TGA, Raman and proton conductivity measurements as discussed in Chapter 4a (Figures 4a.1 and 4a.2). The GO dispersion was then casted on a petri dish and allowed to dry in ambient air as discussed in chapter 4a. The thickness of the resulting membrane was optimized by the volume of the casting solution
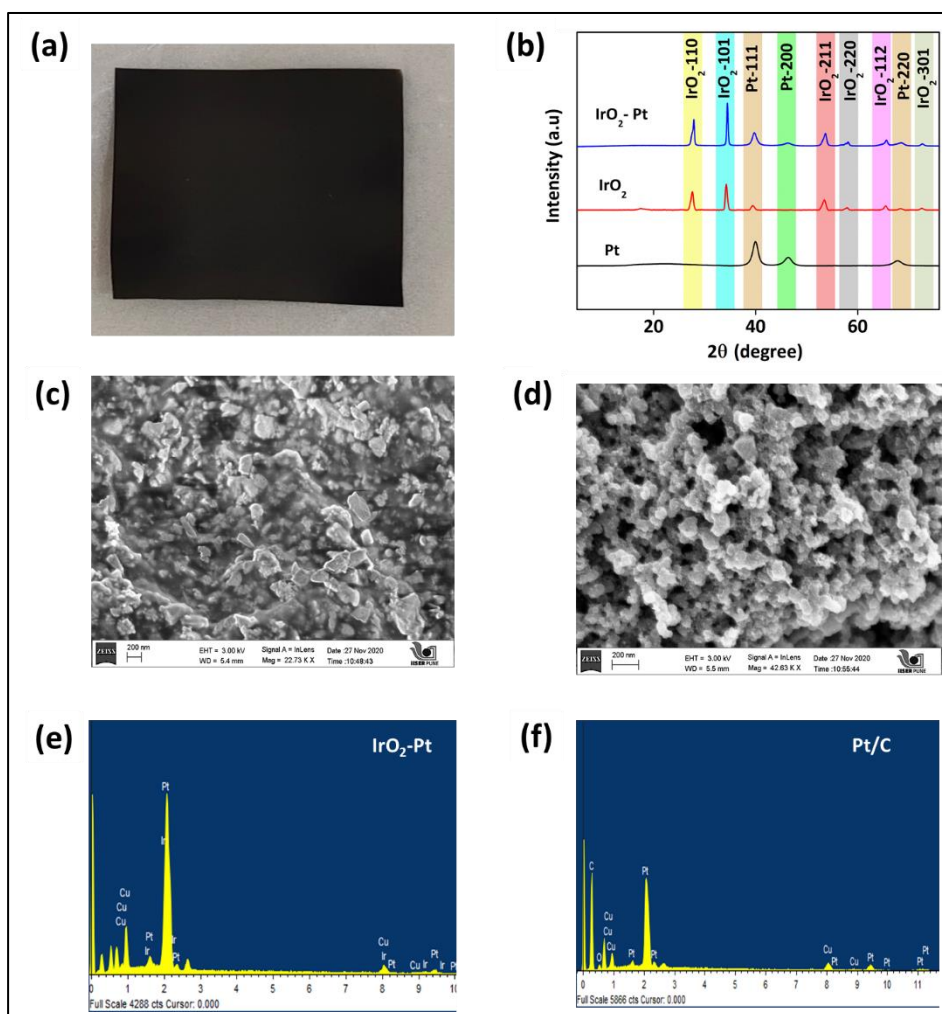
Figure 4b.1: (a) Photograph of freestanding GO membrane of thickness ~50 μm. (b) XRD of bifunctional catalyst (IrO$_2$-Pt) with individual diffraction patterns of Pt and IrO$_2$. (c), (d), (e) and (f) SEM with EDS elemental mapping of composite catalyst IrO$_2$-Pt and Pt/C.

and the weight% of GO dispersion. The photograph of freestanding GO membrane which was peeled off from the petri dish is shown in Figure 4b.1a. Bifunctional catalysts of IrO$_2$-Pt which is active toward oxygen evolution reaction (OER) in the water electrolyzer mode and oxygen reduction reaction in the fuel cell mode was prepared as explained in the experimental section. XRD analysis of the prepared bifunctional catalyst (IrO$_2$-Pt) demonstrates diffraction patterns corresponding Pt and IrO$_2$ in the composite catalyst matching well with their individual diffraction patterns, Figure 4b.1b. This suggests the formation of a well dispersed composite catalyst. To further characterize the bifunctional catalysts, SEM with EDS analysis was performed, Figures 4b.1(c-f). As shown in the EDS elemental mapping, composite catalyst has uniformly accessible Pt and IrO$_2$ domains, Figure4b.1(e and f).
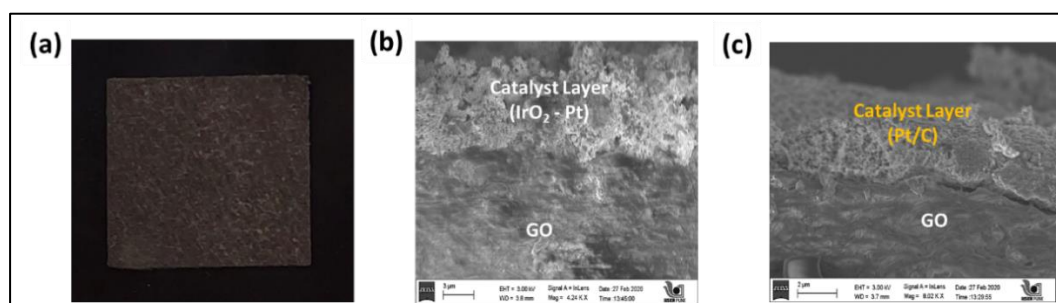
Figure 4b.2: (a) Photograph of MEA for URFC. (b) and (c) cross sectional SEM images showing the well contacted interface of anodic and cathodic catalysts with GO membrane.
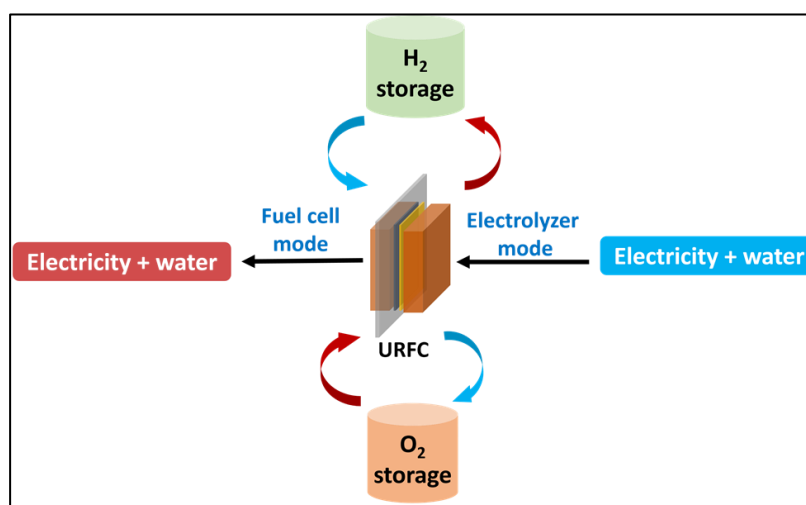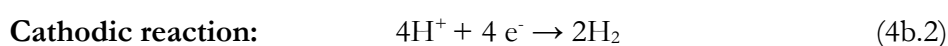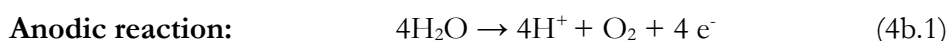

Scheme 4b.1: Schematic representation of GO membrane based unitized regenerative fuel cell.

The GO membrane is sandwiched between the anodic (IrO_2-Pt) and cathodic catalyst Pt/C to construct the membrane electrode assembly (MEA). The photograph of the resulting MEA is shown in Figure 4b.2a. Cross sectional SEM images of GO MEA shows the catalysts layers are intact and graphene oxide membrane is sandwiched between anodic and cathodic catalysts layers, Figure 4b.2b and 4b.2c. As explained in the experimental section, this GO membrane based MEA is utilized in the construction of a unitized regenerative fuel cell. In the electrolyzer mode, the anode is supplied with humidified N_2 at different relative humidity and the water vapor present in the carrier gas will be split into H_2 and O_2 as shown in Scheme 4b.1. In the fuel cell mode, the produced H_2 and O_2 are utilized for electricity generation, Scheme 4b.1.
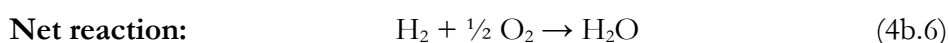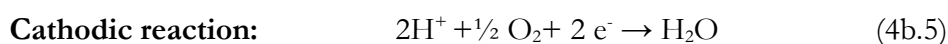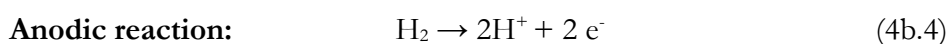
4b.3.2 Electrochemical performance of GO based URFC

The electrochemical performances of GO based URFC was evaluated by recording the current-voltage polarization curves both in the water electrolyzer mode and fuel cell mode, Figure 4b.3a. In the electrolyzer mode, the URFC showed a current density of ~80 mA cm^{-2} at a terminal voltage of ~2 V and in the fuel cell mode the device delivered a current density of ~60 mA cm^{-2} at a peak power density of ~12 mW cm^{-2}, Figure 4b.3a. In the electrolyzer mode, H_2 and O_2 are evolved by water splitting as shown in equations 4b.1 - 4b.3. In the fuel cell mode, H_2 and O_2 are consumed as shown in equations 4b.4 - 4b.6.
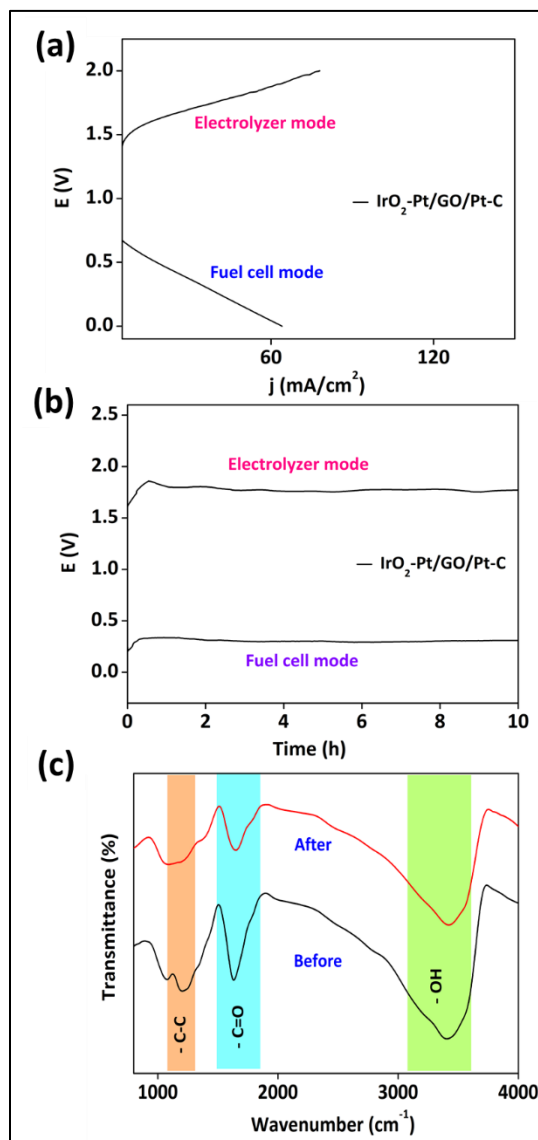
In water electrolyzer mode:

Anodic reaction:	$4H_2O \rightarrow 4H^+ + O_2 + 4\ e^-$	(4b.1)
Cathodic reaction:	$4H^+ + 4\ e^- \rightarrow 2H_2$	(4b.2)
Net reaction:	$2H_2O \rightarrow 2H_2 + O_2$	(4b.3)

In fuel cell mode:

|		
Anodic reaction:	$H_2 \rightarrow 2H^+ + 2\ e^-$	(4b.4)
Cathodic reaction:	$2H^+ + \frac{1}{2}\ O_2 + 2\ e^- \rightarrow H_2O$	(4b.5)
Net reaction:	$H_2 + \frac{1}{2}\ O_2 \rightarrow H_2O$	(4b.6)

The long-term stability of URFC was investigated by constant current test for nearly 10 h and it demonstrates the stability of GO MEA both in the electrolyzer as well as in the fuel cell mode, Figure 4b.3b. The hydrophilic functionalities in GO membrane were found to be intact even after long term stability tests, FTIR spectra, Figure 4b.3c, suggesting the stability of the GO based MEA in the URFC architecture.

Figure 4b.3 (a) Current-voltage characteristics of GO based URFC. In the electrolyzer mode, IrO$_2$-Pt bifunctional catalyst served as the anodic electrocatalyst for oxygen evolution reaction (OER) and Pt/C served as the cathodic electrocatalyst for hydrogen evolution reaction (HER). In the fuel cell mode, Pt/C served as the anodic electrocatalyst for hydrogen oxidation reaction (HOR) and IrO$_2$-Pt served as the cathodic bifunctional electrocatalyst for oxygen reduction reaction (ORR). (b) Chronopotentiometric performance up to 10 h at 30 mA cm^{-2} in the electrolyzer mode and fuel cell mode and (c) FTIR analysis of GO membrane before and after the long-term polarization analysis.

Since Nafion is state of the art membrane in RFCs, the performance is compared with a Nafion 212 membrane of ~50 μm thickness which is similar to the thickness of GO membrane utilized for URFC architecture. The performance comparison by current-voltage polarization and long-term stability tests suggest that Nafion 212 based URFC outperforming GO based URFC, Figure 4b.4a and 4b.4b. This is attributed to the lower

proton conductivity of GO which is at least 10 times lower than Nafion 212 as discussed in Chapter 4a.[33,34] Therefore, to bridge the gap in the performance of GO based URFCs, proton conductivity of GO should be improved substantially. Nevertheless, the data outlined in this chapter indicates that GO is a feasible membrane for URFC architecture.
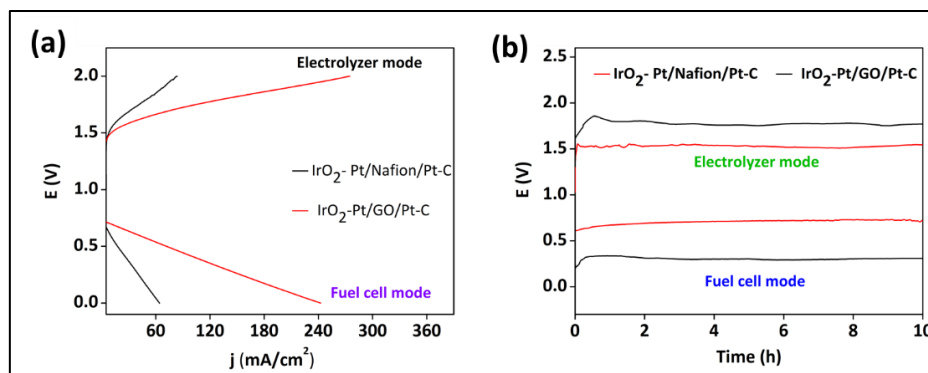
Figure 4b.4: (a) Current-voltage characteristics (b) chronopotentiometric performance up to 10 h at 30 mA cm^{-2} for GO based and Pt based URFCs. In the electrolyzer mode. IrO$_2$-Pt bifunctional catalyst served as the anodic electrocatalyst for oxygen evolution reaction (OER) and Pt/C served as the cathodic electrocatalyst for hydrogen evolution reaction (HER). In the fuel cell mode, Pt/C served as the anodic electrocatalyst for hydrogen oxidation reaction (HOR) and IrO$_2$-Pt served as the cathodic bifunctional electrocatalyst for oxygen reduction reaction (ORR).

4b.4   Conclusions

In this chapter GO is explored as a proton exchange membrane to construct a unitized regenerative fuel cell architecture. GO based MEA with bifunctional IrO$_2$-Pt as the OER catalyst and Pt/C as the HER catalyst demonstrated its capability to split water vapour into H$_2$ and O$_2$ with a near stoichiometric ratio of 2:1 while showing ~80 mA cm^{-2} at a terminal voltage of ~2 V. In the fuel cell mode with Pt/C as the HOR electrocatalyst and IrO$_2$-Pt as the bifunctional ORR electrocatalyst, a peak current density of ~60 mA cm^{-2} was demonstrated at a peak power density of ~12 mW cm^{-2}. The GO based MEA demonstrated its long-term stability in both water electrolyzer mode as well as in the fuel cell mode suggesting its feasibility to construct a unitized regenerative fuel cell architecture.

4b.5   References

1.   Takanabe, K., Photocatalytic Water Splitting: Quantitative Approaches toward Photocatalyst by Design. *ACS Catal.* **2017,** *7* (11), 8006-8022.

2.   Licht, S., Solar Water Splitting To Generate Hydrogen Fuel: Photothermal Electrochemical Analysis. *J. Phys. Chem. B* **2003,** *107* (18), 4253-4260.

3.   Funk, J. E.; Reinstrom, R. M., Energy Requirements in Production of Hydrogen from Water. *Industrial & Engineering Chemistry Process Design and Development* **1966,** *5* (3), 336-342.

4.   Morshedy, A. S.; Abd El Salam, H. M.; El Naggar, A. M. A.; Zaki, T., Hydrogen Production and In Situ Storage through Process of Water Splitting Using Mono/Binary Metal–Organic Framework (MOF) Structures as New Chief Photocatalysts. *Energy & Fuels* **2020,** *34* (9), 11660-11669.

5.   Lyu, H.; Hisatomi, T.; Goto, Y.; Yoshida, M.; Higashi, T.; Katayama, M.; Takata, T.; Minegishi, T.; Nishiyama, H.; Yamada, T.; Sakata, Y.; Asakura, K.; Domen, K., An Al-doped SrTiO$_3$ photocatalyst maintaining sunlight-driven overall water splitting activity for over 1000 h of constant illumination. *Chem. Sci.* **2019,** *10* (11), 3196-3201.

6.   Ahn, J.; Lee, S.; Kim, J. H.; Wajahat, M.; Sim, H. H.; Bae, J.; Pyo, J.; Jahandar, M.; Lim, D. C.; Seol, S. K., 3D-printed Cu$_2$O photoelectrodes for photoelectrochemical water splitting. *Nanoscale Adv.* **2020,** *2*, 5600–5606.

7.   Barber, J., Hydrogen derived from water as a sustainable solar fuel: learning from biology. *Sustain. Energy Fuels* **2018,** *2* (5), 927-935.

8.   Mitlitsky, F.; Myers, B.; Weisberg, A. H., Regenerative Fuel Cell Systems. *Energy & Fuels* **1998,** *12* (1), 56-71.

9.   Paul, B.; Andrews, J., PEM unitised reversible/regenerative hydrogen fuel cell systems: State of the art and technical challenges. *Renew. Sustain. Energy Rev.* **2017,** *79*, 585-599.

10. Kong, F.-D.; Zhang, S.; Yin, G.-P.; Zhang, N.; Wang, Z.-B.; Du, C.-Y., Preparation of Pt/Irx(IrO$_2$)10−x bifunctional oxygen catalyst for unitized regenerative fuel cell. *J. Power Sources* **2012,** *210*, 321-326.

11. Regmi, Y. N.; Peng, X.; Fornaciari, J. C.; Wei, M.; Myers, D. J.; Weber, A. Z.; Danilovic, N., A low temperature unitized regenerative fuel cell realizing 60% round trip efficiency and 10 000 cycles of durability for energy storage applications. *Energy Environ. Sci.* **2020,** *13* (7), 2096-2105.

12. Dutta, K.; Rana, D.; Han, H. S.; Kundu, P. P., Unitized Regenerative Fuel Cells: A Review on Developed Catalyst Systems and Bipolar Plates. *Fuel Cells* **2017,** *17* (6), 736-751.

13. Liu, J. X.; Guo, H.; Yuan, X. M.; Ye, F.; Ma, C. F., Experimental investigation on two-phase flow in a unitized regenerative fuel cell during mode switching from water electrolyzer to fuel cell. *Int. J. Energy Res.* **2018,** *42* (8), 2823-2834.

14. Huang, S.-Y.; Ganesan, P.; Jung, H.-Y.; Popov, B. N., Development of supported bifunctional oxygen electrocatalysts and corrosion-resistant gas diffusion layer for unitized regenerative fuel cell applications. *J. Power Sources* **2012,** *198*, 23-29.

15. Dihrab, S. S.; Sopian, K.; Alghoul, M. A.; Sulaiman, M. Y., Review of the membrane and bipolar plates materials for conventional and unitized regenerative fuel cells. *Renew. Sustain. Energy Rev.* **2009,** *13* (6), 1663-1668.

16. Wang, Y.; Leung, D. Y. C.; Xuan, J.; Wang, H., A review on unitized regenerative fuel cell technologies, part-A: Unitized regenerative proton exchange membrane fuel cells. *Renew. Sustain. Energy Rev.* **2016,** *65*, 961-977.

17. Gabbasa, M.; Sopian, K.; Fudholi, A.; Asim, N., A review of unitized regenerative fuel cell stack: Material, design and research achievements. *Int. J. Hydrogen Energy* **2014,** *39* (31), 17765-17778.

18.   Ito, H.; Maeda, T.; Nakano, A.; Takenaka, H., Properties of Nafion membranes under PEM water electrolysis conditions. *Int. J. Hydrogen Energy* **2011,** *36* (17), 10527-10540.

19.   Hegge, F.; Lombeck, F.; Cruz Ortiz, E.; Bohn, L.; von Holst, M.; Kroschel, M.; Hübner, J.; Breitwieser, M.; Strasser, P.; Vierrath, S., Efficient and Stable Low Iridium Loaded Anodes for PEM Water Electrolysis Made Possible by Nanofiber Interlayers. *ACS Appl. Energy Mater.* **2020,** *3* (9), 8276-8284.

20.   Wang, L.; Zuo, X.; Raut, A.; Isseroff, R.; Xue, Y.; Zhou, Y.; Sandhu, B.; Schein, T.; Zeliznyak, T.; Sharma, P.; Sharma, S.; Hsiao, B. S.; Rafailovich, M. H., Operation of proton exchange membrane (PEM) fuel cells using natural cellulose fiber membranes. *Sustain. Energy Fuels* **2019,** *3* (10), 2725-2732.

21.   Wehkamp, N.; Breitwieser, M.; Büchler, A.; Klingele, M.; Zengerle, R.; Thiele, S., Directly deposited $Nafion/TiO_2$ composite membranes for high power medium temperature fuel cells. *RSC Adv.* **2016,** *6* (29), 24261-24266.

22.   Pourzare, K.; Mansourpanah, Y.; Farhadi, S.; Hasani Sadrabadi, M. M.; Frost, I.; Ulbricht, M., Improving the efficiency of Nafion-based proton exchange membranes embedded with magnetically aligned silica-coated Co_3O_4 nanoparticles. *Solid State Ion.* **2020,** *351*, 115343.

23.   Feng, K.; Tang, B.; Wu, P., Sulfonated graphene oxide–silica for highly selective Nafion-based proton exchange membranes. *J. Mater. Chem A* **2014,** *2* (38), 16083-16092.

24.   Lee, H.; Kim, J.; Park, J.; Joe, Y.; Lee, T., Performance of polypyrrole-impregnated composite electrode for unitized regenerative fuel cell. *J.Power Sources* **2004,** *131* (1), 188-193.

25.   Sadhasivam, T.; Dhanabalan, K.; Roh, S.-H.; Kim, T.-H.; Park, K.-W.; Jung, S.; Kurkuri, M. D.; Jung, H.-Y., A comprehensive review on unitized regenerative fuel

cells: Crucial challenges and developments. *Int. J. Hydrogen Energy* **2017,** *42* (7), 4415-4433.

26. Ioroi, T.; Yasuda, K.; Siroma, Z.; Fujiwara, N.; Miyazaki, Y., Thin film electrocatalyst layer for unitized regenerative polymer electrolyte fuel cells. *J.Power.Sources* **2002,** *112* (2), 583-587.

27. Grigoriev, S. A.; Millet, P.; Dzhus, K. A.; Middleton, H.; Saetre, T. O.; Fateev, V. N., Design and characterization of bi-functional electrocatalytic layers for application in PEM unitized regenerative fuel cells. *Int. J. Hydrog. Energy* **2010,** *35* (10), 5070-5076.

28. Ioroi, T.; Kitazawa, N.; Yasuda, K.; Yamamoto, Y.; Takenaka, H., Iridium Oxide/Platinum Electrocatalysts for Unitized Regenerative Polymer Electrolyte Fuel Cells. *J. Electrochem. Soc.* **2000,** *147* (6), 2018.

29. Moriau, L. J.; Bele, M.; Vižintin, A.; Ruiz-Zepeda, F.; Petek, U.; Jovanovič, P.; Šala, M.; Gaberšček, M.; Hodnik, N., Synthesis and Advanced Electrochemical Characterization of Multifunctional Electrocatalytic Composite for Unitized Regenerative Fuel Cell. *ACS Catal.* **2019,** *9* (12), 11468-11483.

30. Kim, J.-H.; Yun, S.-W.; Shim, K.; You, S.-H.; Jung, S.-M.; Kweon, H.; Joo, S. H.; Moon, Y. H.; Kim, Y.-T., Enhanced Activity and Stability of Nanoporous PtIr Electrocatalysts for Unitized Regenerative Fuel Cell. *ACS Appl. Energy Mater.* **2020,** *3* (2), 1423-1428.

31. Ravi P Pandey , G. S., Murli Manohar Vinod K Shahi Graphene oxide based nanohybrid proton exchange membranes for fuel cell applications: An overview. *Adv Colloid Interface Sci.* **2017** *240*, 15-30.

32. Ehlert, S. M. A. S. P. H. J. Graphene-Based Proton Exchange Membrane for Direct Methanol Fuel Cells. US20160036081A1, **2016**.

33.　Karim, M. R.;　Hatakeyama, K.;　Matsui, T.;　Takehira, H.;　Taniguchi, T.; Koinuma, M.;　Matsumoto, Y.;　Akutagawa, T.;　Nakamura, T.;　Noro, S.-i.; Yamada, T.;　Kitagawa, H.; Hayami, S., Graphene Oxide Nanosheet with High Proton Conductivity. *J. Am. Chem. Soc.* **2013,** *135* (22), 8097-8100.

34.　He, G.;　He, X.;　Wang, X.;　Chang, C.;　Zhao, J.;　Li, Z.;　Wu, H.; Jiang, Z., A highly proton-conducting, methanol-blocking Nafion composite membrane enabled by surface-coating crosslinked sulfonated graphene oxide. *Chem. Commun.* **2016,** *52* (10), 2173-2176.

Chapter 5a

Amplification of Proton Conduction in Graphene Oxide Proton Exchange Membrane

Abstract

In a typical H_2–O_2 fuel cell, the membrane plays a crucial role to exchange the protons from the anodic to the cathodic side. Graphene oxide (GO) is known to conduct the protons because of the presence of oxygen rich hydrophilic functionalities. However, its proton conduction capability is ~10 times lower than state-of-the-art Nafion membrane which makes it inevitable to accelerate GO's proton conduction capability for its advancement towards a potential fuel cell membrane. In this Chapter, GO's proton conduction capability is targeted by introducing hydrogen carrying quinone moieties bearing proton shuttling sulphonic acid side chain into the nano-porous matrix of GO. The coexistence of proton shuttling functionalities and hydrogen carrying functionalities in the molecule introduced into GO interlayers significantly enhanced its proton conduction capability as well as mechanical stability. Fuel cell polarization and kinetic analyses revealed that these multitasking molecules in GO interlayers enhanced the fuel cell performance matrix by ~3 times compared to the pristine GO membranes, suggesting that the functional group factors of target molecules should be considered for the amplification of proton transport in GO-based proton exchange membrane fuel cells.
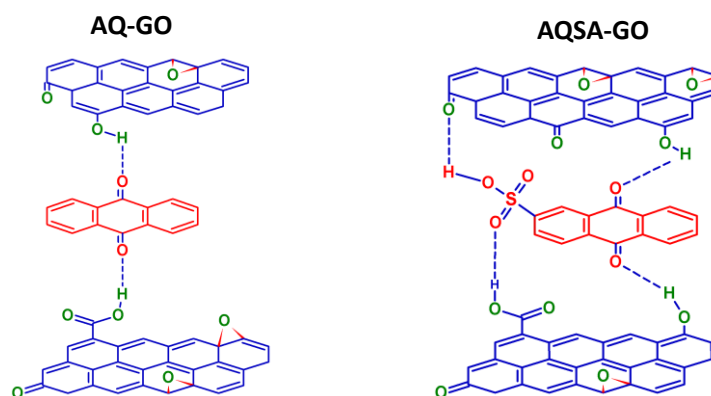
Declaration: The work has been published in the following journal:

5a.1. Introduction

Low temperature of operation and near zero emissions bring the proton exchange membrane fuel cells (PEMFCs) and metal air batteries to the helm of affairs in artificial photosynthesis and electrification of transport.[1-6] Although the power output from a PEMFC is clean, the electricity produced by a PEMFC is very expensive mainly due to the expensive electrocatalysts and high-priced proton exchange membrane (PEM).[7,8] The state-of-the-art PEM produced by Dupont (Nafions) costs more than 600 USD per m^2.[9,10] For these reasons, intensive efforts are dedicated in finding alternative membranes to Nafion-based membranes for PEMFC, however, the unique combinations of latter's chemical functionalities featuring hydrophobicity and hydrophilicity have enormously contributed to its prominent stature among fuel cell membranes.[11,12] It is predicted that graphene oxide (GO) is able to conduct the protons because of the presence of oxygen rich hydrophilic functionalities and is also an effective barrier to molecular fuels.[13,14] These properties make GO as a suitable material to be explored as a proton exchange membrane in PEMFC to bring down the overall cost of electrical energy generation. However, the proton conductivity and mechanical stability of GO should be improved for its advancement towards a practical membrane for fuel cell applications. It is well known that proton conduction capability of GO arises mainly due to the higher density of hydrophilic functionalities like carboxylic, hydroxyl, epoxides, etc.[15-18] This suggests that any enhancement in the density of its hydrophilic functionalities will result in higher proton conduction capability. Equally, any such steps to increase the density of such hydrophilic functionality in GO will also affect its mechanical stability in aqueous environment, which assumes critical importance as water will be formed on the cathodic side of PEMFC during its operation.[19-22] Higher density of hydrophilic functionalities of GO will increase the water wettability of the membrane which will result in the disintegration of the membrane in the long run. To prevent such type of disintegration or to improve the mechanical stability of the GO membrane, hydrophobic functionalities should be introduced into the GO's matrices but any attempt to improve the hydrophobicity (or mechanical integrity) of the membrane under fuel cell conditions will be a daunting task as it will be at the cost of its proton shuttling capability. This trade-off between hydrophobicity and proton

conductivity have so far been a challenge in designing a feasible GO based membrane for PEMFC applications.

In this Chapter, we successfully achieved ~7 times amplification of proton transport in GO based fuel cell membranes by introducing molecules bearing proton conducting (lower pKa) functionalities like -SO_3^- and hydrogen carrying quinone functionalities into GO's interlayers. We have chosen SO_3^- functionalities with lower pKa because of their higher dissociation constant and consequently their higher proton conduction capability.[25,26] Further, this group is known to be responsible for higher proton conduction in state of the art Nafion membrane.[27-29] Also, the quinone functionalities are well known for their hydrogen carrying capability.[30-33] The combined effect of these moieties coupled with the hydrophobicity of the aromatic core of the molecule are exploited in this Chapter to design a feasible membrane with higher proton conduction capability and improved mechanical stability for PEMFC applications.

5a.2. Experimental

5a.2.1. Materials and chemicals

H_2SO_4 (99.99), H_3PO_4 (99.99), HCl (99.99), $KMnO_4$, H_2O_2 (36%), Nafion (0.05 wt%) solution, NaCl, (9,10), tetrahydrofuran (THF 99%), (9,10) anthraquinone (AQ 98%), (9,10) anthraquinone- 2-sulphonic acid (AQSA 98%) were purchased from Sigma Aldrich, India. Commercial ETEK Pt/C (40 wt%) was procured from Johnson-Matthey, India. Triply distilled water was used for all the experiments.

5a.2.2. Preparation of graphene oxide membranes (GO)

Graphene oxide (GO) was prepared by employing an improved Hummer's method.[34,35] In brief, 3.0 g of graphite flakes were added to an acidic mixture of H_2SO_4:H_3PO_4 in a 3:1 ratio, followed by the gradual addition of 16–18 g of potassium permanganate. The mixture was stirred on a magnetic stirrer for precise mixing for almost 3 days. After that, nearly 15 mL of 36 % H_2O_2 was slowly added to the reaction vessel. The reaction mass turned into a golden yellowish color. After that, the reaction mixture was stirred up to 6 h. The formed GO was collected by centrifugation, washed with 1 M HCl followed by triply distilled water and then stored in distilled water. From this, the membranes were prepared after casting the graphene oxide dispersion on a flat petri dish. After complete drying, the membranes were peeled off from the petri dish.

5a.2.3. Preparation of composite membranes (AQ-GO & AQSA-GO)

The homogeneous solution of (9,10) Anthraquinone (AQ) or (9,10) Anthraquinone-2-sulphonic acid (AQSA) in tetrahydrofuran (THF) was prepared by continuous ultra-sonication for more than 6 h. Then, the required amounts of GO were supplemented to the reaction mass followed by sonication for 10 h for mixing. From the above prepared homogeneous solutions, membranes were casted on flat glass petri dishes and allowed to air dry. After drying, the membranes were peeled off. The number of moles of AQSA and AQ per gram of GO were kept constant in the reaction mixture for comparing the performance between the AQSA composite GO (AQSA-GO) and AQ composite GO (AQ-GO) membranes, and the UV-Vis analysis of the final membrane revealed ~0.5 millimoles of AQSA and AQ per gram of GO. The thickness of the membranes was maintained by controlling the weight % of the GO in the dispersion.

5a.2.4. Physicochemical characterizations

UV-Visible spectroscopic analysis (Perkin Elmer Lambda 950) was carried out in the range of 200–800 nm using a quartz cuvette. FTIR analysis was carried out for the membranes in the range 500–4000 cm^{-1} using a Bruker Alpha ATR-FTIR. The thermal stabilities of the membranes were measured by thermogravimetric analysis using a STA6000 machine over the temperature range of 30–800°C with a scan rate of 10°C min^{-1} under nitrogen flow (30 mL min^{-1}). A Bruker D8 Advance X-ray diffraction machine was used for the analysis of diffraction patterns. Raman spectra were recorded using a Raman microscope (LabRAM HR, Horbia Jobin Yvon). AFM images were recorded for GO dispersions using Agilent instruments. The GO samples were dropcasted on a freshly cleaved mica surface for this purpose. The imaging was carried out under tapping mode using the TAP-190AL-G50 probe from Budget sensors with a nominal spring constant of 48 N m^{-1}.

5a.2.5. Proton conductivity measurements

To measure proton conductivities, electrochemical impedance spectra were acquired in the frequency range of 100 kHz to 10 mHz at 0 V vs. open circuit voltage (OCV) with a 10 mV AC excitation signal using a Princeton Applied Research (PARSTAT 2273) potentiostat/galvanostat at a relative humidity (RH) of 30 % in the temperature range 25–60°C. The high frequency intercept on the real axis in the Nyquist plot was taken

to calculate the electrolyte resistance of the membrane. Proton conductivity of the respective membranes was calculated using the following equation:[36,37]

$$\sigma = T/(R*A) \qquad (5a.1)$$

where σ is the proton conductivity of the membrane, T is the thickness of the membrane, R is the resistance of the membrane estimated from electrochemical impedance analysis and A is the area of the membrane. The ion exchange capacity (IEC) of the membranes were measured using classical acid-base titration techniques.[18,36] Samples were soaked in a 0.1 M HCl solution for 24 h followed by washing with distilled water to remove excess HCl. After that, the samples were placed in 1 M NaCl aqueous solution for 24 h to release the protons from the membranes. Back titration was carried out with a standardized 0.1 M NaOH aqueous solution with phenolphthalein indicator to measure the H^+ ions in the solution. By using the following equation, the IEC values (meq g^{-1}) were calculated:

$$IEC = (V_{NaOH} * C_{NaOH})/W_{dry} \qquad (5a.2)$$

Where, V_{NaOH} is the consumed volume of NaOH, C_{NaOH} is the concentration of the NaOH and W_{dry} is the weight of the completely dry membrane (g). I–V characteristics were determined by four probe conductivity measurements using a Keithley 2400.

### 5a.2.6. Fuel cell characterizations

The catalyst ink was prepared by sonicating the Pt/C (40 wt%) catalyst in 2-propanol with 5 wt% Nafion ionomer and the ink was sprayed onto the carbon cloth. The membrane electrode assembly (MEA) was fabricated by sandwiching the membrane between the Pt/C anode (0.25 mg cm^{-2}) and Pt/C cathode (0.25 mg cm^{-2}) electrodes by applying a pressure of 10 MPa at 50 °C for 5 min. Fuel cell performance was carried out at 30 % RH (relative humidity) with H_2 and O_2 gases at a flow rate of 100 mL min^{-1}.

5a.3. Results and discussion

### 5a.3.1. Physiochemical characterizations of membranes

GO was prepared by the improved Hummers method.[34,35] The prepared GO was thoroughly characterized by a variety of physicochemical techniques as discussed below. (9,10)- Anthraquinone- 2-sulphonic acid (AQSA), possessing strongly polar (–SO_3H) and non-polar (aromatic ring) features, was introduced at the GO interplanes (~0.5 mM g^{-1}) by intercalation (see experimental section for more details). –SO_3H group is well known for its higher proton conduction capability in state-of-the-art Nafion membrane [27-29] and quinones are well known for their hydrogen carrying capabilities.[30-33] So, the coexistence

of hydrogen carrying functionality and proton conducting functionality coupled with non-polar aromatic ring in the same molecule should enhance the proton conduction capability and improve the mechanical stability of resulting GO composite membrane. To investigate the effect of $-SO_3H$ groups in proton transport separately, (9,10) anthraquinone (AQ) at the same mole ratio ($\sim$0.5 mM g^{-1}) was introduced separately into the GO interlayers to make an AQ-GO composite membrane.
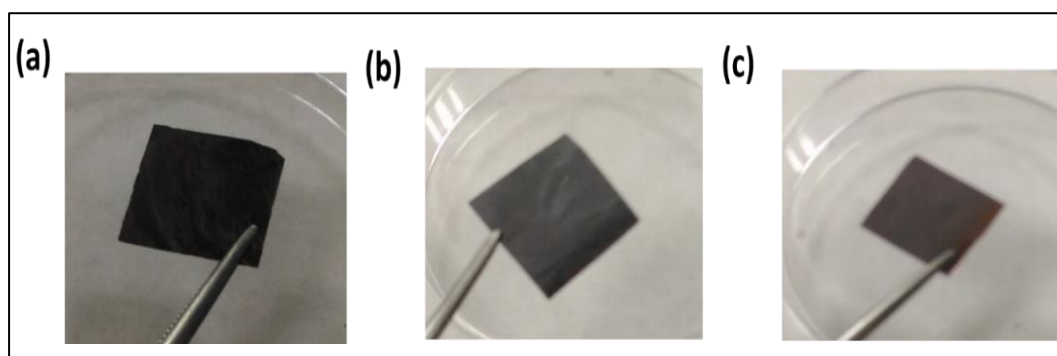
Figure 5a.1: Photographs of (a) GO, (b) AQSA-GO and (c) AQ-GO membranes.

After the successful preparation of GO dispersion, they were dropcasted on a petri dish. Thickness of the membrane were maintained almost constant by controlling the weight % of GO in the casting dispersion. After dropcasting on the petri dish, the membranes were kept for air drying and then peeled out from the petri dish to obtain free standing GO membranes as shown in Figure 5a.1. Atomic force microscopy (AFM), Figure 5a.2 shows the preservation of sheet like structure of GO even after introducing the molecules into the GO's interlayers. The heights of the GO sheets are found to be in the range 3-4 nm, Figure 5a.2.
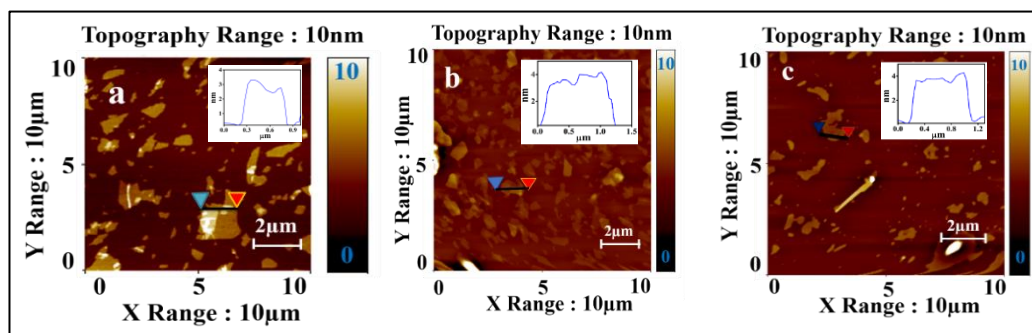
**Figure 5a.2:** AFM images of (a) GO, (b) AQSA-GO and (c) AQ-GO.

Contact angle images of the GO membranes reveal an increase in water contact angle ongoing from GO ($\sim$63°) to AQ-GO ($\sim$82°) and AQSA-GO ($\sim$80°), Figure 5a.3, which suggest an enhancement in hydrophobic characteristics of the membrane on

introduction of AQSA and AQ molecules probably due to the non-polar aromatic ring in these molecules. The slight reduction in water contact angle in AQSA-GO compared to AQ-GO could be due to the presence of hydrophilic –SO₃H groups.
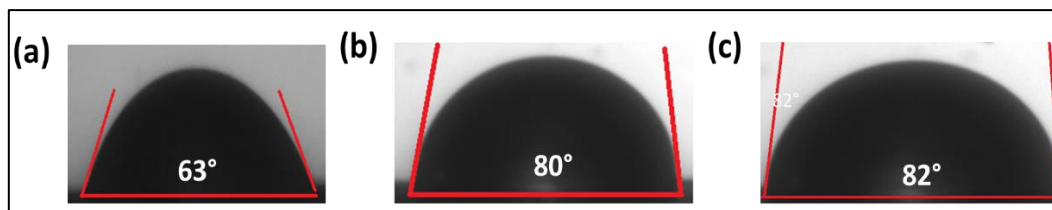
Figure 5a.3: Contact angle images of (a) GO, (b) AQSA-GO and (c) AQ-GO membranes.

XRD patterns of GO and composite GO membranes (Figure 5a.4a) indicate a noticeable downshift in 2θ values of GO's (001) plane on introducing AQ and AQSA, indicating the molecules mainly prefer the interplanar sites in GO. However, the shift in 2θ values of GO's (001) plane on introducing AQSA is substantial compared to a marginal shift in the case of AQ-GO. This in turn suggests that on introducing AQ, the GO (001) plane expands slightly (~0.01 nm), however noticeably in the case of AQSA doped GO (~0.09 nm). This noticeable difference between the two composite membranes is attributed to the presence of comparatively extensive hydrogen-bonding interactions in AQSA-GO due to the presence of quinone functionality and SO_3^- functionality in AQSA molecule. Raman spectra demonstrates a slight increase in I_D/I_G ratio (Figure 5a.4b, Table 5a.1) on introducing AQ and AQSA into GO's matrices, which indicates that the functionalizing strategy affects the defect density in GO's matrix.
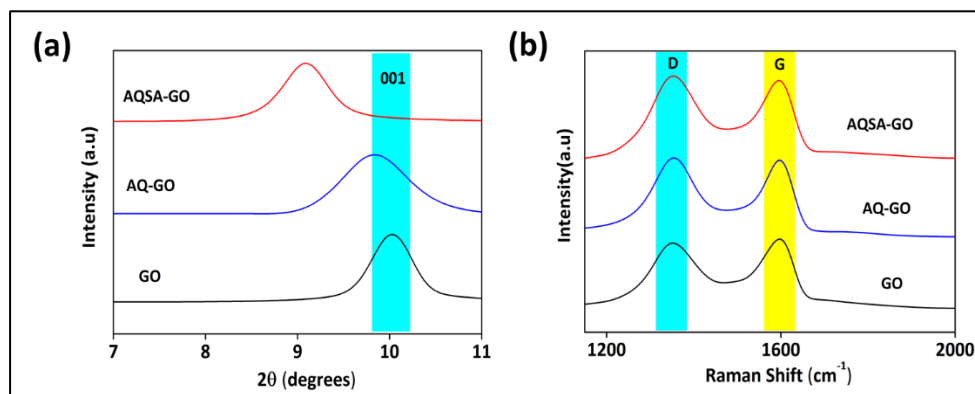

Figure 5a.4: (a) XRD pattern, (b) Raman spectra of GO, AQ-GO and AQSA-GO.

**Table 5a.1:** I_D/I_G ratio ratios of GO, AQ-GO and AQSA-GO membranes.

Membranes	I_D/I_G ratio
GO	0.93

AQ-GO	1.01
AQSA-GO	1.02

The UV-Vis spectra of GO do show some alterations in π-π* transition on introducing AQ, however, the transition remained almost unaffected in AQSA functionalized with GO affirming a difference in the type of interactions with GO's matrix, Figure 5a.5. Differences in the type of interactions between AQSA and AQ with GO ma-
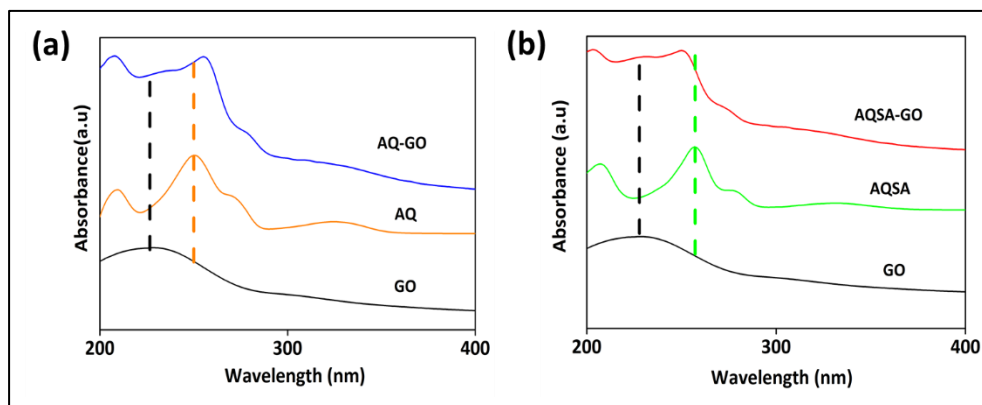
Figure 5a.5: UV-Vis spectra of (a) GO, AQ and AQ-GO & (b) GO, AQSA and AQSA-GO.
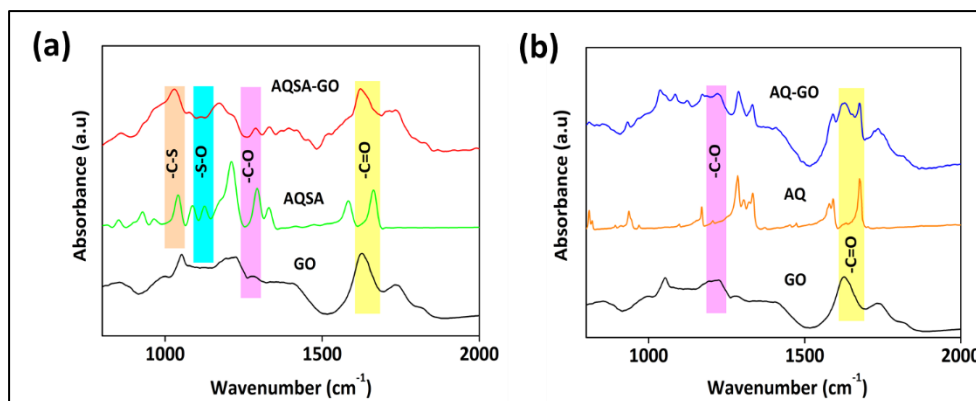
Figure 5a.6: FTIR spectra of (a) GO, AQSA and AQSA-GO and (b) GO, AQ and AQ-GO.

-trix are further evident in the π-π* transitions of quinones, which demonstrate a blue shift for the former compared to a redshift for the latter, Figure 5a.5. This hints towards dominant H-bonding interactions in AQSA-GO compared to AQ-GO. Extensive H-bonding interaction between AQSA and GO can be seen further in the FTIR spectral pattern where significant spectral broadening, spectral shifts and emergence and disappearance of certain spectral patterns compared to the individual counterparts are evident in AQSA doped membranes, Figure 5a.6a. H-bonding is reported to cause peak

broadening, peak shifts, emergence and disappearance of FTIR spectral vibrations.[38-41] For example, a comparison of $\upsilon_{C=O}$ vibrations at 1660 cm^{-1} in pure AQSA, demonstrates its disappearance in the AQSA-GO composite membrane (red trace, Figure 5a.6a), pointing to the interactions of this functional groups with the functionalities of GO matrix. Further the $-SO_3H$ vibrations observed at 1086 and 1122 cm^{-1} in AQSA [42,43] exhibited noticeable spectral broadening and shifts, affirming their participation as well in the H-bonding interactions with GO matrix, Figure 5a.6a. However, in AQ composite membranes, Figure 5a.6b (blue line), $\upsilon_{C=O}$ vibrations and majority of the other characteristic vibrations of individual counterparts are maintained in the AQ-GO composite membranes without noticeable spectral broadening and shifts. The possibility of H-bonding interaction between AQ and GO matrix cannot be ruled out, however the H-bonding interactions between AQSA and GO matrix is comparatively extensive compared to AQ and GO. In essence, these physicochemical characterizations highlight the successful introductions of these moieties into the GO's interlayers. Further, the investigation of ion exchange capacity (IEC), another desirable fuel cell relevant parameter reflecting the ion intake by the membrane increased noticeably in AQSA-GO membrane compared to AQ-GO membrane, Table 5a.2. IEC values indicate the number of protons the membrane functionalities can hold per gram of the material and it reflects the number of ion exchange moieties present in the membrane.[18,36] The IEC value of GO is ~0.36 meq g^{-1} which increased marginally in AQ-GO to ~0.47 meq g^{-1} but substantially in AQSA-GO to 0.79 meq g^{-1}. It should be emphasized that the IEC value of AQSA-GO is closer to the state-of-the-art Nafion membranes (~0.9 meq g^{-1})[44-46], which indicate a substantial boost in ion transport capacity of GO after introducing AQSA molecule.

Table 5a.2: Ion exchange capacities (IEC) of GO, AQ-GO and AQSA-GO membranes.

Membranes	IEC (meq g^{-1})
GO	0.36
AQ-GO	0.43
AQSA-GO	0.79

To utilize these membranes as proton exchange membranes, membranes should be mechanically stable in an aqueous environment because the cathodic side of the fuel cell will generate water during the operation. The mechanical integrity of membranes in

aqueous conditions were investigated by keeping the membranes in water for several hours, Figure 5a.7. AQSA-GO and AQ-GO membranes are found to be intact in water even after several days of incubation whereas the pristine GO membrane did not last for more than few hours of incubation clearly suggesting the improvement in the mechanical stability of GO on introducing AQ and AQSA molecules. The enhancement in the mechanical stability of composite membranes in water is attributed to the non-polar domains (aromatic rings) in AQSA and AQ molecules. Therefore, the abundant non-polar domains (aromatic rings) and polar domains (-C=O, –SO₃H) in AQSA-GO and AQ-GO (-C=O) is expected to improve the fuel cell relevant transport properties of the membrane along with their mechanical stability, however the situations should be different for the former because of the extensive H-bonding interactions.
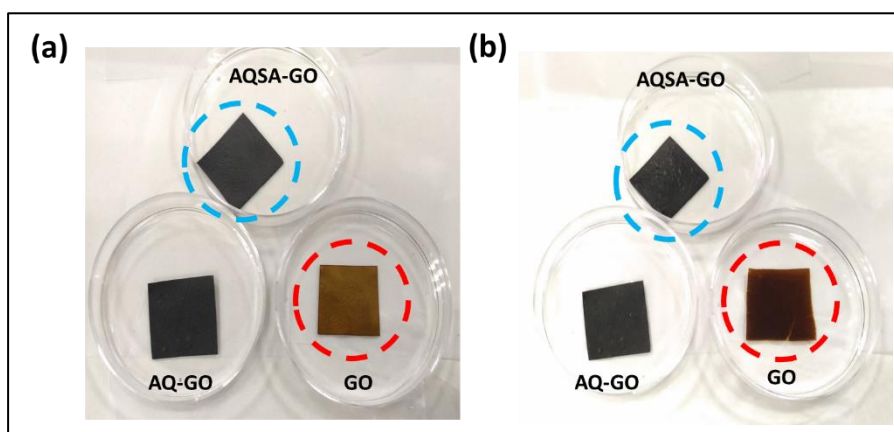

Figure 5a.7: Mechanical disintegration test of the membranes in aqueous conditions at different time intervals. (a) at 0 minutes and (b) after 24 h.

### 5a.3.2 Proton conductivities and fuel cell investigations of membranes

It should be emphasized that the abnormally high proton shuttling capability in ice and water is derived mainly from H-bonding interactions [47,48] and therefore the presence of H-bonding interactions in AQSA-GO should lead to superior proton conductivity. Electrochemical impedance spectroscopy (EIS) is a powerful tool to investigate the charge transport in PEMs. The proton conductivities extracted from the electrochemical impedance analysis indicate a lower membrane resistance for the AQSA-GO composite membrane compared with AQ-GO membrane and pristine GO membrane, Figure 5a.8a and 8b. The higher proton conductivity of AQSA-GO membrane is attributed mainly to the presence of hydrogen carrying quinone functionality and proton-conducting SO_3^- functionality and also to the existence of extensive H-bonding interactions between AQSA and GO. Further, the activation energy parameters for the membranes were extracted from

the Arrhenius plot to investigate the proton conduction capabilities of the membranes, Figure 5a.8c. Significant decrease in activation energy is observed in AQSA composite membranes compared to AQ-GO and pure GO membranes, Figure 5a.8d which further indicate the advantages of introducing AQSA over AQ to GO interlayers.
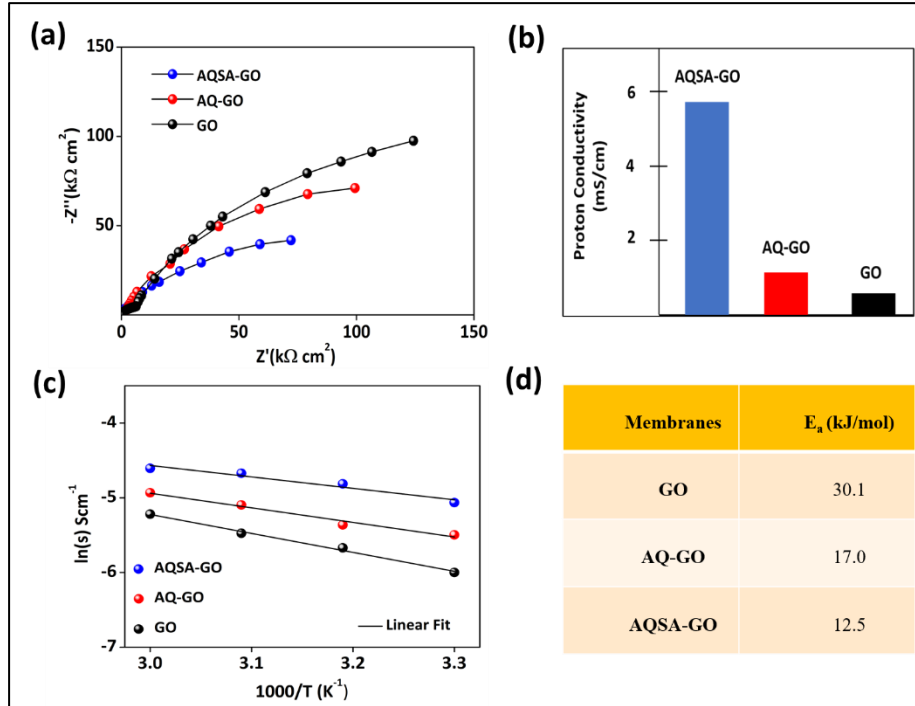

Figure 5a.8: (a) Electrochemical impedance spectra (EIS) of GO, AQ-GO and AQSA-GO membranes at 25 °C. EIS is recorded in the frequency range of 100 kHz to 10 mHz with 10 mV AC excitation signal. (b) Room temperature proton conductivities of GO, AQ-GO and AQSA-GO membranes extracted from Figure 5a.8a, (c) Arrhenius plots for GO, AQ-GO and AQSA-GO membranes and (d) activation energy values of GO, AQ-GO and AQSA-GO membranes extracted from Figure 5a.8c.
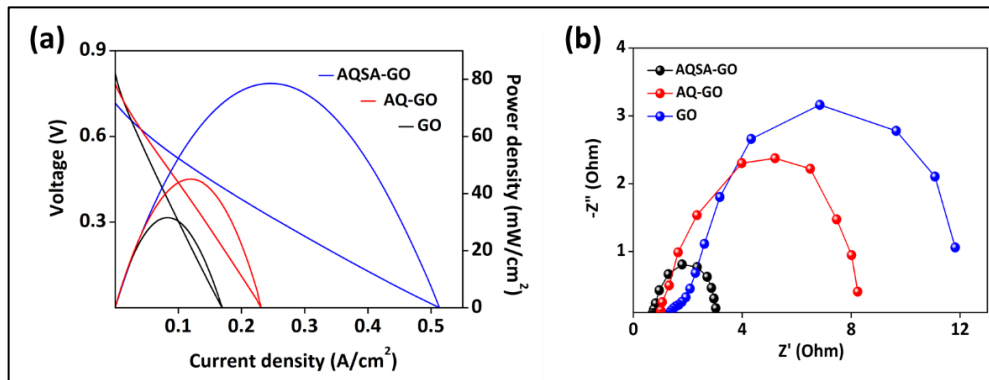
Figure 5a.9: (a) Fuel cell polarization curves of GO, AQ-GO and AQSA-GO carried out at 25 $^\circ$C at 30 % RH with a H_2 and O_2 flow rate of 100 mL min^{-1}. (b) Impedance plot of GO, AQ-GO and AQSA-GO in the fuel cell mode in the frequency range of 100 kHz to 10 mHz at 0 V vs. open circuit voltage with a 10 mV excitation signal.

The fuel cell performance curves of GO membrane electrode assembly indicate a noticeable enhancement in the performance of AQ-GO which is significantly boosted on incorporation of AQSA, Figure 5a.9a. It should be noted that this result is in line with proton conductivity studies, Figure 5a.8. The peak power density and peak current density are amplified by ~3 times (compared to pure GO) on incorporation of AQSA which supports the higher proton conduction capability of the AQSA-GO composite membrane, Figure 5a.8b. The impedance spectra collected in the fuel cell mode, Figure 5a.9b, clearly demonstrates a noticeable decrease in electrolyte resistance and charge transfer resistance on incorporation of molecules and that is quite marked in the case of AQSA-GO membranes. This is interesting given the fact that on all the studied membranes the conf-
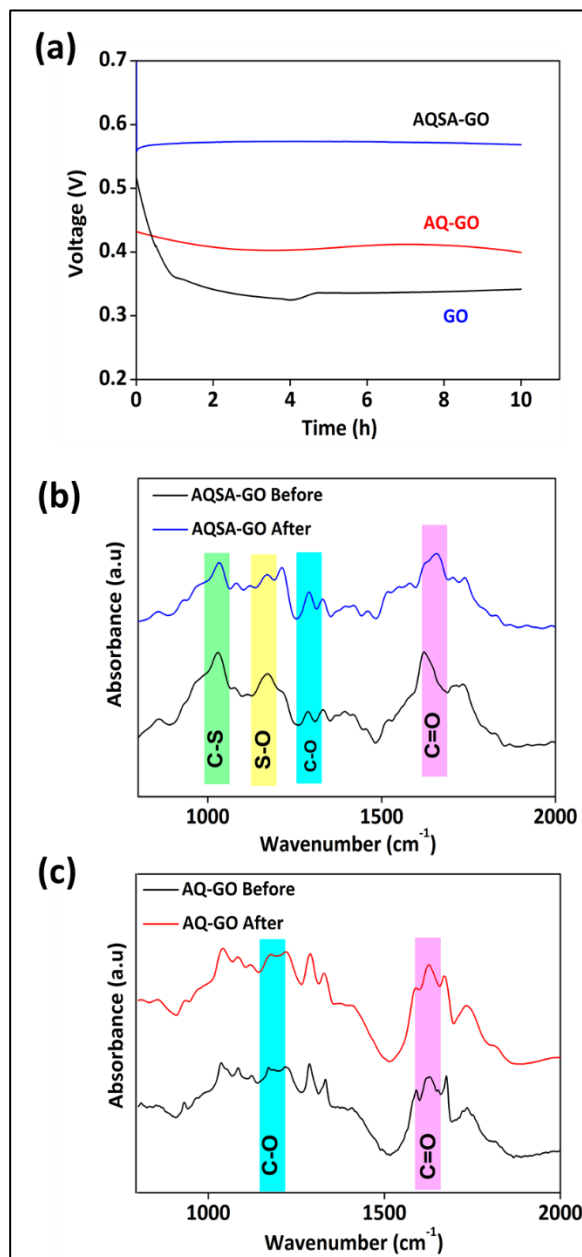
Figure 5a.10: (a) Long term galvanostatic analysis (at 25 $^{\circ}$C and at 30 % RH) at 0.1 A cm^{-2} with a H$_2$ and O$_2$ flow rate of 100 mL min^{-1}. (b) and (c) FTIR spectra of the membranes before and after the long term galvanostatic polarization of AQ-GO and AQSA-GO based fuel cells.

-iguration of membrane electrode assembly and the fuel cell parameters remain the same with the only difference being the nature of the molecules. As the semicircles will have contributions from either half-cell reactions, it is reasonable to argue that the presence of AQSA and AQ molecules in the membrane noticeably influences the charge transfer kinetics at the three-phase boundary. The long-term polarization, Figure 5a.10a, suggests the composite membranes are stable under chemically harsh conditions prevailing in a fuel cell and FTIR analysis before and after the long term galvanostatic analysis, Figure 5a.10b and Figure 5a.10c reveal the well preservation of functionalities of molecules even after long term polarization, suggesting their decent stability in GO's matrices.

5a.4. Conclusions

We have successfully designed a strategy to enhance the proton conduction capability of GO membrane, by introducing molecules bearing hydrogen carrying quinone functionalities and proton conducting SO$_3^-$ moieties into GO's matrices. The electrochemical impedance analysis of composite membrane indicates a higher proton conduction capability and lower activation energy for proton transport in AQSA-GO composite membrane compared with AQ-GO and pristine GO membrane which in turn highlight the role of extensive host guest H-bonding interactions in proton conduction. The fuel cell performance suggests amplification in peak power density and peak current density by ~3 times in AQSA-GO based fuel cells compared to pristine GO membrane-based fuel cells, suggesting the performance of GO based fuel cells can be targeted by incorporating guest molecules with suitable functionalities. Long term stability tests in combination with FTIR further demonstrate the well preservation of molecules in GO's nanoporous matrix. This study reveals that polarity factors of molecules should be given utmost importance when new molecules are designed for boosting the fuel performance of GO based PEMFC.

5a.5. References

1.   Gao, Y.; Zhang, L.; Ding, X.; Sun, L., Artificial photosynthesis – functional devices for light driven water splitting with photoactive anodes based on molecular catalysts. *Phys. Chem. Chem. Phys* **2014,** *16* (24), 12008-12013.

2.   Klahr, B.; Gimenez, S.; Fabregat-Santiago, F.; Bisquert, J.; Hamann, T. W., Electrochemical and photoelectrochemical investigation of water oxidation with hematite electrodes. *Energy Environ. Sci.* **2012,** *5* (6), 7626-7636.

3.   Freunberger, S. A., Batteries: Charging ahead rationally. *Nat. Energy.* **2016,** *1* (6), 16074.

4.   Both Engel, A.; Bechelany, M.; Fontaine, O.; Cherifi, A.; Cornu, D.; Tingry, S., One-Pot Route to Gold Nanoparticles Embedded in Electrospun Carbon Fibers as an Efficient Catalyst Material for Hybrid Alkaline Glucose Biofuel Cells. *Chem Electro Chem* **2016,** *3* (4), 629-637.

5.   Kannan, R.; Kakade, B. A.; Pillai, V. K., Polymer Electrolyte Fuel Cells Using Nafion-Based Composite Membranes with Functionalized Carbon Nanotubes. *Angew. Chem. Int. Ed.* **2008,** *47* (14), 2653-2656.

6.   Brun, N.; Wohlgemuth, S. A.; Osiceanu, P.; Titirici, M. M., Original design of nitrogen-doped carbon aerogels from sustainable precursors: application as metal-free oxygen reduction catalysts. *Green Chem.* **2013,** *15* (9), 2514-2524.

7.   Wu, L.; Zhang, Z.; Ran, J.; Zhou, D.; Li, C.; Xu, T., Advances in proton-exchange membranes for fuel cells: an overview on proton conductive channels (PCCs). *Phys. Chem. Chem. Phys* **2013,** *15* (14), 4870-4887.

8.   Du, X.; Yu, J.; Yi, B.; Han, M.; Bi, K., Performances of proton exchange membrane fuel cells with alternate membranes. *Phys. Chem. Chem. Phys* **2001,** *3* (15), 3175-3179.

9.   Li, J.; Yuan, X.; Liu, S.; He, Z.; Zhou, Z.; Li, A., A Low-Cost and High-Performance Sulfonated Polyimide Proton-Conductive Membrane for Vanadium Redox Flow/Static Batteries. *ACS Appl. Mater. Interfaces* **2017,** *9* (38), 32643-32651.

10.   Abdul Aziz, M.; Oh, K.; Shanmugam, S., A sulfonated poly(arylene ether ketone)/polyoxometalate–graphene oxide composite: a highly ion selective membrane for all vanadium redox flow batteries. *Chem. Commun.* **2017,** *53* (5), 917-920.

11.   Luo, T.; Zhang, Y.; Xu, H.; Zhang, Z.; Fu, F.; Gao, S.; Ouadah, A.; Dong, Y.; Wang, S.; Zhu, C., Highly conductive proton exchange membranes from sulfonated polyphosphazene-graft-copolystyrenes doped with sulfonated single-walled carbon nanotubes. *J. Membr. Sci.* **2016,** *514*, 527-536.

12.   Kucernak, A. R.; Muir, B., Analysis of the electrical and mechanical time response of solid polymer–platinum composite membranes. *Electrochim. Acta* **2001,** *46*, 1313-1322.

13.   Karim, M. R.; Hatakeyama, K.; Matsui, T.; Takehira, H.; Taniguchi, T.; Koinuma, M.; Matsumoto, Y.; Akutagawa, T.; Nakamura, T.; Noro, S.-i.; Yamada, T.; Kitagawa, H.; Hayami, S., Graphene Oxide Nanosheet with High Proton Conductivity. *J. Am. Chem. Soc.* **2013,** *135* (22), 8097-8100.

14.   Dikin, D. A.; Stankovich, S.; Zimney, E. J.; Piner, R. D.; Dommett, G. H. B.; Evmenenko, G.; Nguyen, S. T.; Ruoff, R. S., Preparation and characterization of graphene oxide paper. *Nature* **2007,** *448* (7152), 457-460.

15.   Ko, T.; Kim, K.; Lim, M.-Y.; Nam, S. Y.; Kim, T.-H.; Kim, S.-K.; Lee, J.-C., Sulfonated poly(arylene ether sulfone) composite membranes having poly(2,5-benzimidazole)-grafted graphene oxide for fuel cell applications. *J. Mater. Chem.* **2015,** *3* (41), 20595-20606.

16.   Thimmappa, R.; Devendrachari, M. C.; Kottaichamy, A. R.; Tiwari, O.; Gaikwad, P.; Paswan, B.; Thotiyl, M. O., Stereochemistry-Dependent Proton Conduction in Proton Exchange Membrane Fuel Cells. *Langmuir* **2016,** *32* (1), 359-365.

17.   Ravikumar; Scott, K., Freestanding sulfonated graphene oxide paper: a new polymer electrolyte for polymer electrolyte fuel cells. *Chem. Commun.* **2012,** *48* (45), 5584-5586.

18.   Kumar, R.; Mamlouk, M.; Scott, K., Sulfonated polyether ether ketone – sulfonated graphene oxide composite membranes for polymer electrolyte fuel cells. *RSC Adv.* **2014,** *4* (2), 617-623.

19.   Falcão, D. S.; Rangel, C. M.; Pinho, C.; Pinto, A. M. F. R., Water Transport through a Proton-Exchange Membrane (PEM) Fuel Cell Operating near Ambient Conditions: Experimental and Modeling Studies. *Energy Fuels* **2009,** *23* (1), 397-402.

20.   Feindel, K. W.; Bergens, S. H.; Wasylishen, R. E., Insights into the Distribution of water in a Self-Humidifying H_2/O_2 Proton-Exchange Membrane Fuel Cell Usi--ng 1H NMR Microscopy. *J. Am. Chem. Soc.* **2006,** *128* (43), 14192-14199.

21.   Yi, J. S.; Yang, J. D.; King, C., Water management along the flow channels of PEM fuel cells. *Int. J. Hydrog. Energy.* **2004,** *50* (10), 2594-2603.

22.   Wang, Z.; Qu, L.; Zeng, Y.; Guo, X.; Shao, Z.; Yi, B., Investigation of water transport in fuel cells using water transport plates and solid plates. *RSC Adv.* **2018,** *8* (3), 1503-1510.

23.   Chua, C. K.; Pumera, M., Chemical reduction of graphene oxide: a synthetic chemistry viewpoint. *Chem. Soc. Rev.* **2014,** *43* (1), 291-312.

24.   Medhekar, N. V.; Ramasubramaniam, A.; Ruoff, R. S.; Shenoy, V. B., Hydrogen Bond Networks in Graphene Oxide Composite Paper: Structure and Mechanical Properties. *ACS Nano* **2010,** *4* (4), 2300-2306.

25.   Miyatake, K., Membrane Electrolytes membrane electrolytes, from Perfluoro Sulfonic Acid (PFSA) to Hydrocarbon Ionomers. In *Encyclopedia of Sustainability Science and Technology*, Meyers, R. A., Ed. Springer New York: New York, NY, 2012; pp 6538-6565.

26.   Dybtsev, D. N.; Ponomareva, V. G.; Aliev, S. B.; Chupakhin, A. P.; Gallyamov, M. R.; Moroz, N. K.; Kolesov, B. A.; Kovalenko, K. A.; Shutova, E. S.; Fedin, V. P., High Proton Conductivity and Spectroscopic Investigations of Metal–

Organic Framework Materials Impregnated by Strong Acids. *ACS Appl. Mater. Interfaces* **2014,** *6* (7), 5161-5167.

27.   Brandell, D.; Karo, J.; Liivat, A.; Thomas, J. O., Molecular dynamics studies of the Nafion®, Dow® and Aciplex® fuel-cell polymer membrane systems. *J. Mol. Model.* **2007,** *13* (10), 1039-1046.

28.   Yen, C.-Y.; Lee, C.-H.; Lin, Y.-F.; Lin, H.-L.; Hsiao, Y.-H.; Liao, S.-H.; Chuang, C.-Y.; Ma, C.-C. M., Sol–gel derived sulfonated-silica/Nafion® composite membrane for direct methanol fuel cell. *J. Power Sources* **2007,** *173* (1), 36-44.

29.   Vishnyakov, A.; Neimark, A. V., Molecular Simulation Study of Nafion Membrane Solvation in Water and Methanol. *J. Phys. Chem. B.* **2000,** *104* (18), 4471-4478.

30.   Nagao, M.; Kobayashi, K.; Yamamoto, Y.; Hibino, T., Rechargeable PEM Fuel-Cell Batteries Using Quinones as Hydrogen Carriers. *J. Electrochem. Soc.* **2015,** *162* (4), F410-F418.

31.   Son, E. J.; Kim, J. H.; Kim, K.; Park, C. B., Quinone and its derivatives for energy harvesting and storage materials. *J. Mater. Chem.* **2016,** *4* (29), 11179-11202.

32.   Shi, R. R. S.; Tessensohn, M. E.; Lauw, S. J. L.; Foo, N. A. B. Y.; Webster, R. D., Tuning the reduction potential of quinones by controlling the effects of hydrogen bonding, protonation and proton-coupled electron transfer reactions. *Chem. Commun.* **2019,** *55* (16), 2277-2280.

33.   Quan, M.; Sanchez, D.; Wasylkiw, M. F.; Smith, D. K., Voltammetry of Quinones in Unbuffered Aqueous Solution: Reassessing the Roles of Proton Transfer and Hydrogen Bonding in the Aqueous Electrochemistry of Quinones. *J. Am. Chem. Soc.* **2007,** *129* (42), 12847-12856.

34.   Marcano, D. C.; Kosynkin, D. V.; Berlin, J. M.; Sinitskii, A.; Sun, Z.; Slesarev, A.; Alemany, L. B.; Lu, W.; Tour, J. M., Improved Synthesis of Graphene Oxide. *ACS Nano* **2010,** *4* (8), 4806-4814.

35. Chen, J.; Yao, B.; Li, C.; Shi, G., An improved Hummers method for eco-friendly synthesis of graphene oxide. *Carbon* **2013,** *64*, 225-229.

36. Müller, F.; Ferreira, C. A.; Azambuja, D. S.; Alemán, C.; Armelin, E., Measuring the Proton Conductivity of Ion-Exchange Membranes Using Electrochemical Impedance Spectroscopy and Through-Plane Cell. *J. Phys. Chem. B.* **2014,** *118* (4), 1102-1112.

37. Zhao, C.; Lin, H.; Shao, K.; Li, X.; Ni, H.; Wang, Z.; Na, H., Block sulfonated poly(ether ether ketone)s (SPEEK) ionomers with high ion-exchange capacities for proton exchange membranes. *J. Power Sources* **2006,** *162* (2), 1003-1009.

38. Stockton, W. B.; Rubner, M. F., Molecular-Level Processing of Conjugated Polymers. 4. Layer-by-Layer Manipulation 4. Layer by layer manupulation of Polyaniline via Hydrogen-Bonding Interactions. *Macromolecules* **1997,** *30* (9), 2717-2725.

39. Gordon, S. H.; Cao, X.; Mohamed, A.; Willett, J. L., Infrared spectroscopy method reveals hydrogen bonding and intermolecular interaction between components in polymer blends. *J. Appl. Polym. Sci.* **2005,** *97* (3), 813-821.

40. Ryu, I. S.; Liu, X.; Jin, Y.; Sun, J.; Lee, Y. J., Stoichiometric analysis of competing intermolecular hydrogen bonds using infrared spectroscopy. *RSC Adv.* **2018,** *8* (42), 23481-23488.

41. Behera, B.; Das, P. K., Blue- and Red-Shifting Hydrogen Bonding: A Gas Phase FTIR and Ab Initio Study of RR'CO···DCCl₃ and RR'S···DCCl₃ Complexes. *J. Phys. Chem. A.* **2018,** *122* (18), 4481-4489.

42. Laporta, M.; Pegoraro, M.; Zanderighi, L., Perfluorosulfonated membrane (Nafion): FT-IR study of the state of water with increasing humidity. *Phys. Chem. Chem. Phys* **1999,** *1* (19), 4619-4628.

43.   Kavc, T.; Kern, W.; Ebel, M. F.; Svagera, R.; Pölt, P., Surface Modification of Polyethylene by Photochemical Introduction of Sulfonic Acid Groups. *Chem. Mater.* **2000,** *12* (4), 1053-1059.

44.   Harrison, W. L.; Hickner, M. A.; Kim, Y. S.; McGrath, J. E., Poly(Arylene Ether Sulfone) Copolymers and Related Systems from Disulfonated Monomer Building Blocks: Synthesis, Characterization, and Performance – A Topical Review. *Fuel Cells* **2005,** *5* (2), 201-212.

45.   Flint, S. D.;   Slade, R. C. T., Investigation of radiation-grafted PVDF-g-polystyrene-sulfonic-acid ion exchange membranes for use in hydrogen oxygen fuel cells. *Solid State Ion.* **1997,** *97* (1), 299-307.

46.   Chen, S.-L.; Krishnan, L.; Srinivasan, S.; Benziger, J.; Bocarsly, A. B., exchange r--esin/polystyrene sulfonate composite membranes for PEM fuel cells. *J. Membr. Sci.* **2004,** *243* (1), 327-333.

47.   Day, T. J. F.; Schmitt, U. W.; Voth, G. A., The Mechanism of Hydrated Proton Transport in Water. *J. Am. Chem. Soc.* **2000,** *122* (48), 12027-12028.

48.   Li Barnett, I.; Groenzin, H.; Shultz, M. J., Hydrogen Bonding in the Hexagonal Ice Surface. *J. Phys. Chem. A.* **2011,** *115* (23), 6039-6045.

Chapter 5b

Implications of Reduction in Thickness of Graphene Oxide Membrane on Fuel Cell Performance

Abstract

Graphene oxide (GO) contains randomly distributed non-conductive sp^3-C domains with planar acidity making it simultaneously an electrical insulator and a proton conductor. GO's ability for cationic transport with its impermeability to molecular fuels projected them as inexpensive and sustainable membranes for proton exchange membrane fuel cells (PEMFC). Nevertheless, the room temperature proton transport in bulk GO is at least an order lower than that of state-of-the-art Nafion membrane, that in turn challenge the construction of a practical energy conversion device with the former. To reduce the performance gap between state of art Nafion membrane and GO membrane one straight forward approach is the reduction in thickness and we show in this Chapter that this approach has some serious consequences. We show that the proton flux in GO along the H-bonded network projected outward the carbon planes can be significantly amplified by thinning the 2D-carbon layer stacking in GO. This consequently enhanced the room temperature fuel cell performance metrics of thin layer GO based fuel cell with a peak power density of ~410 mW cm^{-2} at a peak current density of ~1300 mA cm^{-2}. This study shows that though thickness reduction enhances the fuel cell performance, equally it also increases fuel crossover (~3 times compared to bulk GO). This suggests that fuel cross over on thickness reduction needs to be addressed if this approach is to be implemented for practical benefits.
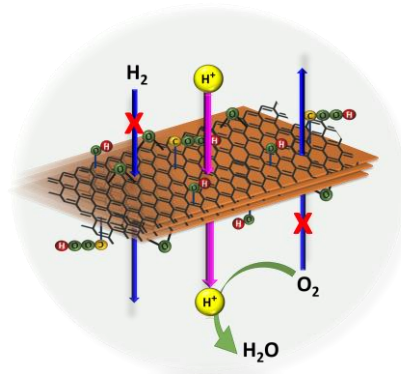
Declaration: The work has been published in the following journal:

ACS Sustainable Chem. Eng. 2019, 7, 16, 14189–14194. Copyright. American Chemical Society.

5b.1. Introduction

Electrochemical energy storage and conversion devices such as batteries, fuel cells, supercapacitors and solar cells have the potential to address environmental pollution and associated climate change.[1-14] Carbon-based membranes have been investigated for proton shuttling in proton exchange membrane fuel cells (PEMFC) due to their fuel barrier nature coupled with their ability to transport cationic species.[15-19] Scott *et.al* reported the first H_2-O_2 fuel cell with a free-standing GO membrane[16,20] which was followed subsequently by many other groups.[21, 22] Matsumoto *et. al* observed that the in-plane proton conductivities of multi-layer GO were higher than single-layer GO by several orders due to increase in conduction pathway, hydration dynamics, and water content.[23] Their blocking experiments with ethylenediamine (EDA) confirmed that the epoxide functionalities on GO plays a dominant role in proton conduction.[23] Kim *et.al* reported that sulfonic acid-functionalized graphene composite membrane with Nafion can be a potential solid acid H^+ ion conducting fuel cell membrane for PEMFC under relatively low humidity.[17] Dong Jin Yoo et.al prepared Nafion composite membranes with Fe_3O_4 nanoparticles anchored over sulfonated graphene oxide for high temperature and low humidity PEMFC applications.[24] The same group fabricated quadratic hybrid membranes comprising Fe_3O_4 nanoparticles anchored over functionalized graphene oxide (FGO), fluorinated poly arylene propane biphenyl (FPAPB) and sulfonated poly ether ether ketone (SPEEK) and observed that magnetically aligned Fe_3O_4-FGO demonstrating better performance metrics compared to randomly oriented Fe_3O_4-FGO composite membranes.[25]

Nevertheless, the room temperature fuel cell performance with graphene oxide (GO) has been found to be very much inferior to the state-of-the-art Nafion membranes.[26-28] This inferior performance metrics with GO is primarily attributed to its almost 10 times lower proton transport compared to Nafion.[20,29,30] The straightforward approach to improve the proton shuttling through GO membrane is the reduction in its thickness as it will reduce the membrane resistance and hence will increase its proton conduction. However, as we show in this Chapter it has some serious implications on the performance of GO based fuel cells. We show that the proton flux in GO along the H bonded network

formed by hydrophilic functionalities projected outward the carbon planes, can be significantly amplified by controlling the 2D-carbon layer stacking with fuel cell performance metrics comparable to Nafion based (of similar thickness) fuel cells. The resulting thin layer GO based fuel cell with non-humidified H_2 and O_2 delivered an open circuit voltage of ~700 mV, a peak power of ~410 mW cm^{-2} at ~1300 mA cm^{-2} peak current, thereby decreasing the cost of electricity per kW significantly from a PEMFC. One of the serious consequences of reducing the thickness is fuel crossover which got enhanced by ~3 times. This fuel crossover is responsible for the reduction in open circuit voltage (OCV) of thin layer GO membrane-based fuel cells (~0.7 V). This study suggests that if this thickness reduction approach has to be applied for practical energy conversion applications, the fuel crossover should be addressed by adopting material's engineering strategies.

5b.2. Experimental

5b.2.1. MEA preparation and fuel cell characterization

The synthesis of graphene oxide dispersive solution is explained in Chapter 4a (experimental section). The catalyst inks for both anode and cathode (0.2 mg cm^{-2} of 20 wt% Pt/C, Johnson Mathey) were prepared by ultrasonicating with isopropanol and Nafion ionomer (5 wt% in isopropyl alcohol). The ink was sprayed onto gas diffusion electrodes (carbon paper) with a hydrophobic micro-porous layer (H2315 T10AC1, Freudenberg FFCCT, Germany). Thin layer GO membrane electrode assembly (MEA) was constructed by spray coating the GO solution onto the anode catalyst layer and then allowed it for air drring. The thickness of the membrane was modulated by controlling the weight % of GO in the dispersion and the volume of GO dispersion used for spray coating. The thin layer spray coated membrane was sandwiched between the catalyst layers by keeping the cathode catalyst layer over the spray coated membrane. MEA was placed between two graphite blocks with an active electrode area of 2 cm^2 formed by the serpentine gas flow channels. Gold-plated steel bolts were drilled into the graphite blocks for electrical contacts. Non-humidified H_2 and O_2 at a flow rate of 0.1 dm^3 min^{-1} were continuously fed to the respective half cells for fuel cell studies. The fuel cell preconditioning was carried out at 0.4 V for an hour before the fuel cell measurements. For bulk GO MEA, the GO solution was casted on smooth glass slide and then air dried.

After peeling off the membrane, it was sandwiched between the anode and cathode catalyst layers as explained above. Cyclic voltammetry in the fuel cell mode was performed with N_2 purged cathode as the working electrode. Linear sweep voltammetry was performed to measure H_2 crossover by scanning the potential positively from the open circuit voltage with the cathode kept under N_2 blanket as the working electrode. Impedance measurements were carried out at the open circuit voltage in the frequency range of 100 kHz to 10 mHz with a 10 mV (peak to peak) AC amplitude. The H_2 crossover rate (H_2 crossover flux in mol $cm^{-2}s^{-1}$) was calculated using the Faraday's law.[31,32]

$$J_{flux} = i_{lim} \: / \: (n * F) \qquad\qquad (5b.1)$$

where, i_{lim} is the limiting current/cm^2 extracted from linear sweep voltammetry, n is the number of electrons involved in the reaction and F is the Faraday constant.

5b.3. Results and discussion

5b.3.1 Physiochemical characterization of MEA

The preparations and characterizations of GO membrane are already explained in Chapter 4a (see experimental section). The optical image of the GO coated Toray carbon paper shows a distinct difference from the uncoated region, Figure 5b.1a and the coated area was nearly uniform Figure 5b.1a. The SEM cross-sectional image of GO coated catalyst layer demonstrate a membrane thickness of ~3 μm and a well contacted interface, Figure 5b.1b. The stacking of individual GO sheets can be seen in the enlarged image, Figure 5b.1c.
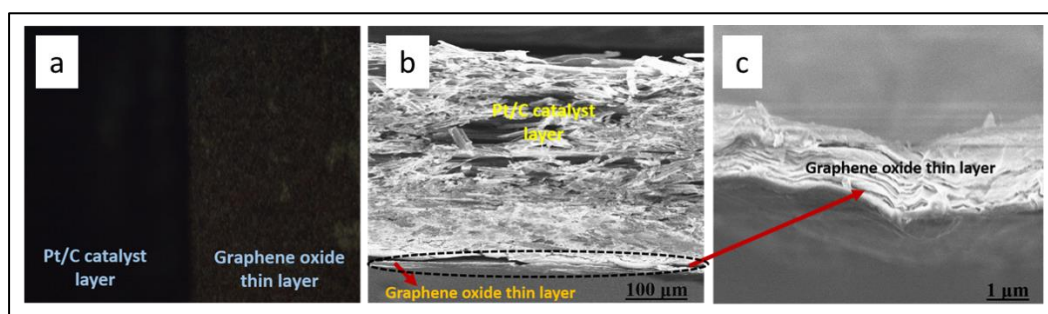
Figure 5b.1: (a) Optical image of spray coated GO regions distinctly standing out from uncoated catalyst (platinum supported on carbon) regions, (b) SEM cross sectional image of thin layer GO-membrane electrode assembly (GO-MEA) and (c) enlarged view of the thin layer GO membrane region in Figure 5b.1b.

5b.3.2 Hydrogen adsorption study of GO MEAs

To investigate the hydrogen adsorption charge in GO based MEAs, cyclic voltammetry of GO based fuel cells (Figure 5b.2) with the cathode (under Ar blanket) as the working electrode vs. anodic half-cell (under H_2 atmosphere) as the counter and reference electrode were carried out which clearly show amplified hydrogen adsorption and desorption peaks close to 0 V vs. RHE for thin film GO based fuel cells compared to bulk GO based fuel cells. This indicates the higher hydrogen adsorption charge in thin layer GO MEA (~1.7 mC cm^{-2}) compared with a GO-MEA of ~25 µm thick (~0.5 mC cm^{-2}). This hydrogen adsorption charge is directly proportional to the proton flux and this suggests that proton flux across the membrane in GO-based membranes can be amplified by thinning the 2D layer stacking.
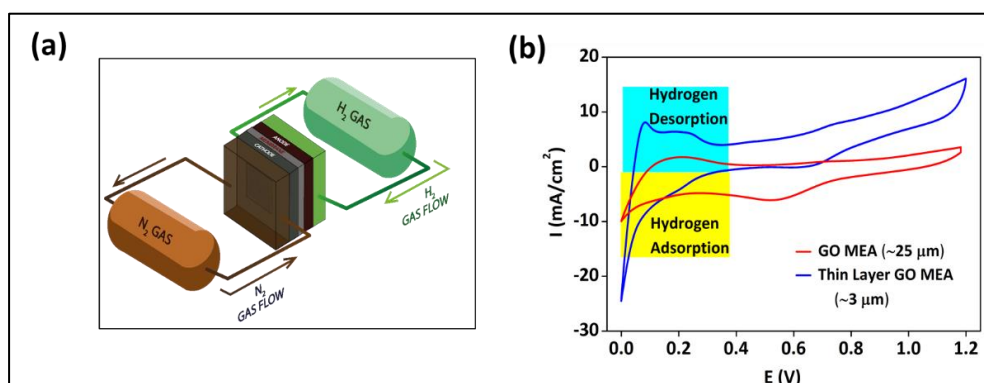
Figure 5b.2: (a) Schematics of the setup used for investigating the hydrogen adsorption charge. The cathode kept under a blanket of Ar was used as the working electrode vs. the anode purged with H_2 as the reference and counter electrodes. (b) Cyclic voltammograms of GO based fuel cells at 20 mV s^{-1} in two electrode configurations as shown in Figure 5b.2a.

5b.3.3 Proton conductance capability measurements of GO MEAs

The electrochemical impedance spectra (EIS) in the fuel cell mode, Figure 5b.3a and Table 5b.1, suggest a significant reduction in electrolyte resistance for thin layer grap-
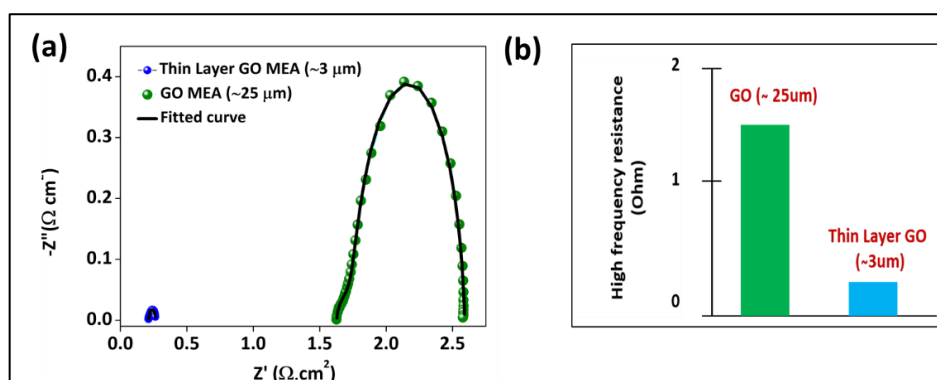
Figure 5b.3: (a) Nyquist plots of GO-MEAs at 0 V vs. OCV and (b) corresponding higher frequency resistance extracted from the Figure 5b.3a.

-hene oxide (GO) compared to GO-MEA of ~25 µm, suggesting the interplay between fuel cell transport phenomena and thickness of the ion conductor. The high frequency resistance (HFR) signaling the membrane resistance is decreased noticeably (~8 times) in thin layer GO compared to GO-MEA of ~25 µm (Figure 5b.3b) signaling the higher proton flux in thin layer GO MEA.

5b.3.4 Fuel cell investigations with GO MEAs

The fuel cell performance at room temperature with non humidified H_2 and O_2 is shown in Figure 5b.4b for thin layer GO (~3 µm thick) in comparison to GO membrane of ~25 µm thickness. Thin layer GO based fuel cell delivered an open circuit voltage of ~700 mV which was lower than that observed on ~25 µm thick GO membrane (~1 V) and it could be due to the higher fuel cross-over when thickness is reduced. The peak power with thin film GO is ~410 mW cm^{-2} at a peak current of ~1300 mA cm^{-2} (Table 5b.1) which are ~5 times higher than ~25 µm thick GO membrane, Table 5b.1 and Figure 5b.4b. All these suggest that the proton flux is inversely proportional to GO membrane thickness as suggested by Karim et.al.,[29] and thickness reduction can lead to the amplication of the fuel cell performance metrics in GO based fuel cells.
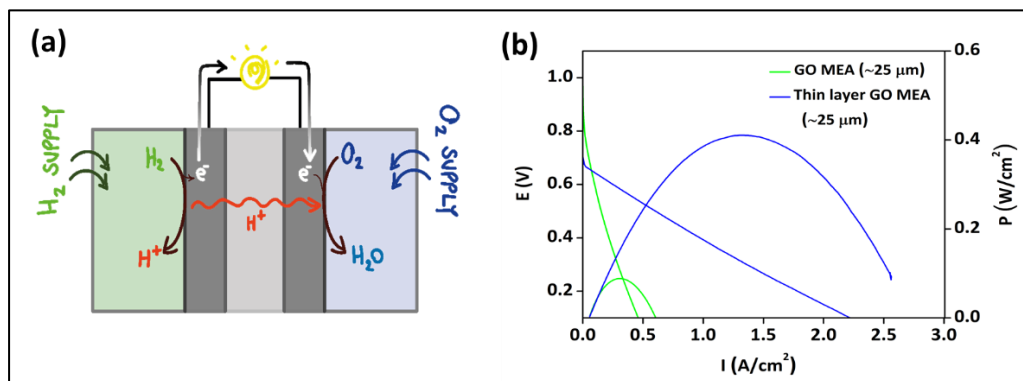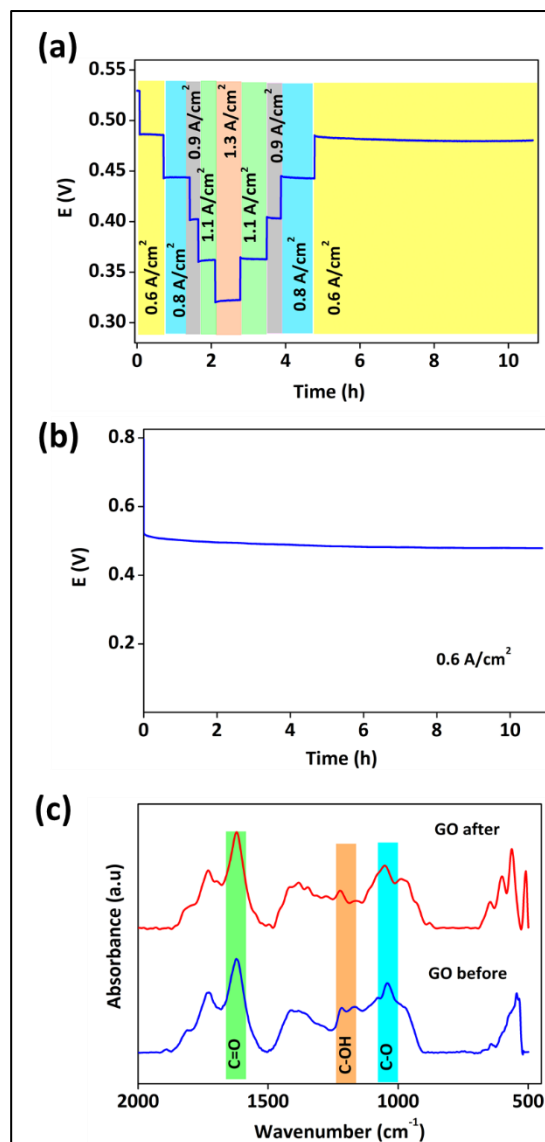

Figure 5b.4: (a) Schematics of GO based fuel cell and (b) room temperature fuel cell polarization curves of GO based fuel cells.

Table 5b. 1. Fuel cell relevant parameters extracted from Figure 5b.4b.

MEA type	Thin Layer GO (~3 µm)	GO (~25 µm)

Peak Current Density (mA/cm²)	1300	240
Peak Power Density (mW/cm²)	410	80
OCV (V)	0.70	0.97

Figure 5b.5: (a) Rate capability of thin film GO MEA at different current densities, (b) durability study of thin film GO MEA at 0.6 A cm⁻² and (c) FTIR spectra of GO membrane before and after the long-term durability test.

Thin layer GO fuel cells demosntrated stable voltage profiles without noticeable decline during long-term stability tests at different current densities, Figure 5b.5a and Figure 5b.5b. Further the stability of thin film GO membrane was investigated by FTIR spectroscopy before and after long term polarization, Figure 5b.5c. FTIR patterns of thin layer GO membrane demonstrated negligible change before and after long term polarization indicating its long-term stability under chosen experimental conditions.
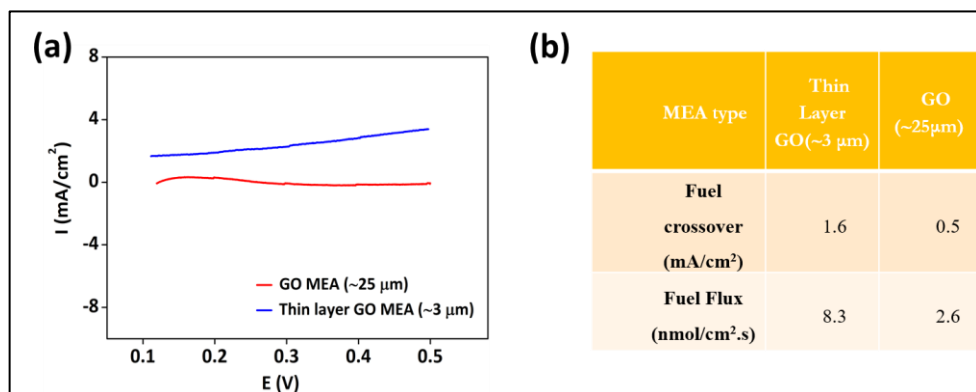
Figure 5b.6: (a) H_2 cross over study in GO based MEAs obtained by scanning the potential of the cathode positively from the OCV at 1 mV s^{-1} scan rate. (b) Fuel cross over parameters extracted from Figure 5b.6a.

In order to assess the fuel cross over during thickness reduction, H_2 cross over was monitored by scanning the potential of the cathode (in Ar blanket) positively from the OCV with respect to the anode kept under the H_2 atmosphere. The corresponding linear sweep voltammetry, Figure 5b.6a, suggest a H_2 cross over current of ~1.6 mA cm^{-2} on thin film GO MEA compared to ~0.50 mA cm^{-2} on GO MEA of ~25 μm thick, suggesting the fuel cross over increases on thickness reduction, which is line with the results on other membranes studied in the literature.[33,34] The crossover hydrogen flux (H_2 crossover flux in mol cm^{-2}s^{-1}) was calculated using the Faraday's law[31,32] and is found to be 8.3 x 10^{-9} mol cm^{-2}s^{-1} on thin layer GO membrane compared to 2.6 x 10^{-9} mol cm^{-2}s^{-1} on GO membrane of ~25 μm thickness, Figure 5b.6b. This may be responsible for the lower OCV with thin layer GO MEA, Figure 5b.4b and Table 5b.1. This further indicates that thickness reduction has serious implications on the performance of GO based fuel cells. Even though the fuel crossover is higher in case of the thin layer GO MEA the comparison of its fuel cell performance with state-of-the-art Nafion membrane of almost similar thickness, suggest that the performance is comparable, Figure 5b.7. This indicates that, though by reducing the thickness of GO membrane the performance gap between Nafion membrane and GO membrane can be bridged, for practical applications with thin layer

GO membrane, the issue of fuel cross over should be addressed by adopting material's engineering strategies.
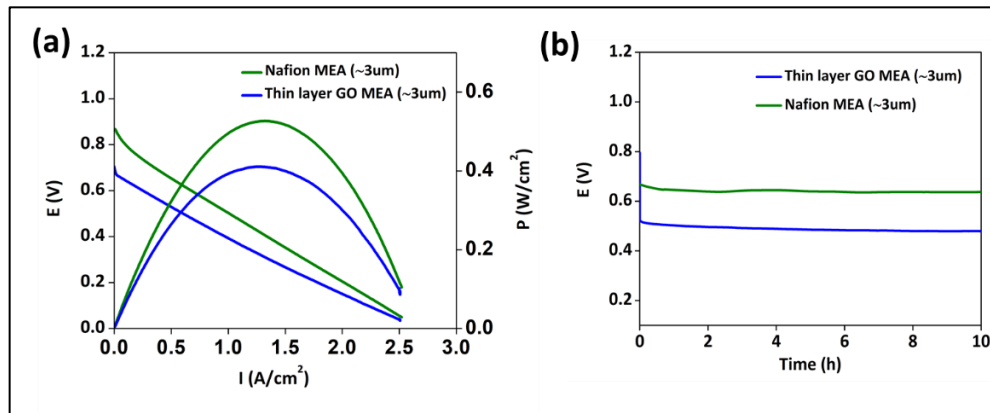
Figure 5b.7: (a) Polarization curves for thin film GO MEA (~3 μm) and thin Nafion MEA (~3 μm) recorded at room temperature and (b) durability study of thin layer GO MEA and thin Nafion MEA of almost the same thickness (~3 μm) at 0.6 A cm^{-2}. Non-humidified H_2 and O_2 at a flow rate of 0.1 dm^3 min^{-1} were continuously fed to the respective half cells for fuel cell studies.

5b.4. Conclusions

We have demonstrated the implications of thickness reduction of GO membrane on its room temperature H_2-O_2 fuel cell performance. Controlled thinning of 2D-carbon layer stacking in GO significantly amplified proton flux compared to GO membranes of higher thickness. Such a fuel cell delivered an OCV of ~700 mV with a peak power density of ~410 mW cm^{-2} at a peak current density of ~1300 mA cm^{-2}. Even through controlled thinning of 2D layer stacking in GO has significantly improved the fuel cell performance metrics, the reduction in the thickness of GO membrane, concomitantly amplified its fuel crossover by ~3 times which in turn might be responsible for its lower OCV in polarization studies. Even though the performance gap between Nafion based fuel cells and GO based fuel cells can be bridged by this approach of thickness reduction, the concomitant enhancement in fuel crossover demands the adoption of material's engineering strategies to address this challenge if this approach has to be implemented in practical devices.

5b.5. References

1.   Mourad, E.; Coustan, L.; Lannelongue, P.; Zigah, D.; Mehdi, A.; Vioux, A.; Freunberger, Stefan A.; Favier, F.; Fontaine, O., Biredox ionic liquids with solid-

like redox density in the liquid state for high-energy supercapacitors. *Nat. Mater.* **2017**, *16* (4), 446-453.

2. Schafzahl, L.; Mahne, N.; Schafzahl, B.; Wilkening, M.; Slugovc, C.; Borisov, S. M.; Freunberger, S. A., Singlet Oxygen during Cycling of the Aprotic Sodium–O_2 Battery. *Angew. Chem. Int. Ed.* **2017**, *56* (49), 15728-15732.

3. Cavaliere, S.; Subianto, S.; Savych, I.; Jones, D. J.; Rozière, J., Electrospinning: designed architectures for energy conversion and storage devices. *Energy Environ. Sci* **2011**, *4* (12), 4761-4785.

4. Miroshnikov, M.; Divya, K. P.; Babu, G.; Meiyazhagan, A.; Reddy Arava, L. M.; Ajayan, P. M.; John, G., Power from nature: designing green battery materials from electroactive quinone derivatives and organic polymers. *J. Mater. Chem. A* **2016**, *4* (32), 12370-12386.

5. Goodwin, S.; Walsh, D. A., Closed Bipolar Electrodes for Spatial Separation of H2 and O_2 Evolution during Water Electrolysis and the Development of High-Voltage Fuel Cells. *ACS Appl. Mater. Interfaces* **2017**, *9* (28), 23654-23661.

6. Bentley, C. L.; Andronescu, C.; Smialkowski, M.; Kang, M.; Tarnev, T.; Marler, B.; Unwin, P. R.; Apfel, U.-P.; Schuhmann, W., Local Surface Structure and Composition Control the Hydrogen Evolution Reaction on Iron Nickel Sulfides. *Angew. Chem. Int. Ed.* **2018**, *57* (15), 4093-4097.

7. Reynard, D.; Dennison, C. R.; Battistel, A.; Girault, H. H., Efficiency improvement of an all-vanadium redox flow battery by harvesting low-grade heat. *J. Power Sources* **2018**, *390*, 30-37.

8. Reddy, M. V.; Subba Rao, G. V.; Chowdari, B. V. R., Metal Oxides and Oxysalts as Anode Materials for Li Ion Batteries. *Chem. Rev.* **2013**, *113* (7), 5364-5457.

9. Liu, S.; Dong, Y.; Zhao, C.; Zhao, Z.; Yu, C.; Wang, Z.; Qiu, J., Nitrogen-rich carbon coupled multifunctional metal oxide/graphene nanohybrids for long-life lithium storage and efficient oxygen reduction. *Nano Energy* **2015**, *12*, 578-587.

10. Lin, M.-C.; Gong, M.; Lu, B.; Wu, Y.; Wang, D.-Y.; Guan, M.; Angell, M.; Chen, C.; Yang, J.; Hwang, B.-J.; Dai, H., An ultrafast rechargeable aluminium-ion battery. *Nature* **2015**, *520* (7547), 324-328.

11. Ghobadi, S.; Işıkel Şanlı, L.; Bakhtiari, R.; Alkan Gürsel, S., Green Composite Papers via Use of Natural Binders and Graphene for PEM Fuel Cell Electrodes. *ACS Sustain. Chem. Eng.* **2017**, *5* (9), 8407-8415.

12. del Cueto, M.; Ocón, P.; Poyato, J. M. L., Comparative Study of Oxygen Reduction Reaction Mechanism on Nitrogen-, Phosphorus-, and Boron-Doped Graphene Surfaces for Fuel Cell Applications. *J. Phys. Chem. C* **2015**, *119* (4), 2004-2009.

13. Gnana kumar, G.; Kirubaharan, C. J.; Udhayakumar, S.; Ramachandran, K.; Karthikeyan, C.; Renganathan, R.; Nahm, K. S., Synthesis, Structural, and Morphological Characterizations of Reduced Graphene Oxide-Supported Polypyrrole Anode Catalysts for Improved Microbial Fuel Cell Performances. *ACS Sustain. Chem. Eng.* **2014**, *2* (10), 2283-2290.

14. Naresh, N.; Wasim, F. G. S.; Ladewig, B. P.; Neergat, M., Removal of surfactant and capping agent from Pd nanocubes (Pd-NCs) using tert-butylamine: its effect on electrochemical characteristics. *J. Mater. Chem. A* **2013**, *1* (30), 8553-8559.

15. Hatakeyama, K.; Karim, M. R.; Ogata, C.; Tateishi, H.; Funatsu, A.; Taniguchi, T.; Koinuma, M.; Hayami, S.; Matsumoto, Y., Proton Conductivities of Graphene Oxide Nanosheets: Single, Multilayer, and Modified Nanosheets. *Angew. Chem. Int. Ed.* **2014**, *53* (27), 6997-7000.

16. Ravikumar; Scott, K., Freestanding sulfonated graphene oxide paper: a new polymer electrolyte for polymer electrolyte fuel cells. *Chem. Commun.* **2012**, *48* (45), 5584-5586.

17. Sahu, A. K.; Ketpang, K.; Shanmugam, S.; Kwon, O.; Lee, S.; Kim, H., Sulfonated Graphene–Nafion Composite Membranes for Polymer Electrolyte Fuel Cells Operating under Reduced Relative Humidity. *J. Phys. Chem. C* **2016**, *120* (29), 15855-15866.

18.   Ko, T.; Kim, K.; Lim, M.-Y.; Nam, S. Y.; Kim, T.-H.; Kim, S.-K.; Lee, J.-C., Sulfonated poly(arylene ether sulfone) composite membranes having poly(2,5-benzimidazole)-grafted graphene oxide for fuel cell applications. *J. Mater. Chem. A.* **2015**, *3* (41), 20595-20606.

19.   Malinowski, M.; Iwan, A.; Tazbir, I.; Boharewicz, B.; Sikora, A.; Stafiniak, A., Polyazomethines and their acid–base interactions with Nafion and Nafion–imidazole membranes for efficient fuel cells. *Sustain. Energy Fuels* **2017**, *1* (8), 1810-1819.

20.   Cao, Y.-C.; Xu, C.; Wu, X.; Wang, X.; Xing, L.; Scott, K., A poly (ethylene oxide)/graphene oxide electrolyte membrane for low temperature polymer fuel cells. *J. Power Sources* **2011**, *196* (20), 8377-8382.

21.   Zarrin, H.; Higgins, D.; Jun, Y.; Chen, Z.; Fowler, M., Functionalized Graphene Oxide Nanocomposite Membrane for Low Humidity and High Temperature Proton Exchange Membrane Fuel Cells. *J. Phys. Chem. C* **2011**, *115* (42), 20774-20781.

22.   Lei, M.; Wang, Z. B.; Li, J. S.; Tang, H. L.; Liu, W. J.; Wang, Y. G., CeO2 nanocubes-graphene oxide as durable and highly active catalyst support for proton exchange membrane fuel cell. *Sci. Rep.* **2014**, *4* (1), 7415.

23.   Tateishi, H.; Hatakeyama, K.; Ogata, C.; Gezuhara, K.; Kuroda, J.; Funatsu, A.; Koinuma, M.; Taniguchi, T.; Hayami, S.; Matsumoto, Y., Graphene Oxide Fuel Cell. *J. Electrochem. Soc.* **2013**, *160* (11), F1175-F1178.

24.   Vinothkannan, M.; Kim, A. R.; Gnana kumar, G.; Yoo, D. J., Sulfonated graphene oxide/Nafion composite membranes for high temperature and low humidity proton exchange membrane fuel cells. *RSC Adv.* **2018**, *8* (14), 7494-7508.

25.   Vinothkannan, M.; Kim, A. R.; Gnana kumar, G.; Yoon, J.-M.; Yoo, D. J., Toward improved mechanical strength, oxidative stability and proton conductivity of an aligned quadratic hybrid (SPEEK/FPAPB/Fe₃O₄-FGO) membrane for application in high temperature and low humidity fuel cells. *RSC Adv.* **2017**, *7* (62), 39034-39048.

26.   Liu, Y.; Wang, J.; Zhang, H.; Ma, C.; Liu, J.; Cao, S.; Zhang, X., Enhancement of proton conductivity of chitosan membrane enabled by sulfonated graphene oxide under both hydrated and anhydrous conditions. *J. Power Sources* **2014**, *269*, 898-911.

27.   Dikin, D. A.; Stankovich, S.; Zimney, E. J.; Piner, R. D.; Dommett, G. H. B.; Evmenenko, G.; Nguyen, S. T.; Ruoff, R. S., Preparation and characterization of graphene oxide paper. *Nature* **2007**, *448* (7152), 457-460.

28.   Wang, C.; Waje, M.; Wang, X.; Tang, J. M.; Haddon, R. C.; Yan, Proton Exchange Membrane Fuel Cells with Carbon Nanotube Based Electrodes. *Nano Lett.* **2004**, *4* (2), 345-348.

29.   Karim, M. R.; Hatakeyama, K.; Matsui, T.; Takehira, H.; Taniguchi, T.; Koinuma, M.; Matsumoto, Y.; Akutagawa, T.; Nakamura, T.; Noro, S.-i.; Yamada, T.; Kitagawa, H.; Hayami, S., Graphene Oxide Nanosheet with High Proton Conductivity. *J. Am. Chem. Soc.* **2013**, *135* (22), 8097-8100.

30.   He, G.; He, X.; Wang, X.; Chang, C.; Zhao, J.; Li, Z.; Wu, H.; Jiang, Z., A highly proton-conducting, methanol-blocking Nafion composite membrane enabled by surface-coating crosslinked sulfonated graphene oxide. *Chem. Commun.* **2016**, *52* (10), 2173-2176.

31.   Haussener, S.; Xiang, C.; Spurgeon, J. M.; Ardo, S.; Lewis, N. S.; Weber, A. Z., Modeling, simulation, and design criteria for photoelectrochemical water-splitting systems. *Energy Environ. Sci.* **2012**, *5* (12), 9922-9935.

32.   Cheng, X.; Zhang, J.; Tang, Y.; Song, C.; Shen, J.; Song, D.; Zhang, J., Hydrogen crossover in high-temperature PEM fuel cells. *J. Power Sources* **2007**, *167* (1), 25-31.

33.   Klingele, M.; Breitwieser, M.; Zengerle, R.; Thiele, S., Direct deposition of proton exchange membranes enabling high performance hydrogen fuel cells. *J. Mater. Chem. A.* **2015**, *3* (21), 11239-11245.

34.   Aricò, A. S; Sebastian, D.; Schuster, M.; Bauer, B.; D'Urso, C.; Lufrano, F.; Baglio, V., Selectivity of Direct Methanol Fuel Cell Membranes. *Membranes* **2015**, *5*, 793-809.

Chapter 6

Summary

In essence, the work presented in this thesis highlights the importance of carbon derived materials as electrodes in energy storage devices and as electrolytes (membranes) in energy conversion devices. Generally, carbon-based materials when utilized in aqueous rechargeable batteries suffer from various challenges like parasitic hydrogen evolution reactions, limited energy density due to underutilization of the dissolved electroactive species, instability of the electrode materials in aqueous environment, etc. The first part of this thesis explores the utilization of carbon derived materials as electrodes in aqueous rechargeable batteries to address some of their state-of-the-art issues and challenges and to investigate their unexplored properties. When it comes to the utilization of these carbon-based materials as electrolytes (membranes) in energy conversion devices such as fuel cells, water electrolyzer and unitized regenerative fuel cells, these materials have not been explored in their pristine form to shuttle protons. Therefore, the second part of this thesis explores the utilization of these carbon derived materials in their pristine form as electrolytes (membranes) in energy conversion devices. Chapter 1 highlights the importance, advantages, issues and challenges of carbon-based materials as electrodes and electrolytes in electrochemical energy storage and conversion devices. Though, carbon-based materials have interesting properties which make them ubiquitous in electrochemical energy systems, their utilization brings forth their own challenges and issues. Chapter 2 shows the applications of functionalized carbon derived materials to enhance the utilization of the dissolved electroactive species in aqueous rechargeable zinc ferricyanide battery. In this chapter, how the activation of coulombic forces at the CNT electrode/electrolyte interface gates the molecular transport by generating a directional electrostatic current contribution over the diffusion is demonstrated. It is demonstrated that, in iron based redox flow battery, this gated molecular flux almost doubles the volumetric energy density without compromising the power capability. Chapter 3 shows how the mode of synthesis of graphene-based materials improves the quality of reduced graphene oxide material with properties relevant for constructing an aqueous rechargeable sodium ion battery by suppressing the parasitic hydrogen evolution reaction chemistry during the charge chemistry and also explains the factors responsible for it. The second part of this thesis examines the utilization of these carbon derived materials as electrolytes (membranes) in energy conversion devices such as fuel cells, water electrolyzers and

unitized regenerative fuel cells. In chapter 4, freestanding GO membrane in its pristine form is explored as electrolyte to construct an atmospheric water electrolyzer and a unitized regenerative fuel cell. Since graphene oxide membrane has lower proton conductivity compared to the state-of-the-art Nafion membrane, how the proton conduction capability of GO membrane can be improved by introducing to its interlayer's proton carrying quinone molecules bearing proton shuttling sulfonic acid groups is explored in Chapter 5a. In Chapter 5b, another method to improve the proton conduction capability of GO membrane is explored by reducing the thickness of the GO membrane. Though this straightforward technique improves the proton conduction of GO, the approach has some serious implications in the performance of GO based fuel cells. It is demonstrated that, though proton flux across the membrane increases on thickness reduction, fuel crossover also increases simultaneously, which needs to be adequately addressed by materials engineering strategies like introducing suitable fillers and additives, adding other polymeric materials to make composite GO membranes etc., if this higher fuel cell performance metrics have to exploited for practical applications.
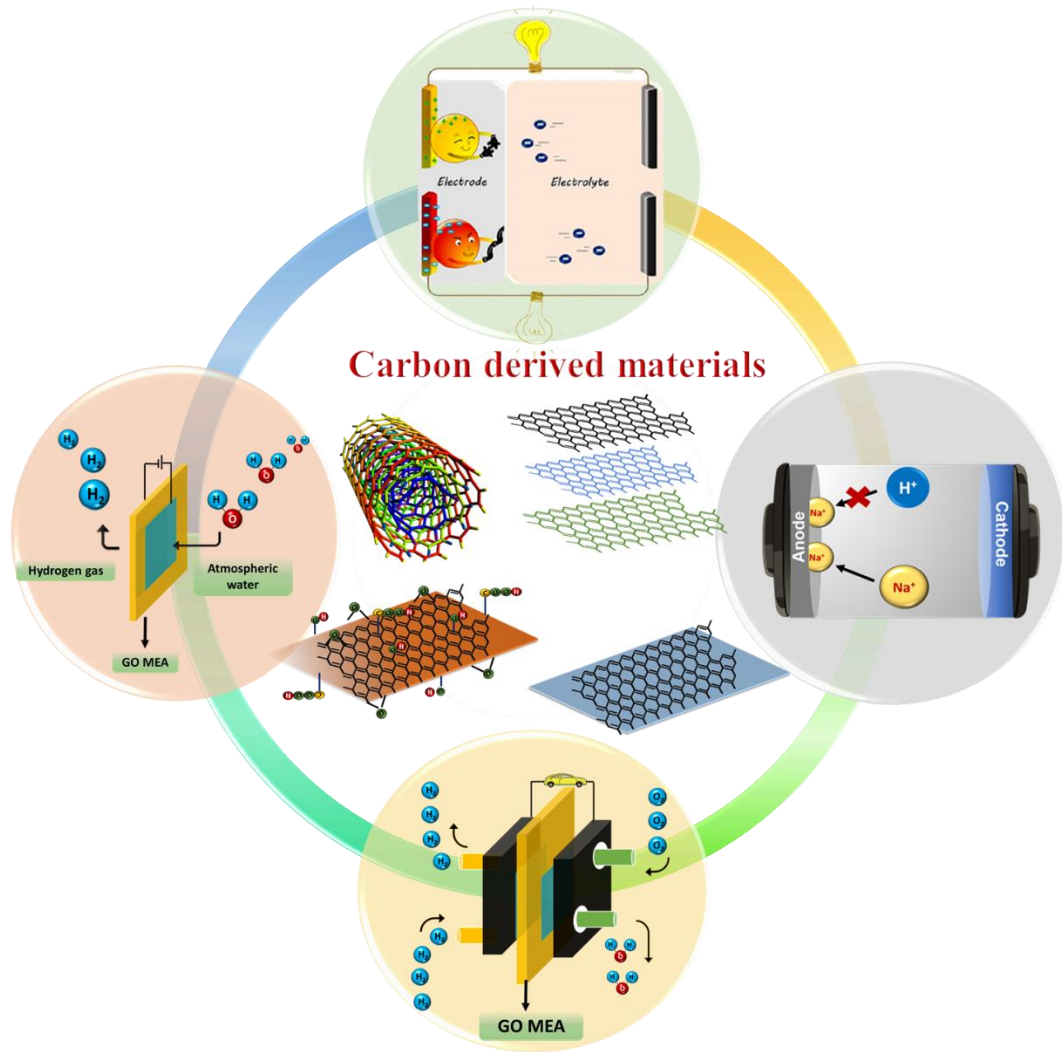
List of Publications

1. **Gautam, M**.; Bhat, Z. M.; Raafik, A.; Le Vot, S.; Devendrachari, M. C.; Kottaichamy, A. R.; Dargily, N. C.; Thimmappa, R.; Fontaine, O.; Thotiyl, M. O., Coulombic Force Gated Molecular Transport in Redox Flow Batteries. *J. Phys. Chem. Lett.* **2021,** *12* (5), 1374-1383.

2. Thimmappa, R*.; **Gautam, M***.; Devendrachari, M. C.; Kottaichamy, A. R.; Bhat, Z. M.; Umar, A.; Thotiyl, M. O., Proton-Conducting Graphene Membrane Electrode Assembly for High Performance Hydrogen Fuel Cells. *ACS Sustainable Chem. Eng.,* **2019,** *7* (16), 14189-14194.

3. Thimmappa, R*.; **Gautam, M.***; Aralekallu, S.; Devendrachari, M. C.; Kottaichamy, A. R.; Bhat, Z. M.; Thotiyl, M. O., A Rechargeable Aqueous Sodium-Ion Battery. *ChemElectroChem* **2019,** *6* (7), 2095-2099.

4. **Gautam, M.**; Chattanahalli Devendrachari, M.; Thimmappa, R.; Raja Kottaichamy, A.; Pottachola Shafi, S.; Gaikwad, P.; Makri Nimbegondi Kotresh, H.; Ottakam Thotiyl, M., Polarity governed selective amplification of through plane proton shuttling in proton exchange membrane fuel cells. *Phys. Chem. Chem. Phys.,* **2017,** *19* (11), 7751-7759.

5. Itagi, M.; Battu, S.; Devendrachari, M. C.; M. Bhat, Z.; Kottaichamy, A. R.; Pandit, D.; **Gautam, M**.; Thimmappa, R.; Sannegowda, L. K.; Thotiyl, M. O., Zinc Battery Driven by an Electro-Organic Reactor Cathode. *ACS Sustainable Chem. Eng.,* **2018,** *6* (11), 15007-15014.

6. Varhade, S.; Bhat, Z. M.; Thimmappa, R.; Devendrachari, M. C.; Kottaichamy, A. R.; **Gautam, M**.; Shafi, S. P.; Kalegowda, Y.; Thotiyl, M. O., A hybrid hydrazine redox flow battery with a reversible electron acceptor. *Phys. Chem. Chem. Phys.,* **2018,** *20* (33), 21724-21731.

7. Christudas Dargily, N.; Thimmappa, R.; Manzoor Bhat, Z.; Devendrachari, M. C.; Kottaichamy, A. R.; **Gautam, M**.; Shafi, S. P.; Thotiyl, M. O., A Rechargeable Hydrogen Battery. *J. Phys. Chem. Lett.* **2018,** *9* (10), 2492-2497.

8. Manzoor Bhat, Z.; Thimmappa, R.; Devendrachari, M. C.; Kottaichamy, A. R.; Shafi, S. P.; Varhade, S.; **Gautam, M**.; Thotiyl, M. O., Fuel Exhaling Fuel Cell. *J. Phys. Chem. Lett.* **2018,** *9* (2), 388-392.

9. Khaire, S.; Gaikwad, P.; Aralekallu, S.; Bhat, Z. M.; Kottaichamy, A. R.; Devendrachari, M. C.; Thimmappa, R.; Shafi, S. P.; **Gautam, M**.; Thotiyl, M. O., An Interface-Controlled Redox Switch for Wastewater Remediation. *ChemElectroChem* **2018,** *5* (2), 362-366.

10. Thimmappa, R.; Fawaz, M.; Devendrachari, M. C.; **Gautam, M**.; Kottaichamy, A. R.; Shafi, S. P.; Thotiyl, M. O., Anisotropic amplification of proton transport in proton exchange membrane fuel cells. *Chem. Phys. Lett.* **2017,** *679*, 1-5.

11. Thimmappa, R.; Devendrachari, M. C.; Kottaichamy, A. R.; Aralekallu, S.; **Gautam, M**.; Shafi, S. P.; Manzoor Bhat, Z.; Thotiyl, M. O., 2.6 V Aqueous Battery with a Freely Diffusing Electron Acceptor. *J. Phys. Chem. C* **2017,** *121* (7), 3707-3713.

12. Thimmappa, R.; Kottaichamy, A. R.; Devendrachari, M. C.; Aralekallu, S.; Shafi, S. P.; **Gautam, M**.; Kotresh, H. M. N.; Thotiyl, M. O., Proton Exchange Membrane Fuel Cell with a Pt-free Cathode and a Freely Diffusing Electron Acceptor. *ChemElectroChem* **2017,** *4* (2), 283-286.

13. Bhat, Z. M.; Thimmappa, R.; Devendrachari, M. C.; Shafi, S. P.; Aralekallu, S.; Kottaichamy, A. R.; **Gautam, M**.; Thotiyl, M. O., A Direct Alcohol Fuel Cell Driven by an Outer Sphere Positive Electrode. *J. Phys. Chem. Lett.* **2017,** *8* (15), 3523-3529.

Copyright Clearance Center   RightsLink®

Home | Help | Email Support | Sign in | Create Account

Coulombic Force Gated Molecular Transport in Redox Flow Batteries

Author: Manu Gautam, Zahid M. Bhat, Abdul Raafik, et al

Publication: Journal of Physical Chemistry Letters

Publisher: American Chemical Society

Date: Feb 1, 2021

Copyright © 2021, American Chemical Society

12/4/2020

Rightslink® by Copyright Clearance Center

RightsLink®

Copyright Clearance Center

Home | Help | Email Support | Sign in | Create Account

ACS Publications
Most Trusted. Most Cited. Most Read.

Proton-Conducting Graphene Membrane Electrode Assembly for High Performance Hydrogen Fuel Cells

Author:
Ravikumar Thimmappa, Manu Gautam, Mruthyunjayachari Chattanahalli Devendrachari, et al

Publication: ACS Sustainable Chemistry & Engineering

Publisher: American Chemical Society

Date: Aug 1, 2019

Copyright © 2019, American Chemical Society

RightsLink®

Home | Help | Email Support | Manu Gautam ∨

A Rechargeable Aqueous Sodium-Ion Battery

Author: Ravikumar Thimmappa, Manu Gautam, Shambhulinga Aralekallu, et al

Publication: ChemElectroChem

Publisher: John Wiley and Sons

Date: Apr 5, 2019

© 2019 Wiley-VCH Verlag GmbH & Co. KGaA, Weinheim

Order Completed

Thank you for your order.

This Agreement between Mr. Manu Gautam ("You") and John Wiley and Sons ("John Wiley and Sons") consists of your license details and the terms and conditions provided by John Wiley and Sons and Copyright Clearance Center.

Your confirmation email will contain your order number for future reference.

License Number: 5020700491489

License date: Mar 02, 2021

🖶 Printable Details

📄 Licensed Content

Licensed Content Publisher	John Wiley and Sons
Licensed Content Publication	ChemElectroChem
Licensed Content Title	A Rechargeable Aqueous Sodium-Ion Battery
Licensed Content Author	Ravikumar Thimmappa, Manu Gautam, Shambhulinga Aralekallu, et al
Licensed Content Date	Apr 5, 2019
Licensed Content Volume	6
Licensed Content Issue	7
Licensed Content Pages	5

📄 Order Details

Type of use	Dissertation/Thesis
Requestor type	Author of this Wiley article
Format	Print and electronic
Portion	Full article
Will you be translating?	No

📄 About Your Work

Title	Manu Gautam
Institution name	IISER Pune
Expected presentation date	Mar 2021

📁 Additional Data

📍 Requestor Location

Requestor Location	Mr. Manu Gautam Department of Chemistry Main Building, IISER,Dr. Homi Bhabha Roa Pune,, Maharashtra 411008 India Attn: Mr. Manu Gautam

📄 Tax Details

Publisher Tax ID	EU826007151

$ Price

Total	0.00 USD

Would you like to purchase the full text of this article? If so, please continue on to the content ordering system located here: Purchase PDF

If you click on the buttons below or close this window, you will not be able to return to the content ordering system.

Total: 0.00 USD

CLOSE WINDOW   ORDER MORE

Rightslink® by Copyright Clearance Center

Copyright Clearance Center   RightsLink®

🏠 Home   ❓ Help   ✉ Email Support   👤 Sign in   👤 Create Account

ACS Publications
Most Trusted. Most Cited. Most Read.

Improved Synthesis of Graphene Oxide

Author: Daniela C. Marcano, Dmitry V. Kosynkin, Jacob M. Berlin, et al

Publication: ACS Nano

Publisher: American Chemical Society

Date: Aug 1, 2010

Copyright © 2010, American Chemical Society

PERMISSION/LICENSE IS GRANTED FOR YOUR ORDER AT NO CHARGE

This type of permission/license, instead of the standard Terms & Conditions, is sent to you because no fee is being charged for your order. Please note the following:

- Permission is granted for your request in both print and electronic formats, and translations.
- If figures and/or tables were requested, they may be adapted or used in part.
- Please print this page for your records and send a copy of it to your publisher/graduate school.
- Appropriate credit for the requested material should be given as follows: "Reprinted (adapted) with permission from (COMPLETE REFERENCE CITATION). Copyright (YEAR) American Chemical Society." Insert appropriate information in place of the capitalized words.
- One-time permission is granted only for the use specified in your request. No additional uses are granted (such as derivative works or other editions). For any other uses, please submit a new request.
If credit is given to another source for the material you requested, permission must be obtained from that source.

BACK   CLOSE WINDOW